UNIVERSITY OF CALIFORNIA

Los Angeles

Galactic Dynamics with Magnetic Fields

A dissertation submitted in partial satisfaction of the

requirements for the degree Doctor of Philosophy

in Physics

by

Gregory Gershom Howes

2004

The dissertation of Gregory Gershom Howes is approved.

Ferdinand V. Coroniti

James C. McWilliams

Mark Morris

Steven C. Cowley, Committee Chair

University of California, Los Angeles

2004

I dedicate this work to my loving parents.

Contents

List of Figures

List of Tables

ACKNOWLEDGMENTS

I would like to thank my collaborators, Mark Morris and Jim McWilliams, for providing invaluable advice and thoughtful guidance through the twists and turns of a doctoral research program. And I would like to extend sincere thanks to my advisor, Steve Cowley, for introducing me to the world of theoretical physics and supporting all my efforts in completing my doctorate.

VITA

October 18,1971	Born, Oakland, California
1993	National Undergraduate Fellow in Plasma Physics and Fusion Engineering University of Wisconsin, Madison
1994	B. A., 3/2 Combined Plan Program in Engineering and Liberal Arts (Physics Sequence) Occidental College Los Angeles, California
1994	B. S., Applied Physics California Institute of Technology Pasadena, California
1995	Rotary Ambassadorial Scholar Victoria University of Wellington, New Zealand
1995	Dip. App. Sci., Geophysics Victoria University of Wellington, New Zealand
1996–97	Adjunct Instructor of Physics Occidental College
1997–1999	Institute for Geophysics and Planetary Physics Fellow Department of Physics and Astronomy University of California, Los Angeles
1997–2000	Department of Energy Fusion Energy Sciences Fellow Department of Physics and Astronomy University of California, Los Angeles
1998	M. S., Physics Department of Physics and Astronomy University of California, Los Angeles

2000	Adjunct Instructor of Physics Occidental College
2000-2001	Graduate Student Researcher Department of Physics and Astronomy University of California, Los Angeles
2001-2002	Dissertation Year Fellowship University of California, Los Angeles

PUBLICATIONS

G. G. Howes and S. C. Cowley and J. C. McWilliams, "Local Buoyant Instability of Magnetized Shear Flows," *Astrophys. J.*, **560**, 617–629 (2001 Oct 20).

J. L. Maron and G. G. Howes, "Gradient Particle Magnetohydrodynamics: A Lagrangian Particle Code for Astrophysical Magnetohydrodynamics," *Astrophys. J.*, **595**, 564–572 (2003 Sep 20).

ABSTRACT OF THE DISSERTATION

Galactic Dynamics with Magnetic Fields

by

Gregory Gershom Howes
Doctor of Philosophy in Physics
University of California, Los Angeles, 2004
Professor Steven C. Cowley, Chair

Contributing to the effort to unravel the origin and understand the evolution of magnetic fields in the universe, this dissertation focuses on the evolution of the Galactic magnetic field through analytical and numerical approaches. The current state of research into magnetism in the universe is reviewed, with particular emphasis on synthesizing a unified view of the various environments in which magnetic fields have been observed. An analytical examination of the stability of magnetic fields in a sheared flow is presented. Gradient Particle Magnetohydrodynamics is a new computational algorithm for MHD simulation developed here with validation tests of the method to display its capabilities. Adaptive Particle Refinement provides a general adaptive framework into which this new algorithm can be fit, promising improved computational efficiency and better stability characteristics. A model for numerical evolution of the magnetized Galactic disk is described. Preliminary results of two-dimensional Galactic disk simulations are

analyzed to demonstrate the potential of this new computational tool and lend insight into the evolution of the Galactic magnetic field.

Chapter 1

Introduction

1.1 Magnetic Fields in the Universe

The identification of a non-thermal radio emission from the interstellar medium of the Milky Way as synchrotron radiation [4, 95, 169]—radiation emitted by relativistic electrons in a magnetic field [167]—marked the first chapter in the study of astrophysical magnetic fields. Subsequent Faraday rotation measure studies of the Milky Way [60] demonstrated that a magnetic field coherent on kiloparsec scales permeates the disk of our Galaxy. The mechanism by which such a large-scale field can be generated and maintained has provoked heated debate among galactic astronomers. Current observations demonstrate magnetic fields ordered on kiloparsec scales of microgauss strength both within galaxies and in clusters of galaxies; a swarm of theories have been proposed to explain various observations. But a complete picture of the origin and evolution of magnetic fields in the universe requires a synthesis of observations and concepts over all time and space scales, from the Big Bang to the present day, from the immense voids of intergalactic space to the subparsec scales of magnetized outflows from accretion

disks.

Proposed theories for the origin and evolution of magnetic fields fall into four general categories:

1. Cosmological Generation: Cosmological magnetogeneration before recombination

2. Protogalactic Dynamo: Dynamo amplification during structure formation

3. Galactic Dynamo: Galactic dynamo production of magnetic fields and ejection of fields into intergalactic regions

4. Compact Objects: Magnetization of large volumes of intergalactic space by highly magnetized jet outflows from compact objects

Numerous variants on these theories exist, as well as the possibility that a combination of these mechanisms may be operating.

For much of the universe the magnetohydrodynamic (MHD) equations provide an accurate description of the dynamics of magnetic fields [171]. In the MHD approximation, the magnetic field is evolved according to the induction equation

$$\frac{\partial \mathbf{B}}{\partial t} = \nabla \times (\mathbf{v} \times \mathbf{B}) + \frac{\eta}{\mathbf{4}\pi} \nabla^{\mathbf{2}} \mathbf{B}, \tag{1.1}$$

where η is the magnetic diffusivity, or molecular resistivity. The first term on the right hand side is the inductive term, the second is the diffusive term. The ionized interstellar medium is highly conductive so the diffusive term tends to be important only for magnetic fields at small scales. A useful approximate formula

for the magnetic diffusivity (in the range of conditions considered here) is given by

$$\eta = \frac{10^7 \text{ cm}^2/\text{s}}{T^{3/2}} \tag{1.2}$$

where the temperature T is given in eV. The plasma temperature in the interstellar medium varies enormously but the hot component is typically $T > 3$ eV. We can estimate the length scale below which resistivity will destroy the magnetic field over the lifetime of the universe, $\tau \sim 10^{10}$ years. This scale can be approximated by

$$L \sim \sqrt{\eta\tau/4\pi} \sim 10^{11} \text{ cm} \sim 10^{-8} \text{ pc} \tag{1.3}$$

At scales much larger than this, the resistive term may be neglected and the magnetic flux evolves as a frozen-in component to the interstellar medium [171]. For a frozen-in magnetic flux, one can derive a scaling relation between the magnetic field strength and the density of the interstellar medium given an isotropic expansion or collapse when the field is too weak to influence the dynamics,

$$B \propto \rho^{2/3}. \tag{1.4}$$

Likewise, the length scale of the magnetic field under the same conditions scales with density as

$$l_B \propto \rho^{1/3}. \tag{1.5}$$

In order for the magnetic field to change in time by (1.1), the field must initially be nonzero. If a magnetic field does not exist in the initial conditions of the universe, the inclusion of non-MHD effects to generate a seed magnetic field is required. Hence, theories typically require two separate processes to generate

the microgauss fields we observe today: the generation of an extremely weak seed field followed by a more efficient dynamo process to amplify that seed field on cosmologically short time scales to the presently observed magnitude. In most cases, the dynamo must be responsible for a field strength amplification of 10–15 orders of magnitude.

The majority of mechanisms for the generation of seed magnetic fields are based on a battery mechanism driven by non-parallel pressure and density gradients. Biermann [22] suggested keeping a pressure term in Ohm's Law, a term that is dropped in the MHD approximation, resulting in an extra term in the magnetic induction equation

$$\frac{\partial \mathbf{B}}{\partial t} = \nabla \times (\mathbf{v} \times \mathbf{B}) + \frac{\eta}{4\pi}\nabla^2 \mathbf{B} + \frac{c\nabla p_e \times \nabla n_e}{n_e^2 e} \tag{1.6}$$

where p_e is the electron pressure and n_e is the electron number density. This extra "battery" term in the induction equation generates magnetic field from zero-field initial conditions. This battery effect is a natural consequence of the fact that electrons and ions have the same charge but different mass. Any phenomenon that drives a non-barotropic flow, $p_e \neq p_e(n_e)$, leads to magnetic field generation through this battery effect. Although Biermann introduced the idea to explain the generation of magnetic fields in stars, a number of other plausible astrophysical causes for the battery production of magnetic fields have been proposed; most of the seed field generation mechanisms discussed below differ in detail but are based in general on this Biermann battery effect. Note also that the presence of two gradients in the battery term means that the battery term becomes non-negligible only at small scale. The seed fields thus generated are on the same scale as the

smallest structures in the environment; depending on the epoch of generation, however, these "small" scales may correspond to large scales, perhaps megaparsec scales, in the present day universe. A final point concerns the relative importance of the two terms in (1.6) as the magnetic field evolves. Initially, for zero or small magnetic field, the battery term dominates, typically effecting linear growth of the magnetic field at small scales. But as this seed field grows, the magnitude of the inductive term approaches that of the battery term. An estimate of the magnetic field strength at which these two terms are equal is informative. For a variation length scale L, the terms are approximately equal when

$$\frac{vB}{L} \sim \frac{cp_e n_e}{n_e^2 eL^2}. \tag{1.7}$$

Substituting $p_e = n_e kT_e$ and solving for B results in the expression

$$B \sim \frac{ckT_e}{veL}. \tag{1.8}$$

A typical temperature of the ionized component of the protogalactic medium is $T \sim 3$ eV. Assuming thermal equilibrium between the ions and electrons in the protogalactic plasma $T_e \sim T_i$, estimating the velocity as the ion thermal velocity $v_{T_i} = (kT_i/m_i)^{1/2}$, and taking the range of fluctuation lengths to be $L \sim 1$ pc to 1 kpc, the range of magnetic field strengths at which the two terms are equal is $B \sim 10^{-19}$G to 10^{-16}G. For field strengths much greater than this, the inductive term dominates, yielding exponential growth of the magnetic field if there exists any shear in the velocity field. This clarifies why a combination of two separate mechanisms are needed to explain the presently observed magnetic fields.

In a highly conducting medium, two types of turbulent dynamo are currently known: the *isotropic dynamo* and the *mean-field dynamo*. The isotropic dynamo—also known as the small-scale or fluctuation dynamo—operates in any homogeneous, isotropic turbulent flow by amplifying the magnetic energy by the random stretching of field lines [12, 94, 111]. Although the isotropic dynamo is indeed a dynamo by virtue of amplifying the magnetic energy at the expense of turbulent kinetic energy, it does *not* amplify the mean magnetic field. Thus, the isotropic dynamo produces a strong but highly tangled magnetic field; the bulk of the magnetic energy is concentrated at small scales [111, 123]. The growth rate of the magnetic field by the isotropic dynamo is determined by the turnover time of the smallest scale eddies in the turbulent cascade; these small eddies have short turnover times so this dynamo amplifies fast. In contrast, the mean field dynamo depends on anisotropy in the turbulence to achieve mean-field amplification via the α–Ω dynamo [130, 145, 159]. The requisite anisotropy—typically provided by rotation, stratification, shear, or strong magnetic fields [17]—leads to a non-zero helicity in the turbulent velocity field. This helicity is what leads to an amplification of the mean field. The mean-field dynamo has a growth rate typical of the turnover rate of the larger scale eddies; the turnover time for these large eddies is long, yielding a slow dynamo. Most studies of dynamo growth have concentrated on *kinematic growth* where the field is too weak to affect the flow. Both the isotropic and the mean-field dynamos will figure prominently in the following discussion of magnetic field generation and maintenance.

This discussion is organized on a principle similar to observational astronomy: as astronomers peer more deeply into space, and hence further back in time, they

necessarily can only observe objects that increase in size. I follow the chronology of the universe from distant times and immense spatial scales to the present day and smaller, nearer objects. I begin with a discussion cosmological mechanisms for magnetogenesis, move next to the immense voids of the intergalactic medium between galaxy clusters, then focus on the galaxy clusters themselves, and finally zoom into the magnetic fields of individual galaxies. I define now some terminology to clarify the discussion:

Intergalactic medium (IGM) the medium filling the universe outside of galaxy clusters

Intracluster Medium (ICM) the medium filling galaxy clusters outside of the constituent galaxies

Interstellar Medium (ISM) the medium filling the galaxy

As an additional reference, a timeline of major events in the history of the universe is presented in Figure 1.1. Magnetic field strengths and scale lengths quoted in this discussion are understood to be values for the comoving magnetic field, the values the field would have at the present time accounting for the expansion of the universe. In discussions of the formation of galaxies, the time of the formation of the galaxy is considered to be the point in time when the material of the galactic disk first becomes virialized. Before that point, we refer to the clumping and collapsing mass as a protogalaxy.

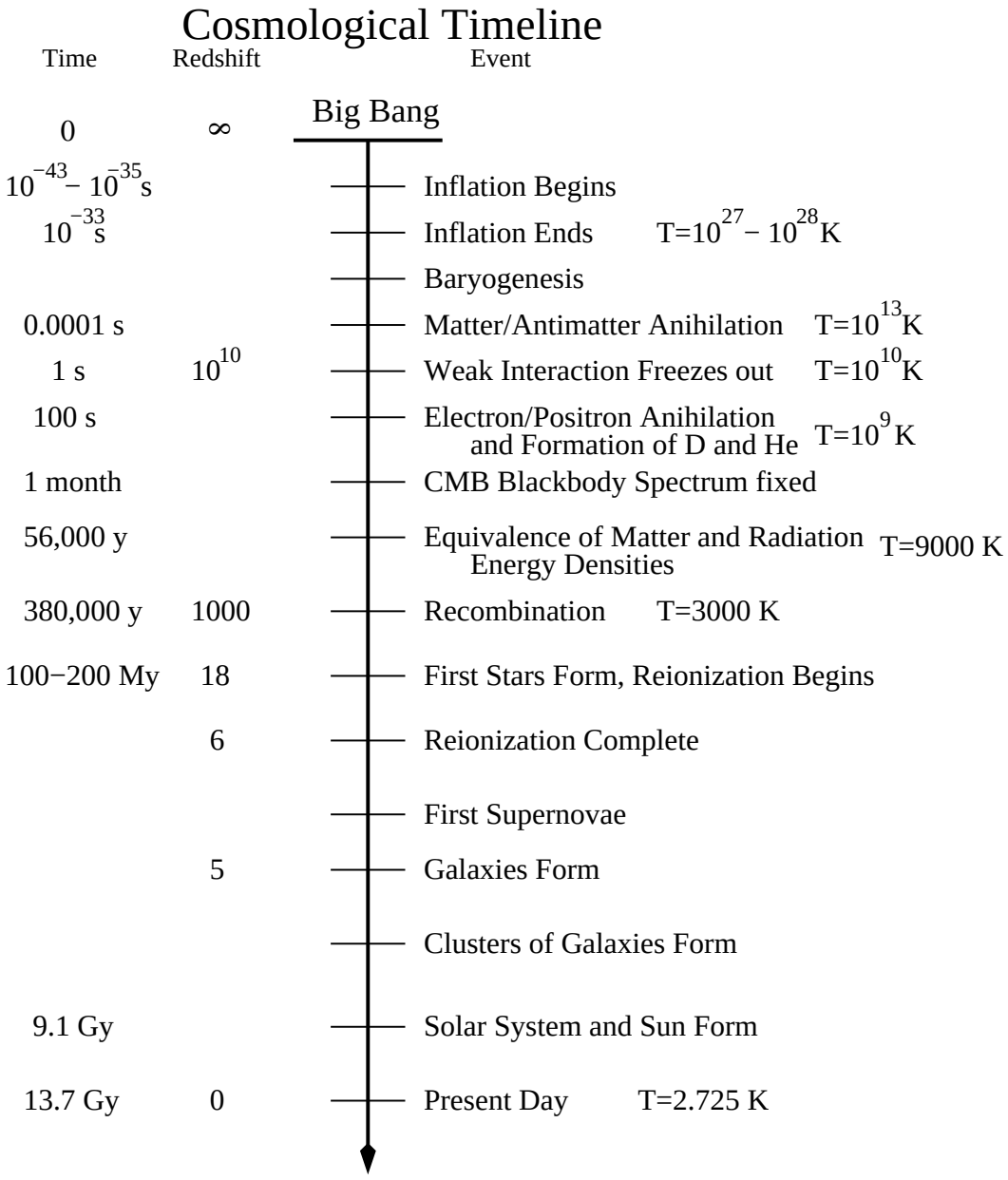

Figure 1.1: Cosmological timeline of of significant events in the history of the universe [191].

1.2 Magnetic Fields in the Early Universe

In this section, evidence for cosmological magnetogenesis is reviewed. Proposed mechanisms include the possibility that magnetic fields existed in the initial conditions, could be produced through some quantum gravitational mechanism, arose by battery action driven by plasma vortical motion during the radiation era, were generated in a quark-hadron phase transition or in an electroweak phase transition, were created through helicity in the electroweak baryogenesis, came about during inflation, or were amplified by vorticity generated by the movement of cosmic strings through the IGM. Grasso and Rubinstein [80] provide a thorough review of many of these particle-physics inspired mechanisms to produce magnetic fields. All of these theories fall within the first category of magnetogenesis models. Magnetic fields produced by any of these processes, however, may not have survived on relevant scales through the radiation era; magnetic and photon diffusion may destroy these fields on comoving scales less than a few megaparsecs [117, 14].

But whether any of these processes created a significant field by the time of recombination is constrained by observations of the Cosmic Microwave Background (CMB) radiation. The observed isotropy of this radiation suggests an upper limit for the field at recombination of a few times 10^{-9} G [2, 11, 180, 53]. This limit is not a strict constraint on a cosmological magnetic field; isotropic compression of a field at this magnitude would yield microgauss strength fields at galactic densities. The next generation of CMB radiation measurements promise the exciting possibility of a direct determination of the magnetic fields at recombination through

an examination of Faraday rotation in the polarization of the CMB [101]. These more sensitive measurements are needed to determine or rule out a cosmological origin for magnetic fields in the universe.

1.3 Intergalactic Magnetic Fields

Perhaps one of the most important unanswered questions in the study of astrophysical magnetic fields is whether the intergalactic voids are permeated by magnetic fields. The discovery of a pervasive magnetic field in the IGM would provide strong evidence that magnetic field strengths had reached a dynamically significant level before the formation of the first galaxies [195]. Indeed, if these voids have been untouched by structure formation they provide a relic of the pre-recombination plasma and field. A direct measurement of the IGM field, however, has not yet been accomplished; only upper limits for the IGM field have been established. Null results from Faraday rotation measure (RM) studies of distant quasars constrain the magnitude of a cosmologically aligned magnetic field to $B_{IGM} < 10^{-11}$ G. If the analysis posits not a cosmological field but a field with a reversal scale of about 1 Mpc, the constraint is eased to allow a field of $B_{IGM} < 10^{-9}$ G [104, 109]. Unfortunately, because of the need for independent estimates for the electron column density and magnetic field reversal scale in the IGM, only model-dependent upper bounds can be derived from these extragalactic measurements of RM [80].

The high conductivity of the IGM means that magnetic flux and magnetic helicity are nearly conserved during the evolution of the universe [80, 43]. This

approximate conservation means that a large-scale magnetic field generated during a cosmologically early epoch would persist throughout the age of the universe and would likely influence structure formation at all scales, from cluster to galaxy to star formation.

One end of the spectrum of thoughts on the magnetic history of the universe suggests that all structure formation occurred in a highly magnetized environment (this corresponds to the first or possibly the second general categories of magnetogenesis theories). A useful yardstick in evaluating the magnetic field in the IGM is to estimate the magnitude of B_{IGM} necessary to produce the observed fields in the ISM of galaxies purely through isotropic compression. Given a density ratio to a galaxy of $\rho_{IGM}/\rho_{ISM} \sim 10^{-6}$ and a galactic magnetic field strength of $B_{ISM} = 10^{-6}$ G, then using (1.4) we require $B_{IGM} = 10^{-10}$ G. These values coincide roughly with the model-dependent upper bounds currently available from observations; the next generation of more sensitive measurements of the magnetic field in the IGM will undoubtedly impact evaluations of the four categories of models. A field strength of a microgauss or stronger would influence the formation of the galactic disk. Since a field of $B_{IGM} = 10^{-10}$ G would yield a microgauss field upon compression to galactic densities, the existence of a significant IGM field will have profound implications for galaxy formation.

1.4 Creating Magnetic Fields During Large Scale Structure Formation

If no magnetic fields existed after recombination, the creation of a seed magnetic field can be accomplished by several mechanisms during structure formation. The anisotropies evident in the CMB radiation reveal density fluctuations present at recombination that seeded the formation of structure in the universe through gravitational collapse. This collapse is likely to have driven both multiple shocks and vortical Kolmogorov turbulence throughout the protogalactic medium. Kulsrud et al. [112] argue that the gravitational collapse from structure formation, driven by the small seed fluctuations in the density, leads to supersonic turbulence in the protogalactic medium. Intersections of the resulting shocks can generate small scale magnetic fields through battery action. Numerical simulations employing a cosmological hydrodynamic code produced seed fields up to 10^{-21} G in magnitude by redshift $z \sim 2$–3. Gnedin, Ferrara, and Zweibel [76] performed detailed numerical simulations to verify a suggestion by Subramanian, Narasimha, and Chitre [181] that the propagation of cosmological ionization fronts through density irregularities during reionization would be a fertile ground for the generation of magnetic fields by the Biermann battery mechanism. Simulations found seed field strengths up to 10^{-19} G, ordered on megaparsec scales, by redshift $z \sim 4$. Davies and Widrow [59] extended the work by Kulsrud et al. [112] to follow the collapse of a protogalaxy, leading to coherent seed fields on the scale of the galaxy of magnitude up to 10^{-17} G by the time the galactic disk has formed. Collectively these arguments suggest that a minute seed field at least of order 10^{-21}–10^{-18} G

with a coherence on at least a scale of tens of kiloparsecs, existed by redshift $z \sim 3$–4.

The seed field created in the protogalactic plasma can also be amplified by the vortical turbulence created by gravitational collapse. Kulsrud et al. [112] showed in an analytic calculation that amplification by the isotropic dynamo, for which the growth rate is on the order of the turn-around time for the smallest eddies in the Kolmogorov turbulent cascade, is probably capable of bringing the magnetic field energy to a saturated state in equipartition with the turbulent kinetic energy. The largest eddy in the turbulence in this tenuous protogalactic medium has a size of megaparsec scale; the mean free path has the scale of hundreds of kiloparsecs [113]. A seed magnetic field, presumably produced either before recombination or during structure formation, will be exponentially amplified by the isotropic dynamo to saturation with the turbulence. The isotropic dynamo, however, is known to amplify the magnetic energy primarily at small (resistive) scales [162]. It has been suggested that collisionless plasma processes can change the generation of magnetic fields at scales below the mean free path [113], but more research is needed before this can be determined. As the protogalactic medium cools, the mean free path decreases, leading to the generation of fields on smaller and smaller scales.

The generation of magnetic fields by the isotropic dynamo during structure formation in the universe depends heavily on the details of the structure formation model. The range of scales of the turbulent energy spectrum in the protogalactic IGM, the robustness of incompressible Kolmogorov-like turbulence during the extremely compressible gravitational collapse of structure formation, the length

of time during which this turbulence persists, and the effectiveness of collisionless plasma processes in inhibiting small-scale magnetic field production are all highly uncertain. This second category of magnetogenesis model clearly merits further investigation. Key observations that would help clarify the issues are:

1. More sensitive observations of the IGM magnetic field. Fields of magnitude 10^{-10} G or greater would be significant.

2. Measurements of fields in objects at redshifts of $z \sim 5$.

3. Measurements of Faraday rotation in the polarization of the CMB to detect fields of magnitude 10^{-10} G or greater.

1.5 Cluster Magnetic Fields

Observations of magnetic fields in galaxy clusters consistently find magnitudes on the order of 1–10 μG and coherence lengths on the order of 10 kpc; these magnetic fields are seen to extend out to at least 0.5 Mpc from the cluster cores [43]. Cooling flow clusters yield local values of the magnetic field up to 10–40 μG [105]. The spatial distribution of RM observations of the Hydra A cluster implies a 6 μG magnetic field coherent on a scale of 100 kpc; the total strength appears to be about 30 μG coherent on scales of 4 kpc [182]. Comparison of hard X-ray emission interpreted as inverse Compton scattering and synchrotron radiation provides evidence against the existence of significantly stronger cluster magnetic fields on scales below the resolution of RM observations [43].

The evidence of ubiquitous, microgauss strength magnetic fields in galaxy clusters raises the key question: where did they come from? More specifically, there are three possible origins of cluster fields: the first is that fields existed prior to cluster formation and were frozen into the cluster, the second that they were generated by dynamo processes in the ICM itself, the third that these fields were ejected from galaxies or compact objects into the cluster medium.

1.5.1 Evidence Against a Pre-Cluster Origin for Magnetic Field

If the observed cluster magnetic fields existed before the formation of the cluster, we can estimate the strength of the IGM field necessary to explain the field in the ICM. Assuming the magnetic field is frozen-in to the IGM and that the collapse occurs isotropically, (1.4) gives the relation between the magnitude of the field and the medium mass density. The ratio of the mass densities is $\rho_{IGM}/\rho_{ICM} \sim 10^{-3}$, so for a cluster field strength of $B_{ICM} \sim 10^{-6}$ G, this yields an intergalactic field of $B_{IGM} \sim 10^{-8}$ G. Constraints on the magnetic field at recombination suggest that the present day field from a cosmological source could be no greater than a few times 10^{-9} G. Additionally, the observations discussed in Section 1.4 exclude an intergalactic field of $B_{IGM} > 10^{-9}$ G, although observational constraints on IGM fields are rather weak. Hence, it appears that the present magnitude of magnetic fields in galaxy clusters is difficult to explain by the cosmological mechanisms of category one.

1.5.2 Evidence for and against Dynamos in Cluster Plasmas

The second possibility is that the ICM magnetic fields are generated within the ICM itself through some dynamo process. Without strong rotation or another source of anisotropy in the cluster dynamics, the amplification of this field must be due to the isotropic turbulent dynamo. This dynamo could have been driven by turbulence excited during the formation of the cluster. Before virialization of the cluster, ample gravitational binding energy is released during the collapse of the cluster to fuel the isotropic dynamo. The cluster fields could have been amplified from an existing field to the present levels; as the gravitational collapse halted and ceased to drive turbulence, the isotropic dynamo could have shut off.

The turbulence in clusters now is believed to be driven by the motion of galaxies through the ICM; the observed velocity dispersion is $\sigma \sim 10^3$ km/s [179, 8]. To estimate the volume filling fraction of the turbulence in the cluster, we compare the total cluster volume to the volume stirred up by all of the cluster galaxies. Using the estimated values given in Table 1.1, the volume of the cluster is $V_c \sim l_c^3 \sim 3.4 \times 10^9$ kpc^{-3}. We approximate the volume stirred by an individual galaxy by $V_g \sim 5l_g^3 \sim 4 \times 10^4$ kpc^{-3}, so the total turbulent volume is $V_t \sim n_g V_g \sim 4 \times 10^7$ kpc^{-3}, or about 1% of the total cluster volume. The time for the galaxies to sweep through the entire volume of the cluster is given by $\tau \sim V_c/(5l_g^2 v_g n_g) \sim 10^9$ years, or about 10% of the lifetime of the cluster. The total magnetic energy contained in the ICM magnetic field is given by $E_B \sim V_c B_{ICM}^2/(8\pi) \sim 9.1 \times 10^{61}$ ergs; the total kinetic energy in the observed ICM turbulence is given by $E_K \sim n_g m_H v_g^2 V_t \sim 8.6 \times 10^{60}$ ergs. The energy released

Cluster size	l_c	1.5 Mpc
Galaxy size	l_g	20 kpc
Number of galaxies	N_g	1000
Velocity of galaxies	v_g	1000 km/s
ICM Magnetic Field	B_{ICM}	5 μG
Cluster Number Density	n_c	10^{-3} cm^{-3}
Cluster Age	τ_c	10^{10} years

Table 1.1: Typical astrophysical quantities for clusters of galaxies.

during gravitational collapse however is of order $10^{62} - 10^{64}$ ergs. Thus on energetic grounds, a turbulent dynamo driven by the flows during formation is highly likely but dynamo action is probably currently inactive. It is not known if fields created by this dynamo could unwind during turbulence free periods (resistive decay is negligible). (See [160] for a different perspective on turbulent dynamos in galaxy clusters.) But the isotropic dynamo generates a spectrum of magnetic energy that peaks at small scales [111, 123, 162], so one must explain the apparent lack of observed small-scale magnetic fields. One possible way of accomplishing this is to begin with a magnetic field that is within a few orders of magnitude of the observed upper bound of IGM fields, $B_{IGM} < 10^{-9}$G. The isotropic dynamo driven by the cluster collapse would only need to amplify the field a few orders of magnitude in the short time of the collapse; and, the strength of the initial magnetic field could be enough to prevent tangling of the field at small scales.

1.5.3 Evidence for Fields Ejected Into Cluster Plasmas

The third possibility is that the magnetic fields in the ICM were generated in a galactic dynamo and subsequently ejected into the ICM. The metallicity of the

cluster plasma is estimated to be about 30% of the solar value, suggesting that the material comprising the ICM has been polluted by material from galaxies [3]. If this material was cycled through galaxies and compact objects, it could certainly have brought the magnetic field with it. A low metallicity in the ICM would have discounted an origin for the ICM fields by ejection from galaxies or compact objects. However, both the magnitude and the coherence length of cluster fields are difficult to explain from a galactic origin. Specifically given a frozen-in field related to the density by (1.4) and a typical galactic number density of $n_c \sim 1$ cm^{-3}, fields from a galactic origin would have a magnitude of $B_{ICM} \sim 10^{-8}$ G, two orders of magnitude smaller than the observed cluster fields. Galactic fields are coherent on kiloparsec scales, so the expansion of the magnetic field coherence length according to (1.5) could explain ICM fields on scales of 10 kpc. But the observations of Hydra A, demonstrating tangled fields of strength up to 30 μG and large-scale coherence up to 100 kpc [182], suggest that a galactic origin for the ICM magnetic field is unlikely without some additional dynamo amplification of the ejected field. One alternative viewpoint is that of the modified galactic dynamo proposed by Parker [146], described later in Section 1.6, whereby magnetic buoyancy causes loops of field to rise from the galactic disk; the frozen-in ISM can drain down along the field line allowing the magnetic field to rise further and to expand in an anisotropic manner that does not follow (1.4). Some topological reconnection is then necessary to release this expanding magnetic field loop from its tie-down points in the galactic disk. Again, the question of scale is difficult to answer by this mechanism since these reconnected field loops would likely form on subkiloparsec scales.

The possibility that cluster magnetic fields were created in and ejected from compact objects inside galaxies has received much recent attention. Active galactic nuclei (AGN) and their associated extragalactic jet and radio lobe systems have been proposed as possible sites for magnetogenesis. Observations of these systems suggest that magnetic fields are critical to the operation of these systems [42]. The magnetized accretion disk around the massive black hole at the center of an AGN can tap the energy of the black hole to produce a highly collimated outflow of magnetized plasma into the ICM [55]. Models suggest that Kelvin-Helmholtz instabilities in a shear layer in such an astrophysical jet can yield fast amplification of the magnetic field [192, 52]. The megaparsec scale magnetized radio lobes in the rarefied IGM are estimated to be overpressured in their environment and to continue expanding even after the source galaxy has passed its active phase; Kronberg et al. [107] claim that the subsequent expansion and diffusion can magnetize large volumes of the IGM. They also argue that the magnetic energy ejected from cluster embedded AGNs is sufficient to account for the observed ICM fields beyond the inner core of the host cluster. Jet and radio lobe systems can yield dynamo amplification of magnetic fields on time scales $\tau < 10^8$ years; this can explain observations of magnetic fields in high redshift quasars [105].

Starburst regions are another possible site for magnetic field generation from compact objects. Observations of starburst galaxy M82 demonstrate significant outflow from the starburst region as well as significant large-scale magnetic field directed out of the galactic plane [105]. This outflow appears to be expelling both ISM plasma as well as magnetic field at greater than the escape velocity for the galaxy. The timescale of the α–Ω dynamo for the out-of-plane field component is

on the order of 10^{10} years yet these outflows occur on a timescale of 10^8 years; the expelled magnetic fields, therefore, must be produced by the outflow phenomenon. A galactic scale version of the Biermann battery has been proposed to explain the dynamo properties of the starburst outflow in M82 [118]. Another theory suggests that a volcanic stage of starburst activity in dwarf galaxies at an early epoch could seed the universe with strong magnetized outflowing winds [108].

An important issue in the discussion of cluster magnetic fields is what process is responsible for limiting the cluster field strength. If galaxies or compact objects are continually injecting magnetic energy into the ICM, what limits the field strength to the order of magnitude of $1 - 10$ μG that is broadly seen across cluster observations? One possible explanation of the uniformity of observed field strengths is that the magnetic field is limited by magnetic buoyancy; if the field strength exceeds an equilibrium value, it rises buoyantly against the gravitational forces of the cluster. This sets the plasma $\beta = 4\pi p/B^2$ to be of order one and the time to rise through the cluster to be of order 3×10^9 years. Stronger fields are effectively boiled off into the IGM.

The arguments for a compact object origin for the cluster magnetic fields are based on energetic grounds. The calculations and modeling of the process of field ejection are crude and suspect. For example, it is not clear exactly how the field "diffuses" into the IGM and ICM; it certainly cannot be resistive diffusion. Another important point issue is the scale of the observed magnetic fields in the ICM. A convincing argument for the production of a coherent field over 100 kpc from compact objects has not been given.

1.6 Galactic Magnetic Fields—Observations

Observations of magnetic fields in spiral galaxies show a uniform field component of strength 3–4 μG ordered on kiloparsec scales [17, 195]. The ratio of uniform, or large-scale, magnetic field strength to random, or small-scale, magnetic field strength is typically around 0.5, but can drop to about 5% in regions of vigorous star formation [195]. Since polarized synchrotron emission and Faraday RM measurements depend differently on the magnetic field volume filling factor, the near equivalence of coincident measurements by each method suggests that the filling factor is not very small [17]. Magnetic field intensities typically increase towards the galactic center and within spiral arms with a larger proportion of magnetic energy at smaller scales in these regions. The field appears to be more well-ordered in interarm regions and in the outer parts of the galactic disk [105]. Strength of the ISM magnetic fields appear to decline more slowly than disk matter density with galactocentric radius [137, 13]. Magnetic field strengths appear to correlate with the neutral hydrogen column densities in galactic disks and in molecular clouds [82].

Coherence scale measurements within the Milky Way are not consistent in the estimation of the size and magnitude of the small-scale magnetic field. For a total magnetic field given by $B_t^2 = B_u^2 + B_r^2$, where B_u is the largest scale component and B_r is the magnitude on smaller scales, polarization measurements of synchrotron radiation suggest $B_u^2 \sim 0.5 B_r^2$ [177] while pulsar RM data yield $B_u^2 \sim 0.1 B_r^2$ [155, 140]. A variety of measurement techniques have found evidence for fluctuation over distance scales from less than a parsec [129] to 50–100 pc

[155, 140] to 1 kpc [93]. Each of these methods samples only a limited range of fluctuation sizes, and each measurement finds a fluctuation at least as large as the uniform field; in some cases it is possible the measurement samples a localized fluctuation atypical of the Galactic disk as a whole. Howard and Kulsurd [88] argue that the belief that the magnetic field in the galaxy does not reverse on small scales is based on the analyses [155] of rotation measures of pulsars [81] that employed only models with fields that changed on scales of the order of 1 kpc.

The dominant energy density is the kinetic energy of the galactic rotation in balance with the gravitational potential energy of the galaxy. Below these, the energy density of the magnetic field is typically in equipartition with the thermal energy density, the cosmic ray energy density and the kinetic energy density of the small-scale turbulent motions [105, 80]. In the Magellenic Clouds and M82, however, the magnetic fields seem to be stronger than equipartition with the turbulent kinetic energy [195].

The geometry of the galactic magnetic field is typically a global field organized on a grand scale, often similar to spiral structure of the ISM density. The azimuthal structure is typically characterized as an Axisymmetric Spiral Structure (ASS) or a Bisymmetric Spiral Structure (BSS); the vertical structure is characterized as odd (dipolar) or even (quadrupolar). Observations show examples of galaxies with field of each type and some galaxies show a mixed structure [17]. A Fourier decomposition of annular rings of the magnetic field are usually well fit by a combination of only the $m = 0$ and $m = 1$ components, indicating a genuine global structure [17]. The pitch angle of the magnetic field is typically about $p = -(10°–35°)$ inclined to the azimuth [17]. RM data give an indication of

two reversals of azimuthal field direction within the solar orbit in the Milky Way [154]; there is also evidence for two more reversals outside of the solar circle [54]. Magnetic field reversals have also been observed in M81 [103]. At Galactic Center of the Milky Way, a strong vertical magnetic field of approximately 1 mG is inferred from observations of nonthermal radio filaments [134]; this strong central field is estimated to contain a significant fraction of the total vertical magnetic flux in the Galaxy [48].

Some galaxies show an extensive radio halo indicating large scale heights for the magnetic field [195]. The magnetoionic scale height of the Milky Way is 1.4 kpc [172] and the scale height of the hot gas is approximately 1 kpc [110, 156]. External edge-on galaxies show full synchrotron widths of 2–4 kpc [99, 90]. Larger halos are typically observed in galaxies with increased star formation activity. Halo magnetic fields are typically associated with outflowing winds driven by supernovae and related stellar activity [87].

1.7 Galactic Magnetic Fields—Theory

Since discovery of the ordered kiloparsec-scale magnetic field in our Galaxy [60], debate on the origin of the Galactic magnetic field has focused on whether a microgauss field existed when the Galaxy was formed or whether the field was generated by some dynamo process during the lifetime of the Galaxy. Recent observations of cluster magnetic fields require a broader view of astrophysical magnetism, but a review of the present view on the galactic dynamo is worthwhile.

Much has been written about the origin of Galactic magnetic fields—most of

this literature has concentrated on the growth of magnetic field in the galactic disk by dynamo action [145, 159, 17]. In many of these theories the galaxy is assumed to have formed with nothing but a miniscule seed field. The subsequent kinematic growth of field due to the α–Ω dynamo has been studied extensively and related to observations. There has been relatively little consideration of the possibility that the field that we observe is the relic of a significantly strong field present at the time of galaxy formation [152, 88]. In this section we will consider the theoretical arguments given for both possibilities.

The field is shaped by the turbulent flows and the galactic rotation. Let us briefly consider the approximate sizes of the flows in our galaxy. The shearing time of the galactic rotation is 2×10^8 years and it has a kinetic energy density in the ISM equivalent to a 300 μG field. Turbulence in the galaxy comes from many sources but the dominant energy input in the disk is from supernova explosions—this energy input is consistent with the observed turbulence levels. The explosions produce flows of order 10 km s^{-1} with scale sizes of order 100 pc. The largest turbulent eddies have energy density equivalent to a 3 μG field and a turnover time of 10^7 years. The smallest turbulent eddies (assuming a Kolmogorov cascade to small viscous scales) have a scale of order 0.1 pc in the warm ISM [123]. These small eddies have an energy density equivalent to a 0.1 μG field and a turnover time of 10^5 years.

Maron et al. [123] consider the evolution of a small seed field in the galactic flows. There are three obvious stages:

- **Stage 1.** While $|\mathbf{B}| \ll 0.1$ μG the small viscous eddies amplify the field via

an isotropic dynamo on a timescale of 10^5 years. The field is highly folded on small sub-viscous scales.

- **Stage 2.** When $3\ \mu\text{G} > |\mathbf{B}| > 0.1\ \mu\text{G}$ the supernova scale eddies amplify the field via an isotropic dynamo on a timescale of 10^7 years. Simulations show that the field remains on the sub-viscous scales and amplifies to equipartition with the turbulence [162].

- **Stage 3.** When $|\mathbf{B}| \sim 3\ \mu\text{G}$ the disk geometry, galactic rotation, helicity in the turbulent flows can play a role on the galactic rotation timescale 2×10^8 years. On this timescale the field must be shaped into the observed field.

Detailed numerical studies resolving the resistive dissipation scales with large magnetic Prandtl number have indeed demonstrated that the magnetic energy spectrum peaks in the subviscous range in Stages 1 and 2 [123, 162]. These simulations did not involve any anisotropy, so without the resulting helicity in the turbulence (or effects from disk geometry), no mean-field dynamo action occurs; but the dynamics at the small scales, which are the critical dynamics underlying the idea of turbulent diffusivity, should be unchanged in the absence of helical forcing. There is no convincing evidence, however, that Stage 3 does produce the observed field structure. Simulations of Stage 3 (even simplified ones) have not been done. Some of the work described in this dissertation is the preparation of simulation tools to perform simplified Stage 3 simulations.

The application of the kinematic mean-field dynamo to galactic disks (see for example [159, 17]) is hard to justify. The timescale for this dynamo is long and

as demonstrated above the field will have attained rough equipartition (the result of Stages 1 and 2) before the mean-field dynamo gets going. The kinematic approximation is thus incorrect. However it is possible (although unproven) that the mean-field dynamo approach is approximately correct for Stage 3. Indeed this debate has a long contentious history. Piddington [152] first suggested that at high magnetic Reynolds number the magnetic field generated at small scales would be strong enough to suppress turbulent diffusion, a necessary ingredient for the operation of the dynamo. Parker [144] countered this argument claiming that reconnection would limit the growth of the magnetic field at small scales. Subsequent numerical simulations called Parker's claim into question by demonstrating reduced turbulent diffusivity even at weak mean-field values [46]. Arguments have been made that the growth of strong small-scale fields will halt the dynamo before large-scale fields can develop [111, 113]. Several researchers attempted to model this effect as quenching of the α-effect and of turbulent diffusivity [46, 187, 135, 71, 29]. In these studies the effect of the small-scale field is modelled by a dependence of α and turbulent resistivity on the mean field. Such models implicitly assume that the small-scale field is somehow proportional to the mean field. This is not true for example in Stages 1 and 2 where the small-scale field, but not the mean field, grows on the fast timescales. In recognition of this suppression of turbulent diffusivity, Parker [146] proposed a modified α–Ω dynamo model where inflation of field loops vertically out of the disk by cosmic ray pressure and magnetic buoyancy could (he claimed) yield fast reconnection and hence solve the diffusivity problem. More recent work has focused on dynamical quenching models constructed to conserve magnetic helicity [71, 29]. The difficult

problem of the quenching of the α-effect and turbulent diffusivity remains controversial. It must be emphasized that it is not clear that the nonlinear Stage 3 dynamo can be modelled via some modified mean-field approach. There is clearly a need for a detailed numerical study of Stage 3 dynamics.

Despite the above reservations about its applicability, the mean field α–Ω dynamo model has been applied to explain the observed magnetic fields in galaxies. It has had some success in reproducing qualitative and some quantitative aspects of observed galactic magnetic fields; here we present a broad overview of dynamo model results to date. The fastest growing mode in the linear dynamo theory is assumed to dominate; realistic dynamo models produce prominent modes of low order, in agreement with the global design seen in observations, a result that is not *a priori* obvious [105]. Dominant field geometries are typically axisymmetric spiral structures with a vertical component that is even across the galactic plane; the fields are predominantly azimuthal due to the strong shear caused by differential rotation. The pitch angles of the magnetic field also lie within the observed range. These large scale field structures are qualitatively consistent with observations. The timescale for α–Ω dynamo amplification is $\tau \sim 10^8 - 10^9$ years. At small galactocentric radii, where differential rotation is weak, the α^2 dynamo [102] operates, leading to a predominantly dipolar field structure in the central region [17, 195].

Observations of microgauss magnetic fields in high redshift objects cast doubt on the ability of the "slow" galactic dynamo operating on the galactic rotation timescale of 10^8 years to yield such large fields when the galaxies at that epoch would only have rotated a few times [105]. Also, slowly rotating galaxies, such

as the Large and Small Magellenic Clouds, demonstrate saturated fields of the same magnitude as larger spiral galaxies, whereas the α–Ω dynamo would suggest weaker equilibrium fields [120, 100, 98, 105]. As well, observations of M82 suggest strong outflows of poloidal (vertical) magnetic field from the disk, occurring on a timescale of 10^8 years; the timescale for replenishment of out-of-plane vertical fields by the galactic dynamo is on the order of 10^{10} years, so it appears that the strong outflows must include some mechanism for fast dynamo action to produce these fields [105]. In addition, both M82 and the Magellenic Clouds appear to contain fields stronger than equipartition with the turbulence, a result that the galactic dynamo cannot accomplish [195]. The strong outflows observed in M82 may also disrupt the standard α–Ω dynamo, preventing the necessary recycling of magnetic field to achieve amplification [105]. Finally, although the cosmic ray energy density appears to be in equipartition with both the magnetic energy density and the turbulent kinetic energy density, the effect of the cosmic rays are neglected in the α–Ω dynamo formalism.

The alternative to a galactic dynamo that generates microgauss magnetic fields within the lifetime of the galaxy is that such a strong field already existed at the formation of the galaxy (regardless of its origin). Such a strong field would have certainly affected the formation of the galactic disk. Therefore, it is useful to examine the consequences of a previously existing field. As well, it is not inconsistent with observation that galaxies have evolved in a magnetized environment of microgauss strength over most of cosmic lookback time [105]. In this case, resistivity is negligible and the field evolves through advective motions in the ISM.

If a significant large-scale magnetic field exists at the point where the galactic disk has formed, most configurations of the initial field will be wrapped into a bisymmetric spiral by the differential rotation in the radial direction with all components displaying an even symmetry about the galactic plane; if the field is initially nearly vertical, differential rotation in the vertical direction will cause the azimuthal field to become an odd function in the vertical direction [194]. The magnitude of the azimuthal component increases linearly with time while the radial distance between reversals decreases as t^{-1}. The number of reversals observed in the Galaxy is about one tenth of the number expected under this scenario. Vertical transport of the field, however, can reduce the number of expected reversals by several processes: a galactic fountain can produce localized hot upflow [168] and cool downflow [36]; also, ambipolar diffusion may cause the magnetic field (frozen-in to the ionized component of the ISM) to drift with respect to the neutrals [88] along the magnetic pressure gradient vertically away from the galactic plane [145]. Turbulence in the ISM is not an important ingredient in this model, so the apparent equipartition of magnetic energy with turbulent kinetic energy appears to be unexplained. However one possibility is that the magnetic field may rise through a magnetic buoyancy instability [145] when the total field strength becomes too large [197]. Indeed such buoyant instabilities arise when the field reaches the observed level where the plasma β is of order one. Since the ISM heating and the turbulence are fed by supernova explosions it is not surprising that the thermal energy density of the plasma and energy density of the turbulence is similar. Thus the equipartition of the magnetic energy with the turbulent kinetic energy can be explained.

Howard and Kulsrud [88] performed a more careful study of the existing field hypothesis to arrive at a more refined model of the field evolution. For a magnetic field threading vertically through the disk, stretching of the field by the galactic differential rotation is limited by magnetic buoyancy and ambipolar diffusion in the vertical direction; both forces tend to tilt the line towards vertical when the field becomes strong. This tilting of the magnetic field out of the plane of the disk reduces the horizontal length of the field in the disk (decreasing both the radial and azimuthal components). The amplification of the field decreases gradually since the radial extent of the field line is reduced. The resulting magnetic structure is primarily azimuthal, but its direction reverses rapidly with radius on a scale of about 100 pc and it slowly decays as the amplification decreases. If the strength of the initial field varies across the galactic disk, the regions of stronger field will dominate, yielding a net Faraday RM when viewed at scales much greater than the reversal scale; additionally, at these scales the field would appear to have an axisymmetric spiral structure. Parker objected that a primordial field would be expelled from the disk through flux expulsion [130] either by ambipolar diffusion [142] or by turbulent diffusion [144, 143]. These objections are incorrect since the vertical field threading the galactic disk cannot be expelled from the disk without unphysical radial motions outward [88].

Regardless of some of the finer details above, it is conclusive that *if* the magnetic field lines are frozen into the plasma component of the ISM, the field lines *must* wrap up tightly, reversing direction on a short radial scale. Beck [17] claimed that this argued for the existence of an effective turbulent diffusion in the ISM,

for without it the field would wind up so tightly that it would resemble no observed galaxy. But Howard and Kulsrud [88] countered that this conclusion is not necessarily at odds with observational data, only that an assumed coherence scale of about 1 kpc has generally been used to analyze Faraday RM data. One consequence of a rapidly reversing field would be occasional large fluctuations in the RM data but little Faraday depolarization of the background radio emission.

The widely held belief that the geometrical structure of galactic magnetic field can distinguish between an existing magnetic field and a dynamo generated magnetic field [175] is found to be false in detailed studies of dynamo theory and existing field theory: appropriate tweaks of dynamo models and quenching prescriptions have produced BSS fields [16], while the appearance of an ASS field may indeed be created by an existing field [88]. The symmetry of the vertical field may be more useful in distinguishing the field origins, but the much smaller magnitude of the vertical component of the field makes conclusive observations elusive [195].

Both dynamo and existing field theories are somewhat incomplete. Although it appears that the cosmic ray energy density, the magnetic energy density, and the turbulent kinetic energy density are all in equipartition, standard mean field dynamo theory neglects the effects of the cosmic rays, and existing magnetic field theory generally neglects the effects of the turbulence in the ISM. Nor does dynamo theory include any connection to the spiral arm structure of the ISM density; and, the prediction of the behavior of a frozen-in field as it passes through the spiral arm density wave, that the field will bend to be more parallel to the spiral arms, has not been observed.

One point of view from which to examine the problem of galactic magnetic fields is to look for any evidence for or against field strength evolution in galaxies since the time of galaxy formation [105]. The microgauss magnetic fields observed in a number of high redshift objects suggests the possibility that galaxies formed in an environment of microgauss fields. If the vertical flux inferred to exist at the Galactic Center of the Milky Way [134] does indeed exist, the total vertical flux in the disk—a conserved quantity in the absence of unphysical motions that remove flux outward radially from the disk—points to an initial vertical field spread out across the disk of strength of order 0.1 μG. If a field of 0.1 μG did exist at the time of galaxy formation, this removes the necessity of the dynamo to explain the microgauss fields in the Galaxy. And such a strong field certainly would have influenced the formation of the galactic disk. Any model proposed to explain the global geometry of the galactic magnetic field must necessarily be a global model. For either a dynamo generated field or an existing field, it is clear that the global geometry of the galactic disk and the boundary conditions of the magnetic field play significant roles in determining the morphology of the large-scale magnetic field.

Although the kiloparsec-scale magnetic fields in the galaxy originally stirred the controversy about their origin, the field at much smaller scales may provide important clues as to this origin. Both theories depend critically on the nature of magnetic diffusion and reconnection in interstellar conditions [195]. The dynamo requires destruction of the magnetic field at a rate which is virtually independent of the ohmic resistivity [197]. One key observation is the pitch angle of the magnetic field in galaxies. Because of the dominance of differential shearing in the flow

of the ISM in the galaxy, any initial field will asymptote in time to a purely azimuthal alignment unless diffusion allows the field to move relative to the flow. It appears difficult to achieve a magnetic pitch angle of 10°–20° in the face of strong differential shearing without a magnetic diffusivity many orders of magnitude greater than ohmic resistivity. And the effect of the vertical structure, including vertical shear in the rotation, may have a significant impact on this issue.

Underlying this discussion of magnetic diffusion is the nature of the interaction between the ISM and the magnetic field. The magnetic field is generally considered to be frozen-in to the ISM because of the small molecular resistivity, and due to limited numerical resolution, the ISM is often modeled simply as a homogeneous fluid with averaged properties. The ISM is, however, an extremely heterogeneous fluid with a vast range of temperatures and densities. The key to this problem of diffusion may lie in the complex interaction of a magnetic field with such a varied medium as the ISM. Clearly this problem cannot be solved without a detailed analysis of the dynamics of field in the full galactic geometry.

1.8 General Discussion

Although much of the historical discussion about astrophysical magnetism has focused on the production of kiloparsec-scale fields in galaxies, recent observations of cluster fields suggest a more unified approach to the examination of magnetic fields in the universe is appropriate. Although more than one mechanism may indeed be involved in the generation of magnetic fields, a more likely and satisfying conclusion would demonstrate that one mechanism is primarily responsible for the

ubiquity of magnetic fields in the universe.

Adopting a more broad approach to examining magnetism in the universe opens up the possibility of focusing on alternative issues that may provide new insight into the problem. Two questions that one can ask about each of the four categories of theories may lend some insight into the more subtle differences: by what mechanism does the magnetic field strength saturate, and how does the spectrum of magnetic energy behave at small scales?

Magnetic fields strengths in similar environments are reasonably uniform across the spectrum of observations. The magnetic fields in galaxies and clusters are likely to have reached equilibrium as the field amplification mechanism saturates in competition with field destruction mechanisms; or perhaps the field amplification mechanism has ceased and field destruction is negligible, leaving a steady value for the field strength. Possible saturation mechanisms include the nonlinear back reaction of a strong magnetic field on the turbulent velocity spectrum, magnetic diffusivity balancing amplification mechanisms, or magnetic buoyancy and ambipolar diffusion allowing strong fields to float away from the galactic plane or out of a galaxy cluster. Each theory, even a cosmological or protogalactic mechanism, must determine some field limiting mechanism to balance the amplification of magnetic field through the strong shear of the differential rotation in galaxies. The current controversy surrounding quenching mechanisms for the α-effect and turbulent diffusivity testifies to the importance of the saturation mechanism.

Another critical issue which may distinguish theories is the production, behavior, and destruction of small-scale magnetic fields. There is a surprising lack of

observational evidence for significant magnetic energy at small scales. Although some observational techniques are insensitive to small-scale fields, other methods capable of detecting magnetic energy at small scales see little evidence of it. It appears that many mechanisms exist, such as the isotropic dynamo, that copiously produce tangled magnetic fields, so to explain the lack of magnetic energy at these scales is a challenge for each theory. It may be critical to find a saturation mechanism that preferentially destroys small-scale magnetic fields. Some possible ways of preventing the tangling of magnetic fields to small scales include anamolously large magnetic diffusivity and initializing with a strong field that will resist bending into small structures.

Beyond evaluating all four categories of theories with a fresh perspective in light of all of the observational data available, the only other way forward is through new observations. A number of critical observations will hopefully be possible in the next decade. More sensitive microwave background maps hope to limit or detect the magnetic field strength at recombination, allowing a more certain judgment on the importance of cosmological mechanisms for field generation. Also, a direct determination or stricter limit on the IGM field will shed light on whether magnetic fields are truly ubiquitous throughout all regions of the universe or have more likely been produced in the more dense structures that formed clusters and galaxies. More observations of galactic and cluster fields at higher resolutions will provide better statistics and perhaps identify trends in magnetic field evolution that will discriminate between the various categories of magnetic field generation mechanisms.

1.9 Aims of this Dissertation

As part of the effort to understand the origin and evolution of magnetic fields in the universe, this dissertation focuses on the evolution of magnetic fields in the Galaxy. The evolution of the magnetic field in a galactic disk is undoubtedly strongly influenced by the geometry and boundary conditions of the disk. Therefore, a global simulation of the galactic disk is likely to provide the most insight into the magnetic field evolution over the lifetime of the disk. High resolution is critical to realistically capturing the high-aspect ratio of the galactic disk in a realistic model. The computational cost of these global simulations will necessarily push the boundaries of current facilities, so efficient algorithms should be chosen to maximize the return from numerical models. For this reason, the new computational algorithm of Gradient Particle Magnetohydrodynamics (GPM) is developed here to perform these global simulations. This Lagrangian method for MHD simulation boasts a natural resolution enhancement in regions of compression, yielding better resolution in the higher density central regions of most interest. To maximize the efficiency of the algorithm and to attain better computational stability, an adaptive framework called Adaptive Particle Refinement (APR) is developed to eliminate wasted computational effort in quiescent regions and to improve resolution in active regions. A Galactic model of the Milky Way is constructed as a basis for simulations of the magnetic evolution of the Galaxy in both two and three dimensions.The new GPM algorithm is then used to perform preliminary 2-D MHD Galactic disk simulations to examine the evolution of an existing field under realistic dynamical motion. This dissertation represents the

beginning of a simulation program that to be continued in future work.

The key achievements of this dissertation are:

- The analysis of buoyancy instabilities in shear flows
- The development and validation of a new MHD simulation algorithm
- The construction of a general adaptive framework for the new algorithm to maximize use of computational resources
- The analysis of preliminary, 2-D MHD Galactic disk simulations

In Chapter 2, the stability of magnetic fields in shear flows is examined analytically and a stability diagram is determined for the growth rate of buoyant instabilities in the Boussinesq limit vs. the Alfvén Mach number. Chapter 3 describes the new GPM algorithm for Lagrangian particle MHD simulation. Validation tests for the GPM algorithm are presented in Chapter 4. In Chapter 5, the Adaptive Particle Refinement (APR) framework for adaptive GPM simulations is laid out and discussed. The Galactic model used for simulations is presented in Chapter 6. Finally, results of Galactic simulations are presented in Chapter 7 and the achievements of this dissertation are summarized in Chapter 8.

Chapter 2

Local Buoyant Instability of Magnetized Shear Flows

2.1 Introduction

The stability of a fluid against convective motion has been extensively studied over the past century. Pioneering examinations of the stability of unmagnetized and magnetized compressible fluids have been conducted by Schwarzschild [166], Newcomb [139], and Parker [145]. These papers have had a profound influence on diverse subjects from the dynamics of astrophysical objects to the confinement of plasma in a fusion device. Here we examine the effects of shear in the magnetic field and of an applied shear plasma flow on stability against gravitational interchange. These effects change the stability properties and our results are important for many applications.

The most general investigation of an astrophysical stability problem should include the effects of differential rotation (including both shear flow and the Coriolis force), gravity, gradients in the equilibrium fluid quantities, and shear within the magnetic field. The inclusion of magnetic shear precludes the possibility of

solving the problem quickly by Fourier transformation; hence, most studies avoid the mathematical complications of modeling a shear magnetic field by idealizing to a parallel, but not necessarily straight, magnetic field. We choose to analyze a more general case in which the magnetic field may have a component of shear. We also include a linear shear flow to approximate the effects of differential rotation and gravity to drive instability.

We neglect the Coriolis force in our stability analysis because the stability boundary of the most unstable mode will be unaffected by rotation for most geometries of astrophysical interest. According to Newcomb [139], in a system with a horizontal magnetic field, the most unstable modes have wavenumber $k \rightarrow \infty$ in the direction perpendicular to the plane defined by the magnetic field and gravity (this is the direction $\hat{\mathbf{B}} \times \hat{\mathbf{g}}$). When there is shear in the magnetic field, the analogous surface is the magnetic shear (constant y') surface depicted in Figure 2.1. In the transformed coordinates described in Section 2.2.1 of the paper, we Fourier transform in y' such that all perturbed quantities vary as $e^{iky'}$ and take the limit that $k \gg 1$. This selects the most unstable mode, retaining only the terms necessary to describe this mode. For most geometries of astrophysical interest, including galactic and accretion disks, the Coriolis term in the momentum equation drops out to lowest order, a consequence of the fact that the most unstable mode of the system occurs at the smallest allowable scale in the problem.

Although the Jeans' instability is indeed stabilized by rotation [185, 77], Shu [170], Zweibel [196], and Terquem [183] state that the stability threshold for the Parker instability is not affected by rotation. This insensitivity to rotation occurs because the Coriolis force does not couple to the problem in the absence of fluid

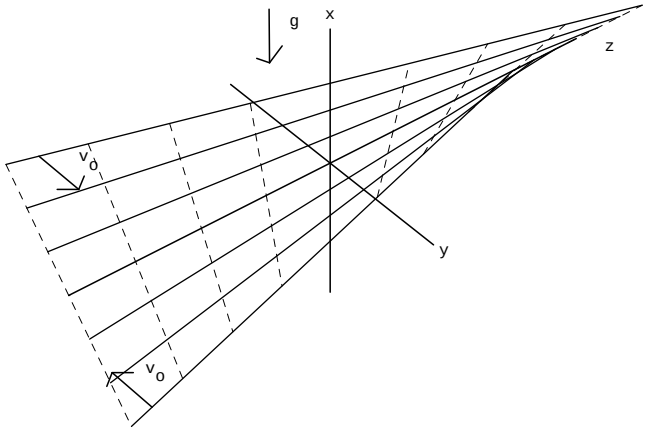

Figure 2.1: The geometry of the shear magnetic field as well as the applied shear flow (shown as v_0) is shown. The magnetic shear (constant y') surface is represented by the magnetic field lines (solid lines) and the dashed lines.

motions; the margin of stability is necessarily the limit that the velocity perturbation $\delta\mathbf{v} \to \mathbf{0}$. The Coriolis force does reduce the growth rate of the Parker instability in an unstable region of parameter space, but it cannot alter the stability boundary [170, 196, 183]. Although here we eliminate the Parker instability through the Boussinesq approximation, the remaining entropy gradient driven interchange-like modes have the same characteristic as the Parker modes: the most unstable modes have a large wavenumber in the direction perpendicular to the magnetic shear surface. Hence, it is not surprising that the stability threshold is unaltered by rotation.

We find, however, that magnetic shear does alter the boundary of marginal stability in parameter space. The stabilization gained by magnetic shear can be understood by examining the characteristic twisting geometry of the unstable mode. The geometry of the magnetic field line perturbation due to this instability is sketched in Figure 2.2. An unstable entropy gradient drives an interchange mode where dense fluid from $x > 0$ drops and light fluid from $x < 0$ rises. But, in the ideal MHD approximation, the field lines are frozen to the fluid and may not cross through each other. To facilitate interchange, a rising (or dropping) section of field line must twist to become parallel to the magnetic field at that height; effectively, the perturbed field line moves only along the magnetic shear surface shown in Figure 2.1. In Figure 2.2, a section of the field line from $x > 0$ twists counter-clockwise as it falls and a section of the field line from $x < 0$ twists clockwise as it rises; this twist occurs about the point where the shear field lines cross ($z = 0$ in this case). Twisting allows these sections to become locally parallel, enabling interchange of the sections. Inclusion of a linear shear

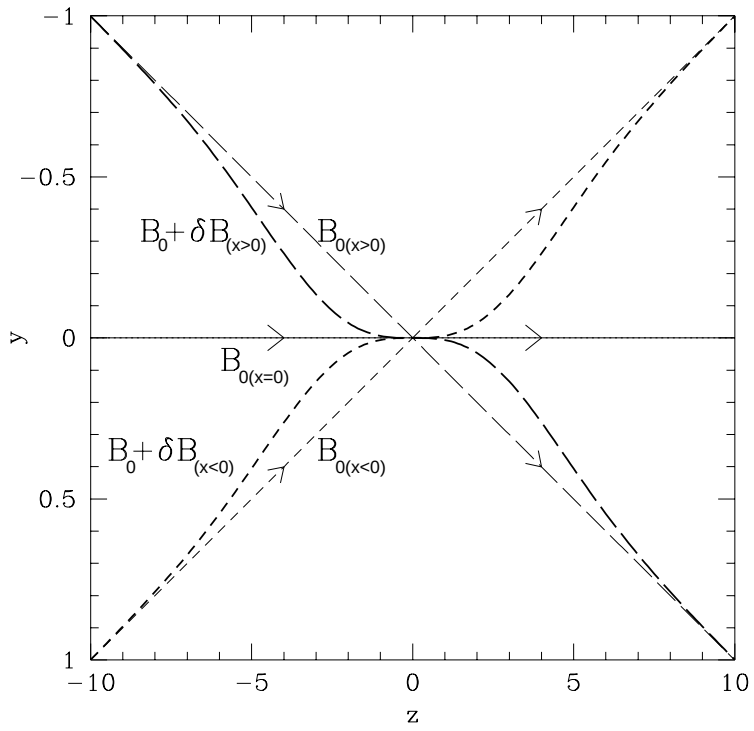

Figure 2.2: The characteristic geometry of the magnetic field line perturbation due to the entropy gradient driven instability. Here we view Figure 2.1 from above (in the $-\hat{\mathbf{x}}$ direction). The long-dashed magnetic field lines lie above the $x = 0$ plane, the short-dashed field lines below. A section of field line from $x > 0$ must twist counter-clockwise as it falls and a section from $x < 0$ must twist clockwise as it rises; interchange can only occur if the two sections of magnetic field are locally parallel.

flow simply causes this twisting mode to propagate with the intersection of the field lines in the z direction. The energy consumed by work done against magnetic tension in twisting the field lines is the root of the stabilization by magnetic shear.

The results of the model described here can help us understand qualitatively the behavior in more complicated geometries. The localized nature of the instability inspires a WKB approach: the growth rate depends on the local value of

parameters and may change as those values vary in space. When there exists a shear flow, the unstable mode travels with the intersection of shear field lines and may move in and out of unstable regions, the disturbance growing or decaying depending on the local conditions.

We construct a simple model to study the effects of magnetic shear and shear flow on the stability properties of a magnetized plasma in a gravitational field. We derive the equations which determine the behavior of this model in the Boussinesq limit. The equations depend on two parameters, the plasma flow Alfvén Mach number and the entropy gradient. We conduct a numerical study of the normal modes of instability and summarize the behavior of the unstable modes by a stability diagram. The stability diagram demonstrates three important characteristics. First, the entropy gradient must exceed a threshold value for unstable mode growth to occur. Therefore, the shear magnetic field can stabilize a nonzero entropy gradient. Second, as expected, shear flow does act to suppress unstable mode growth when the system is at a substantially unstable point in parameter space. But, surprisingly, near marginal stability, shear flow actually enhances the growth rates of the instability and also lowers the threshold entropy gradient necessary for instability. The effect of magnetic shear—to stabilize the plasma and increase the threshold entropy gradient—is diminished by the addition of shear flow. The system can extract energy from the shear flow to further drive the system to instability. Third, as the Alfvén Mach number approaches one, the unstable growth rate is suppressed; the normal modes of the instability are completely stabilized when the plasma flow exceeds the Alfvén speed. Here, the

unstable region in space where a mode can grow moves faster than any perturbation in the system; any disturbance will be swept downstream out of the unstable region, leaving behind a stable plasma.

Analytical work helps us to understand the mechanisms responsible for these characteristics. First, the stability criterion for the case without shear flow is derived demonstrating that a shear magnetic field can support a positive entropy gradient. Next, asymptotic solutions demonstrate analytically that stabilization occurs as the Alfvén Mach number approaches one, yet the threshold entropy gradient for instability goes to zero in the same limit. In addition, a complete WKB solution in the limit of a large growth rate demonstrates both the stabilization by flow at large growth rates and destabilization near marginal stability. Then, a bounded straight field case is solved exactly to show that the lowering of the threshold entropy gradient with increased shear flow is a characteristic of plasma flow along the field lines and not dependent on the magnetic shear in the general model. Finally, energy conservation relations are derived and analyzed.

In Section 2.2, we describe the model under consideration and derive the governing system of equations. The numerical stability analysis for the general model and the stability diagram are presented in Section 2.3.1. Section 2.3.2 contains the analytical results illuminating the characteristics of the stability diagram. We describe an exactly soluble, bounded, straight-field case in Section 2.3.3. Finally, in Section 2.4, the implications of this work on galactic physics, accretion disk physics, solar physics, and tokamak confinement are discussed.

2.2 Derivation of Equations

In this section, we derive the equations for linear perturbations of a vertically stratified atmosphere with shear magnetic field and shear flow in the high-β, or Boussinesq, limit. We motivate and apply a coordinate transformation which casts the problem in its most natural form. Investigating the limit of the most unstable modes, we derive a system of three coupled first-order ordinary differential equations which capture the lowest order behavior of the model.

2.2.1 Setup and Coordinate Transformation

Consider a stationary state for an ideal plasma with mass density $\rho(x)$ and thermal pressure $p(x)$ and an embedded horizontal shear magnetic field given by

$$\mathbf{B_0} = \mathbf{B_0}\left(\hat{\mathbf{z}} + \frac{x}{l_B}\hat{\mathbf{y}}\right). \tag{2.1}$$

We then impose a shear flow on this plasma given by

$$\mathbf{v_0} = v_0\frac{x}{l_v}\hat{\mathbf{y}}, \tag{2.2}$$

and include gravitational acceleration in the vertical direction given by $\mathbf{g} = -g\hat{\mathbf{x}}$. Equilibrium force balance yields

$$\frac{\partial}{\partial x}\left(p + \frac{B^2}{8\pi}\right) = -g\rho. \tag{2.3}$$

Figure 2.1 shows the geometry of this shear magnetic field as well as the imposed shear flow on the system.

The instabilities of this plasma are expected to have a short perpendicular wavelength and a long parallel wavelength (with respect to the magnetic field) so

as to maximize motion in the vertical direction and minimize field line bending [139]. Short perpendicular wavelengths, however, are rapidly sheared apart by the perpendicular shear flow. We would thus like to transform to a coordinate system with two properties: first, that the flow is along the magnetic field lines; and, second, that field lines are coordinate lines. The application of sheared coordinate systems to simplify a problem of this nature is well documented. Roberts and Taylor [158] employed a coordinate system in which the field lines are coincident with the coordinate lines to describe the Rayleigh-Taylor instability of a fluid supported by a shear magnetic field; Goldreich and Lynden-Bell [78] used a shearing coordinate system to attack the problem of local gravitational instabilities in a system with shear flow arising from differential rotation.

We transform the shear velocity to a parallel velocity by transforming to a frame moving in z

$$z' = z + v_f t. \tag{2.4}$$

where $v_f = \frac{l_B}{l_v} v_0$. In this transformed frame, the velocity becomes

$$\mathbf{v'} = \mathbf{v_f} + \mathbf{v_0} = \mathbf{v_f} \left(\hat{\mathbf{z}} + \frac{x}{l_B} \hat{\mathbf{y}} \right),$$

i.e. parallel to $\mathbf{B_0}$. We construct field line coordinates by transforming the y coordinate to

$$y' = y - \frac{x z'}{l_B}. \tag{2.5}$$

The x coordinate is left unchanged, $x' = x$. It is easy to verify that x' and y' are constant along field lines ($\mathbf{B_0} \cdot \nabla x' = \mathbf{B_0} \cdot \nabla y' = 0$) and that $\mathbf{B} = \mathbf{B_0} \nabla x' \times \nabla y'$. The surfaces of constant y' (magnetic shear surfaces) twist from vertical at $z' = 0$ to almost horizontal as $z' \to \pm\infty$. This geometry is shown in Figure 2.1.

At first, introducing the field line coordinates seems unhelpful since it introduces explicit z' dependence into the equations. The problem also has x dependence that arises from the variation of $\mathbf{B}$, $p(x)$, and $\rho(x)$. Indeed, one way to tackle this problem is to Fourier transform in y and z and solve for the x dependence. However, the lowest order solution in the twisting coordinate system is a superposition of these Fourier modes, or, complementarily, a Fourier solution can be constructed by a superposition of these twisting modes [158]. We summarize the relationship between these representations in Appendix A.1. We consider the solutions in the twisting coordinates to be more physically relevant since they are localized in z'.

2.2.2 Application of Ideal MHD

The basic equations of ideal MHD include the momentum equation written in terms of the gradient of total pressure (thermal and magnetic), the magnetic tension force, and the gravitational force,

$$\rho\frac{D\mathbf{v}}{Dt} = -\nabla\left(p + \frac{\mathbf{B^2}}{8\pi}\right) + \frac{\mathbf{B}\cdot\nabla\mathbf{B}}{4\pi} + \rho\mathbf{g}, \tag{2.6}$$

the induction equation in the limit of zero resistivity,

$$\frac{\partial\mathbf{B}}{\partial t} = \nabla\times(\mathbf{v}\times\mathbf{B}), \tag{2.7}$$

the continuity equation,

$$\frac{D\rho}{Dt} = -\rho\nabla\cdot\mathbf{v}, \tag{2.8}$$

and the adiabatic equation of state,

$$\frac{D}{Dt}\left(\frac{p}{\rho^\Gamma}\right) = 0. \tag{2.9}$$

Here $\frac{D}{Dt} = \frac{\partial}{\partial t} + \mathbf{v} \cdot \nabla$ denotes the Lagrangian derivative, $\mathbf{v}$ represents the plasma velocity, and Γ is the adiabatic index. These equations must be evolved subject to the constraint that

$$\nabla \cdot \mathbf{B} = \mathbf{0}. \tag{2.10}$$

Taking (2.6)-(2.9), linearized about the equilibrium ((2.1)–(2.3)), yields:

$$\left(\gamma' + v_f \frac{\partial}{\partial z'}\right) \delta\mathbf{v} + \delta\mathbf{v} \cdot \nabla \mathbf{v_0} = -\frac{\mathbf{1}}{\rho_\mathbf{0}} \nabla \left(\delta\mathbf{p} + \frac{\mathbf{B_0} \delta \mathbf{B}_\parallel}{\mathbf{4}\pi}\right) + \frac{\mathbf{B_0}}{\mathbf{4}\pi\rho_\mathbf{0}} \frac{\partial \delta \mathbf{B}}{\partial\ \mathbf{z}'} + \frac{\delta\mathbf{B} \cdot \nabla \mathbf{B_0}}{\mathbf{4}\pi\rho_\mathbf{0}} - \frac{\mathbf{g}\delta\rho\hat{\mathbf{x}}}{\rho_\mathbf{0}} \tag{2.11}$$

$$\left(\gamma' + v_f \frac{\partial}{\partial z'}\right) \delta\mathbf{B} + \delta\mathbf{v} \cdot \nabla \mathbf{B_0} = \mathbf{B_0} \frac{\partial \delta \mathbf{v}}{\partial \mathbf{z}'} + \delta\mathbf{B} \cdot \nabla \mathbf{v_0} - \mathbf{B_0} \nabla \cdot \delta\mathbf{v} \tag{2.12}$$

$$\left(\gamma' + v_f \frac{\partial}{\partial z'}\right) \delta\rho = -\delta\mathbf{v} \cdot \nabla \rho_\mathbf{0} - \rho_\mathbf{0} \nabla \cdot \delta\mathbf{v} \tag{2.13}$$

$$\left(\gamma' + v_f \frac{\partial}{\partial z'}\right) \delta p = -\delta\mathbf{v} \cdot \nabla \mathbf{p_0} - \mathbf{\Gamma p_0} \nabla \cdot \delta\mathbf{v}, \tag{2.14}$$

where we have taken all quantities to vary in time as $e^{\gamma' t}$.

In a straight field [139] and a shear field [158] without flow, the most unstable perturbations are incompressible to lowest order and have a small horizontal perpendicular wavelength. Such perturbations maximize vertical motion which extracts energy from the gravitational potential energy and minimize horizontal motions which extract no energy. To isolate these motions, we impose the ordering

$$\frac{\partial}{\partial y'} = ik \ \sim \ \mathcal{O}\left(\frac{\epsilon^{-1}}{l_B}\right) \tag{2.15}$$

$$\frac{\partial}{\partial x'} \ \sim \ \mathcal{O}\left(\frac{\epsilon^{-1/2}}{l_B}\right) \tag{2.16}$$

$$\frac{\partial}{\partial z'} \sim \mathcal{O}\left(\frac{1}{l_B}\right) \tag{2.17}$$

$$\frac{x'}{l_B} \sim \mathcal{O}\left(\epsilon^{1/2}\right). \tag{2.18}$$

where $\epsilon = (kl_B)^{-1} \ll 1$ is the ordering parameter or our problem. Clearly, all perturbed quantities vary as $e^{iky'}$. It is also convenient to define the vectors,

$$\mathbf{b} = \frac{\mathbf{B_0}}{B_0} \tag{2.19}$$

$$\mathbf{e}_\wedge = \nabla y' \tag{2.20}$$

$$\mathbf{e}_\perp = \frac{\nabla y' \times \mathbf{B_0}}{B_0}. \tag{2.21}$$

The perturbed plasma velocity and magnetic field are projected along these directions, *i.e.*

$$\delta\mathbf{v} = \delta\mathbf{v}_\perp\mathbf{e}_\perp + \delta\mathbf{v}_\wedge\mathbf{e}_\wedge + \delta\mathbf{v}_\parallel\mathbf{b}$$

$$\delta\mathbf{B} = \delta\mathbf{B}_\perp\mathbf{e}_\perp + \delta\mathbf{B}_\wedge\mathbf{e}_\wedge + \delta\mathbf{B}_\parallel\mathbf{b}.$$

Note that the basis vectors $\mathbf{e}_\perp$, $\mathbf{e}_\wedge$, and $\mathbf{b}$ are neither unit vectors nor constant in space—*e.g.*, $\mathbf{B_0}\cdot\nabla\mathbf{e}_\wedge = -\frac{\mathbf{B_0}}{\mathbf{l_B}}\hat{\mathbf{x}}$. We expand all perturbed quantities in powers of $\epsilon^{1/2}$ and denote order as a superscript—for example, $\delta v_\perp = \sum_{n=0}^{\infty}\delta v_\perp^{(n)}\epsilon^{n/2}$. The ordered, perturbed quantities and operators are substituted into (2.11)–(2.14). (2.12)–(2.14) at $\mathcal{O}(\epsilon^{-1})$ and the $\mathbf{e}_\wedge$ projection of (2.12) yield

$$\delta v_\wedge^{(0)} = \delta B_\wedge^{(0)} = 0. \tag{2.22}$$

Thus, the dominant motion is along the magnetic shear (constant y') surfaces in the $\mathbf{e}_\perp$ direction. (2.12)–(2.14) at $\mathcal{O}(\epsilon^{-1/2})$ produce

$$\nabla\cdot\left(\delta v_\perp^{(0)}\mathbf{e}_\perp + \delta\mathbf{v}_\wedge^{(\mathbf{1})}\mathbf{e}_\wedge\right) = 0. \tag{2.23}$$

Thus, the perpendicular motion is incompressible to lowest order. At $\mathcal{O}(\epsilon^{-1})$, the $\mathbf{e}_\wedge$ component of (2.11) gives

$$\delta p^{(0)} + \frac{B_0 \delta B_\parallel^{(0)}}{4\pi} = 0. \tag{2.24}$$

(2.24) expresses the fact that, on the time scales of interest, pressure balance is achieved across the convective eddies (in the $\mathbf{e}_\wedge$ direction). In a subsidiary expansion, we take the high-β, or Boussinesq, limit ($\beta = \frac{4\pi p_0}{B^2}$). Thus, (2.24) reduces to $\delta p^{(0)} = 0$, and we find from (2.14) that

$$\delta \mathbf{v}^{(\mathbf{0})} \cdot \nabla \mathbf{p_0} = -\mathbf{\Gamma p_0} (\nabla \cdot \delta \mathbf{v})^{(\mathbf{0})}. \tag{2.25}$$

At $\mathcal{O}(\epsilon^{-1/2})$, the $\mathbf{e}_\wedge$ component of (2.11) yields $\delta p^{(1)} + \frac{B_0 \delta B_\parallel^{(0)}}{4\pi} = 0$, or taking the high-$\beta$ limit, $\delta p^{(1)} = 0$. The final stability equations are obtained from the sum and difference of the $\mathbf{e}_\perp$ projections of (2.11) and (2.12) at $\mathcal{O}(1)$ and from (2.13) using (2.25) to substitute for $\nabla \cdot \delta \mathbf{v}$. After some tedious but straightforward algebra, we obtain

$$-(1-M)\frac{dA_+}{dz} = -\gamma A_+ + (1+M)\frac{z}{1+z^2}A_- - \frac{s}{(1+z^2)^{1/2}} \tag{2.26}$$

$$(1+M)\frac{dA_-}{dz} = -\gamma A_- - (1-M)\frac{z}{1+z^2}A_+ + \frac{s}{(1+z^2)^{1/2}} \tag{2.27}$$

$$M\frac{ds}{dz} = -\gamma s - \frac{1}{2}\frac{A_+ - A_-}{(1+z^2)^{1/2}} s_0', \tag{2.28}$$

where A_+ and A_- are the Elsässer variables defined by

$$A_+ = \frac{1}{(1+z^2)^{1/2}} \left(\frac{\delta B_\perp}{B_0} + \frac{\delta v_\perp}{v_A} \right) \tag{2.29}$$

$$A_- = \frac{1}{(1+z^2)^{1/2}} \left(\frac{\delta B_\perp}{B_0} - \frac{\delta v_\perp}{v_A} \right) \tag{2.30}$$

and the entropy is given by

$$s = \frac{g l_B}{v_A^2} \left(\frac{\delta \rho}{\rho_0} \right). \tag{2.31}$$

We have normalized so that $z = z'/l_B$ and $\gamma = \gamma' l_B / v_A$. (2.26)–(2.28) contain two parameters: the Mach number of the plasma flow with respect to the Alfvén speed ($v_A = \frac{B_0}{(4\pi\rho)^{1/2}}$),

$$M = \frac{v_f}{v_A}, \tag{2.32}$$

and the entropy gradient,

$$s_0' = \frac{g l_B^2}{v_A^2} \left(\frac{\rho_0'}{\rho_0} - \frac{p_0'}{\Gamma p_0} \right), \tag{2.33}$$

where the primes denote differentiation by x. With the boundary conditions that $A_+ \to 0$, $A_- \to 0$, and $s \to 0$ as $\mid z \mid \to \pm\infty$, (2.26)–(2.28) define an eigenvalue problem for γ. Solution of the stability equations yields $\gamma(M, s_0')$.

(2.26)–(2.28) have a simple physical interpretation. A_+, the Alfvén wave going in the negative z (upstream) direction, travels at the (normalized) speed $1 - M$. The A_+ wave is coupled to the A_- wave by magnetic and velocity shear (the A_- term in (2.26)). The A_+ wave is driven by gravity via the s term in (2.26). A_-, the Alfvén wave going in the positive z (downstream) direction, travels at speed $1 + M$, is coupled to A_+, and is driven by s. The variable s is proportional to the density or entropy perturbation and it is driven by both Alfvén waves, as seen in (2.28).

2.3 Stability Analysis

In this section, we discuss the unstable eigenvalues ($\mathbf{Re}\ \gamma > \mathbf{0}$) and eigenfunctions of (2.26)–(2.28). We have not examined the stable part of the spectrum in detail although numerical results indicate a continuum along the imaginary γ axis. Two properties of (2.26)–(2.28) show that it is sufficient to examine stability in the region $0 \leq M \leq 1$. First, note that $\gamma(-M, s_0') = \gamma(M, s_0')$ since we can map (2.26)–(2.28) onto themselves by the changes $M \to -M$, $A_+ \to A_-$, $A_- \to A_+$, $z \to -z$, and $s \to s$. Second, note that the three asymptotic solutions as $|z| \to \infty$ are:

$$A_+ \sim e^{\frac{\gamma z}{1-M}} \qquad s, A_- \sim \mathcal{O}\left(\frac{1}{z} e^{\frac{\gamma z}{1-M}}\right) \tag{2.34}$$

$$A_- \sim e^{\frac{-\gamma z}{1+M}} \qquad s, A_+ \sim \mathcal{O}\left(\frac{1}{z} e^{\frac{-\gamma z}{1+M}}\right) \tag{2.35}$$

$$s \sim e^{\frac{-\gamma z}{M}} \qquad A_+, A_- \sim \mathcal{O}\left(\frac{1}{z} e^{\frac{-\gamma z}{M}}\right). \tag{2.36}$$

If $M > 1$, there are no acceptable (decaying) asymptotic solutions as $z \to -\infty$ for $\mathbf{Re}\ \gamma > \mathbf{0}$. Thus, $M > 1$ has no unstable eigenmodes. Physically, this is because all solutions, even the upstream propagating Alfvén wave A_+, are swept downstream.

Without flow, MHD stability equations are self-adjoint [21] and γ^2 is real. With flow, no such property is known and γ^2 can be complex. However, in all our solution methods, γ^2 has been found to be real for this problem, although we have not been able to prove that this is rigorously true. The discrete positive real values for γ correspond to unstable growing modes, and the continuum along the imaginary γ axis represents traveling Alfvén waves.

In Section 2.3.1, we present the numerical solution of (2.26)–(2.28). Various analytical limits that illuminate the numerical solutions are treated in Section 2.3.2. An exactly soluble model with a straight magnetic field that demonstrates qualitatively similar behavior is presented in Section 2.3.3. Finally, in Section 2.3.4, energy constraints on the instability are discussed.

2.3.1 Numerical Solutions

We looked for normal mode growth in the system defined by (2.26)–(2.28) using three different numerical methods. We directly solved for the eigenvalues γ of this system by matrix solution of the corresponding finite difference equations using the commercial numerical routine package LAPACK. We also found the eigenvalues of the equations to high precision using a 1-D shooting code in z driven by an adaptive step-size, fourth order Runge-Kutta method with fifth order correction (RK45). Finally, for (2.26)–(2.28) with γ replaced by $\partial/\partial t$, an initial-value code employing Barton's method [47] for second order accuracy in time was written to determine the fastest growing mode for any choice of parameters. Results from all three codes were consistent.

A stability diagram of unstable normal-mode growth rates and stable regions over the parameter space defined by M and s_0' is presented in Figure 2.3. As we have already noted, no growing mode exists for $M > 1$. As well, it is obvious that for the non-positive values of the entropy gradient, $s_0' \leq 0$, there can be no unstable mode growth since the atmosphere is stably or neutrally stratified; this is demonstrated by the energy arguments presented in Section 2.3.4. Hence,

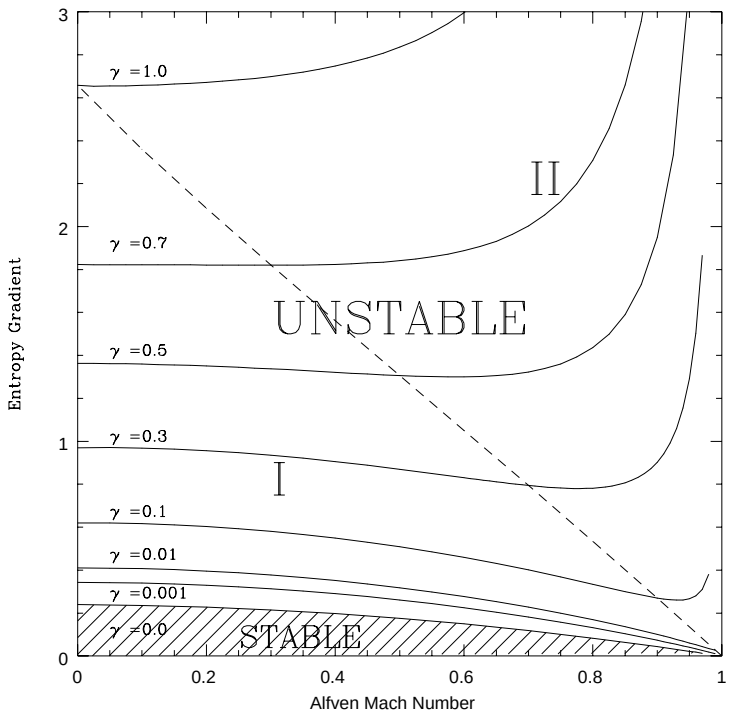

Figure 2.3: Stability diagram for the Boussinesq limit: Contours of constant normalized growth rate γ are plotted over the space of entropy gradient s_0' vs. Alfvén Mach number M. The stable parameter regime is denoted by hashing. The diagonal dotted line denotes $\gamma = 1 - M$, separating unstable region (I), where flow enhances instability growth, from unstable region (II), where flow suppresses the instability.

Figure 2.3 need only cover the region of (M, s_0') parameter space defined by $0 \leq M \leq 1$ and $s_0' > 0$ to include all possible unstable mode growth.

Several features of Figure 2.3 are important to emphasize. First, for a system without plasma flow (along the line $M = 0$), we see that the entropy gradient must exceed a threshold value, $s_0' > 1/4$, in order to become unstable when the fluid is supported by a shear magnetic field. Second, the qualitative effect of increasing the plasma flow (increasing M) on the instability growth rate depends on both

the growth rate and the plasma flow. Away from marginal stability ($\gamma \geq 1$), an increase of the plasma flow—equivalent to moving along a horizontal line to the right on the stability diagram—decreases the instability growth rate as one may expect. Here, the growing perturbation is sheared out horizontally so that less gravitational potential energy is extracted by motions along the magnetic shear (constant y') surface, reducing the instability growth rate. But near marginal stability ($\gamma < 1$), an increase in the shear flow effects the instability growth rate differently depending on the relative orders of the growth rate, γ, and of one minus the Alfvén Mach number, $1 - M$. The diagonal dotted line in Figure 2.3 denotes $\gamma = 1 - M$. In region (II) of the diagram, $\gamma > 1 - M$ and flow suppresses the instability. But, in region (I), where $\gamma < 1 - M$, an increase in the flow actually enhances the instability growth. This unexpected result can be explained with some physical insight. The point where the instability can grow is localized at $z' = 0$ in our transformed coordinates; this is where the magnetic shear (constant y') surface is vertical and motions along that surface can extract the most gravitational potential energy with which to drive the instability. When a shear plasma flow is introduced into the system, this is manifested in our transformed system by a plasma flow along the field lines in the $+z'$ direction. This causes the Alfvén modes in the $+z'$ and $-z'$ directions to propagate at different speeds in our transformed system. The counter-propagating mode (A_+ in our model) is slowed down, spending more time in the region around $z' = 0$ where unstable mode growth occurs. Hence, the instability is enhanced by a shear flow in the plasma. The final point to be gleaned from Figure 2.3 concerns the behavior as $M \rightarrow 1$, or as the Alfvén Mach number approaches one. In this region, every

contour corresponding to a finite growth rate asymptotes to $s_0' \to \infty$; hence, the instability is stabilized as the Alfvén Mach number approaches one.

2.3.2 Analytical Limits

The stability diagram, Figure 2.3, prominently displays the three main characteristics discussed in Section 2.3.1: a threshold entropy gradient, $s_0' > 1/4$, necessary for instability in the system without plasma flow; for increasing plasma flow, a reduction of the unstable growth away from marginal stability, but an enhancement of that unstable mode near marginal stability including a decrease in the threshold entropy gradient necessary for instability; and the stabilization of unstable normal modes as the Alfvén Mach number approaches one. Each of these characteristics is relevant in a different region of the (M, s_0') parameter space of the diagram. By examining the model in each of these regions of parameter space, we can confirm and explain our results analytically.

First, we examine the criterion for instability in the absence of plasma flow; this corresponds to the left vertical axis of the stability diagram where $M = 0$. Next, we conduct an asymptotic analysis in the $M \to 1$ limit—region (II) of the stability diagram—to show that the plasma is indeed stabilized as the Alfvénic Mach number approaches one. Then we investigate the reduction of the threshold for instability with plasma flow; this covers the lower, right-hand side of region (I) of the stability diagram. Finally, a WKB analysis for a large instability growth rate yields the behavior of the system in the central and upper portion of the stability diagram; the suppression of the growth rate by flow in region (II) and

its enhancement in region (I) are verified by the eigenvalue condition $\gamma(M, s_0')$ obtained in this analysis.

Stability Criterion without Flow

Here we obtain the stability criterion for a magnetized fluid supported by a shear magnetic field in the Boussinesq limit with no shear flow. By using the substitution $v = \delta v_\perp/(1+z^2)$, the equations without plasma flow ($M = 0$) can be simplified to a Sturm-Liouville equation of the form

$$\frac{d}{dz}\left[(1+z^2)\frac{dv}{dz}\right] - \left[\gamma^2(1+z^2) - s_0'\right]v = 0 \tag{2.37}$$

over the interval $(-\infty, +\infty)$. The boundary conditions on this system necessitate that $v \to 0$ as $z \to \pm\infty$. From Sturm's First Comparison Theorem [91], we know that, as the eigenvalue γ^2 is increased, the solution will oscillate less rapidly with zeros of the function v leaving the interval $-\infty < z < \infty$ at the boundaries. Thus, if the solution with $\gamma^2 = 0$ oscillates, we can increase γ^2 until the boundary conditions are satisfied, so there will be an unstable solution. Note also that the fastest growing mode has no zeros in the interval and must be even in z.

Let w(z) satisfy (2.37) with $\gamma^2 = 0$. Substituting a series solution of the form

$$w(z) = \sum_{n=0}^{\infty} a_n (1+z^2)^{-(n+\alpha)}. \tag{2.38}$$

in (2.37) (with $\gamma^2 = 0$), we obtain the recurrence relation,

$$\frac{a_n}{a_{n-1}} = \frac{4(n+\alpha-1)^2}{4(n+\alpha-1/4)^2 + s_0' - 1/4}, \tag{2.39}$$

with

$$\alpha = \frac{1}{4} \pm \frac{1}{4}\sqrt{1 - 4s_0'}. \tag{2.40}$$

When $s_0' > 1/4$, solution (2.38) oscillates for $z \to \infty$, and clearly an unstable solution exists. Let us therefore consider stability when $s_0' < 1/4$. We take the positive sign in (2.40); then w^2 is integrable for $z \to \infty$. We note that all a_n are positive if a_0 is positive. We choose $a_0 > 0$ such that $w > 0$. The series solution for $w(z)$ given by (2.38) is non-differentiable at $z = 0$ (as we see below). Thus, we cannot use the solution from (2.38) over the whole interval and must restrict its use to $z > 0$. Let us suppose (for contradiction) that there exists at least one unstable solution of (2.37). Further, let $v_0(z)$ be the most unstable solution—as noted above, $v_0(z)$ must be even in z and have no zeros in the interval $-\infty < z < \infty$. We therefore choose $v_0(z) > 0$ everywhere. It is straight forward to show that

$$v_0(0) \left.\frac{dw}{dz}\right|_{0^+} = \gamma_0^2 \int_{0^+}^{\infty} w v_0 (1 + z^2) dz, \tag{2.41}$$

where the limit 0^+ is infinitesimally above $z = 0$. Since the integral and v_0 in (2.41) are positive, we have stability, $\gamma_0^2 < 0$ (a contradiction), if $\left.\frac{dw}{dz}\right|_{0^+} < 0$. Since every term in the series (2.38) is a monotonically decreasing function of z we expect $\left.\frac{dw}{dz}\right|_{0^+} < 0$, but since the limit is nonuniform we take a more careful approach. We determine the sign of the limit $\left.\frac{dw}{dz}\right|_{0^+}$ from an examination of the convergence of the series. It is straightforward to show that

$$a_n \sim \frac{A}{n^{3/2}} \tag{2.42}$$

as $n \to \infty$ with A a positive constant. Thus, the series for $w(z)$ (see (2.38)) converges for $z \geq 0$. However, the series for $\frac{dw}{dz}$ converges for $z > 0$ but not for

$z = 0$. Let us write for $z \to 0$

$$\frac{dw}{dz} = \sum_{n=0}^{\infty} \frac{-2z(n+\alpha)a_n}{(1+z^2)^{(n+\alpha+1)}} \simeq -Cz - 2\sum_{n=N}^{\infty} \frac{Azn^{-1/2}}{(1+z^2)^n}, \tag{2.43}$$

where C is a positive constant and N is a large number in the range $1 \ll N \ll z^{-2}$. Using $(1+z^2)^{-n} \simeq e^{-nz^2}$, we obtain

$$\begin{aligned} \frac{dw}{dz} &\simeq -Cz - 2A\textstyle\sum_{n=N}^{\infty} n^{-1/2} z e^{-nz^2} \simeq -Cz - 2A\int_N^{\infty} n^{-1/2} z e^{-nz^2} dn \\ &= -Cz - 2A\textstyle\int_{\sqrt{N}z}^{\infty} e^{-p^2} dp \simeq -Cz - 2A\int_0^{\infty} e^{-p^2} dp = -Cz - A\sqrt{\pi}. \end{aligned} \tag{2.44}$$

Thus, the limit of $\frac{dw}{dz}$ as $z \to 0^+$ is $-\sqrt{\pi}A$, *i.e.* negative. From (2.41) we conclude that $\gamma_0^2 < 0$ and there are no unstable modes for $s_0' < 1/4$. Thus, the necessary and sufficient condition for instability is $s_0' > 1/4$.

This criterion can also be written

$$\frac{\rho_0'}{\rho_0} - \frac{p_0'}{\Gamma p_0} > \frac{1}{4}\frac{v_A^2}{g l_B^2}. \tag{2.45}$$

This confirms the result in Figure 2.3—that a threshold value of the entropy gradient, given by (2.45), must be exceeded in order to cause instability when the fluid is supported by a shear magnetic field. Clearly, without magnetic shear ($l_B \to \infty$), the usual criterion, $s_0' > 0$, holds and the motion is the simple interchange of field lines. With magnetic shear, the field lines *must* be bent since the interchange of field lines is impossible with finite displacements—thus magnetic shear is stabilizing.

Asymptotic Solution in the $M \to 1$ Limit

An asymptotic, boundary layer analysis can be carried out in the limit that $M \to 1$. This asymptotic expansion is described in Appendix A.2. The eigenvalue

condition derived for this limit in that appendix is

$$\gamma^2 \simeq s_0'(1 - M^2).$$

This relation explains the upturn towards infinity of the constant growth rate contours in region (II) of Figure 2.3 as $M \to 1$.

Solution in the $\gamma \to 0$, $M \to 1$ Limit

We demonstrate that the threshold entropy gradient for instability (the limit that $\gamma \to 0$) decreases as the plasma flow velocity is increased and that the threshold value of s_0' approaches zero linearly as $M \to 1$. Letting $1 - M \sim \epsilon$, we can redefine the following variables in terms of ϵ: $\gamma = \epsilon\overline{\gamma}$, $A_- = \epsilon\overline{A}_-$, $s = \epsilon\overline{s}$ and $s_0' = \epsilon\overline{s_0'}$. For $M \to 1$, we can drop terms of order ϵ^2 and cancel ϵ from each remaining term to yield the simplified set of equations

$$-\frac{dA_+}{dz} = -\overline{\gamma}A_+ + 2\frac{z}{1+z^2}\overline{A}_- - \frac{\overline{s}}{(1+z^2)^{1/2}} \tag{2.46}$$

$$2\frac{d\overline{A}_-}{dz} = -\frac{z}{1+z^2}A_+ + \frac{\overline{s}}{(1+z^2)^{1/2}} \tag{2.47}$$

$$\frac{d\overline{s}}{dz} = -\frac{1}{2}\frac{A_+}{(1+z^2)^{1/2}}\overline{s_0'}. \tag{2.48}$$

These equations are now independent of ϵ, or, equivalently, are independent of M. The equations will hold true for constant values of $\overline{\gamma}$ and $\overline{s_0'}$. In this case, if we have a negligibly small value $\overline{\gamma} \to 0$, we obtain the corresponding threshold value of $s_0' = \overline{s_0'}(1 - M)$, where $\overline{s_0'}$ is a constant. Thus, the threshold entropy gradient for stability must linearly approach zero as $M \to 1$, as seen in the lower right-hand corner of Figure 2.3.

WKB Analysis

A complete solution of the model for a large growth rate γ can be constructed if we assume an ordering, for a small parameter ϵ, such that $\gamma \sim \mathcal{O}(\epsilon^{-1})$, $\frac{d}{dz} \sim \mathcal{O}(\epsilon^{-1})$, $s \sim \mathcal{O}(\epsilon^{-1})$, and $s_0' \sim \mathcal{O}(\epsilon^{-2})$. In this case, we can neglect the second term on the right hand side of both (2.26) and (2.27). Converting back from Elsässer variables to $\delta B_\perp$ and $\delta v_\perp$ notation, combining the three equations into a single second order equation, and neglecting the term $Ms\frac{d}{dz}\left(\frac{1}{(1+z^2)^{1/2}}\right)$ (which can be shown to be small), yields

$$(1-M^2)\frac{d^2\delta v_\perp}{dz^2} - 2\gamma M\frac{d\delta v_\perp}{dz} - \left[\gamma^2 - \frac{s_0'}{1+z^2}\right]\delta v_\perp = 0. \tag{2.49}$$

Changing variables with an integrating factor to $v = \exp\left(\frac{\gamma M z}{1-M^2}\right)\delta v_\perp$, we obtain

$$\frac{d^2 v}{dz^2} - \frac{1}{(1-M^2)^2}\left[\gamma^2 - \frac{s_0'(1-M^2)}{1+z^2}\right]v = 0. \tag{2.50}$$

We assume a WKB solution of the form $e^{i\int k(z)dz}$ and find

$$v = \overline{v}\exp\left(\pm\frac{i}{1-M^2}\int^z\left[\frac{s_0'(1-M^2)}{1+z'^2} - \gamma^2\right]^{1/2}dz'\right). \tag{2.51}$$

The turning points are at $z = \pm z_0$ where

$$z_0^2 = \frac{s_0'(1-M^2)}{\gamma^2} - 1. \tag{2.52}$$

For $\mid z \mid > z_0$, the WKB solutions are decaying exponentials; in the region $-z_0 < z < z_0$, the WKB solution is an oscillatory function.

In the usual way [18], we obtain the Bohr-Sommerfeld quantization condition

$$\int_{-z_0}^{z_0}\left[\frac{s_0'(1-M^2)}{1+z^2} - \gamma^2\right]^{1/2}dz = 2n\pi(1-M^2). \tag{2.53}$$

The growth rate of the nth mode is then given, for small z_0, by

$$\gamma^2 = \left[s_0' - 2n(s_0')^{1/2}(1-M^2)^{1/2}\right](1-M^2). \tag{2.54}$$

For a large growth rate $\gamma \sim \mathcal{O}(\epsilon^{-1})$ and the lowest, nontrivial eigenmode $n = 1$, we can solve this eigenvalue condition for s_0' to obtain

$$s_0' = \frac{\gamma^2}{1-M^2} + 2\gamma. \tag{2.55}$$

This condition agrees with the behavior of the constant growth rate contours in region (II) of Figure 2.3. Although we do not expect the eigenvalue condition in the WKB approximation to be precise in the limit of small growth rate, $\gamma \sim \mathcal{O}(\epsilon)$, we do find to lowest order the qualitatively correct form,

$$s_0' \sim 1 - M^2, \tag{2.56}$$

that the contours in region (I) decrease like $1 - M^2$.

2.3.3 Bounded, Straight-Field Case

The general model defined by this paper has the characteristic that the shear in the magnetic field localizes the region of instability around where the magnetic shear (constant y') surface is vertical (this corresponds to $z' = 0$ in our transformed coordinate system). With this characteristic as our guide, an exactly soluble, simplified model can be constructed which demonstrates the same qualitative behavior displayed in Figure 2.3. We construct a case with a straight magnetic field and a plasma flow along the field lines which has boundaries at $z = \pm L$. Since the explicit z dependence drops out of the equations in the straight-field

limit ($l_B \to \infty$), we Fourier transform in z to obtain the algebraic dispersion relation

$$(\gamma + iMk_z)\left[(1-M^2)k_z^2 + 2i\gamma Mk_z + \gamma^2 - s_0'\right] = 0. \tag{2.57}$$

If we remove the plasma flow from the system by setting $M = 0$, this dispersion relation agrees with the results of Newcomb [139] for a straight-field without flow in the Boussinesq limit.

We solve for the three solutions for k_z from (2.57) and find the eigenvectors corresponding to each k_z. Constructing general solutions for $\delta B_\perp$, $\delta v_\perp$, and s from these eigenvectors, we find the eigenvalue condition $\gamma(M, s_0')$ that must hold in order to satisfy the three necessary boundary conditions on the system. The boundary conditions we apply are $\delta v_\perp = 0$ at $z = \pm L$ and the upstream boundary condition $s = 0$ at $z = -L$. The eigenvalue condition thus obtained is

$$\gamma^2 = \left[s_0' - \left(\frac{n\pi}{2L}\right)^2 (1-M^2)\right](1-M^2) \tag{2.58}$$

for the nth order unstable mode where $n = 1, 2, 3, \ldots$.

A plot of constant γ contours is displayed in Figure 2.4. Note that the qualitative behavior pointed out in the text in Section 2.3.1 is demonstrated by this simplified model. Therefore, the magnetic shear is not responsible for the unexpected decrease in the stability threshold with shear flow; only a localization of the instability is necessary to demonstrate this characteristic. A quantitative comparison of Figure 2.3 and Figure 2.4 shows that, to yield equivalent growth rates, a much larger entropy gradient must be supplied in the unbounded case with magnetic shear than in the bounded, straight-field model. We can understand the

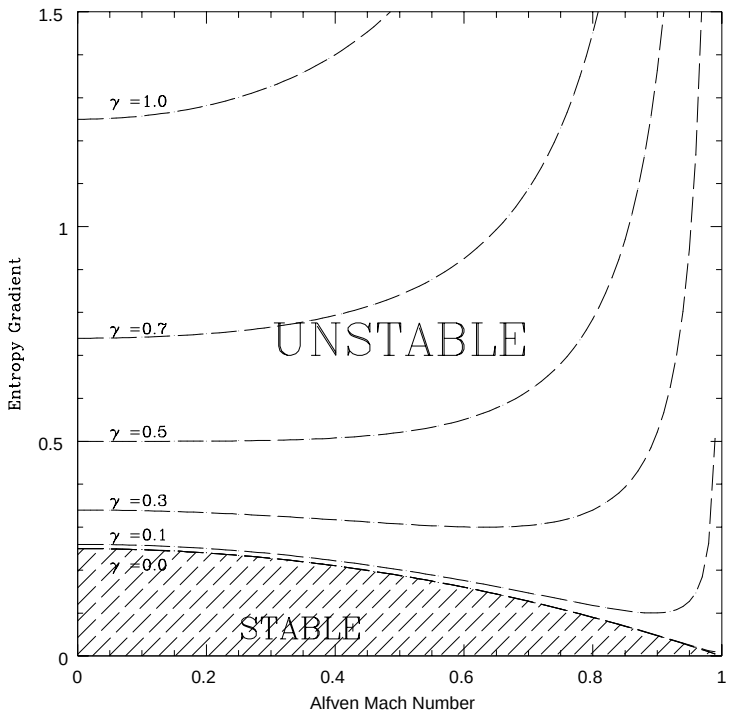

Figure 2.4: The stability diagram for the straight-field case as described by equation (2.58) in section 2.3.3. Note that the qualitative features of the diagram are similar to those in figure 2.3. A value of $L = \pi$ was chosen to plot this diagram.

difference as follows. The energy required to bend the magnetic field lines slows the growth of the instability. In the bounded case, this energy is needed to bend the field line only within the bounded domain. But, in the unbounded model, the bending of the field lines occurs over a larger extent in z, thus requiring more energy and so more effectively suppressing the instability.

2.3.4 Energy Conservation

In the standard way, (2.26)–(2.28) can be combined, replacing γ with the time derivative $\frac{\partial}{\partial t}$, to obtain an energy integral for the model. Converting back to $\delta v_\perp$

and $\delta B_\perp$ using (2.29) and (2.30), we find

$$\frac{\partial}{\partial t}\left\{\frac{1}{2}\int_{-\infty}^{\infty}\left[\frac{\delta B_\perp^2+\delta v_\perp^2}{1+z^2}-\frac{2M\delta B_\perp\delta v_\perp}{1+z^2}-\frac{s^2}{s_0'}\right]dz\right\}=M\int_{-\infty}^{\infty}\frac{s\delta B_\perp}{1+z^2}dz. \quad (2.59)$$

Adopting the terminology of Hayashi and Young [86], we define the integral on the left-hand side of (2.59) as the wave energy of the perturbation. Note that, in the absence of flow ($M=0$), the wave energy is constant in time. (2.59) supplies a limit on the value of s_0' necessary for instability: since the $\delta B_\perp^2$ and $\delta v_\perp^2$ terms are both positive definite, an instability can only develop for $s_0'>0$. In this case, gravitational potential energy from the s^2 term can be harnessed to drive the kinetic energy and field line bending of the instability.

By the same method as above, we find that the wave energy integral for the straight-field model bounded at $z=\pm L$, in Section 2.3.3, has the form

$$\frac{\partial}{\partial t}\left\{\frac{1}{2}\int_{-L}^{L}\left[\delta B_\perp^2+\delta v_\perp^2-\frac{s^2}{s_0'}\right]dz\right\}=\frac{M}{2}\left\{\delta B_\perp^2(-L)-\delta B_\perp^2(L)+\frac{s^2(L)}{s_0'}\right\}. \quad (2.60)$$

Without flow, again, we find that the necessary condition for instability to develop is $s_0'>0$ and that the wave energy integral is constant in time. In the presence of flow, we interpret the terms on the right-hand side of (2.60) as follows: $\delta B_\perp^2(-L)$ represents the flow of magnetic energy into the region, $-\delta B_\perp^2(L)$ represents the flow of magnetic energy out of the region, and $\frac{s^2(L)}{s_0'}$ represents the flow of gravitational potential energy out of the the region.

2.4 Discussion

To study the effect of magnetic shear and shear flow on local buoyant instabilities, we have constructed a simple model in the Boussinesq limit of ideal MHD. Nu-

merical solutions to this model yield a stability diagram of the (M, s_0') parameter space. This stability diagram has three important characteristics. First, there exists a threshold entropy gradient for unstable mode growth, demonstrating that magnetic shear is a stabilizing influence. Second, flow serves to suppress mode growth in a substantially unstable regime, but near marginal stability it lessens the stabilizing effect of magnetic shear, enhancing unstable mode growth rates and lowering the threshold entropy gradient necessary for instability. Third, normal modes of instability are stabilized completely as the Alfvén Mach number approaches one because the disturbance is swept downstream out of the unstable region. Analytical work corroborates these characteristics in the different regions of (M, s_0') parameter space.

In a shear magnetic field without flow, the characteristic shape of the unstable mode is such that the field lines remain on the magnetic shear (constant y') surface shown in Figure 2.1; hence, in the lab frame, the field lines must twist as they fall under gravity to remain on this surface. This occurs because the perturbed field line at any vertical height x must align with the direction of the unperturbed field at that height to facilitate interchange. Unlike the ordinary interchange of straight field lines, if magnetic shear is present, the field line *must* be bent to allow interchange; this is the root of the stabilizing influence of the shear magnetic field. Energy extracted from gravitational potential energy as the field line falls must supply both the kinetic energy of the moving plasma, which is frozen to the field line, and the energy required to bend the field line. Unstable motions are localized about the point where the magnetic shear (constant y') surface is vertical ($z = 0$ in Figure 2.1), because this point is where motions on that surface extract

the most gravitational potential energy while minimizing field line bending. When plasma shear flow is included in the problem, this unstable region moves in the lab frame with the flow velocity v_f in the $-\hat{\mathbf{z}}$ direction. Therefore, this characteristic twisting geometry propagates along z at a speed $v_f = v_0 \frac{l_B}{l_v}$ determined by the local flow speed v_0, flow shear length l_v, and magnetic field shear length l_B. Typical eigenfunctions for an entropy gradient of $s_0' = 0.6$ and Alfvén Mach numbers $M = 0$ and $M = 0.8$ are displayed in Figure 2.5.

The modifications of the stability of a magnetized plasma due to the presence of magnetic shear and shear flow impact several diverse subjects. In solar physics, one of the key processes necessary for the success of the interface dynamo [147, 51] is the storage of an intense toroidal field in the solar tachocline [176] until an instability causes an isolated flux tube to rise into the base of the convection zone [1, 40, 41, 89, 45, 44, 165, 39, 73, 10]. Shear flow is present due to the large differential rotation of the sun in the tachocline region [184, 164], and some magnetic shear probably exists here as well; the impact of shear flow and magnetic shear may alter stability within this region. There are two regions in galactic physics where the conditions in our model may apply: near the center of the galaxy, where there likely exists a region of magnetic shear in which the large-scale magnetic field changes from primarily azimuthal to primarily vertical [195] and shear flow is present through differential rotation, and in the disk of the galaxy, where both magnetic shear and shear flow may be present in the vertical direction away from the mid-plane. In examining the mechanisms for turbulence in accretion disks, Balbus and Hawley [9] pointed out that a previously discovered [188, 49, 50] but unappreciated linear MHD instability, driven by differential

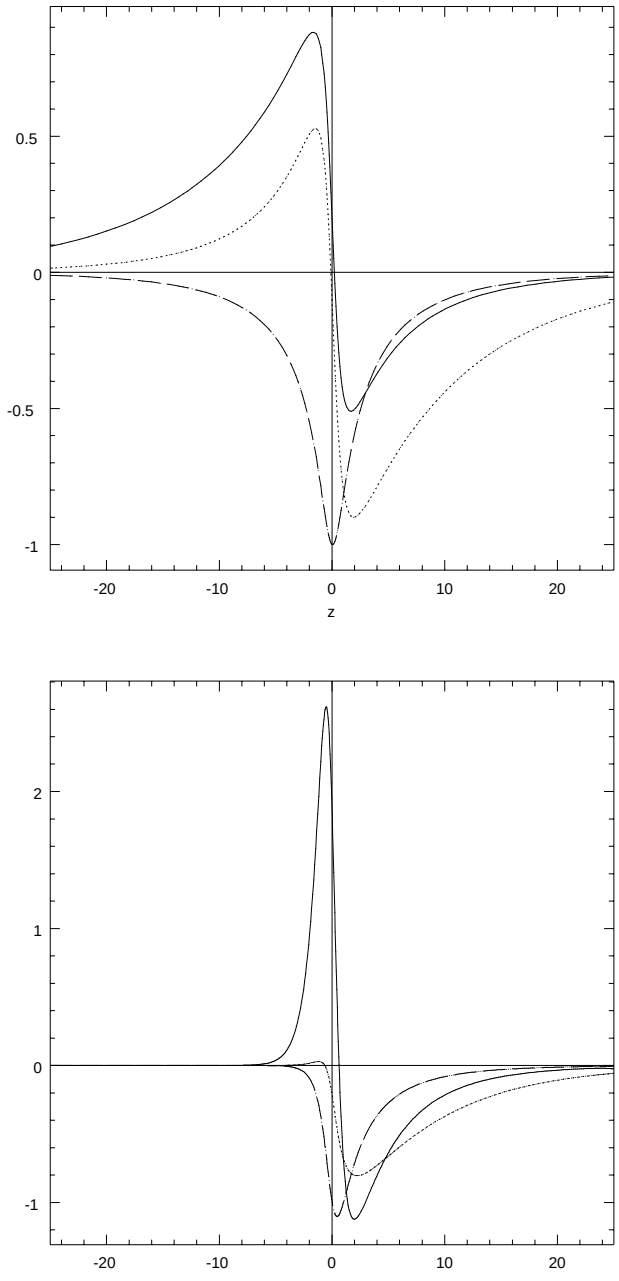

Figure 2.5: Eigenfunctions for entropy gradient $s_0' = 0.6$ and $M = 0$ (left plot) and $M = 0.8$ (right plot). The three functions are A_+ (solid line), A_- (dotted line), and s (dashed line). Note that for the $M = 0.8$ case, where the plasma flow is in the $+z$ direction, the eigenfunctions grow quickly with steep gradients and diminish slowly as you move from left to right.

rotation coupled with magnetic tension, would occur if the accretion disk were threaded by a weak magnetic field. But the Balbus-Hawley instability bends the magnetic field lines extensively; thus, it is stabilized by magnetic tension for large magnetic field strengths [30, 186, 97]. Although the twisting interchange instability studied here depends not on rotation but on an entropy gradient, it has a characteristic geometry that minimizes field line bending and so may be important in regions of large field strength. As is well-known within the fusion community [158], employing a sheared toroidal magnetic field in a tokamak can help to stabilize, or at least suppress, ballooning instabilities (buoyant interchange instabilities driven by pressure and curvature forces). The idea of employing shear flow to further stabilize ballooning instabilities has gained much attention in the past decade [190, 83, 84, 85, 128]. Our work demonstrates that, near marginal stability, shear flow actually lessens the stabilizing effect of magnetic shear, lowering the threshold entropy gradient required for instability and enhancing the unstable mode growth rate. Full stabilization of the plasma will occur only if the Alfvén Mach number of the plasma flow (as defined in our transformed coordinates) exceeds one. The local nature of the instability examined in this work means that our treatment may apply locally in more complicated environments. The instability may behave as a traveling "wave packet" which moves with the intersection of shear magnetic field lines (where the magnetic shear surface is vertical); the disturbance may move in and out of unstable regions, with the perturbation growing where conditions are unstable and decaying in stable regions.

We have extended the model to include compressibility. In this case, the behavior is governed by a system of five coupled, first-order ordinary differential

equations. Five parameters are necessary to describe the system: the Alfvén Mach number, the plasma β, the density gradient, the pressure gradient, and the magnetic field gradient. Over some portions of this five-dimensional parameter space, the growth rate eigenvalue γ does indeed become complex. Producing a simple answer from this more complicated model is quite difficult. Our current research is addressing this difficulty. But, the magnetic-buoyancy instability [145], which depends on compressibility, cannot be investigated without employing this more detailed treatment. We will then be able to relate our work quantitatively to applications such as the stability of magnetic fields in the solar tachocline. One final possible extension of this research is an investigation of the nonlinear behavior using an initial-value code.

Chapter 3

Gradient Particle Magnetohydrodynamics

3.1 Introduction

From the recognition, over a half century ago, of the role of magnetic fields in the confinement [127] and acceleration [70] of cosmic rays and of the realization that astrophysical magnetic fields can be detected through synchrotron emission, the importance of magnetic fields in astrophysics has become increasingly apparent. Early numerical work focused primarily on the gravitational and hydrodynamical forces influencing astrophysical settings, but more recent studies have demonstrated that magnetic fields cannot be neglected in investigations of astrophysical jets [31], accretion disk dynamics [9], molecular cloud collapse and star formation [136]. New observations have found microgauss strength magnetic fields in galactic clusters [43], suggesting that magnetic fields of this strength are far more ubiquitous in the universe than previously believed. Additional observations have shown that extragalactic gaseous systems with redshifts up to $z = 2$ and very early galaxies up to $z = 6$ appear to harbor microgauss or stronger magnetic fields [106],

suggesting that magnetic fields of this strength existed much earlier in the history of the universe than previously thought. In the face of this evidence, the importance of including magnetic fields in numerical work in astrophysics cannot be understated.

Numerical methods for astrophysical fluid simulation can be broadly categorized as either Eulerian or Lagrangian: in the Eulerian approach, a fixed grid is constructed in space and the fluid flows through that grid; and, in the Lagrangian approach, grid points are embedded in and flow with the fluid, so as the fluid flows the mesh connecting the grid points is deformed. These two approaches have complementary strengths and weaknesses. Eulerian codes tend to exhibit higher precision and better conservation properties than Lagrangian codes, but Lagrangian algorithms are usually less diffusive. Computer models of astrophysical problems often require the accurate representation of densities and other fluid quantities that vary over several orders of magnitude, so a method with some means of selective resolution enhancement is desirable. To implement such a resolution enhancement in an Eulerian code using a strategy such as Adaptive Mesh Refinement [20, 19] entails a great deal of complexity. Lagrangian codes, on the other hand, are inherently adaptive: when a fluid is compressed to a high density, the Lagrangian grid points flow with the fluid, yielding increased resolution in the compressed region. This characteristic of Lagrangian methods makes them attractive choices for the simulation of astrophysical phenomena.

Lagrangian numerical methods either employ a deformable mesh or simply follow the paths of unconnected particles (often denoted meshless); I shall refer to these different strategies as Lagrangian *mesh* codes and Lagrangian *particle* codes.

Lagrangian mesh codes face the difficult obstacle of handling severe distortions of the mesh; many mesh-based implementations, in fact, resort to a partial use of Eulerian grids to overcome this difficulty. Lagrangian methods have historically been used to investigate problems of hydrodynamics, the dynamic response of solids, and magnetohydrodynamics (MHD); here we will briefly review existing Lagrangian approaches.

Most Lagrangian numerical methods for MHD are mesh techniques. In particle-in-cell methods [115, 35], fluid quantities are carried by particles, but forces between particles are calculated by interpolation onto a grid. Arbitrary Lagrangian-Eulerian codes [75, 150, 5] include a wide variety of techniques that use Eulerian grids to relax the tangled Lagrangian mesh or to remap the magnetic field for the calculation of the magnetic forces on the particles.

Development of Lagrangian particle methods has traditionally aimed specifically at problems in hydrodynamics or in engineering studies of the dynamic response of materials; the preservation of zero magnetic divergence makes the construction of particle codes for MHD particularly challenging. Smoothed Particle Hydrodynamics (SPH) [122, 74] is the most widely used particle method for hydrodynamic and materials engineering research. Recent variations of SPH to improve performance include Moving Least Squares Particle Hydrodynamics [63, 64] and Renormalized Meshless Derivative [114]. Dilts et al. [66] have also proposed the Tuned Regression Estimation technique for hydrodynamics based on a local regression estimator of the fluid. Attempts to extend the SPH method to include magnetic fields begin nearly two decades ago [151]. Smoothed Particle Magnetohydrodynamics (SPMHD) [178] and Regularized SPH [33] have met with some

success, but have either neglected the issue of accumulated magnetic divergence or been limited to one or two dimensions.

This chapter presents the Gradient Particle Magnetohydrodynamics (GPM) algorithm for 3-D Lagrangian particle simulation of MHD. The implementation of the GPM algorithm for astrophysical MHD simulation is discussed and results from validation tests are presented. The relation of GPM to the technique of local polynomial regression in statistics is explored.

3.2 Lagrangian Particle Methods for MHD

The Lagrangian equations of ideal MHD, written in terms of the vector potential and allowing for an external magnetic field, are

$$\frac{d\mathbf{v}}{dt} = -\frac{1}{\rho}\nabla P + \frac{1}{4\pi\rho}(\nabla \times \mathbf{B}) \times \mathbf{B} \tag{3.1}$$

$$\frac{d\mathbf{A}}{dt} = \mathbf{v} \times \mathbf{B_{ext}} + (\nabla \mathbf{A}) \cdot \mathbf{v} \tag{3.2}$$

$$\frac{d\rho}{dt} = -\rho \nabla \cdot \mathbf{v} \tag{3.3}$$

$$\frac{de}{dt} = -\frac{P}{\rho}\nabla \cdot \mathbf{v}. \tag{3.4}$$

$$\mathbf{B} = \mathbf{B_{ext}} + \nabla \times \mathbf{A} \tag{3.5}$$

The system of MHD equations is closed using the adiabatic equation of state

$$P = (\gamma - 1)\rho e. \tag{3.6}$$

MHD simulation by a Lagrangian particle method begins with the distribution of "particles", which represent fluid elements, throughout the simulation domain. At

the position of each particle, all of the fluid quantities—velocity, vector potential, density, and energy—are known. To advance one particle forward in time, the rates of change of these fluid quantities must be calculated at the position of that particle; these rates of change are given by the left-hand sides of (3.1)–(3.4). To calculate these rates of change, we must know the values *and* the gradients of the fluid quantities at the particle position. Since the values are already known, MHD simulation by a particle method boils down to the determination of gradients of the fluid quantities at all particle positions.

When only the value of a fluid quantity, and not its gradient, is known at each particle position, the determination of the gradient requires knowledge of the values at other particle positions. A radially symmetric smoothing kernel is used to ensure that only nearby particles influence this gradient; the kernel drops to zero at some specified smoothing radius so that only particles falling within the smoothing sphere are considered. Particles within the smoothing sphere are denoted *neighbors*. The number and distribution of neighbors within the smoothing sphere may vary; the smoothing radius must be chosen to include enough neighbors to adequately sample the local fluid environment but not so many neighbors that physically relevant variations are smoothed out. The heart of any numerical method for particle simulation of MHD is an algorithm capable of determining an accurate gradient from a disordered distribution of neighbors.

3.3 Gradient Particle Magnetohydrodynamics

We introduce here the Gradient Particle Magnetohydrodynamics (GPM) algorithm for particle simulation of MHD. This simple algorithm efficiently calculates a least squares polynomial fit of the spatial profile of a given fluid quantity around a chosen particle. Consider a distribution of particles with positions given by $\mathbf{r_i}$; the value of an arbitrary fluid quantity q at particle i is denoted by $q_i = q(\mathbf{r_i})$. A simple 1-D example most clearly demonstrates the GPM algorithm. We want to perform a local polynomial fit of the spatial profile of q around a position x; for a linear fit, we assume a spatial profile $q(x) = A_0 + A_1 x$. We evaluate the quantities $Q_0(x)$ and $Q_1(x)$ given by

$$Q_0(x) = \sum_i q_i m_i W(|x_i - x|, h) \tag{3.7}$$

$$Q_1(x) = \sum_i (x_i - x) q_i m_i W(|x_i - x|, h). \tag{3.8}$$

Here, m_i is the mass of particle i, $W(|x_i - x|, h)$ is a symmetric smoothing kernel of characteristic smoothing radius h, and the sum is performed over all neighbors i. Replacing q_i in (3.7) and (3.8) with our assumed linear profile $q(x)$ yields the matrix equation

$$\begin{pmatrix} Q_0 \\ Q_1 \end{pmatrix} = \begin{pmatrix} S_0 & S_1 \\ S_1 & S_{11} \end{pmatrix} \begin{pmatrix} A_0 \\ A_1 \end{pmatrix}, \tag{3.9}$$

where we define the quantities S_0, S_1, and S_{11} by

$$S_0(x) = \sum_i m_i W(|x_i - x|, h) \tag{3.10}$$

$$S_1(x) = \sum_i (x_i - x) m_i W(|x_i - x|, h) \tag{3.11}$$

$$S_{11}(x) = \sum_i (x_i - x)^2 m_i W(|x_i - x|, h). \tag{3.12}$$

Inversion of the 2×2 matrix in (3.9) yields consistent estimates for the mean and gradient of the fluid quantity q at position x in terms of the calculated sums Q_0 and Q_1. In three dimensions, an analogous procedure can be followed assuming a spatial profile $q(x_1, x_2, x_3) = A_0 + A_1 x_1 + A_2 x_2 + A_3 x_3$ and solving the resulting 4×4 matrix. The GPM algorithm can be further extended to second order by solving the 10×10 matrix resulting from $q(x_1, x_2, x_3) = A_0 + A_1 x_1 + A_2 x_2 + A_3 x_3 + A_{11} x_1^2 + A_{22} x_2^2 + A_{33} x_3^2 + A_{12} x_1 x_2 + A_{13} x_1 x_3 + A_{23} x_2 x_3$.

The GPM algorithm thus extracts the gradients of the fluid quantities at the position of each particle from the fluid quantities of its neighbors. Combining these gradients with the values of the fluid quantities at each particle allows for the calculation of the rates of change of the fluid quantities at that particle. Hence, this algorithm enables the fluid quantities—including the position—at each particle to be stepped forward in time. The particle method resulting from implementation of the GPM prescription enables stable simulation of MHD systems.

3.3.1 Relation to Local Polynomial Regression

As pointed out to the authors by Dilts [65], the idea of a local polynomial fit to a disordered set of data is not new: local polynomial regression has been developed and practiced in the field of statistics for the past twenty five years [69]. Appendix C demonstrates that the GPM algorithm is nearly the same as local polynomial regression. Hence, we can glean a wealth of knowledge from the statistics literature on the subject.

The monograph by Fan and Gijbels [69] succinctly reviews two decades of study of the properties of local polynomial regression; the key points relevant to MHD numerical simulation are summarized here. Local polynomial fitting adapts to any distribution of points, from uniform distributions to random or highly clustered distributions. As well, the error of the method remains of the same order at boundaries without the use of specific boundary kernels. The Epanechnikov kernel, defined by

$$W(t,h) = \begin{cases} 3/4[1-(t/h)^2] & |t/h| \leq 1 \\ 0 & |t/h| > 1 \end{cases}, \tag{3.13}$$

is the optimal kernel in the sense that it minimizes the Mean Squared Error of the regression function. Fan and Gijbels [69] recommend always using an odd order fit when performing local polynomial regression. (The order of the fit, if the aim of the regression is the recover the νth derivative using a polynomial of order p, is defined as $p-\nu$.) Using odd order fits is preferable because, when increasing from a fit of even order $2m$ to a fit of odd order $2m+1$, the extra parameter allows the reduction of error without increasing the variability of the solution. But increasing the order of the fit from $2m+1$ to $2m+2$ causes variability to increase, thus somewhat negating the benefit of a higher order fit. MHD simulation requires a determination of the first derivatives, or $\nu = 1$, so this rule of thumb suggests a quadratic fit ($p = 2$) is best; the tests presented in Chapter 4 thus employ the second-order GPM algorithm. Local polynomial regression is, in fact, nearly 100% asymptotic minimax efficient among all linear smoothers. Fan and Gijbels [69] present a proof of the local truncation error of local polynomial regression: for a smoothing radius h, the error of an odd order fit is $\mathcal{O}(h^{p+1-\nu})$. Therefore, the

local truncation error of the second-order GPM algorithm for fitting the gradients of fluid quantities ($p = 2$, $\nu = 1$) is $\mathcal{O}(h^2)$.

Statisticians are, of course, concerned with the fit of the regression function to a set of unchanging data; for the numerical evolution of an MHD system, the computational stability of repeated local polynomial fits must be determined.

3.4 Physical Implementation Issues

Physical implementation problems that must be addressed for the practical implementation of the GPM numerical method for the simulation of a physical model include maintaining zero magnetic divergence in MHD simulation, using artificial viscosity for capturing shocks, applying boundary conditions, modeling diffusive processes, and preventing density and energy from becoming negative.

3.4.1 Magnetic Divergence

One of the major difficulties in developing a Lagrangian particle code for MHD is the preservation of zero magnetic divergence. It is possible to construct a numerical scheme using the GPM algorithm that evolves the MHD equations using only the magnetic field by replacing (3.2) and (3.5) with the induction equation

$$\frac{d\mathbf{B}}{dt} = \mathbf{B} \cdot \nabla \mathbf{v} - \mathbf{B} \nabla \cdot \mathbf{v}. \tag{3.14}$$

In this case, however, non-zero magnetic divergence builds slowly but steadily, eventually becoming dynamically significant and corrupting the system behavior. To eliminate this problem, we choose to evolve the vector potential, calculating

the magnetic field from the vector potential at each step. Due to the varying number and distribution of neighbors for a given particle, the magnetic divergence is not held at exactly zero, but the magnetic divergence remains dynamically insignificant and does not grow with time during a simulation.

In the implementation described here, we have chosen to calculate the magnetic field from the curl of vector potential as an intermediate step, subsequently determining the magnetic force on the particles from the gradients of the magnetic field. We made this decision so that a first-order GPM method can still be used for MHD problems. An attractive alternative is to eliminate the magnetic field (except for the external field) from the MHD equations entirely by substituting (3.5) into (3.1). In this case, (3.1) depends on second derivatives of the vector potential, so a second-order GPM method would be required for at least the vector potential. This alternative method, however, is computationally unstable.

3.4.2 Artificial Viscosity

Artificial viscosity both accomplishes the damping of high-frequency oscillations and prevents particle interpenetration and free streaming, all potential hazards for Lagrangian codes. A common treatment of artificial viscosity in finite difference calculations involves the addition of a viscous pressure term q that enhances the pressure when $\nabla \cdot \mathbf{v} < \mathbf{0}$ [157]. In the momentum and energy equations, the pressure P is replaced by $P + q$, where

$$q = \begin{cases} -\alpha\rho h c_s \nabla \cdot \mathbf{v} + \beta\rho\mathbf{h^2}(\nabla \cdot \mathbf{v})^\mathbf{2} & \text{if } \nabla \cdot \mathbf{v} < \mathbf{0} \\ 0 & \text{if } \nabla \cdot \mathbf{v} > \mathbf{0}. \end{cases} \tag{3.15}$$

Here α and β are dimensionless constants, h is the smoothing length, ρ is the local density, and c_s is the local sound speed. The term linear in the velocity divergence produces a shear and bulk viscosity [131]; the quadratic term is similar to the von Neumann-Richtmeyer viscosity [189] and prevents the free streaming of particles in strong shocks.

Monaghan and Gingold [133] suggested that for SPH, which is significantly less diffusive than grid-based methods, artificial viscosity is always necessary but that the above formulation smears out shock fronts excessively because $\nabla \cdot \mathbf{v}$ is averaged over all particles in a smoothing radius. They found a more effective artificial viscosity based on interparticle velocity differences [131, 132]. A similar approach to Monaghan [132]—estimating $\nabla \cdot \mathbf{v}$ by the velocity differences between particles—performed well under a first-order Eulerian timestepping scheme but was unstable when using a second-order leapfrog timestep.

Although using a GPM calculation of $\nabla \cdot \mathbf{v}$ in (3.15) does smear out the shocks somewhat, it suppresses post-shock oscillations effectively and yields the correct Rankine-Hugoniot jump conditions. To eliminate the necessity of passing through all particles twice at each timestep, we have found that using the $\nabla \cdot \mathbf{v}$ for each particle from the previous step is satisfactory; the dissipative term q is introduced for purely mathematical reasons, so its precise form is not critical so long as it reproduces shocks correctly [189].

3.4.3 Boundary Conditions

The treatment of particles at the edge of the simulation domain is one of the key challenges for a Lagrangian particle code. The application of specific boundary conditions delineates assumptions about the nature of the physical model beyond the simulation domain and can affect the behavior of particles deep within the domain. Two typical boundary conditions are periodic and open.

Simple and widely used, periodic boundary conditions simply wrap the simulation domain around onto itself. These boundary conditions are easily implemented for a Lagrangian particle code: the neighbors for a particle near the edge of a periodic box will include particles from the opposite edge of the box, and any particle moving beyond the limit of the domain in a given dimension is simply wrapped around to the opposite limit of the same dimension. Taking these two measures, the GPM algorithm behaves in the same manner near the domain boundaries as it does within the bulk of the domain.

But for large-scale astrophysical phenomena in which the system geometry may play an important role—exactly the type of problems for which GPM was developed—periodic boundary conditions are inadequate and more sophisticated open boundary conditions must be used. Specifying a given choice of open boundary conditions is equivalent to making an assumption about the nature of the physical model beyond the domain boundaries. Consider the problem of modeling the Galactic disk. If any interaction with extragalactic objects is neglected, we can specify that all fluid quantities such as density, energy, and velocity drop towards zero with distance from the Galactic center. Such a model conserves en-

ergy and angular momentum. But, a numerical simulation will necessarily cover a finite domain, so we must allow for the transport of energy and momentum through the domain boundaries. This choice leads to radiation boundary conditions: although waves may exit the simulation domain, no wave energy is allowed to enter the domain through the boundaries. Achieving boundary conditions of this nature presents a challenge for Lagrangian particle codes.

The GPM algorithm for the recovery of fluid gradient information suffers a systematic error at the boundary of the domain. A simple 1-D graphical example demonstrating this problem is presented in Figure 3.1. In numerous astrophysical problems, including the isolated Galactic disk, the fluid quantities such as the density decrease exponentially as you move away from the center in the direction normal to the simulation domain boundary. Figure 3.1 shows the particle at the edge of the domain (open circle) and its neighbors within the domain (filled circles); all of the neighbors necessarily lie on one side of the particle. The first-order GPM determination for the gradient of a function in 1-D is simply a weighted sum of two-point slope determinations, as demonstrated by (B.3). The profile shown in Figure 3.1 is an exponentially decreasing function given by the thick solid line. The two-point gradients due to all the possible pairs of points correspond to the slopes of the thin solid lines connecting the neighbors and the particle; the actual gradient of the function at the particle is given by the dashed line. Note that the slopes for all of the two-point gradient determinations are greater than the actual slope of the function at the particle; hence, the gradient at this particle is systematically overestimated. For the simple case of hydrostatic equilibrium in one dimension, the result is that, even if the force due to the pressure gradient

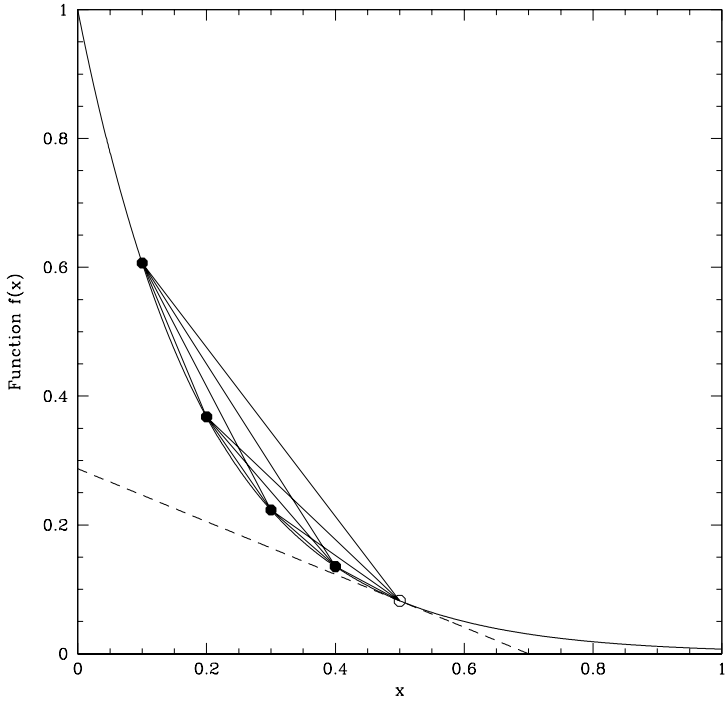

Figure 3.1: Demonstration of the error in GPM gradient determinations at boundaries. If all particles lie on one side of the test particle, it is possible to overestimate the gradient at that point. The exponentially decreasing function (thick solid line) has a gradient at the test particle (open circle) given by the dashed line. The two-point slope determinations for all pairs of neighbors (solid circles) are denoted by the thin lines. The weighted sum of these two-point slope determinations overestimates the actual gradient.

exactly balances other forces in the problem, a stable hydrostatic equilibrium is not achieved because of the error in the pressure gradient—the imbalance leads to an unphysical expansion normal to the boundary.

To rectify this difficulty with open boundary conditions, fixed Eulerian boundary points are placed to specify the domain boundary. Because these boundary points do not move, adjustments of the fluid quantities near the edge compensate for the systematic error in the gradient at the boundary without leading to an unphysical expansion. This hybrid approach, employing an Eulerian grid of points at the boundary to contain the Lagrangian particles within the boundary, affords great flexibility in exerting boundary control. Specification of reflecting boundary conditions is easily accomplished by setting the normal velocity of the boundary points to zero and reflecting any particles that attempt to pass through the boundary. Radiation boundary conditions are more difficult to achieve. For situations in which the behavior near the boundaries is relatively quiescent, allowing the fluid quantities at the boundary points to adjust freely to changes in the fluid allows outgoing waves to leave the system; the fluid quantities at the boundary points are simply updated using the GPM algorithm according to the MHD equations including the advective term. If shock waves cross the boundary, however, this treatment often fails. If one sets the normal velocity to zero at the boundary points but allows particles to pass through the domain boundary and be removed, the boundary more easily handles shocks. This more heavy handed approach still allows the transport of momentum and energy through the boundary with particles, but caution must be taken to ensure that the boundary conditions do not affect the evolution of the bulk of the simulation.

3.4.4 Diffusion

Viscosity, resistivity, and thermal conductivity are diffusive processes that can have an important effect on the evolution of the velocity field, magnetic field, and energy distribution. Although the second-order GPM algorithm can calculate the Laplacian of any fluid quantity, the inclusion of a Laplacian diffusion term in the evolution equations is unconditionally unstable when used with an explicit, second-order timestepping scheme. Hence, an alternative method for applying a physical diffusion process is desirable.

The GPM algorithm returns values not only for the first (and possibly higher order) derivatives, but also for the mean value of a quantity at the particle position. The effect of a physical diffusion is to smooth out the higher order spatial fluctuations of a given field; adjusting the value of that field at a given particle towards the GPM smoothed mean value accomplishes a similar end. A new diffused value can be computed from the old value and the GPM smoothed mean value according to $q_{new} = q_{old} + f_{diff}(q_{GPM} - q_{old})$, where the fractional effect of the diffusion is given by $0 \leq f_{diff} \leq 1$. This effective diffusion can be applied every N_{diff} timesteps. This prescription for incorporating diffusion into a GPM numerical scheme is stable and adequately reproduces the effects of viscosity, resistivity, or thermal conductivity.

The scale over which a chosen diffusive process is applied can be specified independently, yielding a minimum scale for structure in the associated fluid quantity unrelated to the average particle separation in the region. In regions where few particles fall within the diffusive scale length, the effect of the diffusion is negligi-

ble; in regions where many particles fall within the scale length, diffusive effects can be dominant. Hence, the physical processes of viscosity, resistivity, and thermal conductivity are applied consistently to the entire simulation domain, rather than varying according to the local number density of particles. This is important since the effective numerical diffusivity, related to the number density of particles in a given region, will vary throughout the simulation domain; specifying a scale for a given diffusive process ensures that the resulting structure at that scale is not affected by the unphysical numerical diffusivity. This prescription also has the advantage, for example, that the viscous and resistive scale lengths can be varied independently to explore a range of magnetic Prandtl numbers.

3.4.5 Logarithmic Updates for Density and Energy

Density and energy should remain greater than zero throughout the simulation; but, in an astrophysical situation where both quantities approach zero at the outer boundaries, it is possible for the value to become negative as it is advanced in time. We can prevent this problem by choosing to advance these quantities using the logarithm of the value, rather than the value itself. For example, instead of updating the density using (3.3), we can use

$$\frac{d \ln \rho}{dt} = -\nabla \cdot \mathbf{v}. \tag{3.16}$$

We replace the standard second-order leapfrog advancement for density

$$\rho_{n+1} = \rho_{n-1} + 2\Delta t \left. \frac{d\rho}{dt} \right|_n , \tag{3.17}$$

by the formula for the logarithmic case

$$\rho_{n+1} = \rho_{n-1} \exp\left(2\Delta t \left.\frac{d \ln \rho}{dt}\right|_n\right). \tag{3.18}$$

The energy is treated similarly.

3.5 Computational Implementation Issues

Computational implementation issues deal with the suppression of computational instabilities that arise from the accumulation of errors as the simulation progresses; these include maintaining a particle distribution that ensures good sampling of the local environment, ensuring that behavior of particles remains fluid, and eliminating leapfrog timestep splitting instabilities.

3.5.1 Particle Distribution Control

The greatest threat to long-term computational instability that a Lagrangian particle code faces is the maintenence of a "good" particle distribution. "Good" means that enough neighbors are distributed throughout the smoothing sphere for the least squares fit to recover an accurate value for the mean and gradient of each fluid quantity. Because particles flow through the simulation domain following the local fluid velocity, after many timesteps it is possible for a number of particles to become clumped together or for a substantial region to become devoid of particles. Clumps of particles waste computational effort by oversampling of a region; voids endanger the accuracy of the GPM results due to undersampling of a region. Additionally, since the maximum allowable timestep for stability under

the Courant criterion is related to the particle spacing, simulations with clumps of particles will require smaller timesteps to ensure computational stability. Hence, some control of the particle distribution as the simulation progresses is desirable. The particle distribution is controlled by implementing particle separation, particle removal, particle addition, and void filling.

The local average particle separation is closely related to the smoothing length of a given particle. The separation between any two particles, however, can be significantly smaller than the average particle separation. Particles that come too close together yield redundant information about the fluid at the location, lowering the effective simulation resolution for a given number of particles. Particle separation eliminates this potential problem by separating two particles that have come closer together than a specified fraction of the smoothing length. The particles are separated along the line joining them to conserve momentum and other conserved quantities. This separation acts as a diffusion on small scales; the scale of this diffusion, however, is well below the minimum resolved scale given by the smoothing length.

Applications such as astrophysical accretion disks characteristically demonstrate radial inflow of material towards the center driven by a variety of mechanisms for angular momentum transport. Since Lagrangian particles move with the fluid flow, this will lead to an accumulation of particles in the central region. Each particle contributes to the computational cost of a timestep, so if the resolution enhancement in the central region is not needed, removing particles in regions of high particle number density will improve the computational efficiency. Particle removal is implemented by eliminating a particle whose smoothing length

has dropped below a certain threshold. Physical quantities are conserved by combining the offending particle with its nearest neighbor in a conservative manner.

Continuing with the example of an astrophysical accretion disk, the net radial inflow of material means that more particles must be added at the boundaries to prevent a depletion of particles in the outer regions. This particle addition represents an inflow of material through the boundary. To maintain good sampling, the criterion for particle addition ensures that the average particle spacing of the particles near the boundary remains similar to the average particle spacing of the fixed Eulerian boundary points.

Finally, random fluctuations in the particle number density as well as certain flow patterns may lead to the development of significant voids in the particle distribution within the bulk of the simulation volume. The undersampling in a void region may result in poor least squares fitting of the local fluid profile; in the worst cases, this undersampling can drive computational instability. To detect voids, the distance from the particle position to the center of its neighbor distribution is calculated; if the distance exceeds some threshold fraction of the particle smoothing length, then a significant void exists. A new particle can be placed in the void, taking the values for its fluid quantities from an interpolation of the local environment.

The four processes of particle separation, particle removal, particle addition, and void filling ensure the spatial distribution of particles provides an adequate sampling of the local fluid environment over the entire domain throughout the evolution of the simulation.

3.5.2 Fluid Behavior: Smoothing

Because the GPM algorithm fits the local fluid profile with a linear or quadratic function, discontinuities in the fluid state can lead to large errors in GPM gradient determinations due to the significance of higher order derivatives. To prevent this problem, it is necessary to maintain a smooth fluid profile on the scale of the smoothing length. This is accomplished in two ways: discontinuous initial conditions are smoothed before beginning the simulation, and smoothing is applied periodically as the simulation is evolved in time.

Smoothing of initial conditions always employs a linear smoothing and may be performed several times to achieve an adequately smooth profile. Periodic smoothing during the simulation uses either a linear or a quadratic smoothing; frequent linear smoothing is very diffusive, but a quadratic smoothing preserves the low diffusivity characteristic of Lagrangian schemes while maintaining locally smooth conditions. Smoothing is performed using the GPM prescription: the mean values of the fluid quantities returned by the GPM algorithm provide the smoothed estimate q_{sm}. The fluid quantity q is updated with a fractional smoothing weight f_{sm} according to the formula $q_{new} = q_{old} + f_{sm}(q_{sm} - q_{old})$. All fluid quantities are smoothed simultaneously when smoothing is performed.

3.5.3 Leapfrog Timestep Splitting

The second-order leapfrog timestepping scheme is susceptible to a splitting instability where the values at alternate timesteps can drift away from each other [153]. A simple cure for this involves a periodic correction by averaging values at subse-

quent timesteps. For instance, given values for a fluid quantity q at times t_n and t_{n-1}, a corrected value at time $t_{n-1/2}$, accurate to second order, can be calculated by

$$q(t_{n-1/2}) = \frac{q(t_n) + q(t_{n-1})}{2} \tag{3.19}$$

If this measure is taken for both the current timestep and the last timestep, the leapfrog splitting instability is cured for the expense of one half of a timestep.

3.6 Conclusion

The importance of magnetic fields in astrophysical phenomena has become increasingly apparent over the last fifty years. Lagrangian methods are well-suited for numerical investigations in astrophysics. The scientific community has expended much effort on the development of Lagrangian MHD codes. We present here a new algorithm for Lagrangian particle simulation of astrophysical MHD, Gradient Particle Magnetohydrodynamics.

The evolution of an MHD system in a Lagrangian particle code requires the determination of accurate gradients of fluid quantities from a disordered distribution of neighbors. The GPM algorithm employs a local least squares fit to recover this gradient information from the particle distribution. Control of magnetic divergence, a serious challenge for any Lagrangian particle MHD code, is accomplished by evolving the vector potential rather than the magnetic field itself. The GPM algorithm is nearly identical to local polynomial regression in the field of statistics; hence, optimization of any GPM code may benefit from the existing literature on

the properties of local polynomial regression. GPM codes will provide a useful numerical tool for the next generation of research on astrophysical MHD.

Chapter 4

Validation of the GPM Algorithm

This chapter presents the results of validation tests performed using the GPM algorithm described in Chapter 3. Related here are test results for sound waves, MHD waves, a magnetized vortex, hydrodynamic shocks, MHD shocks, and the Kelvin-Helmholtz instability.

All of the simulation results here employ the Epanechnikov kernel given by (3.13) and use a second-order leapfrog timestepping scheme. The adiabatic index used for all tests is $\gamma = 5/3$ unless otherwise noted. For variable smoothing length runs, the number of neighbors specified includes the particle at which the GPM algorithm is being applied.

4.1 Sound Waves

Linear and nonlinear sound wave simulations test the ability of GPM to handle hydrodynamics. Sound wave propagation results, a dispersion relation of the GPM method for varying spatial resolution, and a solution for the nonlinear steepening of a finite amplitude sound wave are presented here.

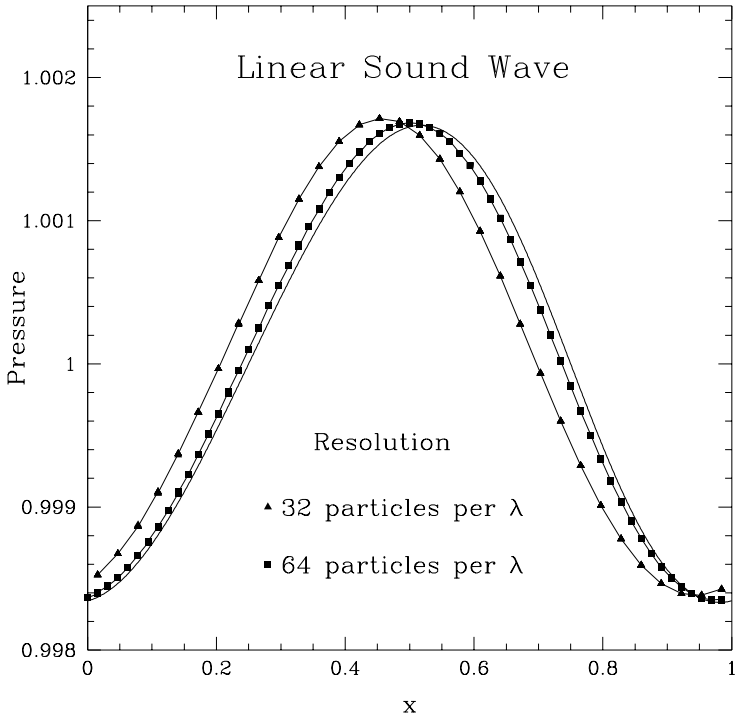

Figure 4.1: First-order 32×8 (triangles) and 64×8 (squares) GPM results for the propagation of a linear sound wave moving in the $+x$ direction with amplitude $\delta v = 0.001 c_s$ at time $t = 10.0$. The analytical result is the solid line and the boxes indicate the GPM results with a connecting line to assist in comparison.

Figure 4.1 shows the propagation of a linear acoustic wave for two spatial resolutions using first-order GPM. In these 2-D periodic runs, particles are initialized with uniformly spaced positions: 32×8 particles in a box of size 1.0×0.25, and double the resolution with 64×8 particles in a box of size 1.0×0.125. Initial conditions impose a single eigenmode moving in the $+x$ direction with a velocity perturbation of $\delta v = 0.001 c_s$, where the sound speed $c_s = 1.0$. Both runs use a Courant fraction of $f_{CFL} \sim 0.5$; smoothing lengths and timesteps are fixed at $h = 0.0625$ with $\Delta t = 0.015625$ and $h = 0.03125$ with $\Delta t = 0.0078125$. The results are plotted at $t = 10.0$, after 10 sound crossing times across the box. The analytical result, given by the solid line in Figure 4.1, includes the effect of nonlinear steepening. Two empirical observations have been made from GPM test simulations of linear sound waves: the phase error, or wave velocity error, is controlled primarily by the spatial resolution, or the number of particles per wavelength; and the amplitude error, or stability, is controlled primarily by the timestep size. The relation of the phase error to the spatial resolution is easily seen in Figure 4.1.

Figure 4.2 presents the dispersion relation for linear sound waves. Parameters are chosen analogously to those specified in the simulations presented in Figure 4.1. These first-order GPM runs use $8, 16, 32, 64$, and 128 uniformly spaced particles in the x direction and always 8 particles in the y direction. Smoothing lengths are fixed at twice the uniform particle spacing and timesteps are chosen using a Courant fraction of $f_{CFL} = 0.5$. The sound speed is measured from the results at $t = 10.0$ for each case. The resolution, or number of particles per wavelength, is indicated on the figure. A resolution of 32 or more particles per wavelength

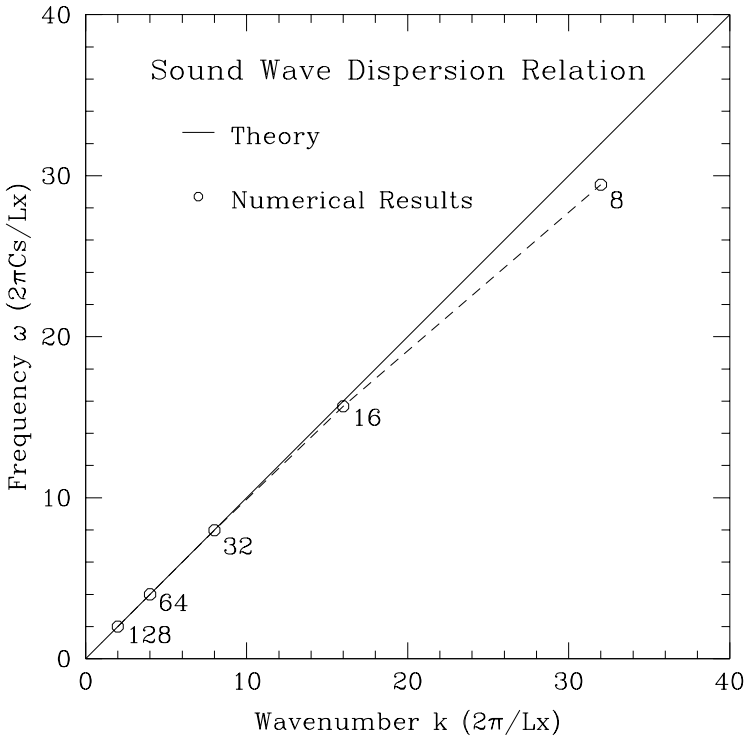

Figure 4.2: Dispersion relation for linear sound wave using the GPM algorithm. The number of particles per wavelength is noted next to each point.

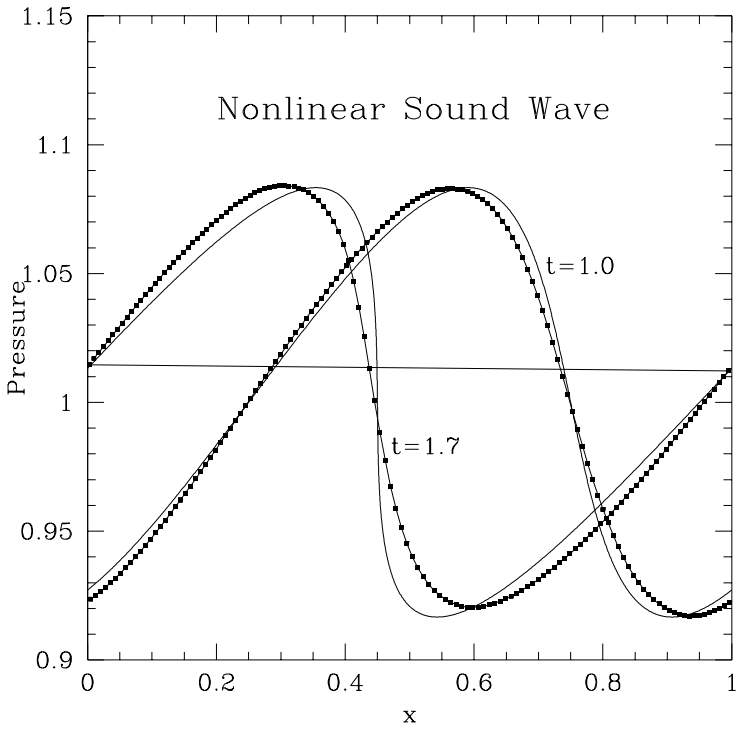

Figure 4.3: The propagation and steepening of a nonlinear sound wave of amplitude $\delta v = 0.05 c_s$ using first-order GPM with 64×8 particles. The analytical solution from an inviscid method of characteristics is given by the solid line and the boxed line shows the GPM results. The analytical solution forms a shock at $t = 1.74$.

produces excellent agreement with the analytical value. The spatial resolution appears to determine the phase error of the propagating wave; amplitude errors are negligible as long as the Courant condition for stability is satisfied.

Figure 4.3 shows the first-order GPM solution of the nonlinear steepening of a finite amplitude sound wave compared to an inviscid method of characteristics solution. 128×8 uniformly spaced particles in a box of size 1.0×0.0625 are used with a variable smoothing length adjusted to include 9 neighbors. The unperturbed sound speed is $c_s = 1.0$ and a timestep of $\Delta t = 0.00390625$ yields

a Courant fraction of $f_{CFL} \sim 0.5$. A single sinusoidal eigenmode moving in the positive x direction of amplitude $\delta v = 0.05 c_s$ is imposed. The analytical formation of a shock in an inviscid fluid occurs at $t = 1.74$; the GPM solutions at $t = 1.0$ and $t = 1.7$ are plotted and compared to the inviscid method of characteristics solutions. Without any artificial viscosity, the GPM results show the onset of post-shock oscillations at $t = 1.7$; therefore, a small artificial viscosity, with $\alpha = 0.05$ and $\beta = 0.10$, is used to suppress this behavior.

4.2 MHD Waves

To test the ability of the GPM algorithm to accurately simulate MHD phenomena, simulations of slow, Alfvén, and fast MHD waves probed the full range of angles between the wave propagation direction $\mathbf{k}$ and the direction of the unperturbed magnetic field $\mathbf{B_{ext}}$. The results of these tests are easily summarized on a polar plot of MHD linear wave propagation as shown in Figure 4.4; for further explanation of this polar plot, see Shu [171]. In this plot, the direction of the magnetic field is along the ordinate and the angle between the magnetic field $\mathbf{B_{ext}}$ and the wave propagation direction $\mathbf{k}$ is the polar angle measured from the ordinate to the abscissa; the radial coordinate corresponds to the magnitude of the wave velocity. The analytical solutions are plotted as solid lines and the boxes represent values obtained by the GPM code. We ran second-order GPM simulations with $32 \times 8 \times 8$ particles on a uniform lattice in a periodic box of size $1.0 \times 0.25 \times 0.25$ cm. The density was set to a uniform $\rho = 1.0$ g/cm^3 and the mean energy and mean magnetic field were chosen to yield a sound speed $c_s = 1.0$ cm/s and an Alfvén speed $v_A = 2.0$ cm/s. We specified a variable smoothing length with 33 neighbors in

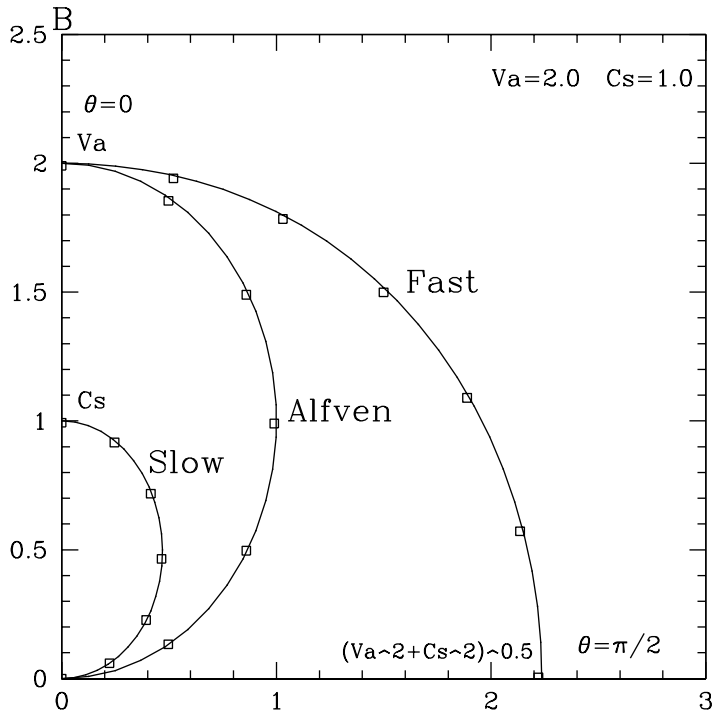

Figure 4.4: Polar plot of the MHD wave speeds vs. the angle between the magnetic field $\mathbf{B_{ext}}$ and the wave propagation direction $\mathbf{k}$. The analytical solutions for slow, Alfvén, and fast MHD waves are indicated by the solid lines; second-order GPM results for $32 \times 8 \times 8$ simulations are given by the boxes.

the smoothing sphere for this fully 3-D calculation and chose a uniform timestep $\Delta t = 0.007$ s (corresponding to Courant number of 0.5 for the fast MHD wave). We initialized each run with the lowest wavenumber eigenmode for each of the three wave types with the amplitude of the velocity perturbation $\delta \mathbf{v} \cdot \hat{\mathbf{k}} = \mathbf{0.001 c_s}$ for the slow and fast waves and $\delta v_z = 0.001 c_s$ for the Alfvén wave. The angles between $\mathbf{B}$ and $\mathbf{k}$ were 0°, 15°,30°, 45°,60°, 75°, and 90°. The wave velocity of the chosen eigenmode was determined after 10 full periods (the period is defined as the time for the wave to return to its original position in the simulation domain). The GPM algorithm gives an excellent agreement with theory for all three MHD waves over the entire range of propagation directions.

The elimination of magnetic divergence is key issue for any proposed Lagrangian particle scheme for MHD. Figure 4.5 compares the effect of evolving vector potential (according to (3.2) and (3.5)) with that of evolving magnetic field directly (using (3.14)) on the evolution of magnetic divergence in our GPM code. To estimate the magnitude of the unphysical magnetic divergence we use $|\nabla \cdot \mathbf{B}|$, and to estimate the magnitude of the physical magnetic effects we use $|\hat{\mathbf{z}} \cdot \nabla \times \mathbf{B}|$. To monitor magnetic divergence, we calculate the mean and maximum of both of these quantities over all particles at each timestep. Figure 4.5 plots the ratio of the means and the ratio of the maxima for the cases with and without vector potential for a fast MHD wave traveling at $\theta = 45°$ with respect to the mean magnetic field. The case without vector potential demonstrates growth of magnetic divergence with time; the case with vector potential inhibits the growth of magnetic divergence, maintaining the maximum magnetic divergence to less than 0.2% of the physical magnetic effects. As a side note, the growing variability of our

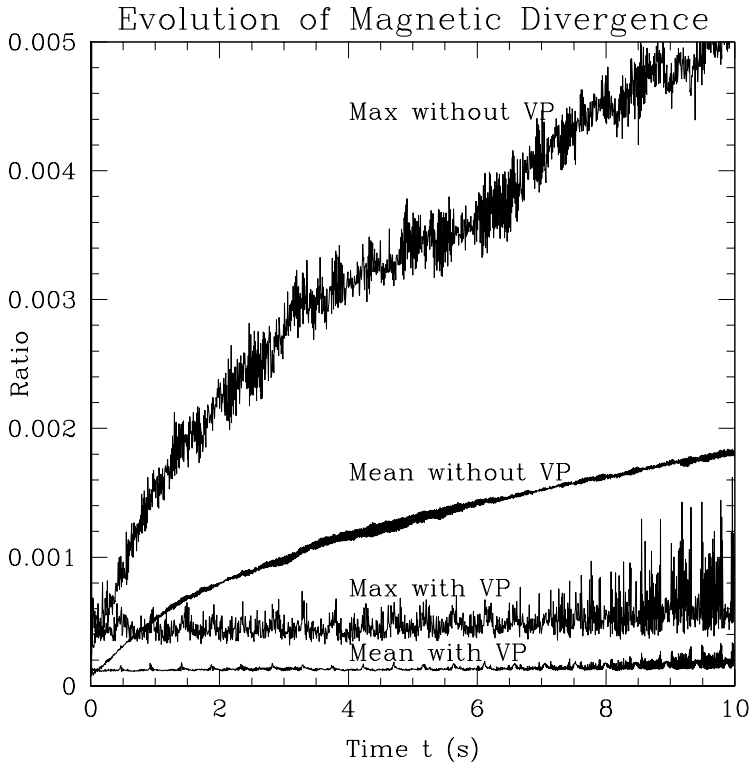

Figure 4.5: The time evolution of the magnetic divergence for a fast MHD wave propagating at an angle $\theta = 45°$ with respect to the magnetic field. This plot compares the approach using magnetic field directly with that using vector potential (VP). Two ratios for each case are plotted: mean($|\nabla \cdot \mathbf{B}|$)/mean($|\hat{\mathbf{z}} \cdot \nabla \times \mathbf{B}|$) and max($|\nabla \cdot \mathbf{B}|$)/ max($|\hat{\mathbf{z}} \cdot \nabla \times \mathbf{B}|$). The magnetic divergence for the case using vector potential remains at a negligible level throughout the simulation.

measure of magnetic divergence between $t = 8.0$ s and $t = 10.0$ s is caused by the growth of a leapfrog timestep splitting instability that can be easily controlled by the technique described in Section 3.5.3. In conclusion, Figure 4.5 demonstrates that the vector potential implementation of GPM maintains magnetic divergence at a negligible level.

4.3 Magnetized Vortex

To test the GPM evolution of magnetic field in an advective problem, we simulated a 2-D vortex flow superimposed with an initially uniform weak magnetic field. The flow is initialized with an azimuthal flow profile of the form

$$v_\phi = v_0 \frac{r}{r_0} e^{(1-r^2/r_0^2)} \tag{4.1}$$

with the values $v_0 = 0.1$ cm/s and $r_0 = 0.1667$ cm in a 2-D periodic box of size 1.0×1.0 cm. The initial weak magnetic field is $\mathbf{B_{ext}} = \mathbf{0.00354}$ G $\hat{\mathbf{x}}$. Second-order GPM is used with a fixed smoothing length $h = 0.123$ cm and artificial viscosity parameters $\alpha = 0.05$ and $\beta = 0.1$. The 32^2 particles are placed on a quasi-random grid and the Courant number is 0.0125 (calculated assuming all particles are separated by a distance $s = 0.03125$ cm). The sound speed is $c_s = 1.0$ cm/s. The radius at the peak of the azimuthal velocity will have undergone one full rotation in a time $t = 10.47$ s. Figure 4.6 shows the GPM results at time $t = 10.0$ s. For comparison, we simulated the same vortex with a spectral MHD code [124]; viscosity and resistivity values of $\nu = 3.0 \times 10^{-4}$ and $\eta = 3.0 \times 10^{-4}$ produced a result comparable to the GPM results. Figure 4.6 shows good agreement between the GPM and spectral codes for both evolved magnetic field

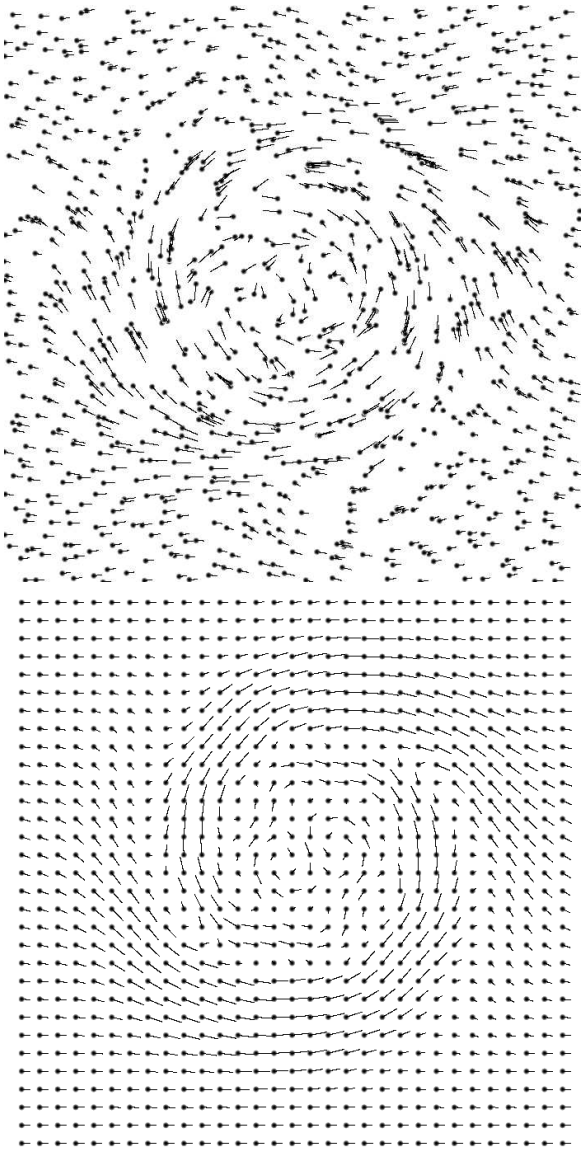

Figure 4.6: GPM (left) and spectral MHD (right) simulation results for the 2-D magnetized vortex. The spheres represent particle positions and the arrows represent magnetic fields. A spectral code does not have particles, and so the particles shown here serve only as markers for the magnetic field arrows.

topology and magnitude. For the GPM calculation, the magnetic field evolution is stable and magnetic structures are resolved to two interparticle radii. The effective viscosity of the GPM code is, in fact, almost as low as that of the spectral simulation.

4.4 Hydrodynamic Shocks

To test the ability of GPM to capture shocks, we used the standard 1-D shock tube test [173] . This test begins with an initial pressure and density discontinuity at an interface and no initial motion; a shock wave propagates to the right into the less dense medium and a rarefaction fan to the left into more dense medium, with a contact discontinuity visible in the density and energy profiles only. We choose the same initial conditions as the Sod [173] paper: $p = 1.0$ and $\rho = 1.0$ to the left of the discontinuity, $p = 0.1$ and $\rho = 0.125$ to the right, and zero velocity everywhere. For this problem, we employ the adiabatic index $\gamma = 1.4$ to retain consistency with the original paper. We run a first-order GPM calculation using 512×8 uniformly spaced particles in a periodic box of size 2.0×0.03125. The x range of the box is $[-0.5, 1.5]$ with the initial discontinuity at $x = 0.5$, but we show only the region $[0.0, 1.0]$. We specify a variable smoothing length with 21 neighbors, a timestep $\Delta t = 0.0009765625$, and an artificial viscosity with $\alpha = 0.5$ and $\beta = 1.0$ for shock capturing. The initial discontinuous profile was smoothed 4 consecutive times using a first-order GPM smoothing algorithm and a smoothing fraction of $f_{sm} = 1.0$. The resulting profiles for density, pressure, energy, and x-component of the velocity are shown in Figure 4.7 at time $t = 0.245$.

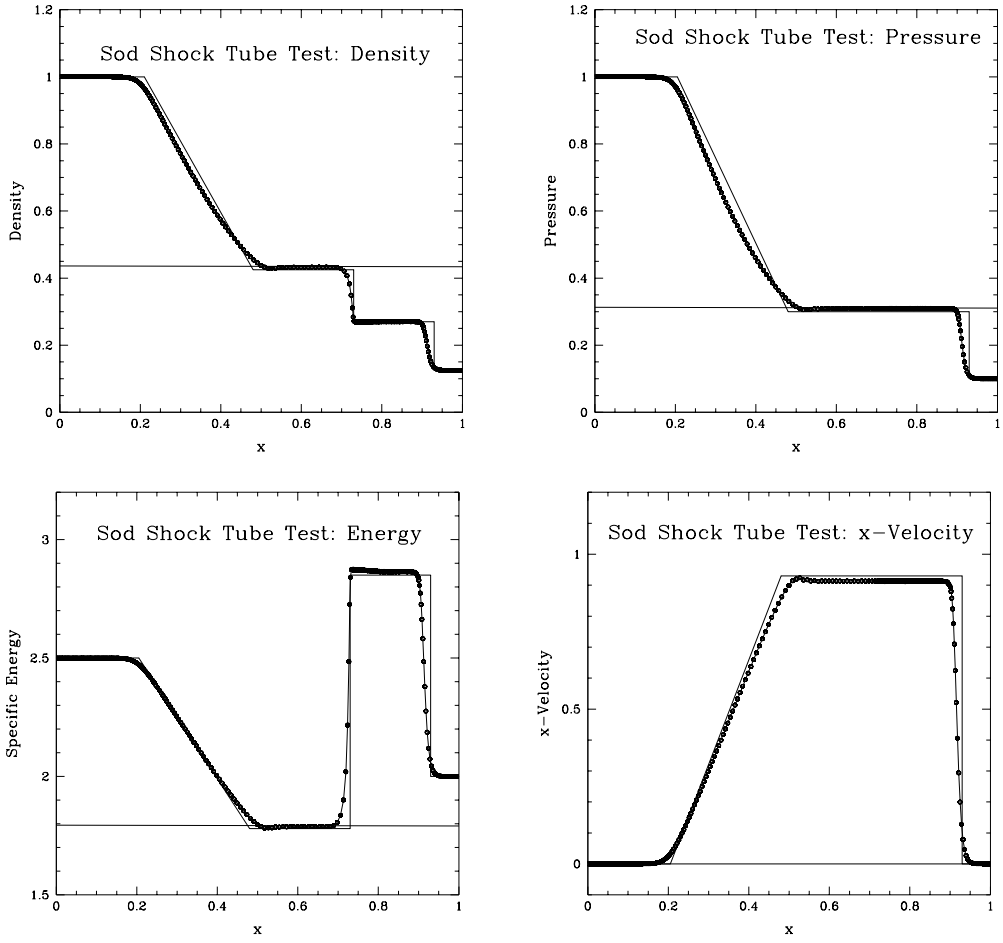

Figure 4.7: The profile results of the standard [173] 1-D shock test for density (upper left), pressure (upper right), energy (lower left), and x-component of velocity (lower right) for the time $t = 0.3$. Note the contact discontinuity visible only in the density and energy profiles. The approximate analytical solution is given by the solid line.

4.5 MHD Shocks

A suitable test of the performance of the GPM method for MHD shocks is the MHD Riemann problem first proposed by Brio and Wu [37]. Because the MHD equations are nonconvex, compound waves (waves consisting of a shock followed by a rarefaction wave of the same family), which do not occur in hydrodynamics, can indeed exist in MHD [37]. The coplanar Riemann problem presented here tests the ability of the scheme to represent shocks, rarefaction fans, and compound waves in MHD flows.

The initial state of the problem involves two discontinuous states at rest in contact at $x = 0$. To the left of the discontinuity, $\rho_l = 1.0$, $\mathbf{v_l} = \mathbf{0}$, $p_l = 1.0$, and $(B_y)_l = 1.0$; to the right, $\rho_r = 0.125$, $\mathbf{v_r} = \mathbf{0}$, $p_r = 0.1$, and $(B_y)_r = -1.0$. Everywhere, $B_x = 0.75$, $B_z = 0$, and the adiabatic index $\gamma = 2$. Please note that the units of $\mathbf{B}$ here are chosen to eliminate the factor of 4π in (3.1) to facilitate comparison with the results of Brio and Wu [37] since there is no known analytical solution to this problem. The simulation includes one spatial dimension and all components of velocity and magnetic field. The domain is given by $x = [-50, 50]$ with 800 particles initially uniformly spaced with separation $s = 0.125$. The chosen timestep is $\Delta t = 0.015625$ (equivalent to a Courant number of approximately 0.5). The second-order GPM algorithm is used with a variable smoothing length set to include 7 neighbors. In shock problems, artificial viscosity and smoothing are needed by GPM to prevent unphysical particle interpenetration and free streaming; the details of these procedures are discussed in sections 3.4.2 and 3.5.2. For this MHD Riemann problem, we use artificial viscosity parameters $\alpha = 3.0$ and

$\beta = 4.0$, we smooth the initial profile twice with a smoothing fraction $f_{sm} = 1.0$, and we apply a first-order smoothing every 16 timesteps with a smoothing fraction $f_{sm} = 0.5$.

Figure 4.8 shows the results at time $t = 10$. The solution consists of the following waves: a fast rarefaction wave (FR) and a slow compound wave (SC) moving to the left; and a contact discontinuity (CD), a slow shock (SS), and a fast rarefaction wave (FR) moving to the right. The foot of the left-moving rarefaction fan is rounded and the states between waves are not entirely constant, but the GPM method recovers the variety of waves in good agreement with results of Brio and Wu [37].

4.6 Kelvin-Helmholtz Instability

The stability of a stratified, heterogeneous fluid when different layers are in relative motion is examined analytically by Chandrasekhar [50]. In this 2-D problem in a square periodic domain defined by $-0.5 \leq x \leq 0.5$ and $-0.5 \leq y \leq 0.5$, the x-component of velocity and density are given by $v_{x1} = -0.5$ and $\rho_1 = 1$ for $|y| > 0.25$ and $v_{x2} = 0.5$ and $\rho_2 = 2$ for $|y| \leq 0.25$. The pressure is $p = 2.5$ and y-velocity is zero everywhere; the adiabatic index is $\gamma = 1.4$. To compare the instability growth rate with that predicted from theory, 256×256 particles are placed on a uniform grid initially to reduce noise and an initial sinusoidal perturbation of magnitude $\delta v_y = 0.001$ and wavenumber $k_x = 2\pi n_x / L_x$ with $n_x = 8$ is applied to the y-velocity.

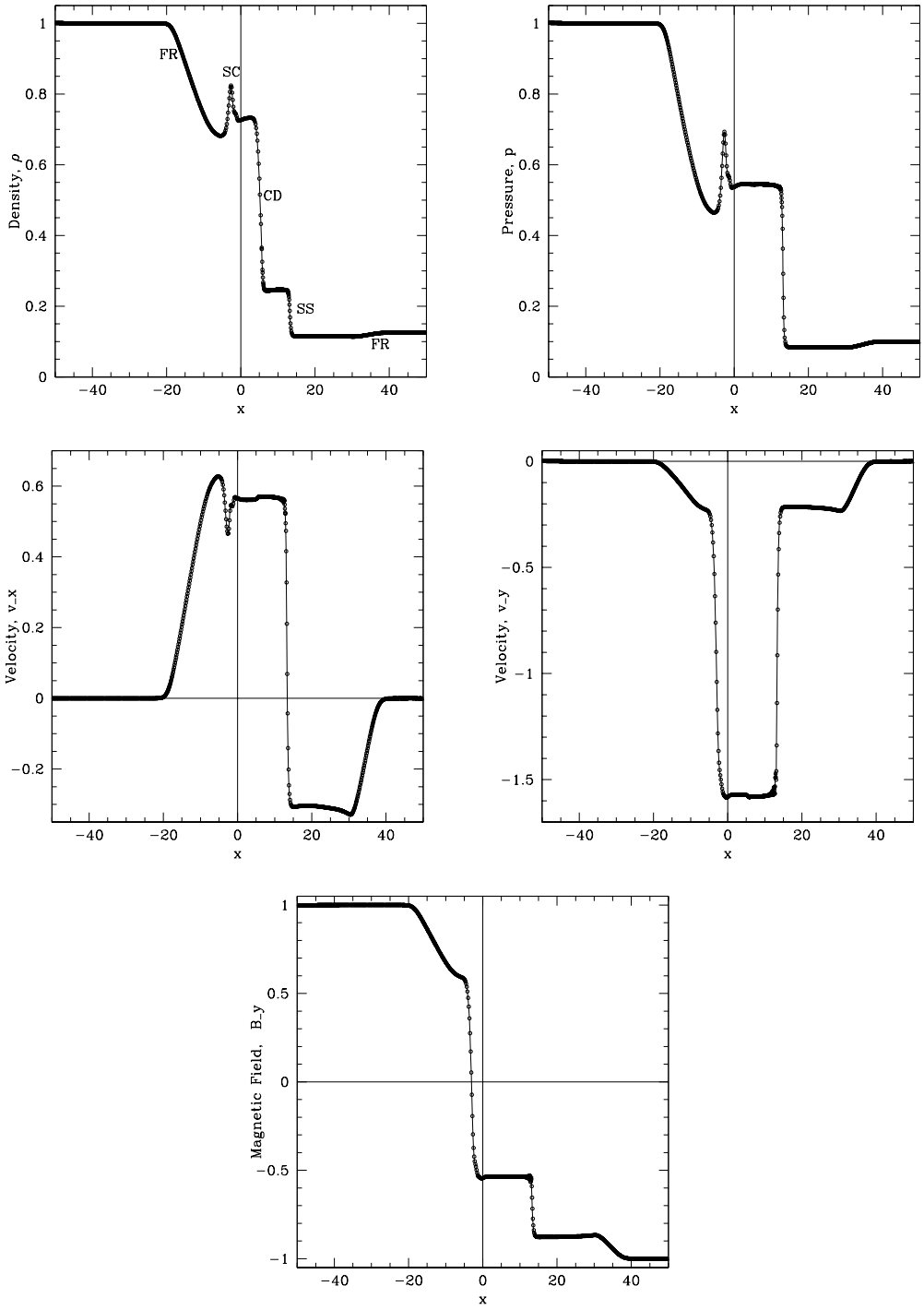

Figure 4.8: Results of the magnetic Riemann problem at $t = 10$. The (a) density, (b) pressure, (c) x-component of velocity v_x, (d) y-component of velocity v_y, and (f) y-component of magnetic field B_y are shown. On the density plot are labelled each wave (from left to right): fast rarefaction wave (FR), slow compound wave (SC), contact discontinuity (CD), slow shock (SS), and fast rarefaction wave (FR).

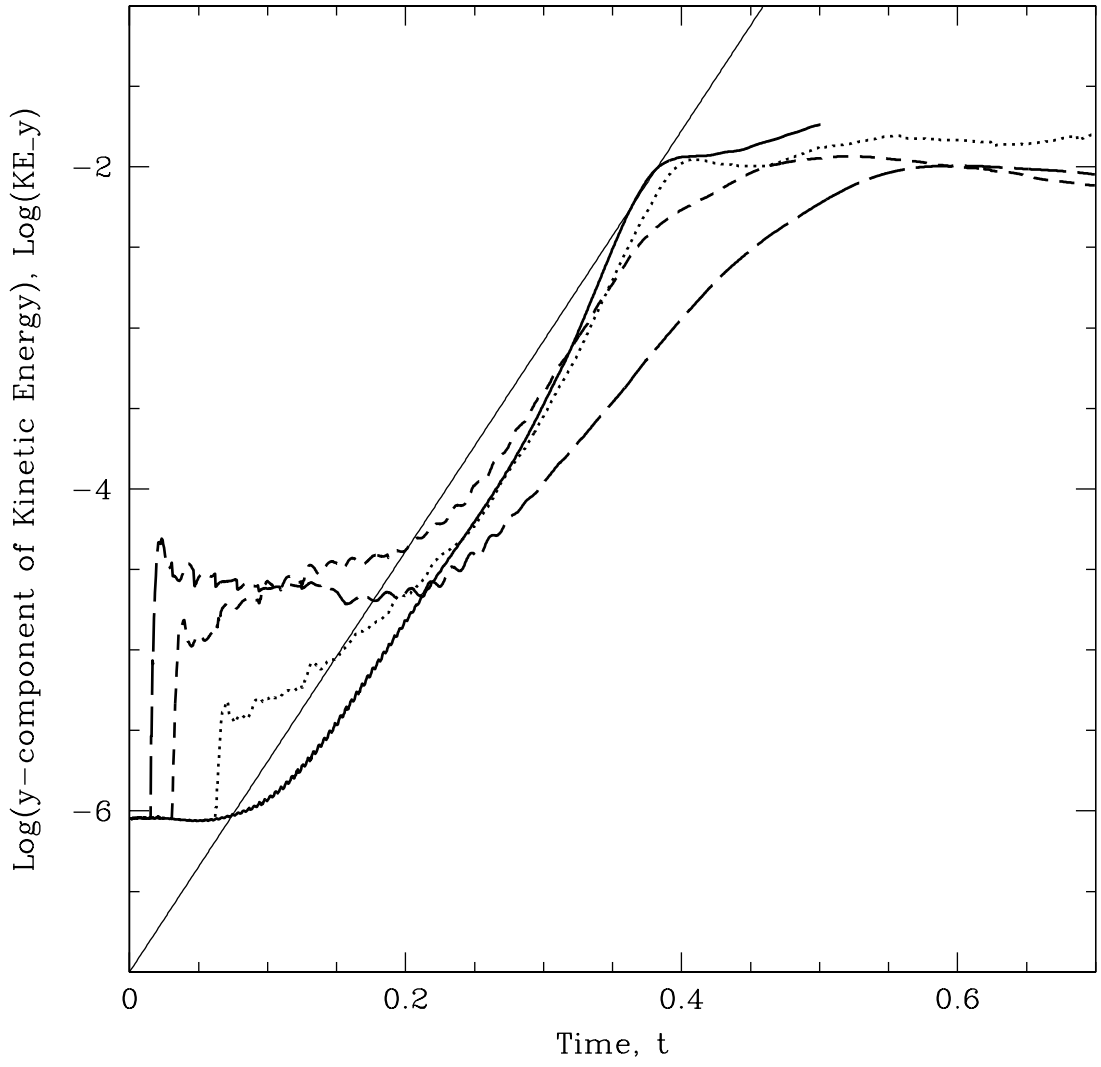

Figure 4.9: The growth of the kinetic energy in the y direction, $E_{ky} = \rho v_y^2$, vs. time. The analytical calculation for energy growth in an inviscid fluid is given by the thin solid line. Four runs are plotted with increasing levels of smoothing: no smoothing (thick solid line), smoothing every 128 steps with $f_{sm} = 0.125$ (dotted line), smoothing every 64 steps with $f_{sm} = 0.25$ (short-dashed line), and smoothing every 32 steps with $f_{sm} = 0.5$ (long-dashed line).

The growth rate of the instability in its linear phase [50] for an inviscid fluid is given by

$$\gamma = k_x |v_{x1} - v_{x2}| \sqrt{\rho_1 \rho_2 / (\rho_1 + \rho_2)^2}. \tag{4.2}$$

Figure 4.9 presents the energy due to motion in the y direction, $E_{ky} = \rho v_y^2$, with time. The analytical solution is given by the thin solid line. Four runs are plotted with increasing levels of smoothing: no smoothing (thick solid line), smoothing every 128 steps with $f_{sm} = 0.125$ (dotted line), smoothing every 64 steps with $f_{sm} = 0.25$ (short-dashed line), and smoothing every 32 steps with $f_{sm} = 0.5$ (long-dashed line). For all runs but the one with the most smoothing, the growth rate of E_{ky}—the slope of the line—matches that of the theory. The smoothing in the last simulation, however, is great enough for the effective viscosity to diminish the instability growth rate; the theoretical growth rate is determined for an inviscid fluid, so it is reasonable that a non-negligible viscosity would decrease the growth rate.

Chapter 5

Adaptive Particle Refinement

5.1 Introduction

The behavior of certain astrophysical problems, such as the long term evolution of the large-scale magnetic field in the Galactic disk, is likely to depend critically on the global geometry and boundary conditions. The Fourier decomposition of annular rings of the observed magnetic field in external galaxies is typically dominated by the $m = 0$ and $m = 1$ components [17]: the large-scale structure of the magnetic field is genuinely global. Only a global model of the system can possibly capture such structure. But limits in computational power inhibit the ability of numerical methods to resolve fine localized structure in global computations. In a barred galaxy, for instance, the dynamics in the shocked regions induced by the bar dominate the rate of mass accretion towards the galactic center [6]; resolving this localized phenomenon is essential to accurately following the magnetic field evolution in the galactic disk [48]. Adaptive numerical methods can overcome the limitations on local resolution imposed by the need to evolve the entire system in a global disk simulation.

The most well developed avenue for introducing adaptivity to a standard numerical method is the technique of Adaptive Mesh Refinement (AMR) [20, 19]. This technique is based on a simple principle. Consider a uniform mesh constructed across the computational domain at low resolution. At each step of the simulation, the truncation error at each grid point is estimated. If this error exceeds a chosen threshold at a grid point, the mesh is refined to smaller scale in the vicinity of that point. The higher resolution of the refined mesh can capture smaller scale structure. This refinement is allowed to compound up to a specified number of levels. Conversely, if the truncation error at a point is below the threshold for a more coarse grid, the mesh can be unrefined there. The achievement of the AMR technique is that computational effort is focused in regions where smaller scale structure in the solution leads to large truncation error.

A path less traveled to realize adaptivity is to adopt a Lagrangian numerical method. In a Lagrangian method, the grid points—often called particles if they represent entities with mass—move at the local velocity. In a fluid simulation, these points represent fluid elements flowing with the local fluid velocity. In regions of compression the local mass density increases; but since the computational points are embedded in the fluid, the local number density of points increases as well. The result is that resolution is enhanced in regions of increased mass density; the Lagrangian approach is inherently adaptive.

The implementation of a simple Lagrangian method is much less complicated than the implementation of a simple AMR method. The Lagrangian approach, however, adapts only to mass density in the problem; the AMR technique is more general in that it adapts based on error in any of the evolved fields. For problems

in which the regions of interest are coincident with regions of compression, the more simple Lagrangian approach is well suited. In studies of molecular cloud collapse, for instance, enhanced resolution is desired in the collapsing cores where the mass density increases. But for other problems, the density based adaptivity of Lagrangian methods does not suffice. In problems involving shocks or the tangling of a magnetic field, the regions where resolution enhancement is desired are not necessarily coincident with regions of increased mass density. In these cases, the more general adaptivity of AMR is superior.

This paper presents Adaptive Particle Refinement (APR), a truly adaptive Lagrangian scheme. Based on the same basic principle as AMR, the aim of this scheme is to wed the simplicity of the Lagrangian approach with the general adaptivity of the AMR method. APR adds or removes particles—in this case the "particles" carry no intrinsic mass, they are simply computational points at which we know information about the fluid—based an estimate of the truncation error at each particle. This eliminates the dependency of the adaptivity on mass density that plagues most Lagrangian techniques, yielding a generally adaptive method. Yet it retains the more simple computational bookkeeping characteristic of Lagrangian codes compared to that required by AMR schemes.

Section 5.2 describes the basic scheme underlying the adaptivity of APR. The additional problem of disconnection for Lagrangian particle methods is described in Section 5.3. Specific issues for the implementation of the APR scheme are discussed in Section 5.4. Control of magnetic divergence using Lagrange multipliers is given in Section 5.5. In Section 5.6, results from the adaptivity scheme proposed here are presented. Finally, a summary of our achievements to date and a

discussion of directions for further refinement of the APR method are contained in Section 5.7.

5.2 Basic Refinement Scheme

The Adaptive Particle Refinement scheme is constructed on the foundation of Gradient Particle Magnetohydrodynamics (GPM) [125], a general algorithm for Lagrangian fluid simulation. See Chapter 3 for a complete description of this algorithm. GPM employs local polynomial regression to find the local gradients of fluid quantities needed to calculate rates of change at each particle. The spatial fit of the gradients can be computed to arbitrary order, although the computational efficiency diminishes rapidly for greater than second order. The ability of GPM to recover fluid gradients to second order, not possible in all Lagrangian schemes, is the particular characteristic that makes possible the construction of an adaptive scheme.

The basis of AMR is truncation error estimation by Richardson extrapolation [20]. I will briefly review the details of the truncation error estimate here. Consider a grid with spacing Δx and a timestep algorithm with timestep Δt. Let $Q_{\Delta x,\Delta t}$ denote a two-level explicit difference operator of order p in both space and time. For a smooth solution $u(x,t)$, the local truncation error τ is found by

$$u(x,t+\Delta t) - Q_{\Delta x,\Delta t}u(x,t) = \tau + \Delta t\mathcal{O}((\Delta t)^{p+1},(\Delta x)^{p+1}) \tag{5.1}$$

where

$$\tau = \Delta t[(\Delta t)^p f(x,t) + (\Delta x)^p g(x,t)]. \tag{5.2}$$

Here the functions f and g depend on the details of the difference operator. Coarsening the mesh and timestep by a factor of two, we can find the analogous relation based on the same value of τ,

$$u(x, t + 2\Delta t) - Q_{2\Delta x, 2\Delta t} u(x, t) = 2^{p+1}\tau + \Delta t \mathcal{O}((\Delta t)^{p+1}, (\Delta x)^{p+1}). \tag{5.3}$$

The truncation error can be solved explicitly by comparing the result of two timesteps of Δt on the grid with spacing Δx with that of a single timestep of $2\Delta t$ on the coarser grid with spacing $2\Delta x$,

$$\tau = \frac{Q^2_{\Delta x, \Delta t} u(x, t) - Q_{2\Delta x, 2\Delta t} u(x, t)}{2^{p+1} - 2} + \Delta t \mathcal{O}((\Delta t)^{p+1}, (\Delta x)^{p+1}). \tag{5.4}$$

Hence, this error estimation by Richardson extrapolation provides the AMR mechanism with an absolute determination of the truncation error that conveniently combines both spatial and temporal errors.

For example, consider the evolution of the equation

$$\frac{\partial q}{\partial t} = \frac{\partial p}{\partial x} \tag{5.5}$$

and let the difference operator $Q_{\Delta x, \Delta t}$ be a second-order leapfrog timestep, centered space derivative so that

$$q_j^{n+1} = Q_{\Delta x, \Delta t}(q_j^n) = q_j^{n-1} + \frac{t^{n+1} - t^{n-1}}{x_{j+1} - x_{j-1}}(p_{j+1}^n - p_{j-1}^n). \tag{5.6}$$

For a mesh spacing of Δx and a timestep of Δt, the position and time are denoted by $x_j \equiv j\Delta x$ and $t^n \equiv n\Delta t$; abbreviated notation for p and q is $p_j^n \equiv p(j\Delta x, n\Delta t)$. Let $\tilde{p}(x, t)$ and $\tilde{q}(x, t)$ denote the exact solutions. Taylor expanding for p and q about (x_j, t^n) for this difference operator produces

$$q(x_j, t^{n+1}) - Q_{\Delta x, \Delta t}(q(x_j, t^n)) = \tau + \Delta t \mathcal{O}((\Delta t)^3, (\Delta x)^3) \tag{5.7}$$

where the truncation error τ takes the form

$$\tau = \Delta t \left[(\Delta t)^2 \left(\frac{1}{3} \left. \frac{\partial^3 \tilde{q}(x,t)}{\partial t^3} \right|_{t^n} \right) + (\Delta x)^2 \left(\frac{1}{3} \left. \frac{\partial^3 \tilde{p}(x,t)}{\partial x^3} \right|_{x_j} \right) \right]. \tag{5.8}$$

Subtracting the result from a single timestep of $2\Delta t$ on a grid with spacing $2\Delta x$ from the result of two timesteps of Δt on the grid with spacing Δx gives the truncation error

$$\tau = \frac{Q^2_{\Delta x, \Delta t}(q(x_j, t^n)) - Q_{2\Delta x, 2\Delta t}(q(x_j, t^n))}{2^3 - 2} + \Delta t \mathcal{O}((\Delta t)^3, (\Delta x)^3). \tag{5.9}$$

For this specific difference operator, the functions f and g from (5.2) are given by

$$f(x,t) = \left. \frac{1}{3} \frac{\partial^3 \tilde{q}(x,t)}{\partial t^3} \right|_{t^n} \tag{5.10}$$

and

$$g(x,t) = \left. \frac{1}{3} \frac{\partial^3 \tilde{p}(x,t)}{\partial x^3} \right|_{x_j}. \tag{5.11}$$

Specifying another difference operator would result in different forms for these functions.

Such a method of determining the truncation error is desirable for an adaptive Lagrangian scheme, so let us consider this possibility. The GPM analogue of this scheme involves taking two successive steps with smoothing length h and timestep Δt and comparing to a single step with smoothing length $2h$ and timestep $2\Delta t$. Consider initially a 2-D distribution of particles on a uniform grid as shown in Figure 5.1. For the two small steps, the smoothing sphere of radius h is indicated by the dashed circle; the five neighbor particles, including the test particle at which the gradient is being computed, are enclosed by circles. For the large single step,

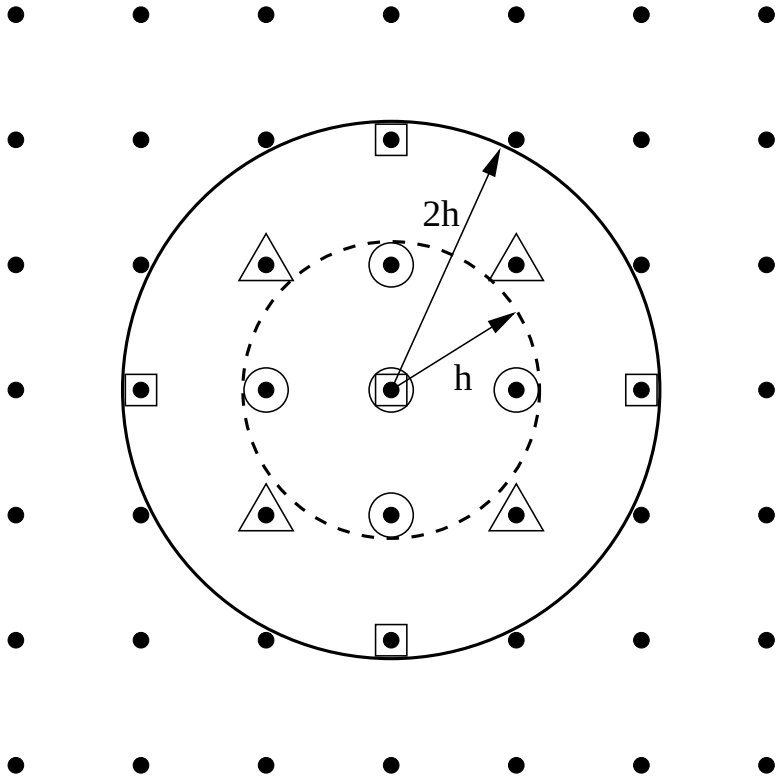

Figure 5.1: Particles distributed on a uniform grid to be used for truncation error estimation by Richardson extrapolation. The two small timesteps employ the smoothing sphere of radius h, given by the dashed circle, and the five neighbors enclosed by circles. The single large timestep must then use the smoothing sphere of radius $2h$, given by the solid circle, and only the five neighbors enclosed by squares.

the smoothing sphere of radius $2h$ is given by the solid circle. But, in order for the subtraction in (5.4) to yield the truncation error correctly, the functions f and g in the truncation error as determined by (5.1) must be identical to the functions f and g in the truncation error from (5.3). These functions depend on the precise explicit difference operator used. In particular, the stencil for the operator Q used in both equations must be identical (apart from the scaling). Hence, only the five neighbors enclosed by squares may be used for the calculation of the single large timestep. (Note that a standard GPM calculation with smoothing radius $2h$ would have used all 13 neighbors within the smoothing sphere, denoted in Figure 5.1 by all the particles enclosed by either circles, squares, or triangles). So, for this prescription for computing the truncation error to succeed, the large timestep must use the same number of neighbors as the small timesteps and must employ the same "stencil"—this amounts to requiring that the scaled particle distribution used for the large timestep to be identical to the particle distribution for the small steps. This is possible only for the special case of particles on a uniform grid. But for a random particle distribution, this prescription for truncation error estimation will fail. Even for a particle distribution initially on a grid, this computation will fail because the particles will move with the flow away from their uniformly distributed positions.

To construct an adaptive Lagrangian scheme, a new technique for error estimation must be devised. The chief difficulty with any idea related to Richardson extrapolation is that increasing the smoothing length—the GPM equivalent of coarsening the grid—necessarily involves a lot of variation due to the somewhat

random nature of the particle distribution in a Lagrangian code. Since GPM performs an order p least squares fit over all particles in the smoothing sphere, it is more natural to reduce the order of the fit than to increase the smoothing length. The AMR technique is based on repeating a calculation at the same order but with varying resolution. A particle code more naturally performs the complementary task: the basis of APR scheme error estimation is to repeat the calculation at the same spatial resolution but with differing order of convergence.

Consider the exact solution $u(x)$ and the local, pth-order GPM solution $u_{x_0}^{(p)}(x)$ centered at point x_0. The weighted error in the fit for a pth-order solution is given by

$$\chi_p^2 = \sum_{i=1}^{N} [u(x_i) - u_{x_0}^{(p)}(x_i)]^2 W(x_i, h) \tag{5.12}$$

where the sum is over all N neighbors in the smoothing sphere of radius h and W is the weighting function. Since $u_{x_0}^{(p)}(x)$ is the solution of the weighted least squares fit problem of local polynomial regression, it is certain that $\chi_{p+1}^2 \leq \chi_p^2$. The behavior of the adaptive scheme is controlled by the ratio of the error in the second-order GPM solution to that of the zeroth- and first-order solutions, χ_2/χ_0 and χ_2/χ_1.

The results of two successive tests, based on these two ratios, define which of the four possible actions the adaptive scheme takes: refine, smooth, unrefine, or nothing. A diagram demonstrating example situations in which each of these actions would occur is presented in Figure 5.2. The value of the fitted function at each particle is plotted as a point on this figure; linear fits to this set of particles are given by the dashed lines, quadratic fits by the solid lines. The first test com-

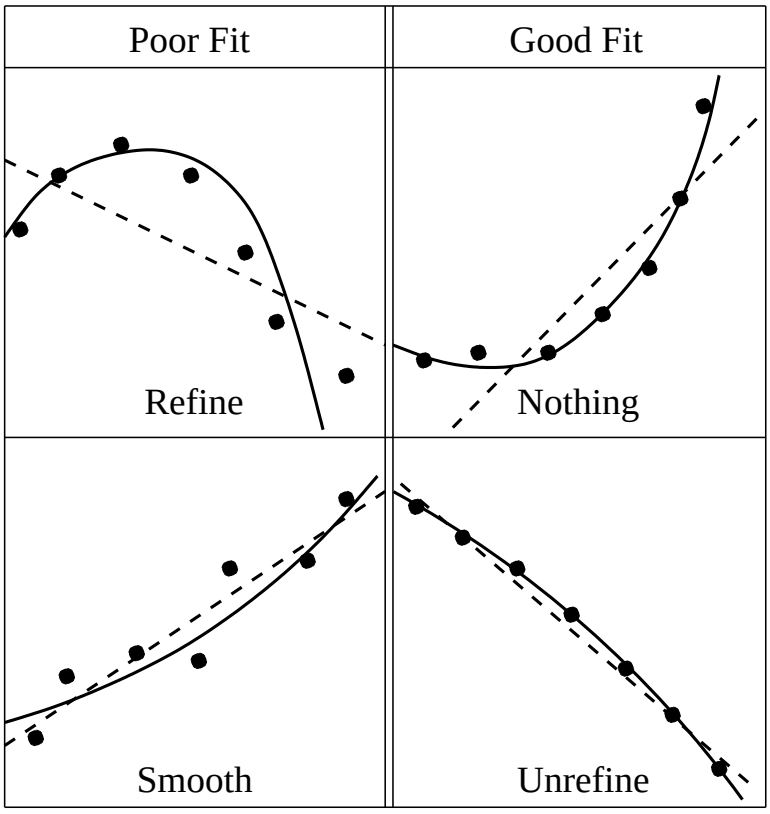

Figure 5.2: The Adaptive Particle Refinement scheme chooses from four potential actions based on the relative error in solutions of varying spatial order. An example calling for each of these actions is shown. The values of the fitted functions at each particle are given by the points, the first-order (linear) fit by dashed lines, and the second order (quadratic) fit by solid lines. Examples of poor fits are given in the left column: in the upper case the particle distribution is refined, in the lower it is smoothed. Good fits are shown in the right column: in the upper case nothing is done, in the lower the particle distribution is unrefined.

pares the quality of the second-order fit, χ_2/χ_0, to a threshold for the maximum acceptable error, $f_{\chi_{max}}$. If $\chi_2/\chi_0 > f_{\chi_{max}}$, the fit is poor; the scheme will either refine, do nothing, or smooth at that point. If $\chi_2/\chi_0 < f_{\chi_{max}}$, the fit is good; the scheme will either do nothing or unrefine.

If the first test determines that the fit is poor, the second test examines the difference in the fit between a first- and second-order method. The left column in Figure 5.2, labeled "poor fit", demonstrates two extreme situations that result in different actions taken by the adaptive scheme. If the second-order solution gives a substantial improvement in error over the first-order solution, the value of χ_2/χ_1 is small. In the upper left box of Figure 5.2, the linear fit (dashed line) is significantly worse than the quadratic fit (solid line). In this case, the adaptive scheme chooses to refine so that increased resolution yields a lower truncation error. A threshold for refinement, f_r, is specified so that the scheme refines for $\chi_2/\chi_1 < f_r$. On the other extreme, the lower left box of Figure 5.2 displays a second-order fit (solid line) that yields no marked improvement over the first-order fit (dashed line). In this case, the value of χ_2/χ_1 approaches the value 1. This typically signifies that there exists some noise in the data causing a poor fit but that there is no meaningful variation in scatter of particle values; smoothing of the values at the current particle retains the local fluid information but diminishes the noise. A threshold for smoothing, $f_{sm} \geq f_r$, is defined such that the scheme smoothes when $\chi_2/\chi_1 > f_{sm}$. If $f_{sm} > f_r$, then there exists a window $f_r < \chi_2/\chi_1 < f_{sm}$ within which the scheme does nothing.

If the first test determines that the fit is good, the second test chooses whether to do nothing or to unrefine. The right column in Figure 5.2, labeled "good fit",

First Test	$\chi_2/\chi_0 > f_{\chi_{max}}$ $\Rightarrow$ Poor Fit	$\chi_2/\chi_0 < f_{\chi_{max}}$ $\Rightarrow$ Good Fit
Second Test	$\chi_2/\chi_1 < f_r$ $\Rightarrow$ Refine	$\chi_2/\chi_1 < f_u$ $\Rightarrow$ Nothing
	$f_r < \chi_2/\chi_1 < f_{sm}$ $\Rightarrow$ Nothing	$\chi_2/\chi_1 > f_u$ $\Rightarrow$ Unrefine
	$\chi_2/\chi_1 > f_{sm}$ $\Rightarrow$ Smooth	

Table 5.1: Summary of the Adaptive Particle Refinement scheme based on the relative error in solutions of varying spatial order. The first test evaluates the quality of second-order solution by comparing it to the zeroth-order solution. The second test judges the improvement of the fit when increasing from first to second order.

provides an example for each of these cases. In the upper right corner of the figure, the quadratic fit (solid line) yields a much better approximation to the particle values than the linear fit (dashed line). In this case, χ_2/χ_1 is small. But if the second-order fit does not significantly improve over the first-order fit, as displayed in the lower right corner of Figure 5.2, the value of χ_2/χ_1 nears 1. In this case, little is gained by the extra computational work required to calculate the second-order solution; therefore, the adaptive scheme may unrefine in this region. The unrefinement threshold, f_u, is chosen so that, if $\chi_2/\chi_1 > f_u$, the adaptive scheme unrefines; otherwise, nothing is done.

The adaptive scheme for APR, based on estimates of the error in the spatial fit, is summarized in Table 5.1. The behavior of the adaptive scheme is controlled by setting the four threshold values, $f_{\chi_{max}}$, f_r, f_{sm}, and f_u; each of these parameters

takes a value between 0 and 1. This error estimation scheme determines when to refine or unrefine the spatial resolution; the separate question of how to refine or unrefine the resolution is addressed in Section 5.4. A simple answer is that particles are added when refining and particles are removed when unrefining. The scheme effectively adds particles locally whenever the fit is poor and a higher order fit leads to a reduction in the error; conversely, it removes particles if the fit is good and the error in the solution is not substantially worsened by dropping from second to first order. Generally, this minimizes the number of particles needed for a second-order fit to meet the established error threshold.

The scheme must also elegantly handle the occasion that the $\chi_0 = 0$ or $\chi_1 = 0$. To achieve this simply, a minimum error threshold, χ_{floor}, is chosen below which the adaptive scheme takes no action. The case that $\chi_0 < \chi_{floor}$ or $\chi_1 < \chi_{floor}$ will occur only when the value of the function is constant or varies perfectly linearly over the smoothing sphere, or when the fluctuations away from constant or linear behavior are very small. Adjustment of χ_{floor} allows adjustment of the minimum sensitivity of the adaptive scheme. For a highly nonlinear problem, it is often desirable to prevent the adaptive scheme from adjusting to linear variations, so χ_{floor} can be set above the magnitude of linear fluctuations. Note that since this value is not normalized, the absolute magnitude must be set independently for each field that is fit by the GPM algorithm.

Note that although the error estimation by Richardson extrapolation used by AMR neatly folds in the timestep errors with the spatial errors, the APR error estimates are strictly spatial. Hence, the timestep must be controlled by

a separate constraint. A suitable choice for timestep constraint is a Lagrangian Courant-Friedrichs-Lewys (CFL) constraint.

$$\frac{|v_{rel}|\Delta t}{\Delta x} \leq 1, \tag{5.13}$$

where the v_{rel} is the maximum of the local wave speed or the relative particle velocity and the particle spacing Δx is related to the smoothing length h, for example $\Delta x = h\sqrt{\pi/N}$ in the 2-D case. The error in the timestepping algorithm is not computed, but tests of the adaptivity have not demonstrated any problems arising from error in the timestep as long as CFL condition is met.

5.3 An Additional Problem: Disconnection

There are, in fact, two separate kinds of errors facing Lagrangian numerical methods: errors arising from the truncation error, and errors arising from the irregular distribution of particles. The first type of error, which in fact is also affected by the distribution of particles, can be handled by adaptive schemes as discussed in Section 5.2. But this adaptivity cannot eliminate all problems that ill-distributed particles can inflict.

The error arising from the particle distribution occurs because certain irregular particle distributions can lead to inadequate sampling of the local environment. Grid-based codes operate using a fixed stencil of grid points, thus ensuring that the local environment is well sampled. But in the Lagrangian approach, the local environment is sampled by finding all of the neighbors of a given particle within a specified smoothing radius. But since the Lagrangian particles move about the simulation domain, it is possible that all of the neighbors will be on one side of

the current particle. Under these conditions, there is no information available within the smoothing sphere about the fluid environment in the region lacking particles. This can lead to an error entirely independent of the error in the fit of the function at all of the particles in the smoothing sphere, a problem unique to the nature of Lagrangian methods. And, worse, in certain circumstances, the error can positively feedback on itself leading to a computational instability. I refer to this particle distribution and environment sampling error as the disconnection error and to the resulting computational instability as the disconnection instability.

Although all Lagrangian methods suffer this disconnection error, not all approaches are susceptible to the computational instability that can arise from it. GPM suffers from both the error and the instability, but Smoothed Particle Hydrodynamics (SPH) [74, 122], a widely used Lagrangian method for hydrodynamic simulation, admits the disconnection error but is immune to the instability. A few simple one-dimensional examples illuminate this issue and demonstrate the potential for a virulent disconnection instability in the GPM method.

Figure 5.3 illustrates the problem of the disconnection error and how it can lead to a computational instability under certain conditions in the GPM method. The figure shows plots of the pressure p vs. the coordinate x, where the solid line indicates the underlying pressure profile. Values of pressure at each particle are indicated by the solid and open circles; the open circle is the test particle at which the calculation of the pressure gradient is to be computed. In this case, the number of neighbors, including the test particle, is specified at $N = 3$; the limits of the smoothing sphere of radius h, adjusted to include only $N = 3$ neighbors, are denoted by the dashed lines. The problem of disconnection, or inadequate

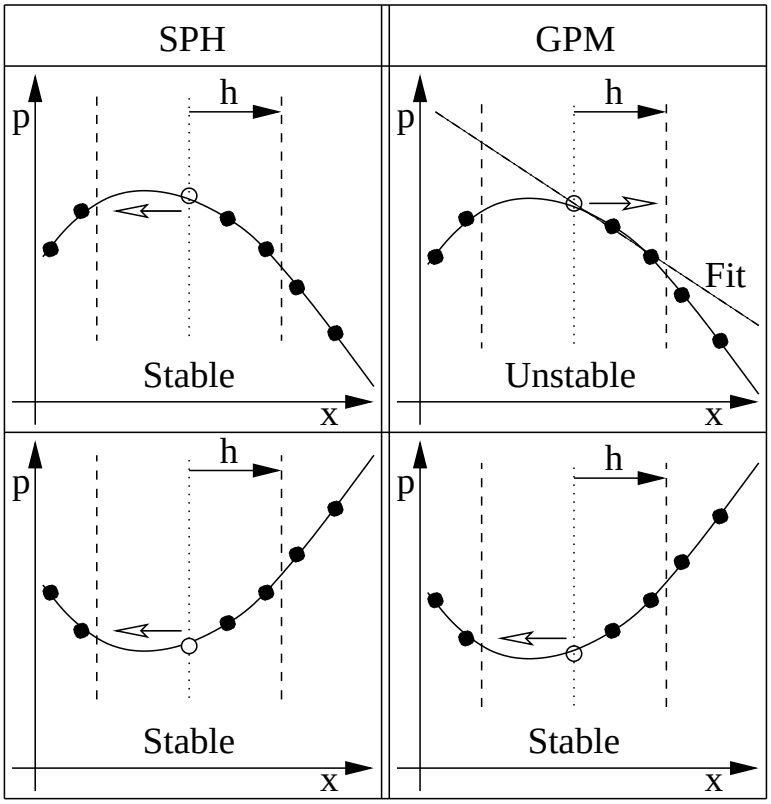

Figure 5.3: Illustration of disconnection in Lagrangian methods. In this 1-D example, the values of pressure vs. position for each particle are indicated by the open and solid circles; the underlying pressure profile is shown as a solid line. The limits of the smoothing sphere of radius h, set to include $N = 3$ neighbors (including the test particle denoted by the open circle), are denoted by the dashed lines. In the SPH cases of the left column, the pressure force is always to the left, closing the disconnection; the leftward directed pressure force in the upper left plot, however, is unphysical. In both of the GPM cases, the computed pressure force agrees in direction with that of the underlying pressure profile. The dynamic motion of the test particle in the upper right case, though, further opens the disconnection, leading to a computational instability.

sampling of the local environment is apparent: all of the neighbors lie on the right side of the test particle, so there is no information about the fluid environment to the left of the test particle. Note that although neighbor number of $N = 3$ is too small to be suitable for actual computational work, it is chosen to simplify this illustration of disconnection.

The upper right corner of Figure 5.3 includes a linear fit (dot-dashed line) to the particles within the smoothing sphere. The error in this linear fit, as would be measured by χ_1 as outlined in Section 5.2, is very small; the resulting gradient, however, does not match the gradient of the underlying pressure profile (solid line) at the test particle. This is the disconnection error. This error is independent of the quality of the fit to the particles within the smoothing sphere; the error exists because the local environment is not adequately sampled.

The disconnection error, however, does not necessarily lead to a computational instability. To understand how the instability can occur, we must investigate the effect of the disconnection error on the dynamics of the system and how those dynamics can worsen or alleviate the disconnection. In a hydrodynamic fluid, a gradient in pressure causes an acceleration down the pressure gradient. In a Lagrangian particle sense, particles will move down the pressure gradient. Let us consider the forces derived by the SPH and GPM methods in this situation where disconnection occurs.

The pressure force in SPH is calculated as a particle-on-particle force; this ensures conservation of momentum in the scheme. The lefthand column of Figure 5.3 shows the behavior of the SPH method when disconnection occurs. Because the

pressure force is approximated by a particle-on-particle force, the pressure force (open arrow) on the test particle will necessarily be to the left. In the lower left plot of the figure, this is in fact the correct behavior; in the upper left plot, however, the force from the true pressure gradient is in the opposite direction, so the leftward directed pressure force is unphysical and represents the manifestation of the disconnection error in SPH. The dynamic effect on the particle distribution is, in either case, to close the disconnection and eventually reestablish contact with the fluid environment to the left of the test particle.

In GPM, the pressure force is calculated from the local gradient of the pressure as determined by a local least squares fit of the values of pressure at the particles within the smoothing sphere. For simplicity in this example, we consider a first-order GPM method and examine the linear fit to the values of pressure at the particles within the smoothing sphere. The righthand column in Figure 5.3 illustrates the behavior of the GPM algorithm in the case of disconnection. The upper right plot shows the linear fit (dot-dashed line) to the particles within the smoothing sphere. The gradient of the pressure is overestimated by this linear fit compared to the true gradient at the test particle of the underlying pressure profile (solid line); this is the manifestation of the disconnection error in GPM. Note that, using the GPM algorithm, the pressure force (open arrow) is in the same direction as the true underlying pressure gradient. The lower right plot shows a pressure force to the left, again agreeing with the direction of the underlying pressure gradient. But the dynamic effect on the particle distribution is different between these two cases: in the lower right plot, the test particle is forced in the direction to close the disconnection and regain contact with the fluid environment

to the left; but, in the upper right plot, the test particle is moved further away from the particles to the left, worsening the disconnection. This positive feedback on the disconnection, in this case, leads to a virulent computational instability.

The best course to handle the error associated with disconnection and to avoid the pernicious disconnection instability is to prevent disconnection from occurring in the first place. Verifying connection to a neighbor in each direction along the coordinate axes is necessary. To achieve this in one dimension is trivial; here I outline a strategy that operates at arbitrary dimensionality. For illustrative purposes, I expound upon the example in two dimensions and touch upon the modifications necessary for a three-dimensional simulation. To discuss the strategy to prevent disconnection, I must define the concept of mutual neighbors: mutual neighbors are two particles for which each is a neighbor of the other. In other words, two particles are mutual neighbors if they lie within each other's smoothing spheres. Consider a 2-D case with a neighbor number $N = 5$, illustrated in Figure 5.4 where the particles are plotted as filled circles (ignore the squares for the moment). Particle 2 is a neighbor of particle 1, but particle 1 is not a neighbor of particle 2; thus, they are not mutual neighbors.

The strategy to prevent disconnection operates by ensuring that there is a mutual neighbor in both directions along each coordinate axis. When the rates of change are to be calculated for particle 2 in Figure 5.4, for example, a Lagrangian method must first determine the $N = 5$ neighbors within the smoothing sphere (counting particle 2 itself as a neighbor). To ensure that there is a mutual neighbor along both directions of each coordinate axis, the smoothing sphere is split into four quadrants along $y = x$ and $y = -x$ in two dimensions. (In three dimensions,

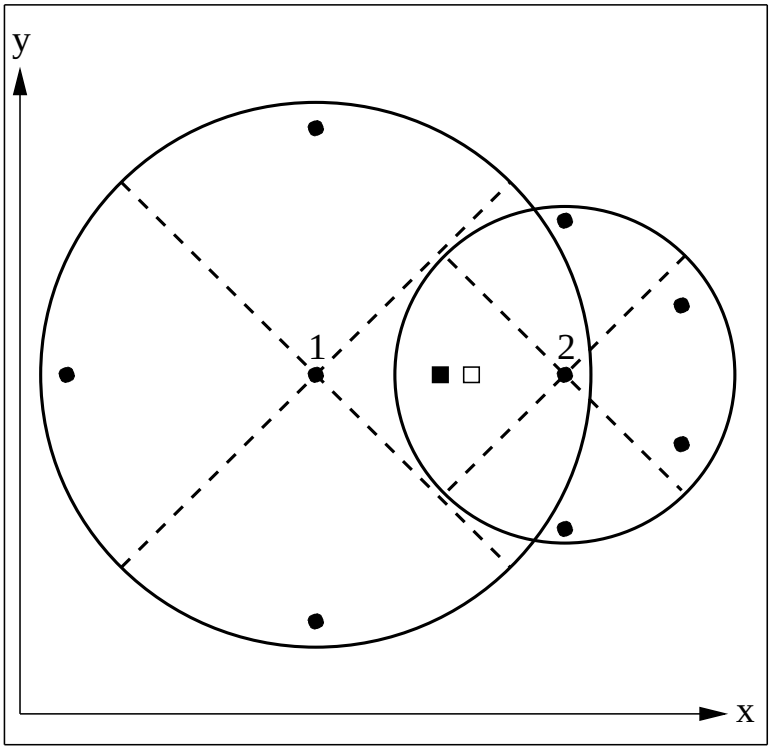

Figure 5.4: Sketch of the problem of disconnection in Lagrangian methods. The smoothing sphere around particle 2 contains no particles (filled circles) in the left-hand quadrant; it is disconnected from the fluid to its left, having no information about the fluid environment in the $-x$ direction. Disconnection may be corrected by a) adding a particle at the center of the empty quadrant (open square) in the smoothing sphere of particle 2, or b) adding a particle midway between particles 1 and 2 (filled square) because particle 2 is the nearest neighbor in the righthand quadrant of particle 1 but is not a mutual neighbor of particle 1.

the sphere is split into 6 "pyramidal" sections along the planes $y = x$, $y = -x$, $z = x$, $z = -x$, $z = y$, and $z = -y$.) These quadrants are marked in Figure 5.4 by the diagonal dashed lines in the smoothing sphere of particle 2. These quadrants are used as the basis for two tests to check for any possible disconnection and correct the problem if a disconnection is detected.

First one must check to see if there exists a disconnection in the neighbor distribution, manifested by an empty quadrant of the smoothing sphere. In the case of the smoothing sphere of particle 2 in the figure, the lefthand quadrant is devoid of neighbors. To reestablish connection to the fluid in that direction (the $-x$ direction), a particle can be added in the center of that quadrant at the position of the open square. The interpolation of the fluid values centered at the added particle position will certainly include a contribution from particle 1 in the figure; the new particle reconnects particle 2 to the fluid environment in the $-x$ direction.

Although in this example the disconnection is eliminated by filling empty quadrants, this measure alone may not be sufficient to patch a disconnection. If particle 1 in Figure 5.4 was much further to the left, it would not necessarily be included in the smoothing sphere centered on the open square for the interpolation of the new particle values. Particle 2 has no information about the fluid in the $-x$ direction, so it cannot ensure that the problem is corrected. To guarantee that the disconnection is patched, the new particle must placed by particle 1, a particle is not yet suffering disconnection.

The second test to correct the disconnection is to verify that the closest neigh-

bor in each quadrant is a mutual neighbor. In Figure 5.4, particle 1 is not suffering disconnection because no quadrant within its smoothing sphere is devoid of neighbors. But second test will determine that particle 2, its nearest neighbor in the righthand quadrant, is not mutual neighbor. Thus, although particle 1 suffers no disconnection, it can detect if one of its neighbors is disconnected from it. To strengthen the connection between particle 2 and itself, particle 1 adds a particle at a position midway between them, located at the position of the filled square. This measure ensures that the nearest neighbor in each quadrant is a mutual neighbor, solidifying the connection between the fluid environment at particle 1 and that at particle 2.

In summary, the problem of disconnection in the particle distribution is alleviated by a double measure taken when each particle determines the neighbors within its smoothing sphere:

1. If a quadrant contains no neighbor, add a particle in the center of that quadrant.

2. If the closest neighbor in each quadrant is not a mutual neighbor, add a particle midway between.

This disconnection instability is somewhat rare in non-adaptive GPM but does occur occasionally, rendering the GPM method without disconnection protection somewhat fragile. But if the APR scheme for adaptivity is employed, the susceptibility to the disconnection instability is heightened dramatically. The addition of particles under the adaptive scheme leads to a highly non-uniform particle

distribution; this is, of course, the goal of an adaptive algorithm. But such a non-uniform particle distribution greatly increases the probability that a given particle's neighbors will all lie on one side of the particle, leaving an empty quadrant of the smoothing sphere and giving rise to a malignant disconnection.

5.4 Specific APR Implementation Details

Two questions must be answered by any adaptivity scheme: when does the scheme refine or unrefine, and how does the scheme refine or unrefine? The first question is answered by the error estimation scheme described in Section 5.2. But how the adaptivity strategy increases or decreases the local spatial resolution is equally important.

Lagrangian particle methods boast the characteristic advantage that the data structure containing the values describing the fluid at each particle can simply be a list of particles. Some spatial organization of this list is necessary to find the neighbors of a given particle efficiently, but this issue can be dealt with independently of the structure containing the particle data. Therefore, increasing or decreasing the spatial resolution anywhere is as simple as adding or removing particles from the list. The APR scheme developed here simply adds or removes a single particle each time refinement or unrefinement is called for by the error estimation scheme.

At each particle where the error estimation scheme demands refinement, a single particle is added within the smoothing sphere. The position within the sphere is chosen by a weighted, exclusive random procedure. First, a random position is

chosen within the sphere, weighted in the radial direction by the same smoothing function used in the GPM algorithm. Second, the distance from this position to each particle already in the smoothing sphere is calculated; any position within a specified fraction of the smoothing length from another particle is discarded and a new weighted random position is chosen. This process continues until an acceptable position for the new particle is found. This weighted, exclusive random procedure is constructed to place new particles preferentially in voids that exist in the particle distribution within the smoothing sphere. The values of the local fluid environment are then interpolated by a local least squares fit, using the same GPM algorithm, centered at the new position; the mean values derived by an order-p GPM algorithm centered at the new position have an order of convergence $p + 1$.

Unrefinement by the removal of a single particle is even more simple. The particle whose error commands unrefinement is combined with its nearest neighbor. The average position is chosen and the fluid values at the combined particle are summed from the constituent particles in a conservative way.

Additionally, any adaptive scheme must have some means of limiting the level of refinement or unrefinement. This is accomplished simply in the APR framework by specifying a minimum and maximum smoothing length, h_{min} and h_{max}. When the error estimation scheme described in Section 5.2 determines the need for refinement at a given particle, the addition of new particle is prevented if the smoothing length at the current particle $h \leq h_{min}$. In a complementary sense, if unrefinement is desired by the error estimation scheme, a particle is not removed if its smoothing length $h \geq h_{max}$. The minimum and maximum spatial resolution

of the APR scheme is specified easily by setting these smoothing length limits h_{min} and h_{max}.

The adaptive scheme can add, smooth, or remove a particle at each existing particle as it loops through the list of particles to calculate the rates of change. Newly added particles are added to the end of the list and can themselves call for particle addition, smoothing, or removal. Thus, much refinement can occur in one timestep during a single pass over all the particles. To prevent an exponential runaway in this refinement, the adaptive algorithm can be limited so that the variation of particle smoothing lengths over the current particle's smoothing sphere does not exceed a limiting value, h_∇. The implementation of this adaptivity control finds the minimum and maximum values of the smoothing length, h_{min} and h_{max}, of all the neighbors in the smoothing sphere—note that these values are local minimum and maximum values of smoothing length within the smoothing sphere, not to be confused with the global smoothing length limits described in the previous paragraph. If the ratio $h_{max}/h_{min} > h_\nabla$, then refinement and unrefinement are inhibited. Exceptions occur in two cases: if the current particle $h = h_{min}$, then unrefinement is allowed, and if the current particle $h = h_{max}$, then refinement is allowed. These exceptions prevent the formation of local minima and maxima in the particle distribution, yielding a clumpy particle distribution, unless the error estimation demands it. The h_∇ control stabilizes the adaptivity scheme, preventing any runaway refinement.

Although the measures described here to stabilize the adaptive scheme do produce a stable method, they represent only the first attempts at developing

such a scheme. Further development and testing of the adaptivity scheme may lead to improved performance.

5.5 Magnetic Divergence Control

In the evolution of the magnetic field $\mathbf{B}$ for magnetohydrodynamic (MHD) simulation using GPM, the maintenance of zero magnetic divergence, $\nabla \cdot \mathbf{B} = \mathbf{0}$, is a key issue. If the magnetic field is evolved computationally according to magnetic induction equation (here in Lagrangian form where $d/dt = \partial/\partial t + \mathbf{v} \cdot \nabla$)

$$\frac{d\mathbf{B}}{dt} = \mathbf{B} \cdot \nabla \mathbf{v} - \mathbf{B} \nabla \cdot \mathbf{v}, \tag{5.14}$$

then the magnetic field may develop a non-zero magnetic divergence due to the finite truncation error inherent in any numerical method. Special care must be taken to prevent any non-zero magnetic divergence from corrupting the calculation.

In a simple application of the GPM algorithm for MHD simulation, each component of the magnetic field is fit independently. Therefore, although the underlying magnetic field may indeed be divergence free, the discrete nature of the computation of gradients of the magnetic field components does not guarantee that

$$\frac{dB_x}{dx} + \frac{dB_y}{dy} + \frac{dB_z}{dz} = 0. \tag{5.15}$$

To observe this constraint, the components of the magnetic field must be fit consistently.

In first-order GPM in three dimensions, the solution of a single component of the field requires the inversion of a 4×4 matrix. To solve for all three components simultaneously would require the inversion of an 9×9 matrix (the mean is then calculated only once and the constraint is used to eliminate one of the gradients in the divergence). Although more expensive computationally, this technique would not be prohibitive for a first-order calculation. But to solve a single component in a second-order calculation, a 10×10 matrix must be inverted. The simultaneous solution of all three components to second order including the four divergence constraints requires the inversion of a 24×24 matrix; the computational cost of this inversion is indeed prohibitive.

A far more elegant solution is to fit for the magnetic field by introducing the divergence constraint into the weighted least squares minimization problem as a Lagrange multiplier. By this method, each component is solved independently as before, but a subsequent step calculates the value of the Lagrange multiplier to correct the initial solutions so that they obey the added constraint.

The first-order GPM algorithm with magnetic divergence control follows these steps. First, the neighbors in the smoothing sphere are identified and the matrix corresponding to the spatial distribution of particles is constructed (this is the matrix $\mathbf{S}$ of (9) in [125] or (3.9) here). The vectors for each field ($\mathbf{Q}$ in the same equation) are computed at the same time. Next, inversion of the matrix and operation on the vectors yields the solution—containing the mean and gradient values—for each field component being fit. For the magnetic field, these solutions represent the best fit to the particle distribution for each component independently; we desire, though, the best fit for each component subject to the

constraint that the magnetic divergence is zero. Thus, in the next step, these unconstrained solutions are used to determine the value of the Lagrange multiplier used to introduce the divergence constraint. Finally, the computed multiplier is then used to correct the unconstrained solutions so that the magnetic divergence criterion is met. The mathematical details of this procedure are presented in Appendix D.

For the second-order GPM algorithm with magnetic divergence control, there are four constraints on the solutions that must be satisfied,

$$\nabla \cdot \mathbf{B} = \mathbf{0}, \quad \frac{d\nabla \cdot \mathbf{B}}{dx} = 0, \quad \frac{d\nabla \cdot \mathbf{B}}{dy} = 0, \quad \frac{d\nabla \cdot \mathbf{B}}{dz} = 0. \tag{5.16}$$

Each of these constraints must be added to the weighted least squares minimization problem with its own Lagrange multiplier. After the solution of each component independently, a subsequent matrix equation must be solved for the four Lagrange multipliers. In the final step, these values can be used to correct the unconstrained component fits so that solution for the magnetic field is divergence free. Appendix D once again provides the details of this calculation.

One important point about this method is that it provides the solution of the magnetic field with zero divergence that most closely fits the values of magnetic field at all neighbor particles. It does not, however, affect the values of the magnetic field on those particles. If the data on the particles were derived from an unphysical magnetic field with non-zero divergence, this technique would find the divergence free solution that most closely fits the data in a weighted least squares sense. But it does not mean that the field represented by the values on the particles is divergence free. This means that, to maintain values of magnetic field

on the particles that represent a divergence free field, some step must be taken to feed the divergence free solution back to the values on the particles. This is done by smoothing the values on the particles periodically towards the divergence free solution computed by this method. This smoothing process is discussed in section 3.2.2 of Maron and Howes [125] and in Section 3.5.2 here. Without such smoothing, the field represented by the values on the particles may accumulate a non-zero divergent component.

5.6 Results

To demonstrate most clearly the ability of the APR scheme to improve efficiently the spatial resolution in regions of large truncation error we use the standard 1-D shock tube test [173]. This test comprises a domain over [0,1] with an initial discontinuity at $x = 0.5$: to the left of the discontinuity $p = 1.0$ and $\rho = 1.0$; $p = 0.1$ and $\rho = 0.125$ to the right; initial velocity is zero everywhere and the adiabatic index is $\gamma = 1.4$. Results are plotted at time $t = 0.245$.

A comparison of the results of adaptive vs. non-adaptive schemes for a 1-D shock test [173] is presented in Figure 5.5. The parameters for the adaptive run were $f_{\chi_{max}} = 0.1$, $f_r = 0.45$, $f_{sm} = 0.45$, $f_u = 0.95$, $h_\nabla = 1.8$, $h_{min} = 0.0005$, $h_{min} = 0.05$, variable smoothing length with $N = 7$ neighbors, $f_{CFL} = 0.125$, and artificial viscosity with $\alpha = 0.5$ and $\beta = 1.0$. For the non-adaptive run, the parameters were second-order GPM, $N_p = 400$ particles, first-order smoothing applied every 32 timesteps with $f_{sm} = 0.25$, variable smoothing length with $N = 7$ neighbors, $\Delta t = 0.0001$, and artificial viscosity with $\alpha = 0.5$ and $\beta = 1.0$.

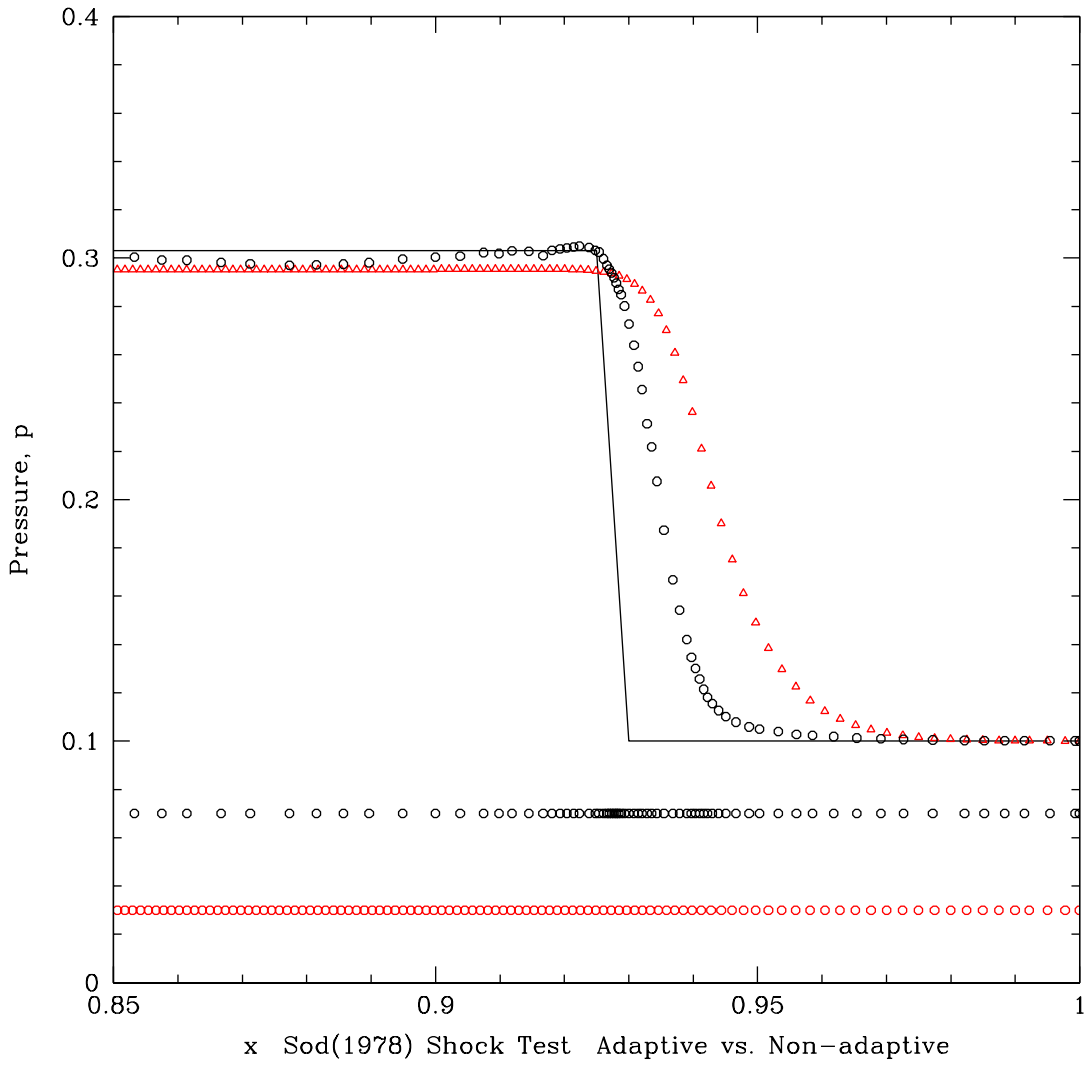

Figure 5.5: Comparison of adaptive and non-adaptive results for the 1-D shock tube [173] at $t = 0.245$. Plotted are a Riemann solver solution (solid line), a non-adaptive GPM solution (triangles), and an APR adaptive GPM solution (circles). Below are plotted the positions of the particles for both of the GPM runs. The adaptive solution more highly resolves the shock front while using fewer overall particles.

This plot focuses on the shock front propagating into the low density medium to the right. A Riemann solver solution (solid line), a non-adaptive GPM solution (triangles), and an adaptive GPM solution (circles) are shown. The shock front is clearly much steeper, with the corners in the pressure profile more well defined, in the adaptive run. Also plotted at the bottom are the positions of the particles for both of the GPM simulations: it is clear that, although the adaptive scheme uses fewer particles, the spatial resolution in the region of the shock front in much higher. The adaptive scheme here used approximately 260 particles, whereas the non-adaptive run employed a constant 400 particles; the adaptive scheme is therefore more efficient.

A plot of the pressure across the shock front and the particle distribution resulting under the adaptive scheme for a 2-D simulation of the same shock test is presented in Figure 5.6. Adaptive run parameters were $f_{\chi_{max}} = 0.1$, $f_r = 0.45$, $f_{sm} = 0.45$, $f_u = 0.95$, $h_\nabla = 1.25$, $h_{min} = 0.001$, $h_{min} = 0.05$, variable smoothing length with $N = 21$ neighbors, $f_{CFL} = 0.125$, first-order smoothing applied every 32 timesteps with $f_{sm} = 0.25$, and artificial viscosity with $\alpha = 0.5$ and $\beta = 1.0$. The simulation box size was 1.0×0.1. Parameters in the non-adaptive run were second-order GPM, $N_p = 4000$ particles, first-order smoothing applied every 16 timesteps with $f_{sm} = 0.5$, variable smoothing length with $N = 21$ neighbors, $\Delta t = 0.0001$, and artificial viscosity with $\alpha = 0.5$ and $\beta = 1.0$. The upper plot shows three results: the squared off shock is a Riemann solver solution, the thick line is the adaptive run which used approximately 4000 particles, and the thin line is a non-adaptive run that used exactly 4000 particles. The adaptive run resolves the shock more sharply. The lower plot in Figure 5.6 shows the particle

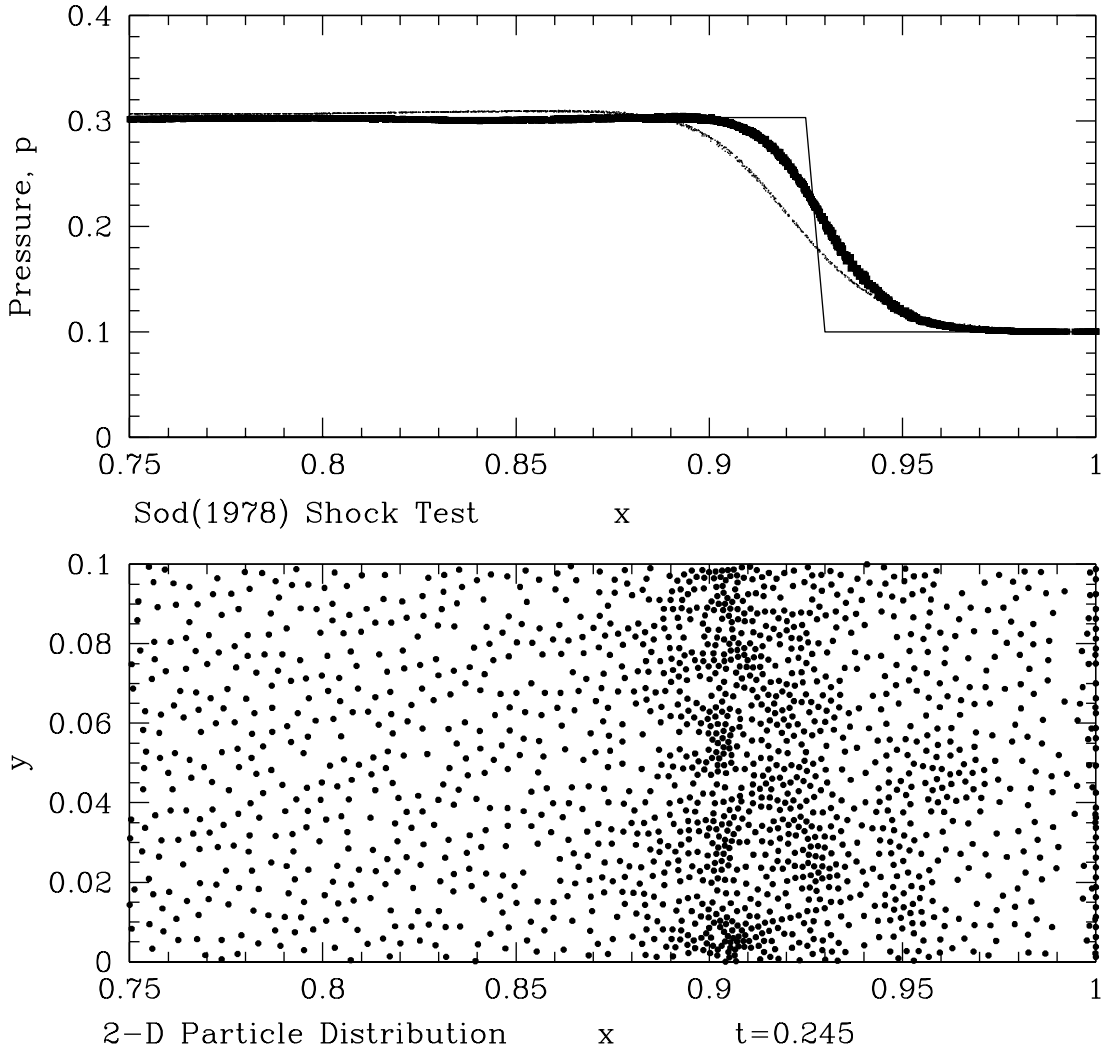

Figure 5.6: The upper plot compares three solutions to the Sod [173] shock test: the squared off line is a Riemann solver solution, the thick line is an adaptive run employing approximately 4000 particles, and the thin line is a non-adaptive run using exactly 4000 particles. The lower plot shows the 2-D particle distribution for the adaptive run.

distribution for the adaptive run. Although the resulting particle distribution across the shock is somewhat clumpy, the spatial resolution has clearly adapted to a much higher value than in the pre-shock or post-shock regions.

The problem of the magnetized vortex, as described in Section 4.3, provides an ideal demonstration of the adaptivity of the APR scheme. The initial velocity is given by (4.1) with the values $v_0 = 0.2$ and $r_0 = 0.1667$ in a 2-D periodic box of size 1.0×1.0. The sound speed is $c_s = 1.0$ and the Alfvén velocity corresponding to the initial field is $v_A = 0.02$. The azimuthal velocity winds up the weak magnetic field in the x-y plane, producing a field with reversals in magnetic field direction with radius. The density and energy remain approximately constant and the scheme adapts to the rapid reversals in the magnetic field.

Figure 5.7 shows the results for an adaptive simulation of the magnetized vortex. In the upper panel, the particle distribution displays the development of a spiral pattern due to the adaptivity responding to the winding up of the magnetic field. A comparison of the cross-section of B_y vs. x over $-0.005 < y < 0.005$ for an adaptive and a non-adaptive simulation is presented in the lower two panels. Parameters chosen for the adaptive run are $f_{\chi_{max}} = 0.1$, $f_r = 0.45$, $f_{sm} = 0.8$, $f_u = 0.95$, $h_\nabla = 1.25$, $h_{min} = 0.005$, $h_{min} = 0.05$, variable smoothing length with $N = 21$ neighbors, $f_{CFL} = 0.25$, second-order smoothing applied every 32 timesteps with $f_{sm} = 0.25$, and artificial viscosity with $\alpha = 0.05$ and $\beta = 0.1$. The non-adaptive runs employs second-order GPM, $N_p = 16384$ particles, second-order smoothing applied every 16 timesteps with $f_{sm} = 0.5$, variable smoothing length with $N = 21$ neighbors, $\Delta t = 0.004$, and artificial viscosity with $\alpha = 0.05$ and $\beta = 0.1$. The plots in Figure 5.7 are made at $t = 5.0$ when the adaptive

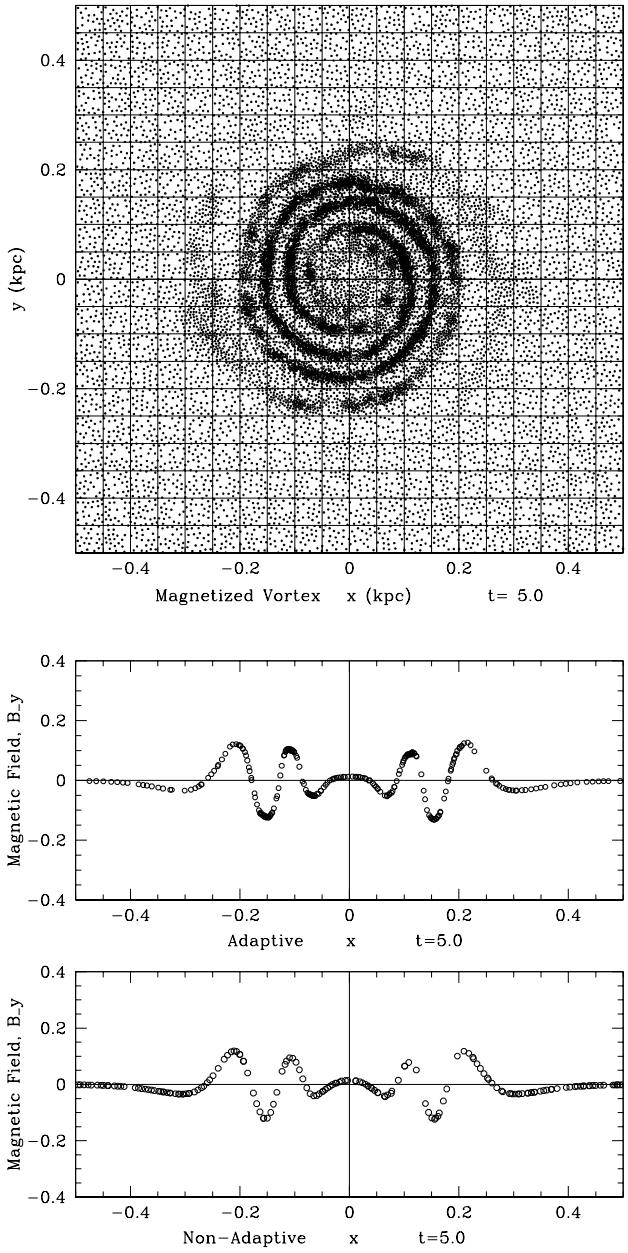

Figure 5.7: For the simulation a magnetized vortex, the upper panel displays the particle distribution for an adaptive run at $t = 5.0$; the spiral pattern reveals the underlying winding up of the weak magnetic field. The lower panels compare the cross-section of B_y vs. x over $-0.005 < y < 0.005$ for an adaptive and a non-adaptive simulation; the adaptive simulation resolves the magnetic field reversals more sharply.

run has $N_p = 15645$ particles and the non-adaptive run has a constant value of $N_p = 16384$ particles.

The increase in spatial resolution for the adaptive run is clear in the lower two panels of Figure 5.7. The regions of high curvature in B_y contain more particles in the adaptive run than in the non-adaptive run, resolving the magnetic field reversals much more sharply even for a slightly fewer total number of particles.

5.7 Conclusions

In the face of limitations on computational power, adaptive algorithms are frequently used to achieve high local spatial resolution in global simulations of astrophysical systems. The adoption of Adaptive Mesh Refinement (AMR) for grid-based methods is commonly used to realize adaptivity; another choice to take advantage of adaptivity is to use a Lagrangian numerical method. The Lagrangian approach is significantly less complicated than the AMR strategy, yet the Lagrangian approach adapts only to mass density and not generally to all evolved fields as AMR does. The new scheme of Adaptive Particle Refinement (APR) is introduced here to combine the simplicity of the Lagrangian approach with the general adaptivity of AMR.

AMR determines the need for refinement according to a truncation error estimate based on an Richardson extrapolation. The nature of Lagrangian methods, however, excludes the possibility of using this strategy for error estimation. Fundamentally, AMR computes this error by varying the resolution while holding

constant the method's order of convergence; APR takes a complementary approach by varying the order of convergence of the method with a constant spatial resolution. The error estimated by the APR strategy determines the action to be taken: refine, smooth, unrefine, or nothing. The APR scheme considers the error in the spatial fit only and does not estimate the timestep related error; the timestep is determined by the Lagrangian Courant condition for stability.

Lagrangian methods, unlike grid-based methods, suffer from two distinct types of error: truncation error and disconnection error. The disconnection error can occur if the distribution of neighbor particles within the smoothing sphere does not adequately sample the local fluid environment. A strategy is outlined here that prevents disconnection by ensuring that a mutual neighbor exists within the smoothing sphere along both directions of each coordinate axis. This reduces the error due a poor distribution of particles and inhibits the growth of the pernicious disconnection instability that can occur in GPM codes.

Implementation of the APR scheme requires some mechanism for refining and unrefining the spatial resolution. This is accomplished by the addition (removal) of a single particle each time refinement (unrefinement) is needed. Addition or removal of a particle involves an interpolation of the local fluid quantities or the conservative combination of the particle with its nearest neighbor. The range of spatial resolution in a simulation is controlled by setting limits for the minimum and maximum smoothing length. Runaway refinement or unrefinement can be prevented by limiting the variation of smoothing lengths over the smoothing sphere.

The elimination of magnetic divergence in a GPM code can be achieved elegantly by the inclusion of the magnetic divergence constraint as a Lagrangian multiplier in the least squares minimization problem. In practice, this requires a subsequent step that applies a correction to the independent, unconstrained fits for each component of the magnetic field.

Results of shock tests demonstrate the ability of the APR scheme to adapt the particle distribution in one and two dimensions to realize a higher spatial resolution than a non-adaptive code using the same total number of particles. Simulation of a magnetized vortex displays clearly the adaptivity responding to the formation of small-scale structure in the magnetic field. The concentration of the particle distribution in only the regions of small-scale structure resolves this structure more clearly than a non-adaptive code.

The potential for a framework for general adaptivity in a Lagrangian particle code is clearly demonstrated by the APR scheme described here. The APR scheme is capable of attaining a high local spatial resolution in regions of small-scale structure while efficiently reducing the number of particles used in more smooth regions. The computational efficiency of this adaptive method enables the simulation of global astrophysical systems without sacrificing the spatial resolution in regions of small-scale activity. Currently, the technique requires a minimum of seven adjustable parameters to control the adaptivity—$f_{\chi_{max}}$, f_r, f_{sm}, f_u, χ_{floor}, h_{min}, and h_{max}. Another parameter, h_∇, can be used to prevent adaptivity from running away in an unstable manner. Further testing and development of the scheme may reduce the number of requisite parameters. The current scheme

is also somewhat sensitive to changes in these running parameters, leading easily to over- or under-refinement. Fine tuning of the APR scheme will lead to a method that is less susceptible to variation in the running parameters. But the initial development of Adaptive Particle Refinement demonstrates the potential for achieving a significant computational advantage over non-adaptive Lagrangian schemes.

Chapter 6

Galactic Model

To study the evolution of the magnetic field in the Milky Way requires a Galactic model that describes the basic dynamics of the ISM in the Galaxy over the timescale of interest. The age of the Galaxy is on the order of 10^{10} years. A study of the magnetic evolution of the Galaxy must cover a minimum of a few 10^9 years. On this timescale, the key dynamical feature to be reproduced by the model is the slow infall of the ISM from large Galactocentric radii toward the Galactic center. On shorter timescales, the Galaxy should be in an approximately steady state of motion about the Galactic center. The aim of this chapter is to construct a simple Galactic model incorporating the minimum number of physical processes to achieve this goal.

A meaningful study of the evolution of the magnetic field in the Galaxy requires a three-dimensional treatment. The magnetic energy in a purely two-dimensional flow must ultimately decay to zero [57, 193]; but in three dimensions, a dynamo can amplify and maintain a magnetic field indefinitely. A fundamental difference exists between two-dimensional and three-dimensional magnetic systems. And, as

suggested by Lubow et al. [121], the vertical structure of the Galaxy may critically determine the evolution of the large-scale magnetic field. Although the numerical work presented in this dissertation is limited to preliminary models in two dimensions, the long-term aim of this work is to conduct three-dimensional simulations of the Galactic magnetic field evolution. Therefore, this chapter focuses on the development of three-dimensional Galactic models; changes appropriate for a two-dimensional model are noted.

6.1 Elements of a Galactic Model

The evolution of the magnetic field in the Galaxy depends on the dynamics of the ISM and on the magnetic diffusive properties of the interstellar environment. The diffusive properties of the ISM are somewhat controversial, so discussion will be postponed to the end of this section. Here the elements of a Galactic model needed to produce qualitatively realistic behavior of the ISM are outlined.

The ISM is a very heterogeneous medium that varies spatially over a large range of densities and temperatures [58]. Limits on computational power mean that this heterogeneous structure must remain largely unresolved in a global simulation of the Galaxy. It is necessary to adopt a homogeneous approximation of the ISM, attempting to maintain fidelity to the gross physical characteristics of the medium. The properties of this homogeneous approximation to the ISM are discussed in Section 6.2.

The dynamical motion of the ISM is dominated by the gravitational potential of the Galaxy due to the distribution of mass in the form of stars, gas, and dark

matter. Over the lifetime of the Galaxy, this gravitational potential certainly evolves; but on the shorter timescale of a few 10^9 years, this change is neglected and a fixed potential is taken. Although the true gravitational potential of the Galaxy contains much structure, stellar orbits at galactocentric radii greater than 5 kpc can be accurately modelled by an axisymmetric model [62]. In the central few kiloparsecs of the Galaxy, however, a non-axisymmetric mass distribution in the Galactic bulge significantly breaks this axisymmetry [134, 32, 23, 15, 28, 72]. Observations of dust lanes at the center of barred galaxies [161] suggest shocks in the gas flow at the leading edges of the bar. Numerous studies have demonstrated that a rotating bar component of the mass distribution leads to strong shocks in the gas flow and induces trailing spiral arms in the gas density [24, 6, 92, 67, 68]. The shocks and spiral structure transport angular momentum outwards in the ISM, allowing the gradual infall of material towards the Galactic center. To effect the desired general behavior of the ISM in a Galactic model, a primarily axisymmetric gravitational potential with a rotating bar potential within the inner few kiloparsecs is sufficient. These elements can produce a disk system with primarily circular motion about the Galactic center on the inner rotation timescale of 10^8 years but with slow accumulation of the ISM radially towards the Galactic center on a timescale of 10^9 years. This model, necessarily a simplification of the true Galactic potential, is detailed in Section 6.3.

Even a model with an exact Galactic gravitational potential, however, would not reproduce the observed characteristics of the Galaxy. A number of other physical processes that act as sources and sinks of energy and density in the ISM are necessary. The strong shocks induced by the bar, for example, lead to compression

of the ISM to high densities and temperatures; additionally, the radial inflow of the ISM leads to a buildup of mass in the Galactic center. In regions of increased mass density, the star formation rate tends to increase acting as a sink for mass density and a source for thermal energy. And, radiative cooling from molecular clouds becomes more efficient as the temperature increases, behaving as a sink for thermal energy. These unresolved physical processes must then be incorporated into the model by prescription, as described in Section 6.5, to reproduce a reasonable Galactic evolution over time scales on the order of 10^9 years.

For an investigation of the magnetic field evolution in the Galaxy, the Galactic model includes these key elements: a homogeneous ISM, a constant axisymmetric gravitational potential, a rotating bar component of the gravitational potential in the inner Galaxy, star formation, and radiative cooling of the ISM. This simple Galactic model neglects a host of other physical effects that affect the evolution of the Galactic magnetic field. As further development requires, the basic Galactic model may be enhanced both by using initial conditions that more closely fit the observations as well as by incorporating more physical processes. Additional complexities of the initial conditions or the physics that may be added in the future include:

- the inhomogeneous distribution of the ISM (all phases of the ISM, particularly including molecular clouds)
- the self-gravity of the ISM
- dynamical friction due to stars

- an evolving, and possibly self-consistent, stellar and dark matter distribution for the Galactic gravitational potential
- spiral structure in the stellar distribution
- stellar mass loss that recycles gas back to the ISM
- heating of the ISM by cosmic rays
- ambipolar diffusion
- turbulent diffusivity to enhance both viscosity and resistivity
- random forcing of the ISM by supernovae and stellar winds to drive turbulence
- injection of energy into molecular clouds from stellar radiation in regions of star formation
- a Galactic wind flowing away from the Galactic disk into the intracluster or intergalactic medium

Equally as important as the dynamics of the ISM to the evolution of the Galactic magnetic field is the effect of magnetic diffusion. Section 1.1 estimates the length scale over which diffusion is important for a homogeneous ISM as $L \leq 10^{-8}$ pc. For larger scales, the magnetic field is assumed to be frozen-in to the ISM. Yet there are several arguments that the effective magnetic diffusion in the ISM is much greater than the molecular value estimated here. The most commonly invoked argument is the concept of turbulent diffusion: turbulent eddies

swirl and mix the magnetic field on small scales on the timescale of the turnover time for the smallest eddy in the turbulent cascade. This turbulent motion quickly transports magnetic energy to small scales where the molecular diffusivity destroys the magnetic flux [144, 143]. Another idea is that the effect of the inhomogeneity of the ISM may alter the effective magnetic diffusivity. Although the magnetic field is well frozen to the hot, fully ionized components of the ISM, within colder molecular clouds ambipolar diffusion enables the magnetic field to move relative to the mass of the ISM. Alternatively, the large scale magnetic field may simply pass around, rather than through, the dense molecular clouds, allowing a large relative velocity between the mass of the ISM and the magnetic field lines. Conclusive evidence has yet to be provided for any of these arguments, so magnetic diffusion is not specified in the model.

6.2 The Computational Approximation of the ISM

Because we cannot resolve the heterogeneous nature of the ISM in a global Galactic disk model, we must make some approximation to its properties. Consider the physical size of a single computational particle in a simulation employing N_p particles of uniform mass in the case that the number density of particles reflects the mass density of the ISM (this constraint need not be met in adaptive simulations). If the ISM density distribution is given by the double exponential law of (6.9), we can estimate the mean interparticle distance l_0 at the Galactic center. The total mass M_D enclosed in a cylindrical simulation domain of radius $R_{out} = 12.0$ kpc

and height $z_{out} = 0.20$ kpc is

$$M_D = M_{ism}\left[1 - \exp\left(-\frac{z_{out}}{z_{ism}}\right)\right]\left[1 - \left(1 + \frac{R_{out}}{R_{ism}}\right)\exp\left(-\frac{R_{out}}{R_{ism}}\right)\right] \tag{6.1}$$

In this case, the mean interparticle distance l_0 is

$$l_0 = \left[\frac{M_D}{M_{ism}}\frac{4\pi z_{ism} R_{ism}^2}{N_p}\right]^{1/3} \tag{6.2}$$

For the parameter values $N_p = 128^3$ particles, $M_{ism} = 10^{10}$ $M_\odot$, $R_{ism} = 4.0$ kpc, and $z_{ism} = 0.040$ kpc, the interparticle distance $l_0 = 15$ pc. Since molecular clouds have a typical scale of 5–50 pc [79], a single computational particle represents one or more dense molecular clouds and the intervening diffuse intercloud medium. Figure 6.1 shows schematically the unresolved structure of the ISM within the volume of single computational particle.

With the wide variation of densities and temperatures contained within the physical extent represented by a single computational particle, we pose the questions: what are the appropriate spatially averaged densities and energies, and to what do these modelled densities and energies correspond in the physical system? The answer to these questions differs depending on whether the dynamic or energetic characteristics of the ISM are under consideration.

If the small-scale structure (on scales less than or equal to the computational particle size) of the ISM is not evolving on the dynamic timescales of interest (*i.e.* undergoing gravitational collapse as a prelude to star formation), the various components of the ISM must be in pressure equilibrium with each other. The diffuse intercloud medium indicated in Figure 6.1 is a spatial average of the warm

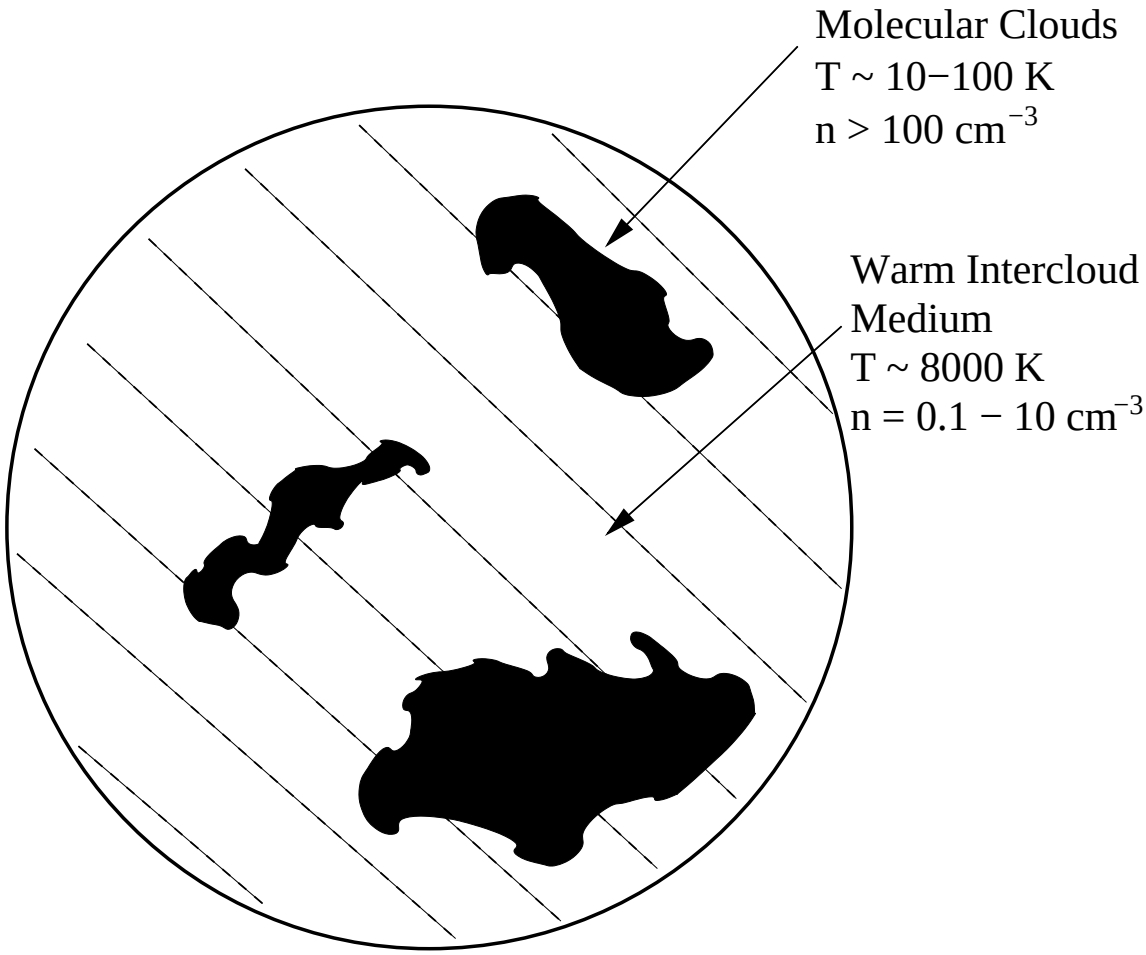

Figure 6.1: This figure shows the unresolved structure of the ISM contained within a single computational particle. With a particle size $l_0 \sim 15$ pc, a single particle may contain one or more cold, dense molecular clouds (size $\sim$ 5–50 pc) and the diffuse intercloud medium. This diffuse intercloud medium is itself an average over the warm ionized medium and the hot coronal component.

ionized medium and the hot coronal component of the ISM. This yields a two-phase ISM of cold, dense molecular clouds and the diffuse intercloud medium. Molecular clouds are typically supported against gravitational collapse by turbulent pressure; for a typical density of $n \sim 100$ cm^{-3} and a turbulent velocity dispersion of $\sigma \sim 1$ km/s, the turbulent pressure $P_{turb} = \rho\sigma^2 \sim 10^{-12}$ erg cm^{-3}. This turbulent pressure in the molecular clouds is generally balanced by the thermal pressure of the warm intercloud medium; for a density of $n \sim 1$ cm^{-3} and a temperature of $T \sim 8000$ K, the thermal pressure of the diffuse intercloud medium is $P_{therm} = nkT \sim 10^{-12}$ erg cm^{-3}. Therefore, the pressure on scales larger than that of a computational particle relates to the thermal pressure of the diffuse intercloud medium and not to that of the cold molecular clouds; the volume averaged thermal energy of the computational particles corresponds to the temperature of the intercloud medium, approximately $T \sim 10^4$ K. The molecular clouds and the intercloud medium each have volume averaged mass densities of order $n \sim 0.5$ cm^{-3} [34]; the appropriate mass density for the computational particles is simply the total mass over the volume, or the sum of these densities, yielding $n \sim 1$ cm^{-3}. Dynamically, the computational particles boast thermal energies characteristic of the diffuse intercloud medium and densities corresponding to the sum of the volume averaged mass densities of the individual components.

Energetically, however, the computational particle corresponds to different properties of the ISM. Although the radiative energy loss per physical particle (molecule, atom, or ion) is greater in the intercloud medium than in the molecular clouds, the number density of molecules in clouds is so much greater than the number density in the intercloud medium that the rate of radiative cooling

is effectively dominated by molecular clouds. The molecular cloud temperatures, therefore, must be estimated in order to calculate the effect on the energy budget due to radiative cooling, as discussed in Section 6.5.2. In addition, since the primary heating mechanism of concern is shock heating due to the bar potential, this heating occurs primarily in the dense molecular clouds.

6.3 Gravitational Potential

The simplified gravitational potential adopted by the Galactic model includes several components: axisymmetric components including a cylindrical stellar disk, a cylindrical stellar bulge, and a spherical halo; and a non-axisymmetric bar component in the inner Galaxy.

6.3.1 The Axisymmetric Component

Dehnen and Binney [62] describe an axisymmetric mass model of the Milky Way Galaxy using five components: a thin stellar disk, a thick stellar disk, the interstellar medium disk, a bulge, and a halo (including any dark matter component). We construct a simpler model with a single stellar disk (subsuming also the mass distribution of the ISM), a central bulge, and a halo. Although the functional forms of the density distributions for these components are typically exponential (as suggested by observations of the surface brightness vs. radius for external galaxies), for simplicity in the computation, power law profiles are assumed. Only a qualitative reproduction of the dynamics of the Galaxy is initially sought, so this simplified model suffices.

The Stellar Disk

The thin stellar disk, the thick stellar disk, and the disk of interstellar gas in the Dehnen and Binney [62] model are combined into a single component for this model. The basic form used for the stellar disk is the Miyamoto-Nagai potential-density pair (a synthesis of Plummer's spherical potential and Kuzmin's flattened potential) [26], given by the paired gravitational potential

$$\Phi_M(R,z) = -\frac{GM}{\sqrt{R^2 + (a + \sqrt{z^2 + b^2})^2}} \tag{6.3}$$

and density distribution

$$\rho_M(R,z) = \left(\frac{b^2 M}{4\pi}\right) \frac{aR^2 + (a + 3\sqrt{z^2 + b^2})(a + \sqrt{z^2 + b^2})^2}{[R^2 + (a + \sqrt{z^2 + b^2})^2]^{5/2}(z^2 + b^2)^{3/2}}. \tag{6.4}$$

Here G is the gravitational constant, M is the total mass, R is the cylindrical radius, z is the vertical height, a is the radial scale, and b is the vertical scale. When $a = 0$, this reduces to Plummer's spherical potential; when $b = 0$, to Kuzmin's flattened potential.

Basing our model on Dehnen and Binney's mass model 1 [62], we choose a stellar disk mass $M_d = 5.0 \times 10^{10}$ $M_\odot$, a radial scale $a_d = 2.0$ kpc, and a vertical scale $b_d = 0.2$ kpc. A comparison of the density for this disk with the combined thin stellar , thick stellar, and ISM disks of Dehnen and Binney is given in figure 6.2.

The Stellar Bulge

The stellar bulge also employs the Miyamoto-Nagai potential-density pair with the parameters: bulge mass $M_b = 5.0 \times 10^9$ $M_\odot$, radial scale $a_b = 0.3$ kpc, and

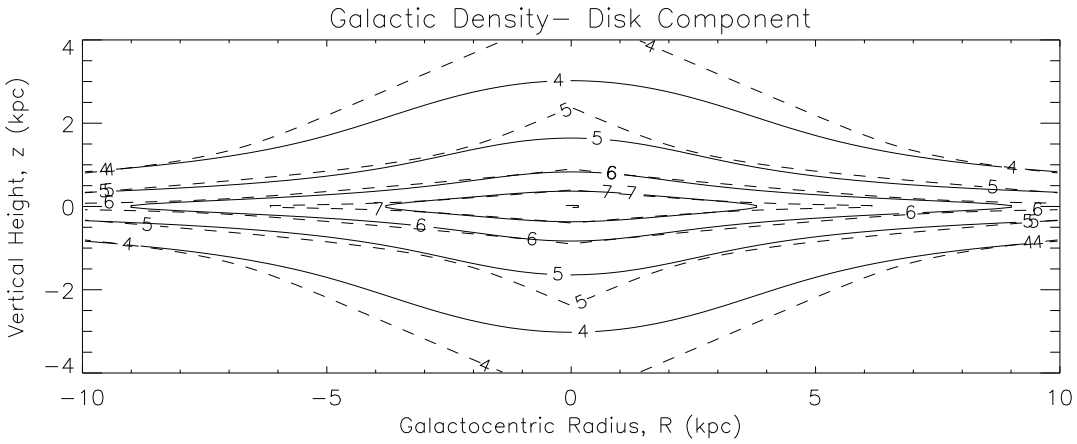

Figure 6.2: Density contour plot comparing the combined thin and thick stellar disks of Dehnen and Binney's mass model 1 (dashed lines) with the Miyamoto-Nagai density (solid lines) using the parameters $M_d = 5.0 \times 10^{10}$ $M_\odot$, $a_d = 2.0$ kpc, and $b_d = 0.2$ kpc. Contours are shown for density values of 0.1, 0.01, 0.001, and 0.0001 $M_\odot/pc^3$ in the R-z plane.

vertical scale $b_b = 0.3$ kpc.

The Halo

To assist in flattening the rotation curve of the Galaxy to conform with observations, a halo component is included in the gravitational potential; we do not distinguish whether the halo mass is comprised of luminous or dark matter since only the gravitational effects are of concern. The functional form taken for this spherical component is

$$\Phi_h(r) = \frac{1}{2} v_\infty^2 \ln(r^2 + a_h^2), \tag{6.5}$$

where r is th spherical radius and a_h is the radial scale length of the halo [27]. The circular velocity due to this component asymptotes to v_∞ as radius increases. Choosing the parameter values so that the rotation curve yields a reasonable value

at large Galactocentric radii yields $a_h = 10.7$ kpc and $v_\infty = 0.18$ kpc/My= 180 km/s.

A plot of the rotation curve for the axisymmetric components of the Galactic model is given in Figure 6.3. Although this model does not reproduce the rotation velocity determined in the solar vicinity ($R \sim 8$ kpc) of $v = 220$ km s^{-1}, it suffices as an initial model; future refinements of the model, including accounting for the non-axisymmetric contribution to the circular velocity (neglected here), can be performed to bring the model more into line with quantitative observations.

6.3.2 The Bar Potential

Through photometry, studies of gas and stellar dynamics, and counts of luminous stars, the presence of a significant stellar bar in the inner Galaxy has been well established [38, 119, 134, 32, 23, 15, 28, 72]. Detailed studies of the hydrodynamic gas flow in barred galaxies have led to a more thorough understanding of the dynamics of the gas at the Galactic center through an explanation of some of the salient features of the Galactic (l, v) diagram [119, 24, 7, 6, 92, 67, 68, 116, 148, 126]. The Galactic model here employs a density distribution given by the $n = 2$ Ferrers ellipsoid [26],

$$\rho = \begin{cases} \rho_0(1 - m^2)^2 & m < 1 \\ 0 & \text{elsewhere,} \end{cases} \tag{6.6}$$

where

$$m^2 = \frac{x^2 + z^2}{a_B^2} + \frac{y^2}{b_B^2} \tag{6.7}$$

and the prolate bar has $b_B > a_B$. The total bar mass is given by $M_B = 32\pi a_B^2 b_B \rho_0/105$. Methods of solving for the gravitational potential due to this

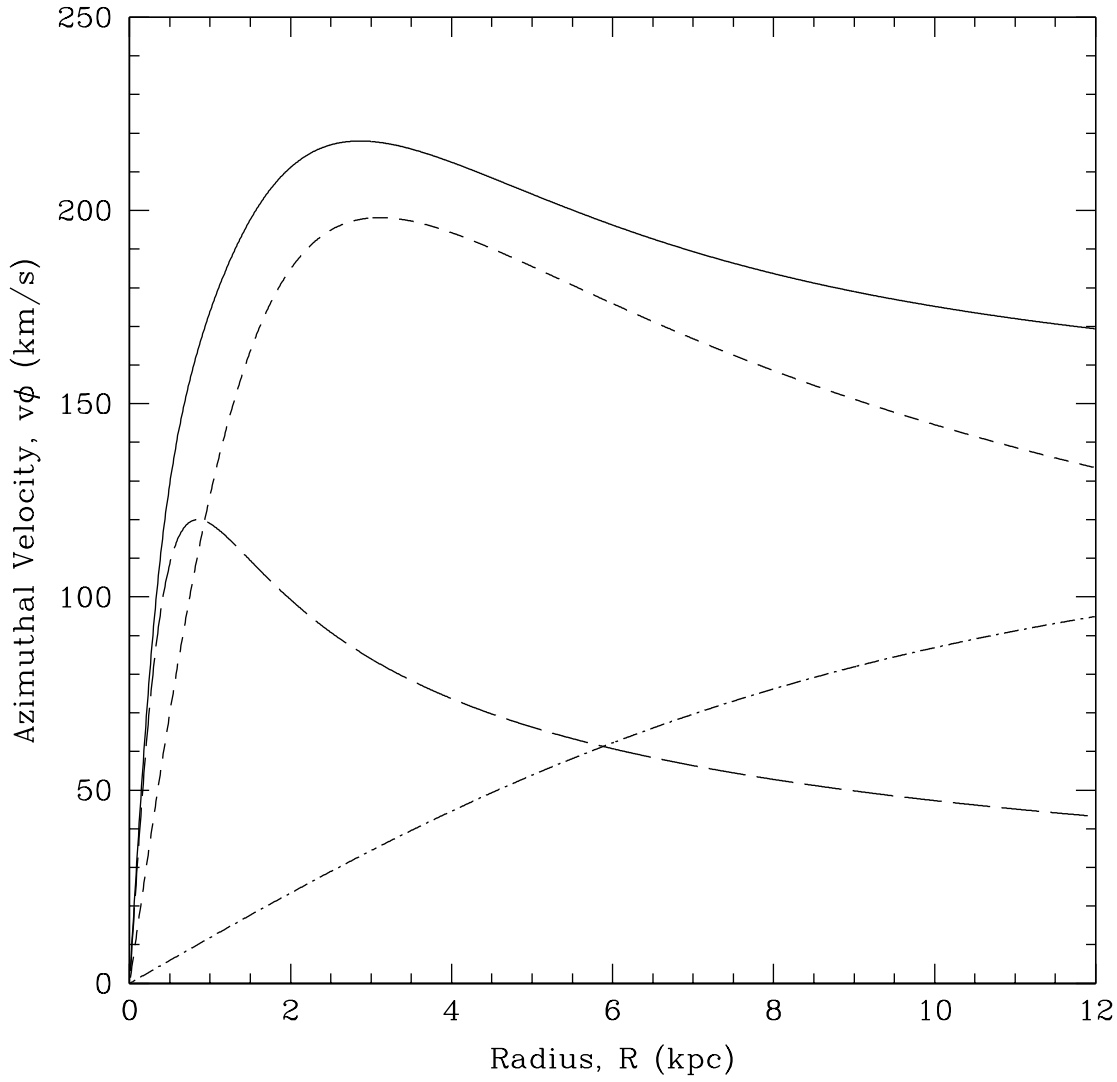

Figure 6.3: A fit of the rotation curve due to the axisymmetric gravitational potential model described in Section 6.3. Broken down by components are curves for the stellar disk (short dash), stellar bulge (long dash), halo (dot-dash), and total of all components (solid).

density distribution have been given by Perek [149] and de Vaucouleurs and Freeman [61]; the solution for the potential and forces for the $n = 2$ ellipsoid are explicitly given in the appendix of Papayannopoulos and Petrou [141]. A rotating bar potential of this form is characterized by four parameters: the semi-minor axis a_B, the semi-major axis b_B, the total bar mass M_B, and the bar pattern rotation speed Ω_p.

Parameter values used in the present Galactic model are $a_B = 1.6$ kpc, $b_B = 4.0$ kpc, $M_B = 1.0 \times 10^{10}$ $M_\odot$, and $\Omega_p = 62.83$ km s^{-1} kpc^{-1}. To avoid large transients in the system response, the bar is introduced gradually over one rotation period (the pattern rotation period corresponding to the chosen $\Omega_p = 62.83$ km s^{-1} kpc^{-1} is $\tau_B = 100$ My). Initially the same amount of mass is distributed in an axisymmetric disk given by the Miyamoto-Nagai potential with parameters $M = M_B$, $a = (a_B + b_B)/2$, and $b = a_B$. The mass is transferred linearly in time from the axisymmetric disk to the bar.

6.4 Initial Conditions of the ISM

Since the evolution of the Galactic magnetic field is dependent upon the dynamics of the ISM, the initial conditions of the ISM form a crucial aspect of the Galactic model. This study makes use of two types of initial conditions: a present-day model with exponential initial conditions that represent the state of the ISM in the Galaxy as we see it today, and an early galaxy model with constant initial conditions that approximate the character of the ISM shortly after the formation of the Galaxy. The strong vertical magnetic flux inferred at the Galactic center [134]

is thought to be the result of the accumulation of infalling material [174, 88, 48]. To model this process, the ISM is initialized with a constant density and magnetic field across the disk; angular momentum transport mechanisms lead to the radial infall of the ISM towards the Galactic center where the frozen-in magnetic field is accumulated. The radial profile of the density in the ISM disk is expected to reach an equilibrium of approximately exponential form, balancing the infall of material with the loss of mass due to star formation. For comparison to observations, this equilibrium can be achieved more quickly by initializing an exponential disk.

The initial conditions of the ISM must specify the density, internal energy, velocity, and magnetic field. The distributions of these quantities must be chosen to yield an equilibrium system. In the absence of a dynamically significant magnetic field, such equilibrium initial conditions are determined using a simple strategy. First, the external gravitational potential due to the stellar mass distribution is specified. Second, the form of the ISM density distribution is chosen. Third, the vertical energy distribution of the ISM is calculated to yield vertical hydrostatic equilibrium,

$$\frac{\partial p(R,z)}{\partial z} = -\rho(R,z)\frac{\partial \Phi(R,z)}{\partial z} \tag{6.8}$$

Fourth, the circular velocity of the ISM is determined so that the net radial acceleration due to the radial component of the gravitational acceleration and the (smaller) radial pressure gradient provides the centripetal acceleration for circular motion about the Galactic center. Unless particularly simple forms for the ISM density and stellar gravitational potential are chosen, the calculation of the energy and velocity profiles is accomplished using numerical integration.

This equilibrium scheme has the advantage that once the stellar (and dark matter) mass distribution and the initial ISM density profile have been specified, there are *no* more free parameters. The choice of vertical hydrostatic equilibrium and radial centripetal balance eliminate the need for any other parameters, dramatically simplifying the parameter space over which models can be constructed. Although this scheme produces a system in equilibrium, however, it is not necessarily a stable equilibrium; free energy can still be extracted from the gravitational potential to drive dynamic evolution of the model on the timescale of the inner rotation time, $\tau \sim 10^8$ years. The system will evolve transiently to a stable equilibrium. The initial system can be advanced numerically for a short time to allow these transient motions to escape the system through the boundaries.

6.4.1 Density Distribution of the ISM

The luminosity profiles of external disk galaxies typically demonstrate exponential behavior with radius and vertical height [25]. For the present-day Galactic model, the density distribution of the ISM is given by a standard double exponential disk,

$$\rho_{ism}(R,z) = \frac{M_{ism}}{4\pi z_{ism} R_{ism}^2} \exp\left(-\frac{R}{R_{ism}} - \frac{|z|}{z_{ism}}\right). \tag{6.9}$$

The parameters chosen for the ISM density distribution are a cylindrical radial scale $R_{ism} = 4.0$ kpc, a vertical scale $z_{ism} = 0.040$ kpc, and a total mass $M_{ism} = 10^{10}$ $M_\odot$, giving a central density of $\rho_{ism}(0,0) \sim 10^9$ $M_\odot/\text{kpc}^3$.

An early galaxy model initializes the ISM with a constant initial density over radius. The fact that such a disk would have an infinite mass presents no problem for a numerical simulation of finite size. The vertical structure in a 3-D disk

maintains an exponential form. The surface density of the disk in this model is specified $\Sigma_{ism} = 10^6$ $M_\odot/\text{kpc}^2$, yielding, for the vertical scale height given above, a density of $\rho_{ism} = 2.5 \times 10^7$ $M_\odot/\text{kpc}^3$.

6.4.2 Internal Energy Distribution of the ISM

After the stellar gravitational potential $\Phi(R, z)$ and the ISM density distribution $\rho_{ism}(R, z)$ have been specified, the energy distribution is determined by mandating vertical hydrostatic equilibrium according to (6.8). Using the adiabatic equation of state

$$p = (\gamma - 1)\rho e, \tag{6.10}$$

where e is the internal energy per unit mass, and assuming $\lim_{|z|\to\infty} p(R, z) = 0$ and $\lim_{|z|\to\infty} \rho(R, z) = 0$, the internal energy profile is given by

$$e(R, z) = \frac{1}{(\gamma - 1)\rho_{ism}(R, z)} \int_{|z|}^{\infty} \rho_{ism}(R, z) \frac{\partial \Phi(R, z)}{\partial z} dz \tag{6.11}$$

It is worthwhile to note here that the true vertical profile of the inhomogeneous ISM is not actually a thermally supported hydrostatic equilibrium but is a bounded oscillation about the Galactic plane of individual molecular clouds with a distribution of vertical kinetic energies. Therefore, the value of the energy at the midplane of the Galactic disk is not necessarily determined by the scale height of the ISM disk as (6.11) would demand.

For a 2-D early galaxy model, it is possible to choose the constant value for the internal energy independently of the disk scale height; though this may violate (6.11), it can be physically justified by the preceding argument. Values often used

when specified in this independent way are $e = 10^{-4}$ kpc^2/My^2, corresponding to a temperature of $T \sim 10^4$K, or a cooler early galaxy model energy of $e = 5 \times 10^{-6}$ kpc^2/My^2, corresponding to $T \sim 600$K.

6.4.3 Velocity Profile of the ISM

The initial equilibrium velocity of the ISM is assumed to be circular motion about the Galactic center with centripetal acceleration provided by the net radial acceleration due to the radial gravitational acceleration and the typically much smaller thermal pressure gradient. Therefore, the vertical and radial components of the velocity are set to zero and the azimuthal component is given by

$$v_\phi(R,z) = \left[R \left(\frac{\partial \Phi(R,z)}{\partial R} + \frac{1}{\rho_{ism}(R,z)} \frac{\partial p(R,z)}{\partial R} \right) \right]^{1/2} \tag{6.12}$$

If the term in parentheses in (6.12) is negative—this only occurs in practice as $R \to 0$ for unphysically large energies—the azimuthal velocity is simply set to zero.

Note that the equilibrium initial conditions for a magnetized system necessarily will include a magnetic contribution to the radial acceleration; however, the magnitude of the initial magnetic field is typically small so that any magnetic contribution may be neglected.

6.4.4 Initial Magnetic Field

The initial magnetic field for a global disk simulation will consist of an external long wavelength component and a fluctuating component on much smaller scales. The hypothesis is that a wide range of initial field configurations will, after being

acted upon by the motion of the Galactic disk, produce a magnetic field with the same general topology as that observed today—a largely azimuthal magnetic field with a strong, vertical component at the center. To produce the present day magnetic field through disk evolution is the goal of this project, so it begs the question to discuss the magnetic field for a present-day Galactic model.

The early galaxy models, though, impose a simple, straight external magnetic field of constant strength with a non-zero vertical flux through the Galactic disk. Ideally, this field should be tilted from vertical so that its radial position varies across the height of the disk; differential rotation of the ISM disk can then produce a strong azimuthal field through field line stretching. (A completely vertical field may provide an interesting, if not physically realistic, point of comparison.) As more complex initial models are developed, the initial magnetic field may be altered by adding a small-scale fluctuating component. The strength of this initial field is taken to be $B \sim 0.1\ \mu$G [48].

6.5 Physical Processes by Prescription

A number of unresolved physical processes that can be added to the ISM dynamics of the Galactic model by prescription include star formation (a density sink), radiative cooling (an energy sink), stellar mass loss (a density source), and heating by cosmic rays (an energy source). Although only star formation and radiative cooling are necessary to model the qualitative dynamics of the Galaxy, stellar mass loss and heating by cosmic rays are simple to include and so are described here.

6.5.1 Star Formation

The imposition of a stellar bar gravitational potential leads to strong shocks and significant angular momentum transport in the ISM; consequently, the ISM undergoes a gradual radial inflow towards the Galactic center. Without a sink for the accumulating mass at the Galactic center, a realistic hydrodynamic evolution of the Galaxy cannot be attained because the rising radial pressure gradient will halt the inflow of the ISM. Star formation behaves in the real Galaxy as a density sink in regions where local density enhancements exceed the Jeans stability criterion for gravitational collapse [26]. (Note that a phase transition to a cold molecular form of the ISM is another means of accomplishing the removal of this density.) We neglect the fact that vigorous star formation also tends to heat the local environment, becoming a source for energy.

Kennicut [96] correlates the global star formation rates in galactic disks and nuclear starbursts with the local gas density. He concludes that a simple Schmidt [163] power law provides an excellent parameterization of the global star formation rate, dependent primarily on the gas density.

Star formation is included by prescription according to the empirical formula given by Kennicut [96]

$$\Sigma_{SFR} = (2.5 \pm 0.7) \times 10^{-4} \left(\frac{\Sigma_{gas}}{1 \text{ M}_\odot \text{ pc}^{-}2} \right)^{1.4 \pm 0.15} \text{M}_\odot \text{ year}^{-1} \text{ kpc}^{-2} \qquad (6.13)$$

where Σ_{SFR} and Σ_{gas} are the disk-averaged star formation rate per unit surface area and gas surface density. Basing our star formation prescription on the relation

above, we use the formula

$$\frac{d\Sigma}{dt} = -\alpha_{SFR}\left(\frac{\Sigma}{\Sigma_0}\right)^N \tag{6.14}$$

where $\alpha_{SFR} = 250\ \mathrm{M}_\odot\ \mathrm{kpc}^{-2}\ \mathrm{My}^{-1}$, $\Sigma_0 = 10^6\ \mathrm{M}_\odot\ \mathrm{kpc}^{-2}$, and $N = 1.4$. Assuming that the vertical distribution of the ISM is exponential with a scale height z_{ism}, we can relate the local volume density to the local surface density by the relation $\Sigma = 2\rho z_{ism}$. Under the approximation that over the simulation domain the ISM scale height remains constant, we model star formation as a sink of the local volume density given by the formula

$$\frac{d\rho}{dt} = -\left(\frac{\alpha_{SFR}}{2z_{ism}}\right)\left(\frac{2\rho z_{ism}}{\Sigma_0}\right)^N \tag{6.15}$$

6.5.2 Radiative Cooling

Neufeld et al. [138] calculates the radiative cooling curves from molecular clouds as a function of temperature and molecular density. The plots in Figure 3 of this paper demonstrate that the cooling power is more sensitive to temperature changes than to density changes; based on this, we construct an approximate model for which the total cooling power is dependent only on temperature, neglecting the variation with molecular number density. In Figure 6.4 is plotted the logarithm of the total cooling power per H_2 molecule in erg s^{-1}, $\ln\Lambda$, vs. the logarithm of the temperature in K, $\ln T$. The data are taken from Figure 3c of Neufeld et al. [138] assuming $n(\mathrm{H}_2) = 10^3$. A fit of these data to the equation $\log\Lambda = m\log T + b$, plotted in Figure 6.4, yields the values $m = 2.6$ and $b = -29.8$. We can use this approximate fit to construct a prescription for the radiative cooling due to molecular clouds.

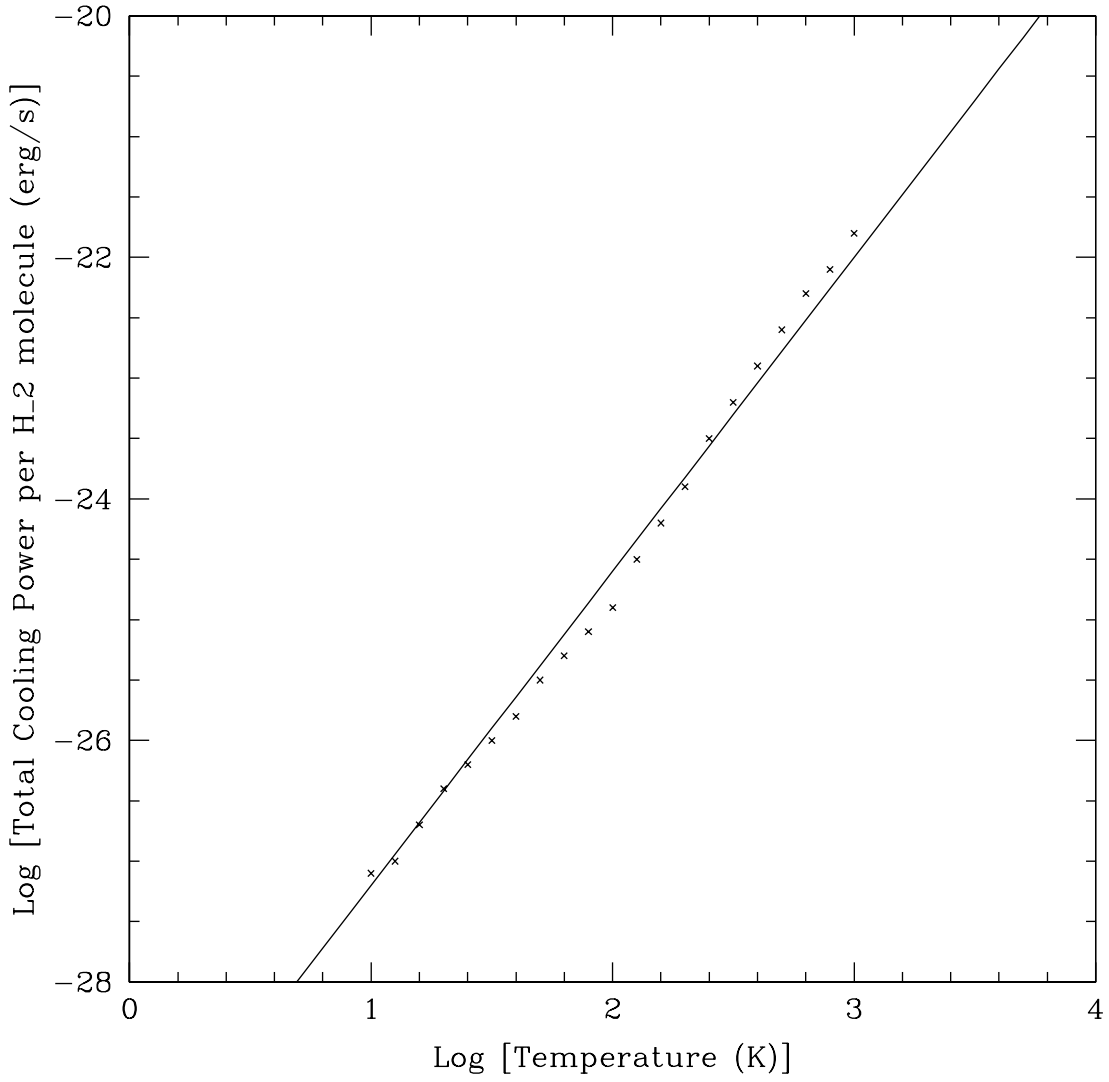

Figure 6.4: A fit of data taken from Figure 3c of Neufeld *et. al.* [138] assuming $n(\mathrm{H}_2) = 10^3$. A fit of these data to the equation $\log \Lambda = m \log T + b$ yields the values $m = 2.6$ and $b = -29.8$.

To determine the temperature of the unresolved molecular clouds from the computational particle temperature in our simulations, we assume a pressure balance between the components of the ISM as seen in Figure 6.1 and as discussed in Section 6.2. Assuming thermal pressure balance, we can find a relation between the temperature of the warm, diffuse intercloud medium and the temperature of the cold, dense molecular clouds

$$T_{H_2} \leq \frac{f_{H_2}}{f_H} T_H. \tag{6.16}$$

The equal sign in (6.16) corresponds to entirely thermal pressure balance; the molecular clouds temperature will be less if turbulent pressure contributes to the support of the molecular clouds.

Using the data from the fit in Figure 6.4, we get a final form of the cooling law

$$\Lambda = a \left(\frac{e \frac{f_{H_2}}{f_H}}{e_0} \right)^m \tag{6.17}$$

where the coefficient $a = 7.77 \times 10^{-10}$ kpc^2 My^{-2} My^{-1}, the exponent $m = 2.6$, the energy per unit mass scale $e_0 = 1.3 \times 10^{-8}$ kpc^2 My^{-2}, the volume filling fraction for cold molecular clouds is $f_{H_2} = 0.001$, and the volume filling fraction for the warm intercloud medium is $f_H = 0.5$.

6.5.3 Stellar Mass Loss

The star formation prescription above represents the conversion of ISM gas into stars as a sink of ISM mass density, but stars also shed gas, adding to the mass density of the ISM. Although the surface density of stars is clearly dependent on radius, a simplifying approximation of a roughly constant surface density of stars

is taken. Stellar mass loss as a source of ISM density is treated according to the relation

$$\frac{d\Sigma}{dt} = \beta_{SML} \tag{6.18}$$

where $\beta_{SML} = 250\ M_\odot\ \mathrm{kpc}^{-2}\ \mathrm{My}^{-1}$. We can think of this as having the same form as the star formation density sink

$$\frac{d\Sigma}{dt} = \beta_{SML} \left(\frac{\Sigma_0}{\Sigma_0}\right)^N \tag{6.19}$$

but using a constant surface density $\Sigma = \Sigma_0$. Converting this to a formula for a volume density source (assuming an exponential distribution of the ISM vertically with constant scale height z_{ism} over the disk), we find

$$\frac{d\rho}{dt} = \frac{\beta_{SML}}{2z_{ism}} \tag{6.20}$$

Although the magnitude of this density source is very small, it can have an effect on regions of very low density. Again, this adds fidelity to the model and has the useful computational benefit that it inhibits the density from dropping to zero.

6.5.4 ISM Heating by Cosmic Rays

Without a source of heating, radiative cooling, over very long timescales, would reduce the temperature of the ISM to unrealistically low values. Observations of the ISM suggest its temperature never drops below a minimum value of $T \sim 10\ \mathrm{K}$ [58]. Heating of the ISM by cosmic rays maintains this minimum temperature in the absence of other sources of heat. As the timescale of this heating is significantly less than the timescale of interest for Galactic dynamics, ISM heating by cosmic

rays is accomplished by including an energy floor in the simulations that corresponds to a temperature of $T \sim 10$ K for the molecular cloud component of the ISM; the current value used is $e_{\rm floor} = 5.0 \times 10^{-6}$ kpc^2 My^{-2}.

Chapter 7

Galactic Disk Results

Preliminary results from GPM simulations of the Galactic disk are analyzed and discussed in this chapter. Although the aim of this project is to conduct Galactic disk simulations to study the evolution of the magnetic field in the Galaxy, development of the computational tools to carry out this project regrettably took more time than anticipated. Little time remained to perform the global disk simulations, so the results here represent only preparatory studies on the path to a more thorough examination of Galactic disk behavior. As the results in this chapter constitute only the initial MHD simulations of the Galactic disk with the new GPM method, no attempt will be made to draw any general conclusions about the subject here.

The past decade has seen numerous hydrodynamic studies in two dimensions of the Galactic disk, with particular emphasis placed on the dynamic effect of the central stellar bar potential [24, 6, 92, 67, 68, 116, 148, 27]. These papers describe hydrodynamic simulations of an isothermal galactic disk, with the ISM flowing in a prescribed stellar gravitational potential of varying complexity. The

simulations presented here extend this work to include an adiabatic, rather than isothermal, equation of state and to follow the magnetic evolution of the Galaxy in the MHD approximation. Two simulations are chosen for the analysis presented in this chapter: both have identical parameters except that one simulation is purely hydrodynamic while the other includes magnetic fields.

7.1 Description of Galactic Simulations

The two simulations presented here are two-dimensional hydrodynamic (bar125) and MHD (bbar125) simulations of the Galactic disk. The simulations employ the second-order GPM algorithm with a second-order leapfrog timestepping scheme. The magnetic field evolution in simulation bbar125 evolves the vector potential according to (3.2). The simulations use the adiabatic equation of state (3.6) and neglect the self-gravity of the ISM. The vertical extent of the disk is assumed to be constant across the disk with an exponential scale height of $z_{ism} = 0.04$ kpc. Star formation and stellar mass loss provide a sink and source for mass density in the ISM; similarly radiative cooling and cosmic ray heating provide a sink and source for thermal energy. Viscosity and resistivity are modelled by a periodic smoothing of velocity and magnetic field over a fixed scale. The running parameters used for both of these simulations are summarized in Table 7.1.

These simulations initialize the ISM as a present-day model as described in Chapter 6: the density and energy distributions are exponential in radius. Since these models are two dimensional, the energy must be specified by the value at the Galactic center, $e_0 = 10^{-4}$ kpc^2 My^{-2}. An initially large magnetic field

Parameter		bar125	bbar125
Timestep	Δt	0.125 My	0.125 My
Courant Fraction	f_{CFL}	0.125	0.125
Adiabatic Index	γ	5/3	5/3
Viscosity scale	h_ν	0.05 kpc	0.05 kpc
Viscosity step	$n_{step\ \nu}$	8	8
Viscosity fraction	f_ν	0.5	0.5
Resistivity scale	h_η	off	0.1 kpc
Resistivity step	$n_{step\ \eta}$	off	32
Resistivity fraction	f_η	off	0.5
Number of particles	N_p	65536	65536
Radial Boundary	R_{out}	12.0 kpc	12.0 kpc
Number of Neighbors	N_n	25	25
Smoothing Order	$\mathcal{O}_{sm}$	2	2
Smoothing step	$n_{step\ sm}$	16	16
Smoothing fraction	f_{sm}	0.5	0.5
Central Energy	e_0	10^{-4} kpc^2 My^{-2}	10^{-4} kpc^2 My^{-2}
Energy Floor	e_{floor}	5×10^{-6} kpc^2 My^{-2}	5×10^{-6} kpc^2 My^{-2}
Density Floor	ρ_{floor}	10^5 $M_\odot$ kpc^{-3}	10^5 $M_\odot$ kpc^{-3}
Magnetic Field Strength	B	0	2.8 μG
Magnetic Field Direction	θ_{xz}	0	45°

Table 7.1: Running parameters for the simulations bar125 and bbar125. The magnetic field direction, θ_{xz}, is the angle from the x-axis in the x-z plane.

was specified in the MHD run with components $B_x = 2$ μG and $B_z = 2$ μG; the unphysically large magnitude, particularly in the vertical component, was chosen so that the magnetic field would accumulate in the center to a dynamically significant value over a short simulation time. The parameters chosen for the the Galactic model, as detailed in Chapter 6, are presented in Table 7.2.

Difficulties with long-term computational stability using the new GPM algorithm to model this rather complicated Galactic model limited the total evolution time of the simulations presented. The hydrodynamic simulation (bar125) stopped at $t = 279$ My and the MHD simulation (bbar125) ran only to $t = 149$ My. Hence, although the qualitative structure of the flow in the Galactic disk agrees with previously published results from hydrodynamic models, drawing firm conclusions from these models is not possible because the transient disturbance caused by the introduction of the stellar bar has not settled down over the short time evolution of these runs.

7.2 Qualitative Comparison of Results

Density color maps and cross sections of the density, energy, and vertical magnetic field are presented in Figure 7.1 (bar125) and Figure 7.2 (bbar125). The data in the density plots in these figures has been rotated to align the major radius of the bar with the vertical axis. The cross section chosen for the density, energy, and vertical magnetic field plots is indicated by the region between the two red lines on the density map.

Parameter		Value
Star Formation (SF)		on
SF Coefficient	α_{SFR}	250 $M_\odot$ kpc^{-2} My^{-1}
SF Exponent	N	1.4
SF Normalization	Σ_0	10^6 $M_\odot$ kpc^{-2}
Stellar Mass Loss (SML)		on
SML Coefficient	β_{SML}	250 $M_\odot$ kpc^{-2} My^{-1}
Radiative Cooling (RC)		on
RC Coefficient	a	7.77×10^{-10} kpc^2 My^{-2} My^{-1}
RC Exponent	m	2.6
RC Normalization	e_0	1.3×10^{-8} kpc^2 My^{-2}
Molecular Cloud Filling Fraction	f_{H_2}	0.001
Warm ISM Filling Fraction	f_H	0.5
ISM Mass	M_{ism}	10^{10} $M_\odot$
ISM Radial Scale	R_{ism}	4.0 kpc
ISM Vertical Scale	z_{ism}	0.04 kpc
Stellar Disk Mass	M_d	5×10^{10} $M_\odot$
Stellar Disk Radial Scale	a_d	2.0 kpc
Stellar Disk Vertical Scale	b_d	0.2 kpc
Stellar Bulge Mass	M_b	5×10^9 $M_\odot$
Stellar Bulge Radial Scale	a_b	0.3 kpc
Stellar Bulge Vertical Scale	b_b	0.3 kpc
Halo Asymptotic Velocity	v_∞	0.180 kpc/My
Halo Radial Scale	a_h	10.7 kpc
Stellar Bar Mass	M_B	10^{10} $M_\odot$
Stellar Bar Minor Radius	a_B	1.6 kpc
Stellar Bar Major Radius	b_B	4.0 kpc
Stellar Bar Rotation Rate	Ω_p	-62.83 km s^{-1} kpc^{-1}
Bar Introduction Rotations	n_{rot}	1.0

Table 7.2: Parameters for the Galactic model used by both bar125 and bbar125.

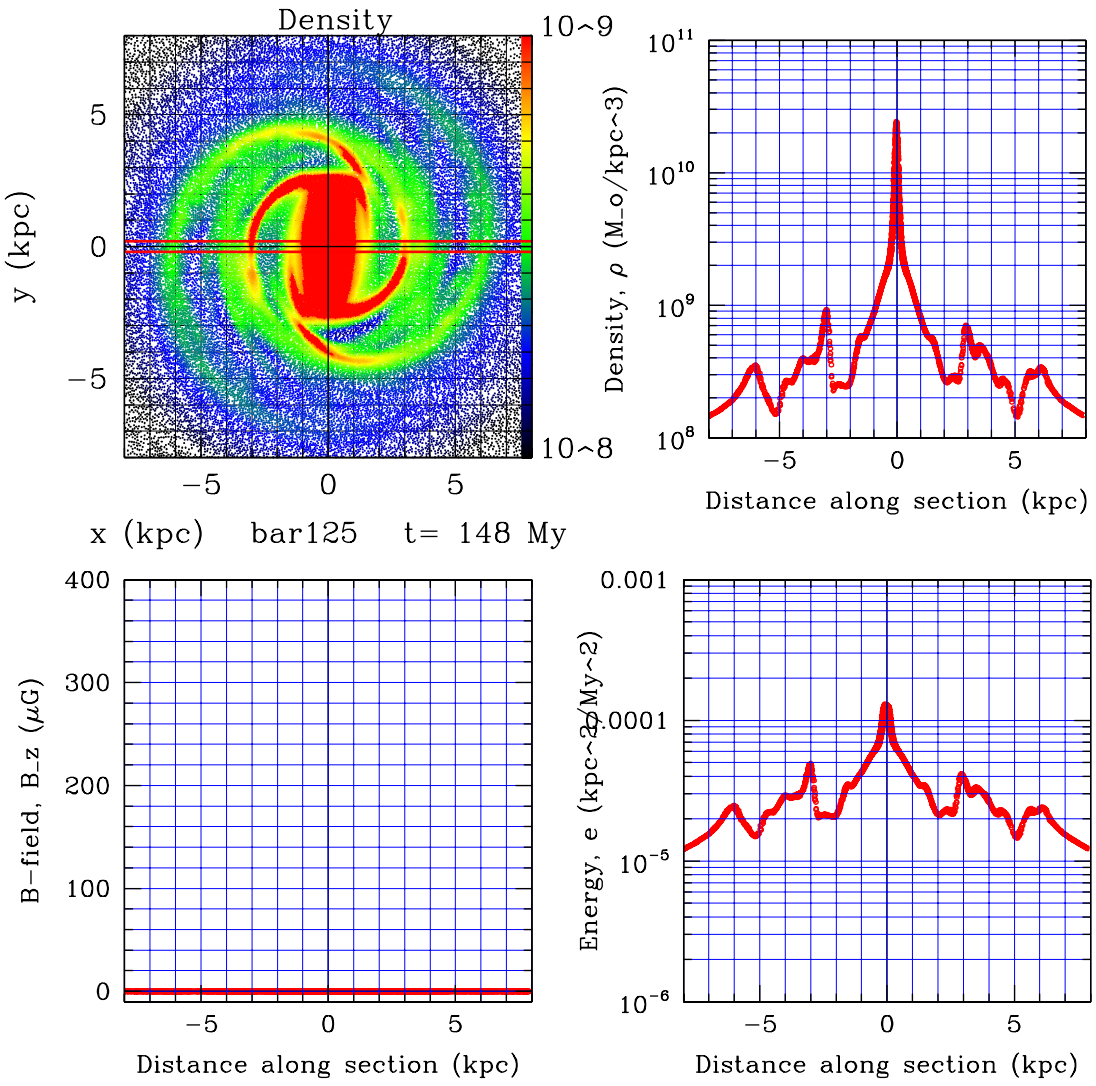

Figure 7.1: Cross section of results from the hydrodynamic simulation bar125 at $t = 148$ My. The upper left plot shows a logarithmic color plot of the density between 10^8 $M_\odot$ kpc^{-3} and 10^9 $M_\odot$ kpc^{-3}; note that the data has been rotated to align the major axis of the bar with the vertical axis of the plot. The cross section chosen is indicated on this plot as the strip within the two parallel red lines. Profiles of density (upper right), energy per unit mass (lower right), and vertical magnetic field (lower left) are shown. This hydrodynamic run had $\mathbf{B} = \mathbf{0}$ everywhere.

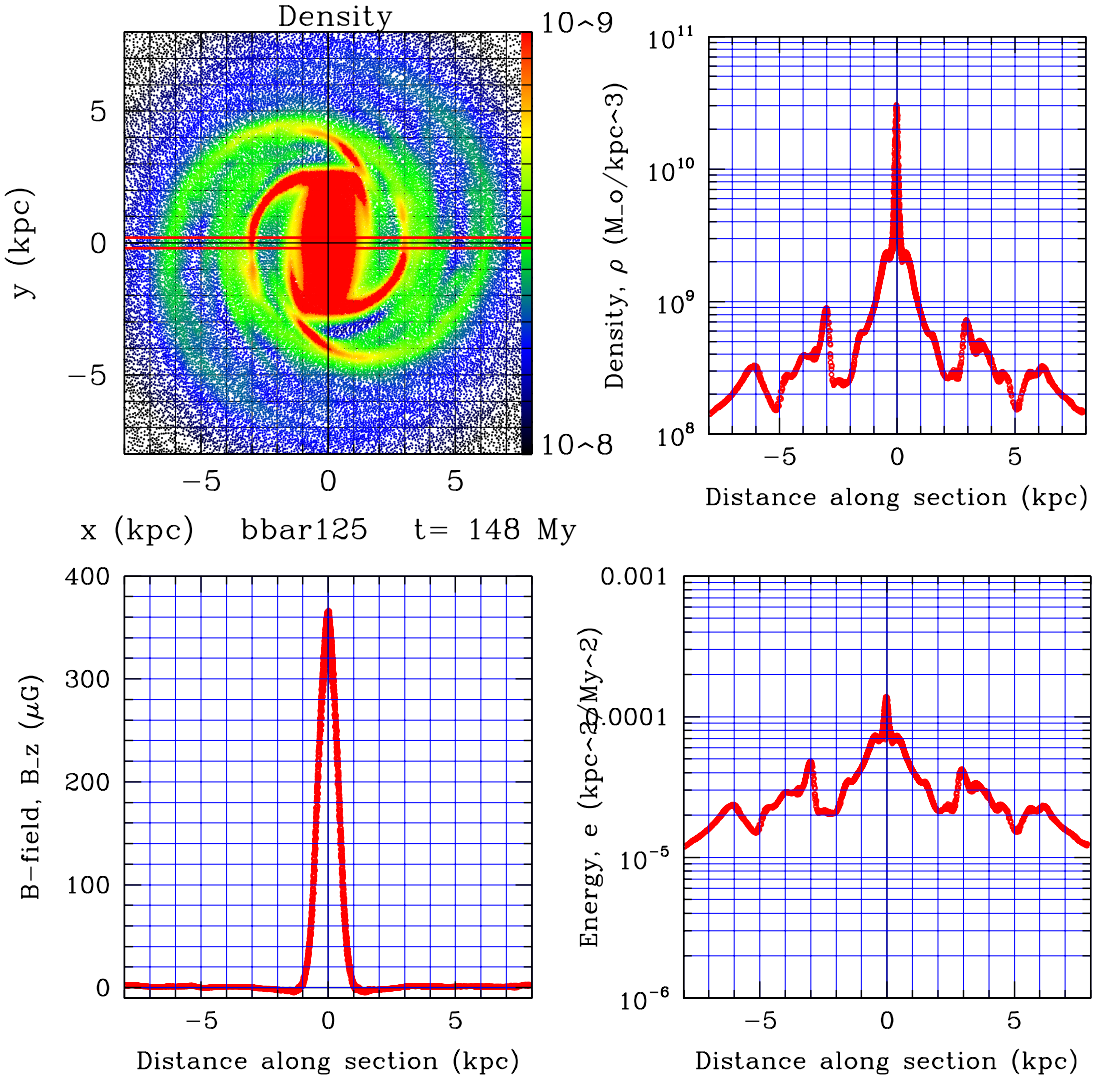

Figure 7.2: Cross section of results from the MHD simulation bbar125 at t = 148 My. The upper left plot shows a logarithmic color map of the density between 10^8 $M_\odot$ kpc^{-3} and 10^9 $M_\odot$ kpc^{-3}; note that the data has been rotated to align the major axis of the bar with the vertical axis of the plot. The cross section chosen is indicated on this plot as the strip within the two parallel red lines. Profiles of density (upper right), energy per unit mass (lower right), and vertical magnetic field (lower left) are shown.

Both simulations show the development of a four-armed trailing spiral structure induced by the central bar. Beyond 4 kpc, these spiral arms combine, leading to a two-armed spiral structure in the outer regions of the disk. This flow structure, although differing in fine detail, agrees qualitatively with previously published hydrodynamic studies [6, 67, 68].

The dense arms emanating from the central bar represent shocks in the fluid flow, as can be seen where the density and energy profiles cross two of these shocks around 3 kpc from the center. The non-axisymmetric gravitational potential of the central bar and the shocks induced by it lead to the outward transport of angular momentum; the ISM gradually falls towards the Galactic center, accumulating mass at the center. This increase in central mass is apparent in the density plot; the central density increases by an order of magnitude within the central half kiloparsec. As the ISM undergoes the gradual infall towards the Galactic center, it drags the frozen-in magnetic field along with it. Although the in-plane component of the magnetic field can be destroyed by resistivity as it is concentrated to small scales near the center (see Figure 7.6), the vertical component builds up. Although star formation provides a sink to remove the rapidly growing central density (and radiative cooling provides a sink for the thermal energy), no analogous sink exists for the vertical magnetic flux. This is demonstrated in the plot of the vertical magnetic field in Figure 7.2; the vertical magnetic flux builds to a large value in this central region.

Since the vertical magnetic field was initialized with a strength about an order of magnitude greater than the typically observed value of $B_z \sim 0.1\ \mu$G, the effect of the vertical flux accumulation in the center becomes dynamically significant

even in this short simulation. Comparing the density plots in Figure 7.1 and Figure 7.2, the MHD simulation (bbar125) develops small shoulders in the region between 0.3 kpc and 0.6 kpc; these shoulders are absent in the hydrodynamic runs (bar125). It appears that the strong vertical magnetic field in this central region enhances the angular momentum transport within the central kiloparsec, producing a greater infall of mass that builds small shoulders in the density profile.

7.3 Mass Inflow Rate

One of the key measures of the long-term Galactic dynamic evolution is the rate of the radial infall of mass. This rate of mass inflow has a great influence on the evolution of the mass distribution in the Galaxy. Whether the inferred strong central magnetic field in the Galaxy [134] contributes to an increased rate of mass flow towards the Galactic center has yet to be determined. Plotted in Figure 7.3 is a comparison of the mass inflow rate dM/dt vs. radius R for the hydrodynamic simulation (bar125—dashed line) and the MHD simulation (bbar125—solid line). Note that a negative value corresponds to mass flowing inward, a positive value to mass flowing outward. Results from both runs agree except for the central kiloparsec where the hydrodynamic rate is larger than the MHD rate. The mass inflow, however, is still dominated at this early point in the simulation by the transient effect of introducing the central bar potential over the initial bar pattern rotation time of 100 My. The regions of positive dM/dt, corresponding to outflow of mass, represent global adjustments to the bar potential. Only after these transient effects have settled down can a meaningful comparison of the hydrodynamic and

MHD mass inflow rates be made. Unfortunately, sufficient time was not available to complete simulations that reached this point in the disk evolution.

7.4 Longitude-Velocity Diagram

The Galactic gravitational potential is best probed through maps of the velocity field of the gas. Molecular emissions from H_I, CO, and CS provide maps of the line-of-sight velocity v_{los} with varying Galactic longitude l and latitude b. Projecting this data onto the l-v_{los} plane produces the longitude-velocity, or (l, v), diagram. Construction of the (l, v) diagram based on the results of a numerical model often provides a useful comparison with observational data.

Figure 7.4 presents the (l, v) diagram constructed from the MHD simulation bbar125 at $t = 148$ My. The diagram does reproduce the qualitative aspects of the observational (l, v) diagram, although the quantitative characteristic values of the diagram do not necessarily agree closely with observational values. A thorough examination of these differences will not be performed here for two reasons: first, the numerical results used to construct this plot are still affected by transient behavior from the introduction of the bar, so these results are only preliminary; and second, the aim of this project is to follow the magnetic evolution of the Galactic disk for which a Galactic model that is merely qualitatively correct is probably adequate.

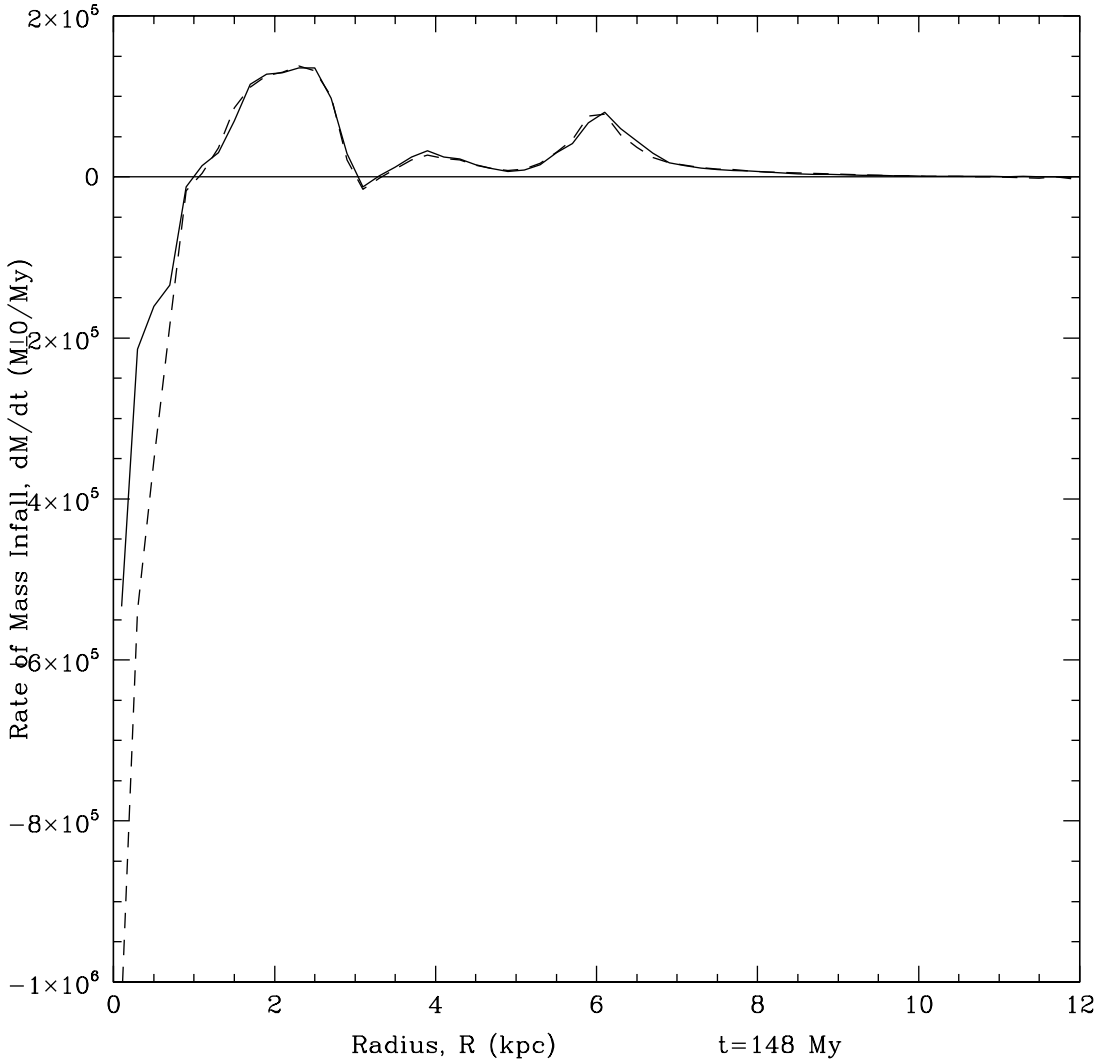

Figure 7.3: Mass inflow dM/dt ($M_\odot$/My) vs. radius R (kpc) for simulations bar125 (dashed) and bbar125 (solid) at time $t = 148$ My. A negative value corresponds to mass flowing inward, a positive value to mass flowing outward.

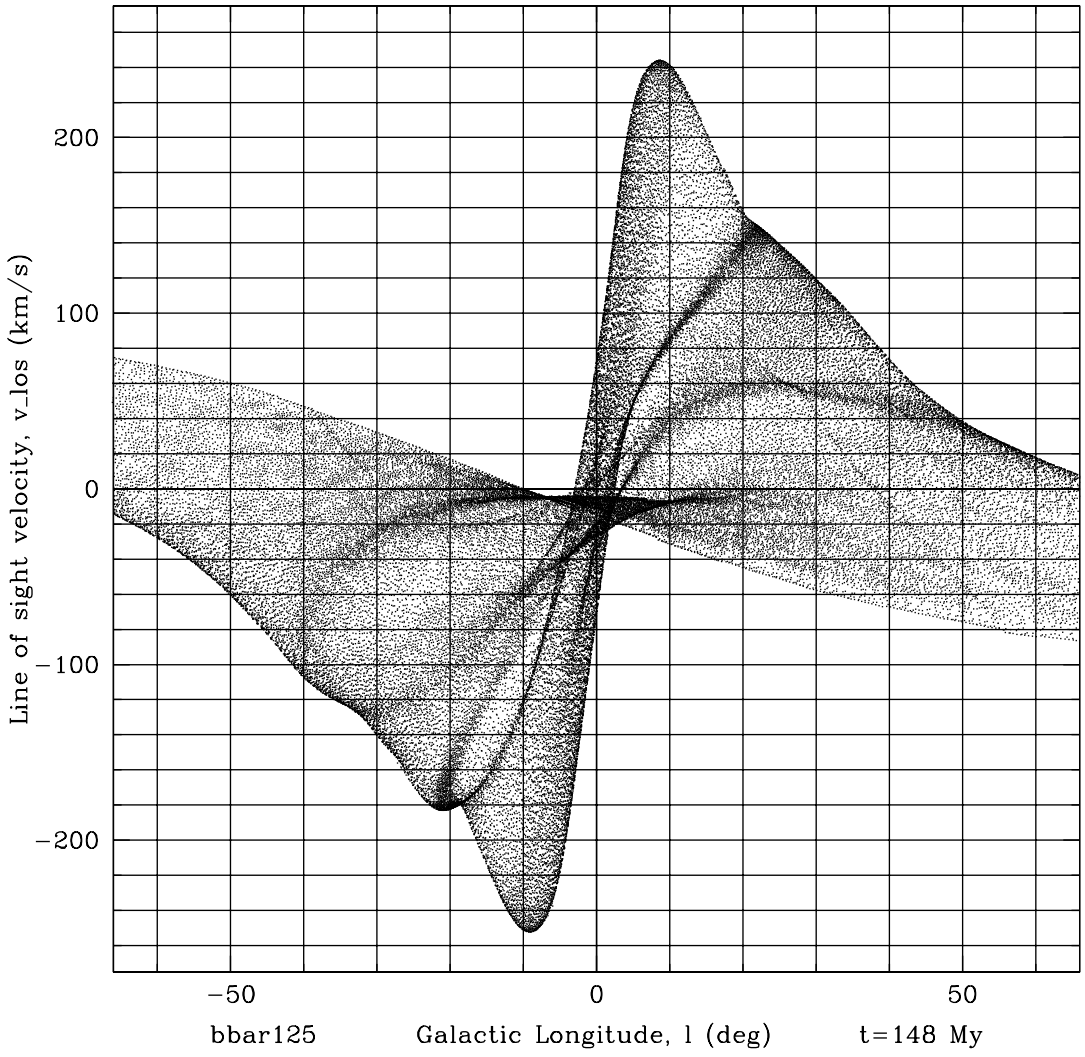

Figure 7.4: Longitude-velocity diagram of line-of-sight velocity v_{los} vs. Galactic longitude l for MHD simulation bbar125 at $t = 148$ My.

7.5 Magnetic Field Evolution

The initial magnetic field in the MHD simulation bbar125 is constant over the disk with components $B_x = 2$ μG and $B_z = 2$ μG. The differential rotation of the Galactic disk winds up the in-plane magnetic field into a roughly azimuthal field that reverses direction with radius. Figure 7.5 and Figure 7.6 present two plots of the in-plane magnetic field. Note that the plots presented in this section have not been rotated to align the major axis of the bar with the vertical plot axis. Figure 7.5 displays field vectors where vector length signifies magnitude and color distinguishes field direction (red for clockwise, $B_\phi < 0$; blue for counterclockwise, $B_\phi > 0$). Figure 7.6 displays a color map of magnetic field intensity; positive values correspond to a counterclockwise azimuthal component, negative values to a clockwise azimuthal component.

In the magnetic field vector plot of Figure 7.5, the magnetic field does indeed become nearly azimuthal with the direction reversing with radius, a bisymmetric spiral structure (BSS). In the center, the large resistive diffusion specified in this simulation begins to reconnect the field. The field in this central region is not amplified much because differential rotation is weak in the center. Resistive diffusion acting in this region tends to decrease the field strength, as demonstrated in the color map of intensity in Figure 7.6. Effectively, we are seeing the beginning of the process of flux expulsion [130]: through diffusion, the horizontal flux is expelled from the central region.

The evolution of the vertical magnetic flux, however, is dramatically different. The gradual flow of the ISM towards the Galactic center drags the magnetic field

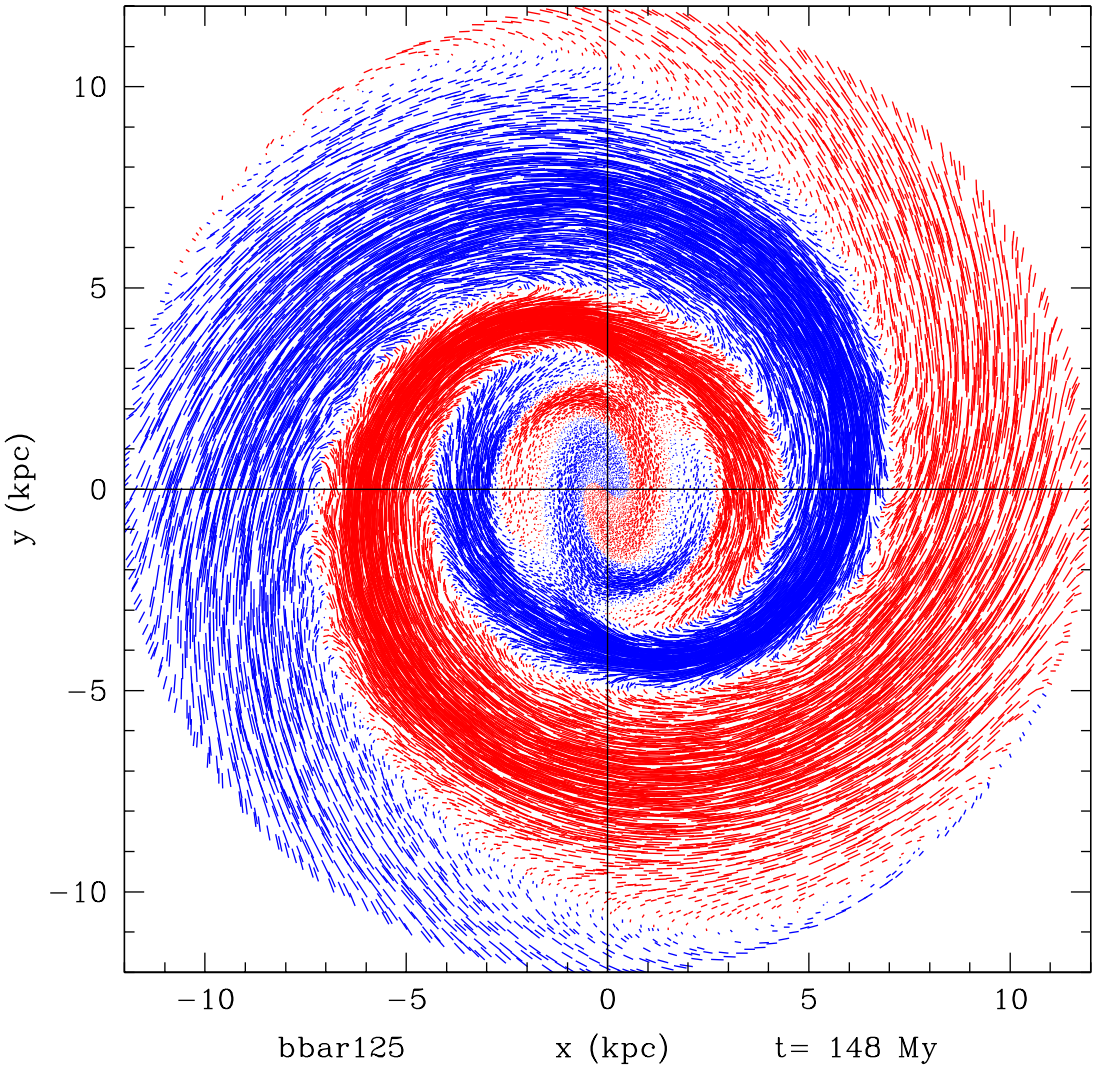

Figure 7.5: The magnetic field vectors are plotted for bbar125 at $t = 148$ My. Vector length corresponds to magnitude. The colors correspond to the sign of the azimuthal component, B_ϕ: red for $B_\phi < 0$, blue for $B_\phi > 0$.

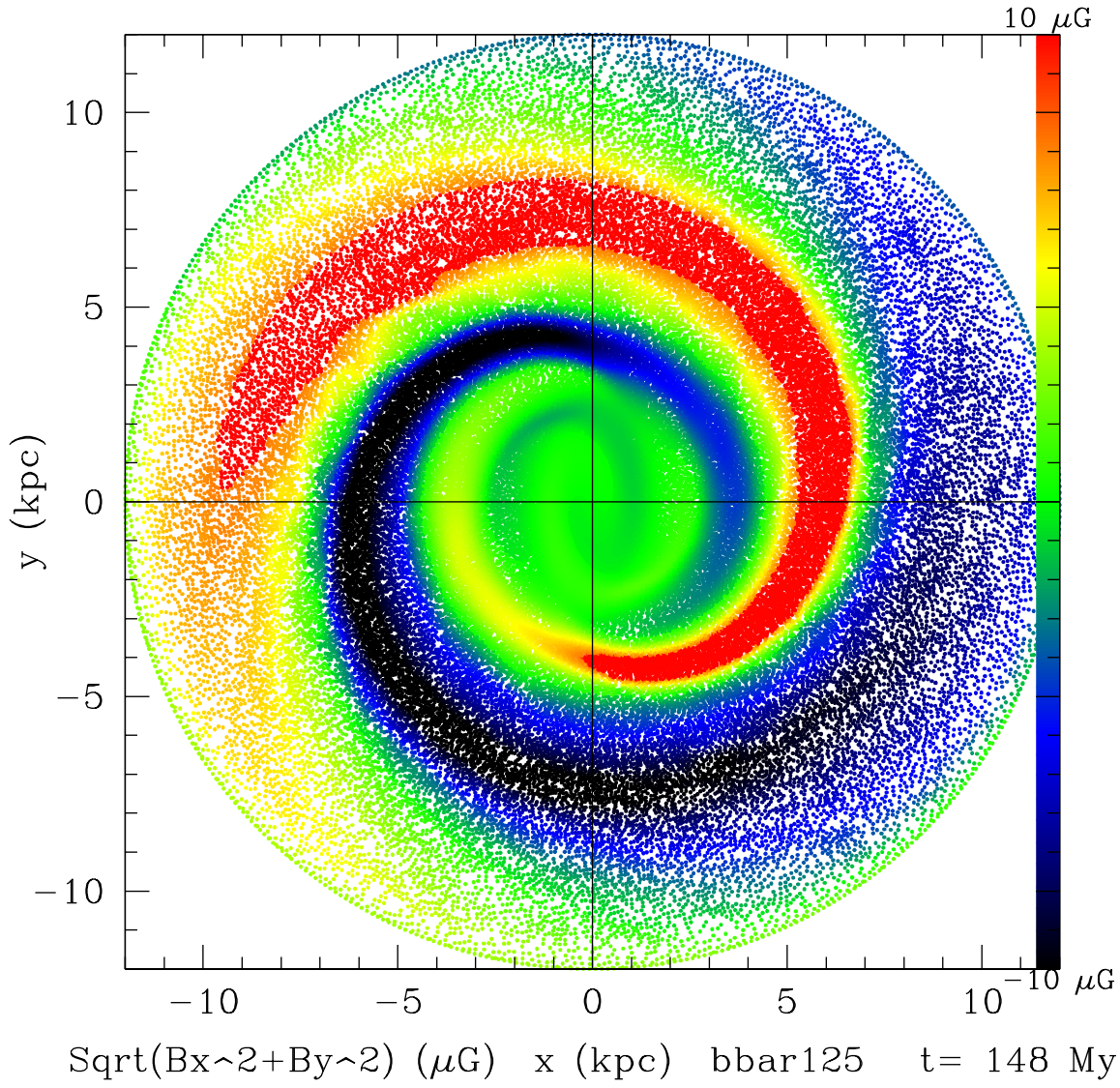

Figure 7.6: The magnitude of the in-plane component of the magnetic field, $\sqrt{B_x^2 + B_y^2}$, is plotted as a color map from -10 μG to 10 μG on a plan view of the Galactic disk. Negative values correspond to a negative (clockwise) azimuthal component, $B_\phi < 0$, while positive values correspond to a positive (counterclockwise) azimuthal component, $B_\phi > 0$.

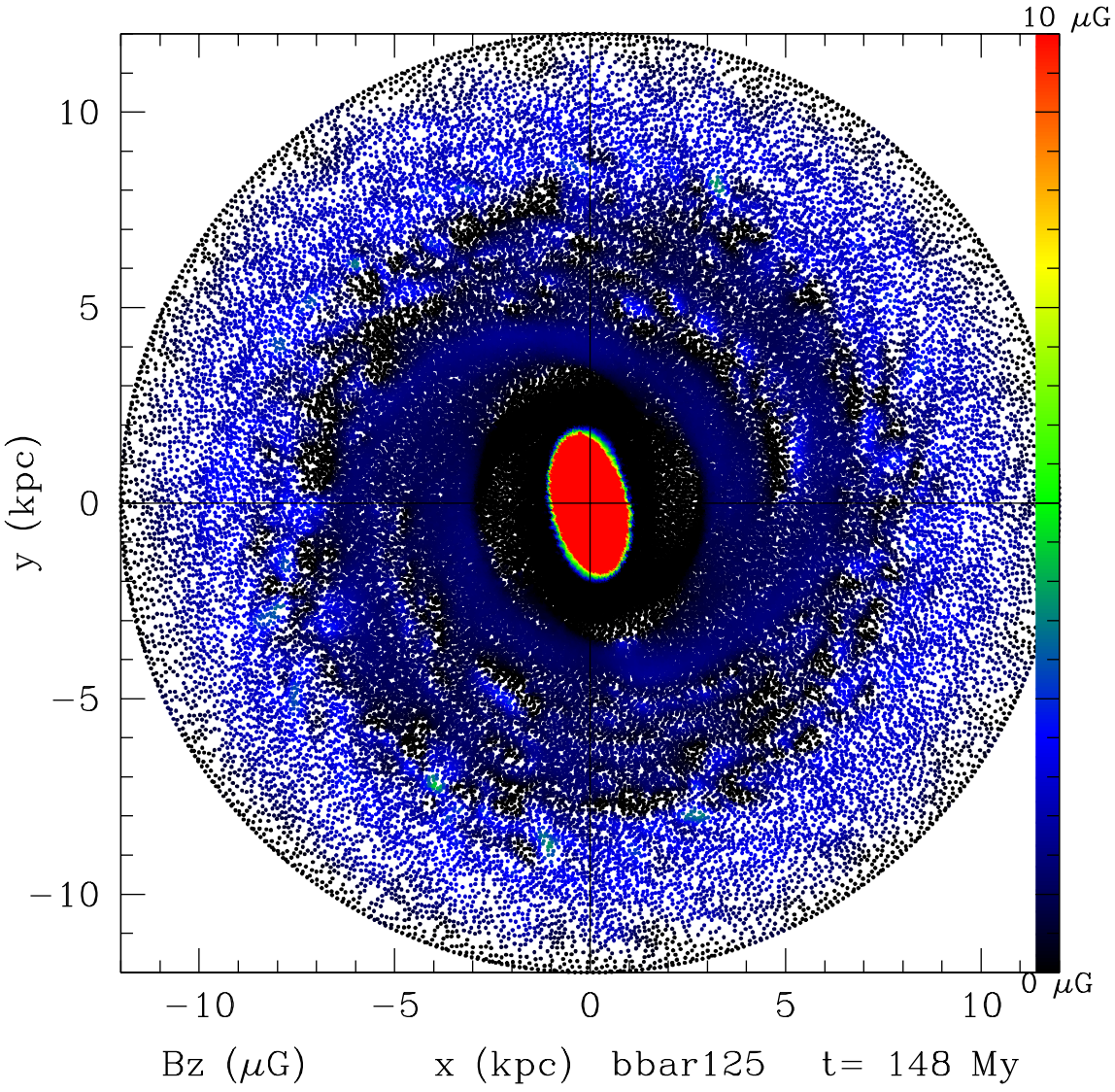

Figure 7.7: The magnitude of the vertical component of the magnetic field, B_z, is plotted as a color map from 0 μG–10 μG on a plan view of the Galactic disk.

along with it. The vertical magnetic flux accumulates in the Galactic center, as demonstrated in the lower left plot of Figure 7.2. A color map of the vertical magnetic field is shown in Figure 7.7, clearly demonstrating the strong accumulation of vertical flux in the central region. The vector potential method used in this simulation (see Section 3.4.1), however, suffers an overshoot problem in the vertical magnetic field. This can be seen where the vertical magnetic field dips below zero near the strong central peak in the lower left plot of Figure 7.2; it is also evident in Figure 7.7 in the black region around the central peak. Thus, although this simulation begins to produce the results we expect, it experiences unphysical numerical problems upon further integration. Implementation of the new technique using Lagrange multipliers to eliminate magnetic divergence is necessary to push these simulations further. Therefore, although the simulation bbar125 provides a taste of the magnetic evolution of the Galactic disk, conclusive results must wait for a more thorough suite of simulations conducted with refinements to the GPM method.

Chapter 8

Conclusion

This dissertation collects the effort to unravel the origin and understand the evolution of magnetic fields in the universe. Most of the work presented here focuses on the evolution of the magnetic field in the Galaxy as an important piece of the puzzle of astrophysical magnetism. In Chapter 1, the literature on the origin of astrophysical magnetism is reviewed with emphasis on tackling this problem within the broad framework of all forms of magnetism in the universe. Chapter 2 presents the results of an analytical investigation of the stability of a shear magnetic field in the presence of velocity shear. The new Gradient Particle Magnetohydrodynamics (GPM) algorithm for the MHD simulation of astrophysical systems is described in Chapter 3 and validation tests of this method are collected in Chapter 4. Adaptive Particle Refinement (APR), an adaptive framework for the GPM algorithm, is developed in Chapter 5 to tackle the challenges of astrophysical simulation in a generally adaptive manner. Chapter 6 describes a realistic Galactic model for 2-D and 3-D simulations aimed at modelling the evolution of the magnetic field in the Galactic disk. Finally, Chapter 7 analyzes the numerical results of hydrodynamic and MHD evolution of the Galactic disk using the GPM algorithm.

Although more work is required before conclusive results about the evolution of the Galactic magnetic field can be established, this dissertation demonstrates the potential of the GPM method developed here for astrophysical MHD simulation. Unfortunately, unforeseen obstacles in the development of this new computational tool consumed most of the time allocated to this project; little time remained to hone the Galactic disk simulation results. The preliminary Galactic disk simulations described in this chapter produce qualitatively similar results to those previously published in hydrodynamic studies. The two simulations described in this chapter detect the dynamic effect of the magnetic field in the central region of the Galactic disk where the vertical flux can accumulate to dynamically significant values. Plots of the mass inflow rate can help to characterize the long-term development of the Galactic mass distribution; construction of the longitude-velocity diagram for numerical results connects these simulations directly to constraints established by observation. Finally, the evolution of the magnetic field can be examined using the new GPM method to determine the effect of the dynamic flow of the ISM on the magnetic field topology and to pinpoint differences between hydrodynamic and MHD models. Future refinement of the GPM method, including incorporation of the APR framework for adaptivity, promises to yield greater insight into the magnetic evolution of the Galactic disk.

Appendix A

Analytical Investigation of Twisting Instability

A.1 Twisting Modes vs. Fourier Modes

In the sheared magnetic field, the local unstable modes can be written in two ways [158]; we call them twisting and Fourier modes. For the reader's convenience, we summarize the essence of the argument here. In the twisted field line coordinates, we obtain the twisted mode where a perturbed quantity $\Phi(x, y, z, t)$ is given by

$$\Phi_T = \overline{\Phi}_T(z, x)e^{iky'+\gamma t} = \overline{\Phi}_T(z, x)e^{iky-ik\frac{xz}{l_B}+\gamma t} \tag{A.1}$$

with $\overline{\Phi}_T$ localized in z and varying weakly in x compared to k^{-1}. But since the origin in z is arbitrary, we can also write

$$\Phi'_T = \overline{\Phi}_T(z - z_0, x)e^{iky-ik\frac{x(z-z_0)}{l_B}+\gamma t}. \tag{A.2}$$

Thus, there are an infinite number of twisting modes, each with a different origin of the twist. We can construct a mode that does not depend on z—a Fourier

mode—by integrating (A.2) over z_0

$$\Phi_F = \int_{-\infty}^{\infty} \Phi'_T(z - z_0, x, y, t) dz_0 = \overline{\Phi}_F \left(\frac{kx}{l_B}, x \right) e^{iky + \gamma t}, \tag{A.3}$$

where

$$\overline{\Phi}_F \left(\frac{kx}{l_B}, x \right) = \int_{-\infty}^{\infty} \overline{\Phi}_T(z', x) e^{-i \frac{kx}{l_B} z' dz'}. \tag{A.4}$$

Thus, the Fourier modes and the twisting modes are related by a Fourier transform. Clearly, the Fourier mode can be made by "adding" twisting modes together (see (A.3)), or vice versa, using the Fourier inversion theorem on (A.4); see Cowley et al. [56] for pictures of this superposition. The Fourier modes are narrowly localized in x—typically $\Delta x \sim \frac{\Delta x}{k \Delta z}$ where Δx is the x width of the Fourier mode and Δz is the z width of the twisting mode. Note this x localization of the Fourier mode is narrow compared to the x variation of the twisting mode. In this paper, we have taken the twisting mode representation for two reasons: first, the role of the flow, we believe, is more intuitive in this picture; and, second, the twisting modes are finite in z extent and therefore represent more easily the evolution of an initial value problem.

A.2 Asymptotic Analysis as $M \to 1$

To demonstrate stabilization as the Alfvén Mach number approaches one, as seen of region (II) of Figure 2.3, we perform an asymptotic analysis of our model in the limit $M \to 1$. For a small dimensionless parameter ϵ, we quantify the order of this limit as $1 - M \sim \mathcal{O}(\epsilon^2)$. We expect the instability growth rate to be $\gamma \sim \mathcal{O}(\epsilon)$. Identifying the terms in the dimensionless system of (2.26)–(2.28) for reference,

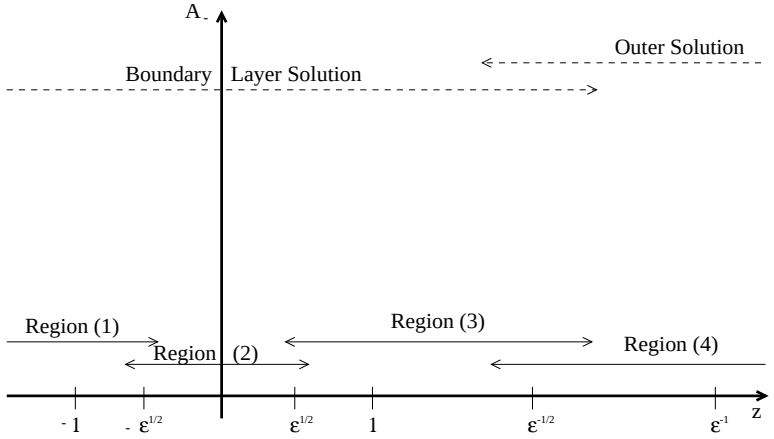

Figure A.1: Regions defined for the asymptotic solution of A_- in the limit $M \to 1$.

we have

$$\underset{(1)}{-(1-M)\tfrac{dA_+}{dz}} = \underset{(2)}{-\gamma A_+} \underset{(3)}{+(1+M)\tfrac{z}{1+z^2}A_-} \underset{(4)}{-\tfrac{s}{(1+z^2)^{1/2}}} \tag{A.5}$$

$$\underset{(5)}{(1+M)\tfrac{dA_-}{dz}} = \underset{(6)}{-\gamma A_-} \underset{(7)}{-(1-M)\tfrac{z}{1+z^2}A_+} \underset{(8)}{+\tfrac{s}{(1+z^2)^{1/2}}} \tag{A.6}$$

$$\underset{(9)}{M\tfrac{ds}{dz}} = \underset{(10)}{-\gamma s} \underset{(11)}{-\tfrac{s_0'}{2}\tfrac{A_+}{(1+z^2)^{1/2}}} \underset{(12)}{+\tfrac{s_0'}{2}\tfrac{A_-}{(1+z^2)^{1/2}}}. \tag{A.7}$$

The boundary conditions demand $A_+, A_-, s \to 0$ as $|z| \to \infty$. Asymptotic solutions in the $M \to 1$ limit can be found in the four regions along z displayed in Figure A.1. Below we find the solutions for each of these regions and, by matching the solutions between these regions, we obtain an eigenvalue condition on the growth rate demonstrating stabilization as the Alfvén Mach number approaches one. First, we obtain two reductions of (A.5)–(A.7); one over a boundary layer where $|z| \ll \epsilon^{-1}$, and the other over an outer region where $|z| \gg 1$. Then, we present the solutions in each of the four regions in Figure A.1.

As the Alfvén Mach number approaches one, regions (1), (2), and (3) of Figure A.1 behave like a boundary layer region: we expect derivatives to be large and thus take $\frac{d}{dz} \sim \mathcal{O}(\epsilon^{-1})$. We treat $z \sim \mathcal{O}(1)$ over these three regions. Balance of the dominant terms (9) and (11) in (A.7) shows that $s \sim \mathcal{O}(\epsilon A_+)$. In turn, this demands that terms (5) and (8) must balance in (A.6), yielding the ordering $A_- \sim \mathcal{O}(\epsilon^2 A_+)$. Adopting the specified ordering allows us to drop terms (6), (7), (10), and (12) from (A.5)–(A.7); term (3), although one order in ϵ smaller than the other terms in (A.5), will contribute in the regions for $z > 1$, so we retain it in order to be certain that our first order correction in region (3) is valid. The remaining equations can be combined to a single third-order equation in A_- and simplified by the substitution $z = \sinh\theta$ to obtain

$$\frac{2M(1-M)}{s_0'}\frac{d^3A_-}{d\theta^3} - \frac{2\gamma M}{s_0'}\cosh\theta\frac{d^2A_-}{d\theta^2} + \frac{dA_-}{d\theta} - \tanh\theta A_- = 0. \tag{A.8}$$

In region (4), we find the smoothly varying outer solution over which $z \sim \mathcal{O}(\epsilon^{-1})$. We expect that $\frac{d}{dz} \sim \mathcal{O}(\epsilon)$ here. By insisting that terms (9) and (10) balance with term (11) in (A.7), we find that $s \sim \mathcal{O}(A_+)$. Similarly, by balancing terms (5) and (6) with term (8) in (A.6), we obtain $A_- \sim \mathcal{O}(A_+)$. This ordering allows us to drop terms (1) and (7) in (A.5)–(A.7). Approximating $(1+z^2)^{1/2} \simeq z$, substituting $A_- = zB_-$, and combining the equations, we obtain the second-order equation

$$\begin{aligned} M(1+M)z^2\frac{d^2B_-}{dz^2} &+ \left[(1+2M)\gamma z^2 + 3M(1+M)z - \tfrac{(1+M)s_0'}{2\gamma}\right]\tfrac{dB_-}{dz} \\ &+ \left[\gamma^2 z^2 + (1+3M)\gamma z + M(1+M) - s_0'\right]B_- = 0. \end{aligned} \tag{A.9}$$

To find the solution in region (1), we assume an eikonal solution for (A.8). Neglecting the trivial constant solution, we find two independent solutions of the

form

$$A_- \sim \frac{1}{(1+z^2)^{3/4}\left[(1+z^2)^{1/2}+z\right]^{1/2}} \exp\left(\frac{\gamma}{2(1-M)}\left[z+(1+z^2)^{1/2}\right]\right) \quad \text{(A.10)}$$

$$A_- \sim \frac{z+(1+z^2)^{1/2}}{(1+z^2)^{1/2}} \exp\left(\frac{\gamma}{2(1-M)}\left[z-(1+z^2)^{1/2}\right]+z\left[z-(1+z^2)^{1/2}\right]\right). \quad \text{(A.11)}$$

To get the behavior for $|z| \gg 1$, we can expand $(1+z^2)^{1/2} \simeq |z| + 1/2|z|$. For region (1), we note that $z < 0$ and, retaining only the dominant terms, we obtain solutions of the form

$$A_- \sim \frac{1}{z} \exp\left(\frac{-\gamma}{4(1-M)z}\right) \quad \text{(A.12)}$$

$$A_- \sim \frac{1}{z^2} \exp\left(\frac{\gamma z}{1-M}\right). \quad \text{(A.13)}$$

The boundary conditions impose that $A_- \to 0$ as $z \to -\infty$, so our solution in region (1) must be entirely of the form of (A.13), a growing solution in the $+z$ direction. To determine the behavior of (A.10) and (A.11) in the overlap with region (2), we take the limit $|z| \ll 1$ and approximate $(1+z^2)^{1/2} \simeq 1 + z^2/2$ to get the two solutions

$$A_- \sim \exp\left(\frac{\gamma}{2(1-M)}\left[z+z^2/2\right]\right) \quad \text{(A.14)}$$

$$A_- \sim \exp\left(\frac{\gamma}{2(1-M)}\left[z-z^2/2\right]\right). \quad \text{(A.15)}$$

One of these solutions must smoothly match onto the solution for region (2).

Region (1)'s solution will be valid as we move in the $+z$ direction until the eikonal approximation, $\frac{\gamma z}{1-M} \gg 1$, breaks down. The failure of this condition occurs in region (2) of Figure A.1 where $z \sim \mathcal{O}(\epsilon)$. For region (2), we expand

(A.8) about $z = 0$. For $z \ll 1$, $\cosh\theta \simeq 1$ and $\tanh\theta \simeq \theta$ where $\theta \ll 1$, so we can drop the last term of (A.8). Letting $f = \frac{dA_-}{d\theta}$ and using the integrating factor $f = B_- \exp\left(\frac{\gamma \sinh\theta}{2(1-M)}\right)$ to simplify the result, we obtain the equation

$$\frac{d^2 B_-}{d\theta^2} - \left[\frac{\gamma^2 \cosh^2\theta}{4(1-M)^2} - \frac{\gamma \sinh\theta}{2(1-M)} - \frac{s_0'}{2M(1-M)}\right] B_- = 0. \tag{A.16}$$

Neglecting the central term in the coefficient of B_- because it is an order ϵ smaller than the other terms, we can cast (A.16) in the form of Hermite's equation for which the solutions are well known. Therefore, for the $n = 0$ Hermite polynomial, the solution in region (2) is

$$A_- \sim \int^z \exp\left(\frac{\gamma}{2(1-M)}(z' - z'^2/2)\right) dz', \tag{A.17}$$

and the eigenvalue condition on the growth rate imposed by Hermite's equation is

$$\gamma^2 = \frac{2s_0'(1-M)}{M} - 2(2n+1)\gamma(1-M) \tag{A.18}$$

for the nth Hermite polynomial. Thus, we find that the solution in region (1) given by (A.15) matches smoothly onto our solution in region (2).

In region (3), we once again assume an eikonal solution for (A.8) and find the two solutions given by (A.10) and (A.11). To match with region (2), find the $|z| \ll 1$ limit of these equations, yielding once more (A.14) and (A.15); we observe that (A.15) for the small z limit of region (3) matches (A.17) for region (2). In the $|z| \gg 1$ limit of eqrefeq:a-1a and (A.11) for region (3), we obtain the solutions (for $z > 0$)

$$A_- \sim \frac{1}{z^2} \exp\left(\frac{\gamma z}{1-M}\right) \tag{A.19}$$

$$A_- \sim \exp\left(\frac{-\gamma}{4(1-M)z}\right). \tag{A.20}$$

To continue our asymptotic solution, we must smoothly match one of these region (3) solutions to the solution for region (4) in the overlap around $z \sim \mathcal{O}(\epsilon^{-1/2})$.

In region (4), we assume eikonal solutions for (A.9) in the limit $z \to 0$. The two solutions found are

$$A_- \sim z \tag{A.21}$$

$$A_- \sim \exp\left(\frac{-s_0'}{2\gamma M z}\right). \tag{A.22}$$

Hence, we can match the solution given by (A.20) in region (3) with the solution given by (A.22) in region (4) if

$$\frac{\gamma}{4(1-M)} = \frac{s_0'}{2\gamma M}. \tag{A.23}$$

But, this is identical to the lowest order of the eigenvalue condition, (A.18). To complete our asymptotic solution, we must find that a solution to (A.9) in the limit $z \to \infty$ which satisfies the boundary condition that $A_- \to 0$ as $z \to \infty$. In this limit, the two solutions take the form

$$A_- \sim \exp\left(\frac{-\gamma z}{M}\right) \tag{A.24}$$

$$A_- \sim \exp\left(\frac{-\gamma z}{1+M}\right). \tag{A.25}$$

Both of these solutions satisfy the boundary condition as $z \to \infty$.

Now that we have seen that it is possible to construct a complete asymptotic solution in the limit $M \to 1$, let us examine this solution more closely. Beginning in region (1) at the left of Figure A.1, the boundary conditions demand that the

solution must be solely of the form of (A.13). But, as behavior in regions (1), (2), and (3) is governed by (A.8), the eikonal approximation must break down in region (2) in order for the solution in region (1) to convert to the solution given by (A.20) in region (3) so that smooth matching may be accomplished with (A.22) in region (4). The failure of the eikonal approximation around $z = 0$ yields a reduction of (A.8) to the Hermite-type (A.16). The requirement that a solution to this equation exist imposes the eigenvalue condition, (A.18). This single condition can also be used to smoothly match (A.20) in region (3) to (A.22) in region (4). Finally, region (4) is governed by (A.9). In the limit $z \to 0$, this equation yields a matching solution in the overlap with region (3); and, in the limit $z \to \infty$, it provides two solutions which both satisfy the boundary conditions as $z \to \infty$. Therefore, the single condition necessary to find a smooth solution which satisfies the boundary conditions is the eigenvalue condition, (A.18). To lowest order, this condition can be written in a more recognizable form in the limit $M \to 1$ as

$$\gamma^2 \simeq s_0'(1 - M^2). \tag{A.26}$$

Thus, in region (II) of Figure 2.3, where $\gamma \gg 1 - M$, the behavior is clearly demonstrated—that stabilization occurs as the Alfvén Mach number approaches one.

Appendix B

Alternative Form of the GPM Algorithm

Alternative forms of the GPM formulae for the mean, gradient, and higher-order derivatives provide a more transparent understanding of just how the GPM algorithm calculates these quantities and simplify the task of proving computational stability and convergence. For first-order GPM in one dimension, these forms can be derived by inverting the matrix in (3.9) to solve for A_0 and A_1 and employing the summation formula

$$\left(\sum_{i=1}^{N} A_i\right)\left(\sum_{j=1}^{N} B_j\right) = \sum_{i=1}^{N} A_i B_i + \sum_{i=1}^{N-1}\sum_{j>i}^{N} (A_i B_j + A_j B_i) \tag{B.1}$$

to simplify the result. Following this procedure, the mean and gradient of q for an arbitrary particle distribution can be written as

$$q_{GPM}(x) = \frac{\sum_{i=1}^{N-1}\sum_{j>i}^{N} m_i m_j \left[q_i - \left(\frac{q_i - q_j}{x_i - x_j}\right)(x_i - x)\right](x_i - x_j)^2 W_i W_j}{\sum_{i=1}^{N-1}\sum_{j>i}^{N} m_i m_j (x_i - x_j)^2 W_i W_j} \tag{B.2}$$

$$\frac{dq(x)}{dx}_{GPM} = \frac{\sum_{i=1}^{N-1}\sum_{j>i}^{N} m_i m_j \left[\frac{q_i - q_j}{x_i - x_j}\right](x_i - x_j)^2 W_i W_j}{\sum_{i=1}^{N-1}\sum_{j>i}^{N} m_i m_j (x_i - x_j)^2 W_i W_j} \tag{B.3}$$

where we use the abbreviation $W_i = W(|x_i - x|, h)$ and the sum is over the N neighbor particles. We interpret the evaluation of the mean and gradient of q by one-dimensional, first-order GPM as a weighted sum for all possible pairs of neighbor particles. We define the two-point weighting function

$$W_{ij}(x_i - x, x_j - x, h) = m_i m_j (x_i - x_j)^2 W(|x_i - x|, h) W(|x_j - x|, h). \qquad \text{(B.4)}$$

The GPM mean evaluation sums the gradient-corrected mean weighted by W_{ij} for all possible pairs of neighbor particles; the gradient evaluation likewise finds the weighted sum of first derivatives calculated by each pair.

For the second-order GPM algorithm in one dimension, a similar procedure to that presented for the first-order case can be followed to yield, after considerable algebra,

$$< q(x) >= \frac{1}{D_1} \sum_{i=1}^{N-1} \sum_{j>i}^{N} \sum_{k=1}^{N-1} \sum_{l>k}^{N} \left[\frac{(\overline{q}_{kl} x_{ij} \tilde{x}_{ij} - \overline{q}_{ij} x_{kl} \tilde{x}_{kl})}{x_{ij} x_{kl} (\overline{x}_{ij} - \overline{x}_{kl})} \right] W_{ijkl} \qquad \text{(B.5)}$$

$$< \frac{dq(x)}{dx} >= \frac{1}{D_2} \sum_{i=1}^{N-1} \sum_{j>i}^{N} \sum_{k=1}^{N-1} \sum_{l>k}^{N} \left[\frac{(q_{kl} x_{ij} \overline{x}_{ij} - q_{ij} x_{kl} \overline{x}_{kl})}{x_{ij} x_{kl} (\overline{x}_{ij} - \overline{x}_{kl})} \right] W_{ijkl} \qquad \text{(B.6)}$$

$$< \frac{d^2 q(x)}{dx^2} >= \frac{1}{D_2} \sum_{i=1}^{N-1} \sum_{j>i}^{N} \sum_{k=1}^{N-1} \sum_{l>k}^{N} \left[\frac{2(q_{ij} x_{kl} - q_{kl} x_{ij})}{x_{ij} x_{kl} (\overline{x}_{ij} - \overline{x}_{kl})} \right] W_{ijkl} \qquad \text{(B.7)}$$

with the denominator terms given by

$$D_1 = \sum_{i=1}^{N-1} \sum_{j>i}^{N} \sum_{k=1}^{N-1} \sum_{l>k}^{N} \left[\frac{\tilde{x}_{ij} - \tilde{x}_{kl}}{\overline{x}_{ij} - \overline{x}_{kl}} \right] W_{ijkl}$$

$$D_2 = \sum_{i=1}^{N-1} \sum_{j>i}^{N} \sum_{k=1}^{N-1} \sum_{l>k}^{N} W_{ijkl}.$$

We have defined a four point weighting function

$$W_{ijkl}(x_i, x_j, x_k, x_l, h) = m_i m_j m_k m_l x_{ij}^2 x_{kl}^2 (\overline{x}_{ij} - \overline{x}_{kl})(\tilde{x}_{ij} - \tilde{x}_{kl}) W_i W_j W_k W_l \quad \text{(B.8)}$$

and used the following abbreviations

$$\begin{aligned} x_{ij} &= x_i - x_j \\ \overline{x}_{ij} &= (x_i - x) + (x_j - x) \\ \tilde{x}_{ij} &= (x_i - x)(x_j - x) \\ q_{ij} &= q_i - q_j \\ \overline{q}_{ij} &= q_j(x_i - x) - q_i(x_j - x). \end{aligned}$$

Appendix C

Linear Polynomial Regression and GPM

The GPM algorithm for the determination of gradient information is nearly identical to the solution for a weighted least squares regression problem using a local polynomial fit. Expressed in the statistical terminology of Fan and Gijbels [69], for a set of n data $(X_1, Y_1), \ldots, (X_n, Y_n)$ we can estimate a regression function $m(x)$ using a polynomial of order p given by a Taylor expansion around the point x_0

$$m(x) = \sum_{j=0}^{p} \beta_j (x - x_0)^j. \tag{C.1}$$

The least squares regression problem seeks to minimize

$$\sum_{i=1}^{n} \left\{ Y_i - \sum_{j=0}^{p} \beta_j (X_i - x_0)^j \right\}^2 K_h(X_i - x_0) \tag{C.2}$$

with respect to all β_j. Here $K_h(t) = K(t/h)/h$ where K is a symmetric kernel function to locally weight each datum point. If $\hat{\beta}_j, j = 0, \ldots, p$ is the solution to the least squares problem, it is clear that the νth derivative $m^{(\nu)}(x_0)$ is estimated by $\hat{m}_\nu(x_0) = \nu! \hat{\beta}_j$.

Matrix notation most clearly demonstrates the relationship between the GPM algorithm and weighted least squares theory. The weighted least squares problem given by (C.2) can be written as

$$\min_{\beta}(\mathbf{y}-\mathbf{X}\beta)^{\mathbf{T}}\mathbf{W}(\mathbf{y}-\mathbf{X}\beta). \tag{C.3}$$

Here $\mathbf{X}$ is the $n \times p$ design matrix of the problem given by

$$\mathbf{X} = \begin{pmatrix} 1 & (X_1 - x_0) & \cdots & (X_1 - x_0)^p \\ \vdots & \vdots & & \vdots \\ 1 & (X_n - x_0) & \cdots & (X_n - x_0)^p \end{pmatrix}, \tag{C.4}$$

and the $n \times n$ diagonal matrix of weights is

$$\mathbf{W} = \mathrm{diag}\{\mathbf{K_h}(\mathbf{X_i} - \mathbf{x_0})\}. \tag{C.5}$$

The vectors of the data and polynomial coefficients are $\mathbf{y} = (\mathbf{Y_1} \cdots \mathbf{Y_n})^{\mathbf{T}}$ and $\beta = (\beta_0 \cdots \beta_p)^T$. Weighted least squares theory gives the solution vector

$$\hat{\beta} = (\mathbf{X^T W X})^{-1}\mathbf{X^T W y}. \tag{C.6}$$

If equation (3.9) of the GPM prescription is written in matrix notation as $\mathbf{Q} = \mathbf{SA}$, it can be easily shown for $p = 1$ that

$$\mathbf{Q} = \mathbf{X^T W y}, \quad \mathbf{A} = \hat{\beta}, \quad \mathbf{S} = \mathbf{X^T W X}. \tag{C.7}$$

Local polynomial regression and the GPM formulation are the same except that GPM includes a mass m_i for each particle to allow a variation of weighting among particles.

Appendix D

Magnetic Divergence Control using Lagrange Multipliers

D.1 First Order

We choose to minimize the sum of the weighted squared differences at each neighbor particle with the divergence of magnetic field constraint added in as a Lagrange multiplier. We will minimize the function χ with respect to each of the coefficients of the polynomial fit, A^j_α,

$$\chi = \sum_{i=1}^{N}\sum_{j=1}^{D}\left[\sum_{\alpha=0}^{D} A^j_\alpha(\mathbf{x_0})(\mathbf{x_{i\alpha}} - \mathbf{x_{0\alpha}}) - \mathbf{B^j}(\mathbf{x_i})\right]^2 W(\mathbf{x_i}, \mathbf{h}) + \mathbf{2}\lambda\sum_{\mathbf{j=1}}^{\mathbf{D}}\mathbf{A^j_j}(\mathbf{x_0}) \quad \text{(D.1)}$$

Here we take the coefficients of the polynomial fit,

$$A^j_\alpha = \frac{\partial B^j}{\partial x_\alpha} \quad \text{(D.2)}$$

where the number of dimensions in the problem is D, the number of neighbors in the smoothing sphere is N, $j = 1, 2, \ldots, D$, $\alpha = 0, 1, 2, \ldots, D$. The vector component of the magnetic field is written with the component index as a superscript,

$B^j \equiv B_j$, to maintain consistency with the notation of the $(D+1)$ element vectors $\mathbf{A^j}$, $\mathbf{b^j}$, and $\mathbf{u^j}$.

It is understood that

$$\mathbf{x^T} = (\mathbf{1}, \mathbf{x}, \mathbf{y}, \mathbf{z}) \tag{D.3}$$

and

$$\left(\frac{\partial}{\partial \mathbf{x}}\right)^T = \left(1, \frac{\partial}{\partial x}, \frac{\partial}{\partial y}, \frac{\partial}{\partial z}\right) \tag{D.4}$$

As well, the position about which the least squares fit is centered is given by $\mathbf{x_0}$, where the component $x_{00} = 0$.

Setting the derivatives $\partial\chi/\partial A^j_\alpha = 0$ gives the set of equations

$$\sum_{i=1}^{N}\sum_{\beta=0}^{D} A^j_\beta(\mathbf{x_0})(\mathbf{x_{i\beta}}-\mathbf{x_{0\beta}})(\mathbf{x_{i\alpha}}-\mathbf{x_{0\alpha}})\mathbf{W}(\mathbf{x_i},\mathbf{h}) = \sum_{\mathbf{i=1}}^{\mathbf{N}} \mathbf{B^j}(\mathbf{x_i})(\mathbf{x_{i\alpha}}-\mathbf{x_{0\alpha}})\mathbf{W}(\mathbf{x_i},\mathbf{h}) - \lambda\delta_{\mathbf{j}\alpha} \tag{D.5}$$

for the values $j = 1, 2, \ldots, D$ and $\alpha = 0, 1, 2, \ldots, D$.

For a given j, we can write this in matrix form

$$\mathbf{M}\cdot\mathbf{A^j} = \mathbf{b^j} - \lambda\mathbf{u^j} \tag{D.6}$$

where $\mathbf{M}$ is a $(D+1)\times(D+1)$ matrix with elements given by

$$M_{\alpha\beta} = \sum_{i=1}^{N}(x_{i\alpha} - x_{0\alpha})(x_{i\beta} - x_{0\beta})W(\mathbf{x_i},\mathbf{h}) \tag{D.7}$$

and $\mathbf{b^j}$ is a $(D+1)$-element vector with elements

$$b^j_\alpha = \sum_{i=1}^{N} B^j(\mathbf{x_i})(\mathbf{x_{i\alpha}} - \mathbf{x_{0\alpha}})\mathbf{W}(\mathbf{x_i},\mathbf{h}) \tag{D.8}$$

and $\mathbf{u^j}$ is a $(D+1)$-element unit vector of all zeros with the value 1 in the jth place.

The solution for the coefficients $\mathbf{A^j}$ is found by inverting the matrix M giving

$$\mathbf{A^j} = \mathbf{M^{-1}} \cdot \mathbf{b^j} - \lambda \mathbf{M^{-1}} \cdot \mathbf{u^j} \tag{D.9}$$

where $\mathbf{A^j}$ depends on the as yet unknown Lagrange Multiplier λ. Each element of this solution can be written in summation form as

$$A^j_\alpha = \sum_{\beta=0}^{D} M^{-1}_{\alpha\beta} b^j_\beta - \lambda \sum_{\beta=0}^{D} M^{-1}_{\alpha\beta} u^j_\beta \tag{D.10}$$

Note that the definition of the unit vector $\mathbf{u^j}$ means that the βth component of the unit vector can be represented in summation form by the Kronecker Delta such that $u^j_\beta = \delta_{\beta j}$. This enables us to eliminate the sum over the index β by

$$\sum_{\beta=0}^{D} M^{-1}_{\alpha\beta} u^j_\beta = \sum_{\beta=0}^{D} M^{-1}_{\alpha\beta} \delta_{\beta j} = M^{-1}_{\alpha j}, \tag{D.11}$$

leaving us with the equation

$$A^j_\alpha = \sum_{\beta=0}^{D} M^{-1}_{\alpha\beta} b^j_\beta - \lambda M^{-1}_{\alpha j} \tag{D.12}$$

The constraint for zero magnetic divergence that is incorporated using the Lagrange Multiplier can be written

$$\sum_{j=1}^{D} A^j_j(\mathbf{x_0}) = \mathbf{0} \tag{D.13}$$

Substituting in the solutions for A^j_α as a function of λ allows us to solve for the unknown λ, giving

$$\lambda = \frac{\sum_{j=1}^{D} \sum_{\beta=0}^{D} M^{-1}_{j\beta} b^j_\beta}{\sum_{j=1}^{D} M^{-1}_{jj}} \tag{D.14}$$

Plugging this solution back into the equation for A^j_α gives the final answer

$$A^j_\alpha = \sum_{\beta=0}^{D} M^{-1}_{\alpha\beta} b^j_\beta - \left(\frac{\sum_{k=1}^{D} \sum_{\beta=0}^{D} M^{-1}_{k\beta} b^k_\beta}{\sum_{k=1}^{D} M^{-1}_{kk}} \right) \sum_{\beta=0}^{D} M^{-1}_{\alpha j} \tag{D.15}$$

for each value of $\alpha = 0, 1, \ldots, D$. Cast in the form of a matrix equation,

$$\mathbf{A^j} = \mathbf{M^{-1}} \cdot \mathbf{b^j} - \left(\frac{\sum_{\mathbf{k=1}}^{\mathbf{D}} (\mathbf{M^{-1}} \cdot \mathbf{b^k})_\mathbf{k}}{\sum_{\mathbf{k=1}}^{\mathbf{D}} \mathbf{M^{-1}_{kk}}} \right) \mathbf{M^{-1}_{(j)}} \tag{D.16}$$

where $\mathbf{M^{-1}_{(j)}}$ denotes the jth column of the $(D+1) \times (D+1)$ matrix $\mathbf{M^{-1}}$.

D.2 Second Order

For a second order fit, the function χ that we wish to minimize is given by

$$\begin{gathered} \chi = \sum_{i=1}^{N} \sum_{j=1}^{D} \left[\sum_{\alpha=0}^{D} \sum_{\beta \geq \alpha}^{D} A^j_{(\alpha\beta)}(\mathbf{x_0})(\mathbf{x_{i\alpha}} - \mathbf{x_{0\alpha}})(\mathbf{x_{i\beta}} - \mathbf{x_{0\beta}}) - \mathbf{B^j}(\mathbf{x_i}) \right]^2 W(\mathbf{x_i}, \mathbf{h}) \\ +2 \sum_{\alpha=0}^{D} \lambda_\alpha \sum_{j=1}^{D} (1 + \delta_{\alpha j}) A^j_{(\alpha j)}(\mathbf{x_0}) \end{gathered} \tag{D.17}$$

We define the coefficients of the second-order polynomial fit by

$$A^j_{(\alpha\beta)} = \frac{\partial^2 B_j}{\partial x_\alpha \partial x_\beta} \tag{D.18}$$

Setting the derivatives $\partial\chi / \partial A^j_{\alpha\beta} = 0$ yields the set of equations

$$\begin{gathered} \sum_{i=1}^{N} \sum_{\gamma=0}^{D} \sum_{\delta \geq \gamma}^{D} A^j_{\gamma\delta}(\mathbf{x_0})(\mathbf{x_{i\gamma}} - \mathbf{x_{0\gamma}})(\mathbf{x_{i\delta}} - \mathbf{x_{0\delta}})(\mathbf{x_{i\alpha}} - \mathbf{x_{0\alpha}})(\mathbf{x_{i\beta}} - \mathbf{x_{0\beta}}) \mathbf{W}(\mathbf{x_i}, \mathbf{h}) = \\ \sum_{i=1}^{N} B^j(\mathbf{x_i})(\mathbf{x_{i\alpha}} - \mathbf{x_{0\alpha}})(\mathbf{x_{i\beta}} - \mathbf{x_{0\beta}}) \mathbf{W}(\mathbf{x_i}, \mathbf{h}) - \sum_{\mathbf{\gamma=0}}^{\mathbf{D}} \lambda_\gamma \delta_{\mathbf{j}\beta} (\mathbf{1} + \delta_{\gamma \mathbf{j}}) \end{gathered} \tag{D.19}$$

for the values $j = 1, 2, \ldots, D$, $\alpha = 0, 1, 2, \ldots, D$, and $\beta = \alpha, \alpha + 1, \ldots, D$.

For a given j, we have a system of M linear equations, where $M = \sum_{\mu=0}^{D} (\mu + 1)$. We want to write this system of M equations as a matrix equation. For the two

indices (α, β) defining the coefficients of the polynomial fit $A^j_{(\alpha,\beta)}$, we must find an equivalent single index $m = 1, 2, \ldots, M$ to specify the elements of the matrix equation. The equation to convert from the pair of indices (α, β) to the single index m is

$$m(\alpha, \beta) = \beta - D + \sum_{\mu=0}^{\alpha}(D + 1 - \mu) \tag{D.20}$$

Hence, the basis functions of our polynomial fit in second order are given by

$$X_m \equiv x_\alpha x_\beta \tag{D.21}$$

so that in $D = 3$ dimensions we have

$$\mathbf{X^T} = \left(\mathbf{1}, \mathbf{x}, \mathbf{y}, \mathbf{z}, \mathbf{x^2}, \mathbf{xy}, \mathbf{xz}, \mathbf{y^2}, \mathbf{yz}, \mathbf{z^2}\right) \tag{D.22}$$

We will refer to the single index $m = m(\alpha, \beta)$ by the simplified notation $(\alpha\beta)$.

With these simplifications, the matrix equation for a given j can be written

$$\mathbf{M} \cdot \mathbf{A^j} = \mathbf{b^j} - \sum_{\gamma=\mathbf{0}}^{\mathbf{D}} \lambda_\gamma(\mathbf{1} + \delta_{\gamma\mathbf{j}})\mathbf{u}^{(\gamma\mathbf{j})} \tag{D.23}$$

where the $M \times M$ matrix $\mathbf{M}$ has elements given by

$$M_{(\alpha\beta)(\gamma\delta)} = \sum_{i=1}^{N}(x_{i\alpha} - x_{0\alpha})(x_{i\beta} - x_{0\beta})(x_{i\gamma} - x_{0\gamma})(x_{i\delta} - x_{0\delta})W(\mathbf{x_i}, \mathbf{h}) \tag{D.24}$$

and the M-element vector $\mathbf{b^j}$ has elements

$$b^j_{(\alpha\beta)} = \sum_{i=1}^{N} B^j(\mathbf{x_i})(\mathbf{x_{i\alpha}} - \mathbf{x_{0\alpha}})(\mathbf{x_{i\beta}} - \mathbf{x_{0\beta}})\mathbf{W}(\mathbf{x_i}, \mathbf{h}) \tag{D.25}$$

and the M-element vector $\mathbf{u}^{(\gamma\mathbf{j})}$ is a unit vector of all zeros with the value 1 in the mth $=(\gamma j)$th place. Note that if $\gamma > j$, we just switch the values of the

indices to calculate the single index m; this is allowed because the definition of the coefficients $A^j_{\alpha\beta}$ is symmetric with respect to an interchange of the indices α and β.

Inversion of the $M \times M$ matrix $\mathbf{M}$ yields the solution for the vector of coefficients $\mathbf{A^j}$

$$\mathbf{A^j} = \mathbf{M^{-1}} \cdot \mathbf{b^j} - \sum_{\gamma=\mathbf{0}}^{\mathbf{D}} \lambda_\gamma (\mathbf{1} + \delta_{\gamma \mathbf{j}}) \mathbf{M^{-1}} \cdot \mathbf{u}^{(\gamma \mathbf{j})} \tag{D.26}$$

where $\mathbf{A^j}$ depends on the $D+1$ unknown Lagrange Multipliers λ_γ. Each element of this solution can be written in summation form as

$$A^j_{(\alpha\beta)} = \sum_{(\gamma\delta)=0}^{M} M^{-1}_{(\alpha\beta)(\gamma\delta)} b^j_{(\gamma\delta)} - \sum_{\gamma=0}^{D} \lambda_\gamma (1 + \delta_{\gamma j}) \sum_{(\mu\nu)=0}^{M} M^{-1}_{(\alpha\beta)(\mu\nu)} u^{(\gamma j)}_{(\mu\nu)} \tag{D.27}$$

Once again, we employ the fact that in summation formation the components of the unit vector $\mathbf{u}^{(\gamma \mathbf{j})}$ can be written in terms of the Kronecker Delta $u^{(\gamma j)}_{(\mu\nu)} = \delta_{(\gamma j)(\mu\nu)}$ to reduce the above expression to

$$A^j_{(\alpha\beta)} = \sum_{(\gamma\delta)=0}^{M} M^{-1}_{(\alpha\beta)(\gamma\delta)} b^j_{(\gamma\delta)} - \sum_{\gamma=0}^{D} \lambda_\gamma (1 + \delta_{\gamma j}) M^{-1}_{(\alpha\beta)(\gamma j)} \tag{D.28}$$

The constraint of zero magnetic divergence provides $D+1$ constraints on the coefficients $A^j_{\alpha\beta}$. For each $\alpha = 0, 1, \ldots, D$, we have

$$\sum_{j=1}^{D} (1 + \delta_{\alpha j}) A^j_{\alpha j}(\mathbf{x_0}) = \mathbf{0} \tag{D.29}$$

Substituting $A^j_{\alpha j}$ in this equation using the solution above yields, for each $\alpha = 0, 1, \ldots, D$, the equation

$$\sum_{\gamma=0}^{D} \lambda_\gamma \sum_{j=1}^{D} (1 + \delta_{\alpha j})(1 + \delta_{\gamma j}) M^{-1}_{(\alpha j)(\gamma j)} = \sum_{j=1}^{D} (1 + \delta_{\alpha j}) \sum_{(\mu\nu)=0}^{M} M^{-1}_{(\alpha j)(\mu\nu)} b^j_{(\mu\nu)} \tag{D.30}$$

This set of $D+1$ linear equations can be written as a matrix equation

$$\mathbf{N} \cdot \lambda = \mathbf{c} \tag{D.31}$$

where the elements of the $(D+1) \times (D+1)$ matrix $\mathbf{N}$ are given by

$$N_{\alpha\gamma} = \sum_{j=1}^{D} (1 + \delta_{\alpha j})(1 + \delta_{\gamma j}) M^{-1}_{(\alpha j)(\gamma j)} \tag{D.32}$$

and the elements of the $(D+1)$-element vector $\mathbf{c}$ are given by

$$c_\alpha = \sum_{j=1}^{D} (1 + \delta_{\alpha j}) \sum_{(\mu\nu)=0}^{M} M^{-1}_{(\alpha j)(\mu\nu)} b^j_{(\mu\nu)} \tag{D.33}$$

The solution for the vector of Lagrange Multipliers λ is found by inverting the the $(D+1) \times (D+1)$ matrix $\mathbf{N}$,

$$\lambda = \mathbf{N^{-1}} \cdot \mathbf{c} \tag{D.34}$$

In summation form, the solution for each λ_γ is given by

$$\lambda_\gamma = \sum_{\alpha=0}^{D} N^{-1}_{\gamma\alpha} c_\alpha \tag{D.35}$$

Substituting the solution to the Lagrange Multipliers into the solution for the coefficients $A^j_{(\alpha\beta)}$ gives

$$A^j_{(\alpha\beta)} = \sum_{(\gamma\delta)=0}^{M} M^{-1}_{(\alpha\beta)(\gamma\delta)} b^j_{(\gamma\delta)} - \sum_{\gamma=0}^{D} (1 + \delta_{\gamma j}) \sum_{\sigma=0}^{D} N^{-1}_{\gamma\sigma} c_\sigma M^{-1}_{(\alpha\beta)(\gamma j)} \tag{D.36}$$

In matrix form, the solution can be written

$$\mathbf{A^j} = \mathbf{M^{-1}} \cdot \mathbf{b^j} - \sum_{\gamma=\mathbf{0}}^{\mathbf{D}} (\mathbf{1} + \delta_{\gamma\mathbf{j}}) \left(\mathbf{N^{-1}} \cdot \mathbf{c} \right)_\gamma \mathbf{M^{-1}_{(\gamma j)}} \tag{D.37}$$

where $\mathbf{M^{-1}_{(\gamma j)}}$ denotes the (γj)th column of the $M \times M$ matrix $\mathbf{M^{-1}}$ and $\left(\mathbf{N^{-1}} \cdot \mathbf{c}\right)_\gamma$ denotes the γth element of the vector $\mathbf{N^{-1}} \cdot \mathbf{c}$. We also use the definitions

$$c_\alpha = \sum_{k=1}^{D} (1 + \delta_{\alpha k}) \left(\mathbf{M^{-1}} \cdot \mathbf{b^k}\right)_{(\alpha k)} \tag{D.38}$$

$$N_{\alpha\gamma} = \sum_{k=1}^{D} (1 + \delta_{\alpha k})(1 + \delta_{\gamma k}) M^{-1}_{(\alpha k)(\gamma k)} \tag{D.39}$$

$$M_{(\alpha\beta)(\gamma\delta)} = \sum_{i=1}^{N} (x_{i\alpha} - x_{0\alpha})(x_{i\beta} - x_{0\beta})(x_{i\gamma} - x_{0\gamma})(x_{i\delta} - x_{0\delta}) W(\mathbf{x_i}, \mathbf{h}) \tag{D.40}$$

$$b^j_{(\alpha\beta)} = \sum_{i=1}^{N} B^j(\mathbf{x_i})(\mathbf{x_{i\alpha}} - \mathbf{x_{0\alpha}})(\mathbf{x_{i\beta}} - \mathbf{x_{0\beta}}) \mathbf{W}(\mathbf{x_i}, \mathbf{h}) \tag{D.41}$$

D.3 Implementation Notes

The implementation of magnetic divergence correction using Lagrange Multipliers is easily added to a GPM code. The magnetic divergence correction occurs as a secondary step after the three components of the magnetic field have undergone an unconstrained fit. This correction depends only on the values of the uncorrected fit as well as the matrix elements of the inverse spatial matrix $\mathbf{M^{-1}}$.

Although the formulas in terms of the original problem for the divergence corrected fits are complicated, expressed in terms of the uncorrected fits they become simple. I'll denote the uncorrected solutions with the superscript **U** and the corrected values with the superscript **C**.

The first order formula becomes

$$A^{j\mathbf{C}}_\alpha = A^{j\mathbf{U}}_\alpha - \lambda M^{-1}_{\alpha j} \tag{D.42}$$

where the Lagrange Multiplier is given by

$$\lambda = \frac{\sum_{j=1}^{D} A_j^{j\mathbf{U}}}{\sum_{j=1}^{D} M_{jj}^{-1}} \tag{D.43}$$

The second order formula becomes

$$A_{(\alpha\beta)}^{j\mathbf{C}} = A_{(\alpha\beta)}^{j\mathbf{U}} - \sum_{\gamma=0}^{D} \lambda_\gamma (1 + \delta_{\gamma j}) M_{(\alpha\beta)(\gamma j)}^{-1} \tag{D.44}$$

where the Lagrange Multipliers are given by

$$\lambda = \mathbf{N^{-1}} \cdot \mathbf{c} \tag{D.45}$$

where

$$N_{\alpha\gamma} = \sum_{j=1}^{D} (1 + \delta_{\alpha j})(1 + \delta_{\gamma j}) M_{(\alpha j)(\gamma j)}^{-1} \tag{D.46}$$

and

$$c_\alpha = \sum_{j=1}^{D} (1 + \delta_{\alpha j}) A_{(\alpha j)}^{j\mathbf{U}} \tag{D.47}$$

Bibliography

[1] J. A. Adam. Stability of aligned magnetoatmospheric flow. *Journal of Plasma Physics*, 19:77–86, 1978.

[2] J. Adams, U. H. Danielsson, D. Grasso, and H. Rubinstein. Distortion of the acoustic peaks in the cmbr due to a primordial magnetic field. *Physics Letters B*, 388:253–258, 1996.

[3] A. Aguirre, L. Hernquist, J. Schaye, N. Katz, D. H. Weinberg, and J. Gardner. Metal enrichment of the intergalactic medium in cosmological simualtions. *The Astrophysical Journal*, 561:521–549, 2001.

[4] H. Alfven and N. Herlofson. Cosmic radiation and radio stars. *Physical Review*, 78:616–616, 1950.

[5] T. D. Arber, A. W. Longbottom, C. L. Gerrard, and A. M. Milne. A staggered grid, lagrangian-eulerian remap code for 3-d mhd simulation. *Journal of Computational Physics*, 171:151–181, 2001.

[6] E. Athanassoula. The existence and shapes of dust lanes in galactic bars. *Monthly Notices of the Royal Astronomical Society*, 259:345–364, 1992.

[7] E. Athanassoula. Morphology of bar orbits. *Monthly Notices of the Royal Astronomical Society*, 259:328–344, 1992.

[8] N. A. Bahcall. The relation between velocity dispersion and central galaxy density in clusters of galaxies. *The Astrophysical Journal*, 247:787–791, 1981.

[9] S. A. Balbus and J. F. Hawley. A powerful local shear instability in weakly magnetized disks 1. linear analysis. *The Astrophysical Journal*, 376:214–222, 1991.

[10] G. Barnes, K. B. MacGregor, and P. Charbonneau. Gravity waves in a magnetized shear layer. *The Astrophysical Journal*, 498:L169–L172, 1998.

[11] J. D. Barrow, P.G. Ferreira, and J. Silk. Constraints on a primordial magnetic field. *Physical Review Letters*, 78:3610–3613, 1997.

[12] G. K. Batchelor. *Proc. R. Soc. London*, 201:405, 1950.

[13] E. Battaner, J. L. Garrido, M. L. Sanchez-Saavedra, and E. Florido. Magnetic fields in the milky way neighborhood as deduced from warps in spiral galaxies. *Astronomy and Astrophysics*, 251:402–410, 1991.

[14] E. Battaner and H. Lesch. On the physics of primordial magnetic fields. *Anales de Fisica*, 95:213–225, 2000.

[15] S. F. Beaulieu, K. C. Freeman, A. J. Kalnajs, P. Saha, and H.-S. Zhao. Dynamics of the galactic bulge using planetary nebulae. *The Astrophysical Journal*, 120:855–871, 2000.

[16] R. Beck. Magnetic fields in normal galaxies. *Phil. Trans. R. Soc. Lond.*, 358:777–796, 2000.

[17] R. Beck, A. Brandenburg, D. Moss, A. Shukurov, and D. Sokoloff. Galactic magnetism: Recent developments and perspectives. *Annual Review of Astronomy and Astrophysics*, 34:155–206, 1996.

[18] C. M. Bender and S. A. Orszag. *Advanced Mathematical Methods for Scientists and Engineers*. McGraw-Hill, 1978.

[19] M. J. Berger and P. Colella. Local adaptive mesh refinement for shock hydrodynamics. *Journal of Computational Physics*, 82:64–84, 1989.

[20] M. J. Berger and J. Oliger. Adaptive mesh refinement for hyperbolic partial differential equations. *Journal of Computational Physics*, 53:484–512, 1984.

[21] I. B. Bernstein, E. A. Frieman, M. D. Kruskal, and R. M. Kulsrud. *Proceedings of the Royal Society*, A244:17, 1958.

[22] L. Biermann. *Z. Naturforsch*, 5a:65–71, 1950.

[23] J. Binney, O. Gerhard, and D. Spergel. The photometric structure of the inner galaxy. *Monthly Notices of the Royal Astronomical Society*, 288:365–374, 1997.

[24] J. Binney, O. E. Gerhard, A. A. Stark, J. Bally, and K. I. Uchida. Understanding the kinematics of the galactic centre gas. *Monthly Notices of the Royal Astronomical Society*, 252:210–218, 1991.

[25] J. Binney and M. Merrifield. *Galactic Astronomy*. Princeton University Press, Princeton, 1998.

[26] J. Binney and S. Tremaine. *Galactic Dynamics*. Princeton University Press, Princeton, 1987.

[27] N. Bissantz, P. Englmaier, and O. Gerhard. Gas dynamics in the milky way: a second pattern speed and large-scale morphology. *Monthly Notices of the Royal Astronomical Society*, 340:949–968, 2003.

[28] N. Bissantz and O. Gerhard. Spiral arms, bar shape, and bulge microlensing in the milky way. *Monthly Notices of the Royal Astronomical Society*, 330:591–608, 2002.

[29] E. G. Blackman and A. Brandenburg. Dynamic nonlinearity in large scale dynamos with shear. *The Astrophysical Journal*, 579:359–373, 2002.

[30] O. M. Blaes and S. A. Balbus. Local shear instabilities in weakly ionized, weakly magnetized disks. *The Astrophysical Journal*, 421:163–177, 1994.

[31] R. D. Blandford. Magnetic fields in astrophysics. *The Astronomical Journal*, 88:245–252, 1983.

[32] L. Blitz and P. Teuben, editors. *Unsolved problems of the Milky Way*, volume 169 of *Proceedings of the IAU Symposium*, Dordrecht, 1996. Kluwer.

[33] S. Borve, M. Omang, and J. Trulsen. Regularized smoothed particle hydrodynamics. *The Astrophysical Journal*, 561:82–93, 2001.

[34] A. Boulares and D. P. Cox. Galactic hydrostatic equilibrium with magnetic tension and cosmic-ray diffusion. *The Astrophysical Journal*, 365:544–558, 1990.

[35] J. U. Brackbill, D. B. Kothe, and H. M. Ruppel. Flip: a low-dissipation, particle-in-cell method for fluid flow. *Computer Physics Communications*, 48:25–38, 1988.

[36] A. Brandenburg, D. Moss, and A. Shukurov. Galactic fountains as magnetic pumps. *Monthly Notices of the Royal Astronomical Society*, 276:651–662, 1995.

[37] M. Brio and C.C. Wu. An upwind differencing scheme for the equations of ideal magnetohydrodynamics. *Journal of Computational Physics*, 75:400–422, 1988.

[38] W. B. Burton and H. S. Liszt. The gas distribution in the central region of the galaxy. i. atomic hydrogen. *The Astrophysical Journal*, 225:815–842, 1978.

[39] P. Caligari, F. Moreno-Insertis, and M. Schussler. Emerging flux tubes in the solar convection zone. i. asymmetry, tilt, and emergence latitude. *The Astrophysical Journal*, 441:886–902, 1995.

[40] P. S. Cally. Complex eigenvalue bounds in magnetoatmospheric shear flow. i. *Geophysical and Astrophysical Fluid Dynamics*, 23:43–55, 1983.

[41] P. S. Cally and J. A. Adam. Complex eigenvalue bounds in magnetoatmospheric shear flow. ii. *Geophysical and Astrophysical Fluid Dynamics*, 23:57–67, 1983.

[42] C. L. Carilli, R. A. Perley, and J. H. Dreher. Discovery of the bow shock of cygnus a. *The Astrophysical Journal*, 334:L73–L76, 1988.

[43] C. L. Carilli and G. B. Taylor. Cluster magnetic fields. *Annual Review of Astronomy and Astrophysics*, 40:319–348, 2002.

[44] F. Cattaneo, T. Chiueh, and D.W. Hughes. Buoyancy driven instabilities and nonlinear breakup of a sheared magnetic layer. *Journal of Fluid Mechanics*, 219:1–23, 1990.

[45] F. Cattaneo and D.W. Hughes. The nonlinear breakup of a magnetic layer: Instability to interchange modes. *Journal of Fluid Mechanics*, 196:323–344, 1988.

[46] F. Cattaneo and S. I. Vainshtein. Suppresion of turbulent transport by a weak magnetic field. 376:L21–L24, 1991.

[47] J. Centrella and J. R. Wilson. Planar numerical cosmology. ii. the difference equations and numerical tests. *The Astrophysical Journal Supplement*, 54:229–249, 1984.

[48] B. D. G. Chandran, S. C. Cowley, and M. Morris. Magnetic flux accumulation at the galactic center and its implications for the strength of the pregalactic magnetic field. *The Astrophysical Journal*, 528:723–733, 2000.

[49] S. Chandrasekhar. *Proceedings of National Academy of Science*, 46:253, 1960.

[50] S. Chandrasekhar. *Hydrodynamic and Hydromagnetic Stability*. Oxford University Press, 1961.

[51] P. Charbonneau and K. B. MacGregor. On the generation of equipartition-strength magnetic fields by turbulent hydromagnetic dynamos. *The Astrophysical Journal*, 473:L59–L62, 1996.

[52] D. A. Clarke. Jets in extragalactic radio sources. In H. K. R editor, *Jets in Extragalactic Radio Sources: Ringberg Workshop Proceedings*. Springer, 1993.

[53] C. A. Clarkson and A. A. Coley. Magnetic fields and the cosmic microwave background. *Classical and Quantum Gravity*, 18:1305–1310, 2001.

[54] A. W. Clegg, J. M. Cordes, J. H. Simonetti, and S. R. Kulkarni. Rotation measures of low latitude extragalactic sources and the magnetoionic structure of the galaxy. *The Astrophysical Journal*, 386:143–157, 1992.

[55] S.A. Colgate, H. Li, and V. Pariev. The origin of the magnetic fields of the universe: The plasma astrophysics of the free energy of the universe. *Physics of Plasmas*, 8:2425–2431, 2001.

[56] S. C. Cowley, R.M. Kulsrud, and R. Sudan. Considerations of ion-temperature-gradient-driven turbulence. *Physics of Fluids B*, 3:2767–2782, 1991.

[57] T. G. Cowling. *J. Mech. Appl. Math.*, 10:129, 1957.

[58] A. N. Cox, editor. *Allen's Astrophysical Quantities*. Springer, Berlin, 4th edition, 1999.

[59] G. Davies and L. M. Widrow. A possible mechanism for generating galactic magnetic fields. *The Astrophysical Journal*, 540:755–764, 2000.

[60] R. D. Davies. *Nature*, 218:435, 1968.

[61] G. de Vaucouleurs and K. C. Freeman. *Vistas in Astronomy*, 14:163–290, 1972.

[62] W. Dehnen and J. Binney. Mass models of the milky way. *Monthly Notices of the Royal Astronomical Society*, 294:429–438, 1998.

[63] G. A. Dilts. Moving-least-squares-particle hydrodynamics. i. consistency and stability. *Int. J. Numer. Meth. Engng.*, 44:1115–1155, 1999.

[64] G. A. Dilts. Moving least-squares particle hydrodynamics. ii. conservation and boundaries. *Int. J. Numer. Meth. Engng.*, 48:1503–1524, 2000.

[65] G. A. Dilts. private communication, 2002.

[66] G. A. Dilts, A. Haque, and J. Wallin. Report, Los Alamos National Laboratory, 2001.

[67] P. Englmaier and O. Gerhard. Two modes of gas flow in a single barred galaxy. *Monthly Notices of the Royal Astronomical Society*, 287:57–68, 1997.

[68] P. Englmaier and O. Gerhard. Gas dynamics and large-scale morphology of the milky way galaxy. *Monthly Notices of the Royal Astronomical Society*, 304:512–534, 1999.

[69] J. Fan and I. Gijbels. *Local Polynomial Modelling and Its Applications*. Chapman and Hall, New York, 1996.

[70] E. Fermi. *Physical Review*, 75:1169, 1949.

[71] G. B. Field and E. G. Blackman. Dynamical quenching of the α^2 dynamo. *The Astrophysical Journal*, 572:685–692, 2002.

[72] O. Gerhard. Mass distribution in our galaxy. *Space Science Reviews*, 100:129–138, 2002.

[73] P. A. Gilman and Fox P. A. Joint instability of latitudinal differential rotation and toroidal magnetic fields below the solar convection zone. *The Astrophysical Journal*, 484:439–454, 1997.

[74] R. A. Gingold and J. J. Monaghan. Smoothed particle hydrodynamics: Theory and application to non-spherical stars. *Monthly Notices of the Royal Astronomical Society*, 181:375–389, 1977.

[75] N. Y. Gnedin. Softened lagrangian hydrodynamics for cosmology. *The Astrophysical Journal Supplement*, 97:231–257, 1995.

[76] N. Y. Gnedin, A. Ferrara, and E. G. Zweibel. Generation of the primordial magnetic fields during cosmological reionization. *The Astrophysical Journal*, 539:505–516, 2000.

[77] P. Goldreich and D. Lynden-Bell. I. gravitational stability of uniformly rotating disks. *Monthly Notices of the Royal Astronomical Society*, 130:97–124, 1965.

[78] P. Goldreich and D. Lynden-Bell. Ii. spiral arms as sheared gravitational instabilities. *Monthly Notices of the Royal Astronomical Society*, 130:125–158, 1965.

[79] P. F. Goldsmith. In D. J. Hollenbach and Jr. H. A. Thronson, editors, *Interstellar Processes*, page 51. Reidel, Dordrecht, 1987.

[80] D. Grasso and H. R. Rubinstein. Magnetic fields in the ealry universe. *Physics Reports*, 348:163–266, 2001.

[81] P. A. Hamilton and A. G. Lyne. Faraday rotation measurements on 163 pulsars. *Monthly Notices of the Royal Astronomical Society*, 224:1073–1081, 1987.

[82] J. L. Han and G. J. Qiao. The magnetic field in the disk of our galaxy. *Astronomy and Astrophysics*, 288:759–772, 1994.

[83] A. B. Hassam. Stabilization of tokamak microturbulence by driven poloidal rotation. *Comments on Plasma Physics and Controlled Fusion*, 14:275–286, 1991.

[84] A. B. Hassam. Poloidal rotation of tokamak plasmas at super poloidal sonic speeds. *Nuclear Fusion*, 36:707–720, 1996.

[85] A. B. Hassam. Velocity shear stabilization of interchange modes in elongated plasma configurations. *Physics of Plasmas*, 6:3772–3777, 1999.

[86] Y.-Y. Hayashi and W. R. Young. Stable and unstable shear modes of rotating parallel flows in shallow water. *Journal of Fluid Mechanics*, 184:477–504, 1987.

[87] C. Heiles. Supernovae versus models of the interstellar medium and the gaseous halo. *The Astrophysical Journal*, 315:555–566, 1987.

[88] A. M. Howard and R. M. Kulsrud. The evolution of a primordial galactic magnetic field. *The Astrophysical Journal*, 483:648–665, 1997.

[89] D.W. Hughes and F. Cattaneo. A new look at the instability of a stratified horizontal magnetic field. *Geophysical and Astrophysical Fluid Dynamics*, 39:65–81, 1987.

[90] E. Hummel. In G. Fabbians and *et. al.*, editors, *Windows on Galaxies*, page 141. Kluwer, Dordrecht, 1990.

[91] E. L. Ince. *Ordinary Differential Equations*. Dover, 1926.

[92] A. Jenkins and J. Binney. Dynamics of gas near the galactic centre. *Monthly Notices of the Royal Astronomical Society*, 270:703–719, 1994.

[93] T. J. Jones, D. Klebe, and J. M. Dickey. Infrared polarimetry and the galactic magnetic field. ii. improved models. *The Astrophysical Journal*, 389:602–615, 1992.

[94] A. P. Kazantsev. *Sov. Phys. JETP*, 26:1031, 1968.

[95] K. O. Keipenheuer. Cosmic rays as the source of general galactic radio emission. *Physical Review*, 79:738–739, 1950.

[96] R. C. Kennicut. Star formation in galaxies along the hubble sequence. *Annual Review of Astronomy and Astrophysics*, 36:189–231, 1998.

[97] L. L. Kitchatinov and G. Rüdiger. Global magnetic shear instability in spherical geometry. *Monthly Notices of the Royal Astronomical Society*, 286:757–764, 1997.

[98] U. Klein, R. F. Hayes, R. Wielebinski, and D. Meinert. A radio continuum survey of the magellenic clouds. *Astronomy and Astrophysics*, 271:402–412, 1993.

[99] U. Klein, R. Wielebinski, and R. Beck. A survey of the distribution of λ 2.8 cm radio continuum in nearby galaxies. *Astronomy and Astrophysics*, 133:19–26, 1984.

[100] U. Klein, R. Wielebinski, R. F. Hayes, and D. F. Malin. A new radio continuum survey of the magellenic clouds at 1.4 ghz. *Astronomy and Astrophysics*, 211:280–292, 1989.

[101] A. Kosowsky and A. Loeb. Faraday rotation of microwave background polarization by a primordial magnetic field. *The Astrophysical Journal*, 469:1–6, 1996.

[102] F. Krause. *Interstellar Magnetic Fields*. Springer, Berlin, 1987.

[103] M. Krause, R. Beck, and E. Hummel. The magnetic field structures in two nearby spiral galaxies ii: The bisymmetric spiral magnetic field in m82. *Astronomy and Astrophysics*, 217:17–30, 1989.

[104] P. P. Kronberg. *International Astronomical Union Symposium*, 140:187, 1976.

[105] P. P. Kronberg. Extragalactic magnetic fields. *Rep. Prog. Phys.*, 57:325–382, 1994.

[106] P. P. Kronberg. Intergalactic magnetic fields. *Physics Today*, 55(12), 2002.

[107] P. P. Kronberg, Q. W. Dufton, H. Li, and S. A. Colgate. Magnetic energy of the intergalactic medium from galactic black holes. *The Astrophysical Journal*, 57:178–186, 2001.

[108] P. P. Kronberg, H. Lesch, and U. Hopp. Magnetization of the intergalactic medium by primeval galaxies. *The Astrophysical Journal*, 511:56–64, 1999.

[109] P. P. Kronberg and M. Simard-Normandin. New evidence on the origin of rotation measures in extragalctic radio sources. *Nature*, 263:653–656, 1976.

[110] S. Kulkarni and C. Heiles. In D. J. Hollenbach and Jr. H. A. Thronson, editors, *Interstellar Processes*, page 87. Reidel, Dordrecht, 1987.

[111] R. M. Kulsrud and S. W. Anderson. The spectrum of random magnetic fields in the mean field dynamo theory of the galactic magnetic field. *The Astrophysical Journal*, 396:606–630, 1992.

[112] R. M. Kulsrud, R. Cen, J. P. Ostriker, and D. Ryu. The protogalactic origin for cosmic magnetic fields. *The Astrophysical Journal*, 480:481–491, 1997.

[113] R. M. Kulsrud, S. C. Cowley, A. V. Gruzinov, and R. N. Sudan. Dynamos and cosmic magnetic fields. *Phys. Rep.*, 283:213–226, 1997.

[114] N. Lanson and J. P. Vila. Meshless methods for conservation laws. *Mathematics and Computers in Simulation*, 55:493–501, 2001.

[115] J. N. Leboeuf, T. Takima, and J. M. Dawson. A magnetohydrodynamic particle code for fluid simulation of plasmas. *Journal of Computational Physics*, 31:379–408, 1979.

[116] C.W. Lee, H.M.Lee, H. B. Ann, and K.H. Kwon. Smoothed particle hydrodynamic simulations of galactic gaseous disk with bar: Distribution and kinematic structure of molecular clouds toward the galactic center. *The Astrophysical Journal*, 513:242–251, 1999.

[117] H. Lesch and G. T. Birk. Can large-scale magnetic fields survive during the pre-recombination era of the universe. *Physics of Plasmas*, 5:2773–2776, 1998.

[118] H. Lesch, A. Crusius, R. Schlickeiser, and R. Wielebinski. Ring currents and poloidal magnetic fields in nuclear regions of galaxies. *Astronomy and Astrophysics*, 217:99–107, 1989.

[119] H. S. Liszt and W. B. Burton. The gas distribution in the central region of the galaxy. iii. a barlike model of the inner-galaxy gas based on improved h i data. *The Astrophysical Journal*, 236:779–797, 1980.

[120] N. Loiseau, U. Klein, A. Greybe, R. Wiebelinski, and R. F. Haynes. Thermal and nonthermal emission from the small magellenic cloud. *Astronomy and Astrophysics*, 178:62–76, 1987.

[121] S. H. Lubow, J. C. B. Papaloizou, and J. E. Pringle. Magnetic field dragging in accretion discs. *Monthly Notices of the Royal Astronomical Society*, 267:235–240, 1994.

[122] L. B. Lucy. A numerical approach to the testing of the fission hypothesis. *The Astronomical Journal*, 82:1013–1024, 1977.

[123] J. Maron, S. Cowley, and J. McWilliams. The nonlinear magnetic cascade. *The Astrophysical Journal*, 603:569–583, 2004.

[124] J. L. Maron and P. M. Goldreich. Incompressible mhd turbulence. *The Astrophysical Journal*, 554:1175–1196, 2001.

[125] J. L. Maron and G. G. Howes. Gradient particle magnetohydrodynamics: A lagrangian particle code for astrophysical magnetohydrodynamics. *The Astrophysical Journal*, 595:564–572, 2003.

[126] R. Häfner, N. Wyn Evans, W. Dehnen, and J. Binney. A dynamical model of the inner galaxy. *Monthly Notices of the Royal Astronomical Society*, 314:433–452, 2000.

[127] A. Schlüter and L. Biermann. *Z. Naturforsch.*, 5A:237, 1950.

[128] R. L. Miller, F. L. Waelbroeck, A. B. Hassam, and R. E. Waltz. Stabilization of ballooning modes with sheared toroidal rotation. *Physics of Plasmas*, 2:3676–3684, 1995.

[129] A. H. Minter and S. R. Spangler. Observations of turbulent fluctuations in the interstellar plasma density and magnetic field on spatial scales of 0.01 to 100 parsecs. *The Astrophysical Journal*, 458:194–214, 1996.

[130] H. K. Moffatt. *Magnetic Field Generation in Electrically Conducting Fluids*. Cambridge University Press, Cambridge, 1978.

[131] J. J. Monaghan. Particle methods for hydrodynamics. *Computer Physics Reports*, 3:71–124, 1985.

[132] J. J. Monaghan. Smoothed particle hydrodynamics. *Annual Review of Astronomy and Astrophysics*, 30:543–574, 1992.

[133] J. J. Monaghan and R.A. Gingold. Shock simulation by the particle method sph. *Journal of Computational Physics*, 52:374–389, 1983.

[134] M. Morris and E. Serabyn. The galactic center environment. *Annual Review of Astronomy and Astrophysics*, 34:645–701, 1996.

[135] D. Moss, A. Brandenburg, K. J. Donner, and M. Tomasson. Models for the magnetic field of m81. *The Astrophysical Journal*, 409:179–189, 1993.

[136] T. Ch. Mouschovias. In A. Ferrara, C. F. McKee, C. Heiles, and P. R. Shapiro, editors, *The Physics of the Interstellar Medium and Intergalactic Medium*, volume 80 of *ASP Conference Series*, page 184, San Francisco, 1995. Astronomical Society of the Pacific.

[137] A. H. Nelson. In R. Beck and R. Gräve, editors, *Interstellar Magnetic Fields*, page 142. Springer, Berlin, 1993.

[138] A. Neufeld, S. Lepp, and G. J. Melnick. Thermal balance in dense molecular clouds: Radiative cooling rates and emission line luminosities. *The Astrophysical Journal Supplement*, 100:132–147, 1995.

[139] W. A. Newcomb. *Physics of Fluids*, 4:391, 1961.

[140] H. Ohno and S. Shibata. The random magnetic field in the galaxy. *Monthly Notices of the Royal Astronomical Society*, 262:953–962, 1993.

[141] T. Papayannopoulos and M. Petrou. On the nature of orbits in realistic bar potentials. *Astronomy and Astrophysics*, 119:21–27, 1983.

[142] E. N. Parker. The dynamical state of the interstellar gas and field. iv. evolution of the disk of interstellar gas. *The Astrophysical Journal*, 154:49–56, 1968.

[143] E. N. Parker. Extragalactic cosmic rays and the galactic magnetic field. *Astrophysics and Space Science*, 24:279–288, 1973.

[144] E. N. Parker. The generation and dissipation of solar and galactic magnetic fields. *Astrophysics and Space Science*, 22:279–291, 1973.

[145] E. N. Parker. *Cosmical Magnetic Fields: Their Origin and Activity*. Clarendon, Oxford, 1979.

[146] E. N. Parker. Fast dynamos, cosmic rays, and the galactic magnetic field. *The Astrophysical Journal*, 401:137–145, 1992.

[147] E. N. Parker. A solar dynamo surface wave at the interface between convection and nonuniform rotation. *The Astrophysical Journal*, 408:707–719, 1993.

[148] P. A. Patsis and E. Athanassoula. Sph simulations of gas flow in barred galaxies. effect of hydrodynamical and numerical parameters. *Astronomy and Astrophysics*, 358:45–56, 2000.

[149] L. Perek. Distribution of mass in oblate stellar systems. *Advances in Astronomy and Astrophysics*, 1:165–287, 1962.

[150] R. E. Peterkin, M. H. Frese, and C. R. Sovinec. Transport of magnetic flux in an arbitrary coordinate ale code. *Journal of Computational Physics*, 140:148–171, 1998.

[151] G. J. Phillips and J. J. Monaghan. A numerical method for three-dimensional simulations of collapsing, isothermal, magnetic gas clouds. *Monthly Notices of the Royal Astronomical Society*, 216:883–895, 1985.

[152] J. H. Piddington. The galactic magnetic field and cosmic rays. *Australian Journal of Physics*, 23:731–750, 1970.

[153] W. A. Press, S. A. Teukolsky, W. T. Vetterling, and B. P. Flannery. *Numerical Recipes in C: The Art of Scientific Computing*. Cambridge University Press, Cambridge, second edition, 1992.

[154] R. Rand and A. G. Lyne. New rotation measures of distant pulsars in the inner galaxy and magnetic field reversals. *Monthly Notices of the Royal Astronomical Society*, 268:497–505, 1994.

[155] R. J. Rand and S. R. Kulkarni. The local galactic magnetic field. *The Astrophysical Journal*, 343:760–772, 1989.

[156] R. J. Reynolds. The power requirement of the free electron layer in the galactic disk. *The Astrophysical Journal*, 349:L17–L19, 1990.

[157] P. J. Roache. *Computational Fluid Dynamics*. Hermosa, Albequerque, 1975.

[158] K. V. Roberts and J. B. Taylor. *Physics of Fluids*, 8:315, 1965.

[159] A. A. Ruzmaikin, A. M. Shukurov, and D. D. Sokoloff. *Magnetic Fields of Galaxies*. Kluwer, Dordrecht, 1988.

[160] A. A. Ruzmaikin, A. M. Shukurov, and D. D. Sokoloff. The dynamo origin of magnetic fields in galaxy clusters. *Monthly Notices of the Royal Astronomical Society*, 241:1–14, 1989.

[161] A. Sandage. *The Hubble Atlas of Galaxies*. Carnegie Institute of Washington, Washington DC, 1961.

[162] A. A. Schekochihin, S. C. Cowley, J. L. Maron, and J. C. McWilliams. Saturated state of the nonlinear small-scale dynamo. *Physical Review Letters*, 92:084504/1–4, 2004.

[163] M. Schmidt. The rate of star formation. *The Astrophysical Journal*, 129:243–58, 1959.

[164] J. Schou et al. Helioseismic studies of differential rotation in the solar envelope by the solar oscillations investigation using the michelson doppler imager. *The Astrophysical Journal*, 505:390–417, 1998.

[165] M. Schussler, P. Caligari, A. Ferriz-Mas, and F. Moreno-Insertis. Instability and eruption of magnetic flux tubes in the solar convection zone. *Astronomy and Astrophysics*, 281:L69–L72, 1994.

[166] K. Schwarzschild. *Nachr. Kgl. Ges. Wiss. Göttingen*, page 41, 1906.

[167] J. Schwinger. On the classical radiation of accelerated electrons. *Physical Review*, 75:1912–1925, 1949.

[168] P. R. Shapiro and G. B. Field. Consequences of a new hot component of the interstellar medium. *The Astrophysical Journal*, 205:762–765, 1976.

[169] I. S. Shklovskii. *Ast. Zhur. SSSR*, 30:577, 1953.

[170] F. H. Shu. The parker instability in differentially-rotating disks. *Astronomy and Astrophysics*, 33:55–72, 1974.

[171] F. H. Shu. *The Physics of Astrophysics Volume II: Gas Dynamics*. University Science Books, Sausalito, 1992.

[172] M. Simard-Normandin and P. P. Kronberg. Rotation measures and the galactic magnetic field. *The Astrophysical Journal*, 242:74–94, 1980.

[173] G. A. Sod. A survey of several finite difference methods for systems of nonlinear hyperbolic conservation laws. *Journal of Computational Physics*, 27:1–31, 1978.

[174] Y. Sofue and M. Fujimoto. The vertical large-scale magnetic fields in spiral galaxies. *Publications of the Astronomical Society of Japan*, 39:843–848, 1987.

[175] Y. Sofue, M. Fujimoto, and R. Wielebinski. Global structure of magnetic fields in spiral galaxies. *Annual Review of Astronomy and Astrophysics*, 24:459–497, 1986.

[176] E. A. Spiegel and J.-P. Zahn. The solar tachocline. *Astronomy and Astrophysics*, 265:106–114, 1992.

[177] T. A. T. Spoelstra. Linear polarization of the galactic radio emission at frequencies between 408 and 1411 mhz. ii. discussion. *Astronomy and Astrophysics*, 135:238–248, 1984.

[178] R. F. Stellingwerf and R. E. Peterkin. Technical report, Mission Research Corporation, Albequerque, 1990.

[179] M. Struble and H. Rood. A compilation of redshifts and velocity dispersions for abell clusters (epoch 1991.2). *The Astrophysical Journal Supplement*, 77:363–377, 1991.

[180] K. Subramanian and J. D. Barrow. Microwave background signals from tangled magnetic fields. *Physical Review Letters*, 81:3575–3578, 1998.

[181] K. Subramanian, D. Narasimha, and S. M. Chitre. Thermal generation of cosmological seed magnetic fields in ionization fronts. *Monthly Notices of the Royal Astronomical Society*, 271:L15–L18, 1994.

[182] G. B. Taylor and R. A. Perley. Magnetic fields in the hydra a cluster. *The Astrophysical Journal*, 416:554–562, 1993.

[183] C. Terquem and J.C.B. Papaloizou. On the stability of an accretion disk containing a toroidal magnetic field. *Monthly Notices of the Royal Astronomical Society*, 279:767–84, 1996.

[184] M. J. Thompson et al. Differential rotation and dynamics of the solar interior. *Science*, 272:1300–1305, 1996.

[185] A. Toomre. On the gravitational stability of a disk of stars. *The Astrophysical Journal*, 139:1217–1238, 1964.

[186] V. A. Urpin. On the hydromagnetic stability of weakly magnetized stellar radiative zones. *Monthly Notices of the Royal Astronomical Society*, 280:149–152, 1996.

[187] S. I. Vainshtein and F. Cattaneo. Nonlinear restrictions on dynamo action. *The Astrophysical Journal*, 393:165–171, 1992.

[188] E. P. Velikhov. *Soviet Physics JETP*, 36:995, 1959.

[189] J. VonNeumann and R. D. Richtmeyer. A method for the numerical calculation of hydrodynamic shocks. *Journal of Applied Physics*, 21:232–237, 1950.

[190] F. L. Waelbroeck and L. Chen. Ballooning instabilities in tokamaks with sheared toroidal flows. *Physics of Fluids B*, 3:601–610, 1991.

[191] E. L. Wright. Brief history of the universe. private communication, 2004.

[192] D. S. De Young. Turbulent generation of magnetic fields in extended extragalactic radio sources. *The Astrophysical Journal*, 241:81–97, 1980.

[193] Y. B. Zeldovitch. *Sov. Phys. JETP*, 4:460, 1957.

[194] E. G. Zweibel. In A. Ferrara, C. F. McKee, C. Heiles, and P. R. Shapiro, editors, *The Physics of the Interstellar Medium and Intergalactic Medium*, volume 80 of *ASP Conference Series*, pages 524–544, San Francisco, 1995. Astronomical Society of the Pacific.

[195] E. G. Zweibel and C. Heiles. Magnetic fields in galaxies and beyond. *Nature*, 385:131–136, 1997.

[196] E. G. Zweibel, R. M. Kulsrud, and E. N. Parker. The stabilizing effect of reacceleration, microturbulence, and rotation on parker's instability. *The Astrophysical Journal*, 201:63–73, 1975.

[197] E. G. Zweibel and C. F. McKee. Equipartition of energy for turbulent astrophysical fluids: Accounting for the unseen energy in molecular clouds. *The Astrophysical Journal*, 439:779–765, 1995.